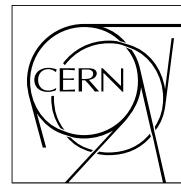


The Compact Muon Solenoid Experiment
Analysis Note

The content of this note is intended for CMS internal use and distribution only



31 May 2019 (v8, 07 May 2020)

Searches for heavy resonances decaying into a Z boson and Higgs boson in the semileptonic final states with RunII data

Pascal Baertschi, Alberto Zucchetta, Ben Kilminster

Abstract

This analysis note describes the search for heavy resonances decaying into a Z boson and a Higgs boson, where the Z boson decays leptonically (electrons, muons or neutrinos) and the Higgs either decays hadronically into pair of b-quarks or the inclusive decay channel. Final states with either two or zero leptons and a Higgs-tagged jet are investigated. The search is performed in the boosted regime for resonances with mass larger than 800 GeV up to 5 TeV. Model-independent upper limits are derived as a function of the resonance mass and natural width, and interpreted within the Heavy Vector Triplet theoretical framework.

1 Contents

2	1	Introduction	4
3	1.1	Theoretical motivations	4
4	2	Datasets and samples	7
5	2.1	Signal	7
6	2.2	Background samples	10
7	2.3	Data	18
8	2.4	Trigger	19
9	3	Physics objects	25
10	3.1	Vertex and Pile-up	25
11	3.2	Electrons	25
12	3.3	Muons	31
13	3.4	Taus	36
14	3.5	Jets	36
15	3.6	Jet pile-up mitigation	36
16	3.7	b-tagging	37
17	3.8	Missing Energy	40
18	3.9	VBF	40
19	4	Boson reconstruction	48
20	4.1	Z boson to neutrinos	48
21	4.2	Z boson to leptons	48
22	4.3	Higgs reconstruction	48
23	5	Event selection	49
24	5.1	Leptonic selection	49
25	5.2	Hadronic selection	49
26	5.3	Topology and event cleaning	50
27	6	Data-simulation comparison	53
28	6.1	2016	53
29	6.2	2017	79
30	6.3	2018	105
31	7	Top control regions	131
32	8	Alpha ratio background prediction	137
33	8.1	Background normalization	138
34	8.2	Background shape	149
35	8.3	Background prediction	163
36	8.4	Alpha method validation	167
37	8.5	Signal modeling	172
38	9	Systematic uncertainties	184
39	9.1	Main background uncertainties	184
40	9.2	Triggers	185
41	9.3	Leptons	185
42	9.4	Jet energy scale and resolution	186
43	9.5	Jet mass scale and resolution	186

44	9.6	Higgs mass extrapolation uncertainty	187
45	9.7	b-tagging	187
46	9.8	Missing Energy	188
47	9.9	Prefire	188
48	9.10	Pile-up	188
49	9.11	QCD renormalization and factorization scale	189
50	9.12	Uncertainties on the alpha	190
51	9.13	Summary	190
52	10	Results	194
53	10.1	Fit pulls	199
54	10.2	Impacts	202
55	10.3	Bias tests	204
56	10.4	Goodness of fit	204
57	11	Summary	207

DRAFT

58 General information

59 Data:

- 60 • NanoAOD2016B-H (35.9 fb^{-1})
- 61 • NanoAOD2017B-F (41.5 fb^{-1})
- 62 • NanoAOD2018A-D (59.7 fb^{-1})

63 Monte Carlo:

- 64 • RunIISummer16NanoAODv6-PUMoriond17_Nano25Oct2019_102X_mcRun2_asymptotic_v7-
v1
- 65 • RunIIFall17NanoAODv6-PU2017_12Apr2018_Nano25Oct2019_102X_mc2017_realistic_v7-
v1
- 66 • RunIIAutumn18NanoAODv6-Nano25Oct2019_102X_upgrade2018_realistic_v19-
v1

70 Pile-up: minimum bias cross section 69200 mb, full dataset profile

71 Background estimation: “alpha” method

72 Open items:

73 Changes with respect to v1:

- 74 • Added QCD and EWK correction for DY samples
- 75 • Removed OR with MET triggers
- 76 • Added OR with Photon triggers for SingleElectron
- 77 • Changed electron trigger SF to approved by EGammaPOG ones
- 78 • Added VBF Control plots
- 79 • Fixed lepton isolation for Higgs jet

80 Changes with respect to v2:

- 81 • Added VBF control plots
- 82 • Section about Prefiring added

83 Changes with respect to v3:

- 84 • added additional information as requested by Object contacts
- 85 • NanoAODv6 samples used
- 86 • fixed b-tagging scale factor and uncertainty
- 87 • Tuning of fits
- 88 • Section on Jet energy scale and resolution, Jet mass scale and resolution
and Higgs mass extrapolation uncertainty added

90 Changes with respect to v4:

- 91 • Information about uncertainty on alpha added
- 92 • Sections about Bias test and Goodness of fit added

93 Changes with respect to v5:

- 94 • Exclusion limit added for no VBF and VBF signal only
- 95 • Bias test for VBF signal only added

96 Changes with respect to v6:

- 97 • Fisher F-test for fit to data added
- 98 • Cross sections for VBF signal added
- 99 • top SF for VBF added

¹⁰⁰ **Changes with respect to v7:**

- ¹⁰¹ • Unblinded results

¹⁰² 1 Introduction

¹⁰³ This analysis searches for signal of heavy resonances decaying into a Z boson (denoted as Z)
¹⁰⁴ and a Higgs boson (H). In turn, the Z boson is identified through its leptonic decays ($\ell = e, \mu$)
¹⁰⁵ or a pair of neutrinos ($\nu\bar{\nu}$). The Higgs boson H is expected to hadronically decay primarily into
¹⁰⁶ a pair of b-quarks. The investigated final states consists of two b-quarks or the inclusive decay
¹⁰⁷ channel and zero or two charged leptons. In the case of the zero-lepton channel, a large amount
¹⁰⁸ of missing energy is measured in the detector. In the leptonic channels, leptons are identified in
¹⁰⁹ the detector and limit the presence of the background, while the hadronic Higgs decay collects
¹¹⁰ the largest possible fraction of Higgs events.

¹¹¹ The search is performed by examining the distribution of the reconstructed ($m_{\ell\ell bb}/m_{\ell\ell jj}$) or
¹¹² transverse mass (m_{vvbb}^T/m_{vvjj}^T) for a localized excess using data measured in 2016, 2017 and
¹¹³ 2018 combined in one dataset. The signal strength and the background normalization are
¹¹⁴ determined from data in appropriate control regions built from the jet mass sidebands, and
¹¹⁵ extrapolated to the signal region through extrapolation functions derived from Monte Carlo
¹¹⁶ (“ α -method”).

¹¹⁷ 1.1 Theoretical motivations

¹¹⁸ 1.1.1 Heavy Vector Triplet

¹¹⁹ Although the Higgs boson discovery by the ATLAS and CMS [1–3] collaborations imposes
¹²⁰ strong constraints on theories beyond the Standard Model (SM), the extreme fine tuning in
¹²¹ quantum corrections required to have a light fundamental Higgs boson with mass close to
¹²² 125 GeV [4–7] suggests that the SM may be incomplete, and not valid beyond a scale of a
¹²³ few TeV. Various dynamical electroweak symmetry breaking scenarios which attempt to solve
¹²⁴ this naturalness problem, such as Minimal Walking Technicolor [8–10], Little Higgs [11–13], or
¹²⁵ composite Higgs models [14–16], predict the existence of new resonances decaying to a vector
¹²⁶ boson plus a Higgs boson.

¹²⁷ The result of the search is primarily interpreted in a model-independent way within a sim-
¹²⁸ plified approach based on a phenomenological Lagrangian that incorporates Heavy Vector
¹²⁹ Triplets (HVT) [17]. In these models, new heavy vector bosons (V^\pm, V^0) that couple to the
¹³⁰ Higgs and SM gauge bosons with the parameters g_V and c_H and to the fermions via the com-
¹³¹ bination $(g_2/g_V)c_F$. The parameter g_V represents the strength of the new vector boson interac-
¹³² tion, while c_H and c_F represent the couplings to the Higgs and the fermions respectively, and
¹³³ are expected to be of order unity in most models.

The additional Lagrangian term resulting from the introduction of the heavy triplet has the form:

$$\begin{aligned} \mathcal{L}_V = & -\frac{1}{4}D_\mu V_\nu^a D^\mu V^{\nu a} + \frac{m_V^2}{2} V_\mu^a V^{\mu a} \\ & + ig_V c_H V_\mu^a H^\dagger \tau^a \bar{D}^\mu H + \frac{g^2}{g_V} c_F V_\mu^a \sum_f \bar{f}_L \gamma^\mu \tau^a f_L \\ & + \frac{g_V}{2} c_{VVV} \epsilon_{abc} V_\mu^a V_\nu^b D^\mu V^{\nu c} + \text{quadrilinear terms} \end{aligned}$$

- ¹³⁴ Two benchmark models [17] are considered. In the first model, referred to as model A, the
¹³⁵ branching fractions to fermions and gauge bosons are comparable, as in some extensions of the
¹³⁶ SM gauge group [18]. In this weakly coupled model, $g_V \sim g \sim 1$, $c_H = -g^2/g_V^2$, $c_F \sim 1$
¹³⁷ For model B, fermionic couplings are suppressed, as for example in a composite Higgs model.
¹³⁸ Vector bosons then are strongly coupled, leading to $g_V \lesssim 4\pi$, $c_H \sim c_F \sim 1$. This model B is
¹³⁹ particularly interesting for the present search, since it predicts signal cross sections in the order
¹⁴⁰ of fb for resonances up to $2 \sim 3$ TeV, branching ratios to vector bosons close to the unity, and
¹⁴¹ thus being accessible at the LHC Run-II.

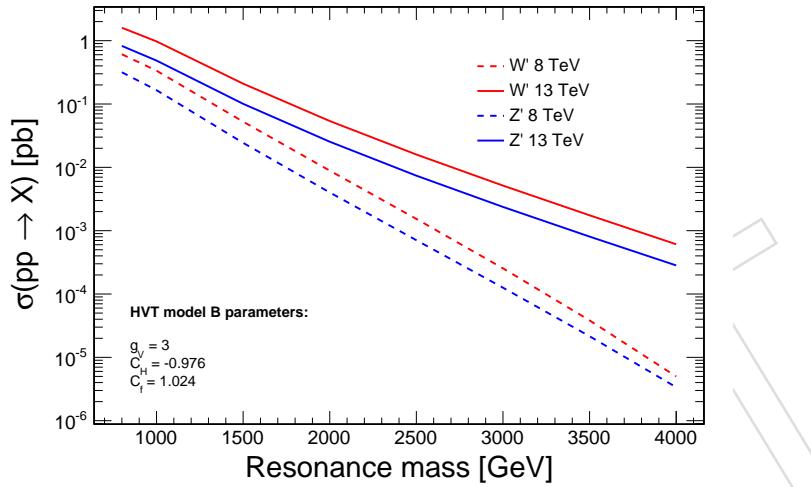


Figure 1: Resonance cross sections as a function of their mass for the HVT benchmark model B.

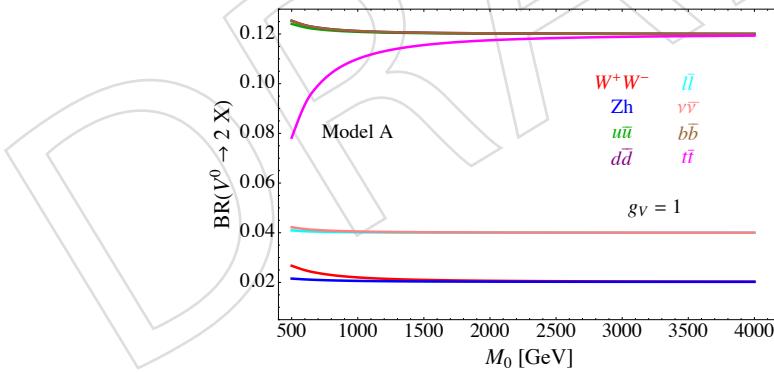


Figure 2: Branching ratios as a function of the resonance mass for the HVT benchmark model A

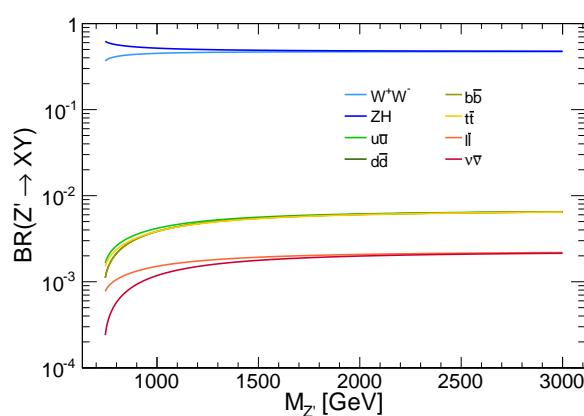


Figure 3: Branching ratios as a function of the resonance mass for a Z' in the HVT model B.

142 2 Datasets and samples

143 The Monte Carlo samples belong to the RunIISummer16NanoAODv6,
144 RunIIFall17NanoAODv6 and RunIIAutumn18NanoAODv6 campaign for 2016, 2017 and
145 2018, respectively. They are generated simulating the PU conditions, using the
146 PUMoriond17_102X_mcRun2_asymptotic PU scenario for 2016, the
147 PU2017_new_pmx_102X_mc2017_realistic PU scenario for 2017 and the
148 102X_upgrade2018_realistic PU scenario for 2018. Parton showering and hadronization
149 processes are performed with PYTHIA 8.205 [19, 20] with the CUETP8M1 [21, 22], CP5 [23] un-
150 derlying event tune for 2016 and 2017/2018, respectively. A full detector simulation and event
151 reconstruction has been performed with GEANT4 [24] and CMSSW. The CUETP8M2 tune is
152 used for top quark pair production [25] in 2016 and the CP5 tune for 2017 and 2018.

153 2.1 Signal

154 Heavy Vector Triplet samples are generated at leading order with the MADGRAPH5 2.6 [26]
155 generator. The signal samples are produced within the HVT framework, benchmark model
156 B. However, the widths of the resonances are set to 0.1% of the resonance masses, in order to
157 fulfill the narrow-width approximation. The Z' resonances are forced to decay into a Z boson
158 and a Higgs boson. In turn, the Z bosons are forced to decay into pairs of leptons or neutrinos.
159 There is no restriction of the decay channels for the Higgs boson. The signal samples and their
160 cross section in the HVT model B are reported in Table 1 and in Table 2 for the VBF production.

DRAFT

Sample name	σ (pb) (HVT model B)
ZprimeToZHToZinvHinc_narrow_M-800_13TeV-madgraph	$0.855309 \cdot 0.567236$
ZprimeToZHToZinvHinc_narrow_M-1000_13TeV-madgraph	$0.509804 \cdot 0.517614$
ZprimeToZHToZinvHinc_narrow_M-1200_13TeV-madgraph	$0.271104 \cdot 0.500699$
ZprimeToZHToZinvHinc_narrow_M-1400_13TeV-madgraph	$0.146961 \cdot 0.492143$
ZprimeToZHToZinvHinc_narrow_M-1600_13TeV-madgraph	$0.00822156 \cdot 0.487091$
ZprimeToZHToZinvHinc_narrow_M-1800_13TeV-madgraph	$0.00473673 \cdot 0.483825$
ZprimeToZHToZinvHinc_narrow_M-2000_13TeV-madgraph	$0.00279823 \cdot 0.481578$
ZprimeToZHToZinvHinc_narrow_M-2500_13TeV-madgraph	$8.15289e-3 \cdot 0.478265$
ZprimeToZHToZinvHinc_narrow_M-3000_13TeV-madgraph	$2.57265e-3 \cdot 0.476530$
ZprimeToZHToZinvHinc_narrow_M-3500_13TeV-madgraph	$8.50838e-4 \cdot 0.475504$
ZprimeToZHToZinvHinc_narrow_M-4000_13TeV-madgraph	$2.88261e-4 \cdot 0.474847$
ZprimeToZHToZinvHinc_narrow_M-4500_13TeV-madgraph	$9.84981e-5 \cdot 0.474400$
ZprimeToZHToZinvHinc_narrow_M-5000_13TeV-madgraph	$3.39139e-5 \cdot 0.474847$
ZprimeToZHToZinvHinc_narrow_M-5500_13TeV-madgraph	$1.12173e-5 \cdot 0.474847$
ZprimeToZHToZinvHinc_narrow_M-6000_13TeV-madgraph	$3.65280e-6 \cdot 0.474847$
ZprimeToZHToZlepHinc_narrow_M-800_13TeV-madgraph	$0.855309 \cdot 0.567236$
ZprimeToZHToZlepHinc_narrow_M-1000_13TeV-madgraph	$0.509804 \cdot 0.517614$
ZprimeToZHToZlepHinc_narrow_M-1200_13TeV-madgraph	$0.271104 \cdot 0.500699$
ZprimeToZHToZlepHinc_narrow_M-1400_13TeV-madgraph	$0.146961 \cdot 0.492143$
ZprimeToZHToZlepHinc_narrow_M-1600_13TeV-madgraph	$0.00822156 \cdot 0.487091$
ZprimeToZHToZlepHinc_narrow_M-1800_13TeV-madgraph	$0.00473673 \cdot 0.483825$
ZprimeToZHToZlepHinc_narrow_M-2000_13TeV-madgraph	$0.00279823 \cdot 0.481578$
ZprimeToZHToZlepHinc_narrow_M-2500_13TeV-madgraph	$8.15289e-3 \cdot 0.478265$
ZprimeToZHToZlepHinc_narrow_M-3000_13TeV-madgraph	$2.57265e-3 \cdot 0.476530$
ZprimeToZHToZlepHinc_narrow_M-3500_13TeV-madgraph	$8.50838e-4 \cdot 0.475504$
ZprimeToZHToZlepHinc_narrow_M-4000_13TeV-madgraph	$2.88261e-4 \cdot 0.474847$
ZprimeToZHToZlepHinc_narrow_M-4500_13TeV-madgraph	$9.84981e-5 \cdot 0.474400$
ZprimeToZHToZlepHinc_narrow_M-5000_13TeV-madgraph	$3.39139e-5 \cdot 0.474847$
ZprimeToZHToZlepHinc_narrow_M-5500_13TeV-madgraph	$1.12173e-5 \cdot 0.474847$
ZprimeToZHToZlepHinc_narrow_M-6000_13TeV-madgraph	$3.65280e-6 \cdot 0.474847$

Table 1: $Z' \rightarrow ZH$ signal samples and production cross sections in HVT model B. Each sample contains 100000 events. The cross section for each relative sample is obtained by multiplying the production cross section by the vector boson branching fractions ($\mathcal{B}(Z \rightarrow \ell\ell) = 0.101$ and $\mathcal{B}(Z \rightarrow \nu\nu) = 0.200$ [27]).

Sample name	σ (pb) (HVT model B)
Zprime_VBF_Zh_Zinvhinc_narrow_M-800_13TeV-madgraph	3.352141e-3 · 0.500874
Zprime_VBF_Zh_Zinvhinc_narrow_M-1000_13TeV-madgraph	1.094491e-3 · 0.496030
Zprime_VBF_Zh_Zinvhinc_narrow_M-1200_13TeV-madgraph	4.226482e-4 · 0.495921
Zprime_VBF_Zh_Zinvhinc_narrow_M-1400_13TeV-madgraph	1.819783e-4 · 0.492476
Zprime_VBF_Zh_Zinvhinc_narrow_M-1600_13TeV-madgraph	8.366986e-5 · 0.499822
Zprime_VBF_Zh_Zinvhinc_narrow_M-1800_13TeV-madgraph	4.172603e-5 · 0.492498
Zprime_VBF_Zh_Zinvhinc_narrow_M-2000_13TeV-madgraph	2.155255e-5 · 0.490429
Zprime_VBF_Zh_Zinvhinc_narrow_M-2500_13TeV-madgraph	4.678337e-6 · 0.490559
Zprime_VBF_Zh_Zinvhinc_narrow_M-3000_13TeV-madgraph	1.144028e-6 · 0.494481
Zprime_VBF_Zh_Zinvhinc_narrow_M-3500_13TeV-madgraph	3.064356e-7 · 0.491457
Zprime_VBF_Zh_Zinvhinc_narrow_M-4000_13TeV-madgraph	8.561628e-8 · 0.488809
Zprime_VBF_Zh_Zinvhinc_narrow_M-4500_13TeV-madgraph	2.411154e-8 · 0.491466
Zprime_VBF_Zh_Zinvhinc_narrow_M-5000_13TeV-madgraph	6.836269e-9 · 0.492081
Zprime_VBF_Zh_Zinvhinc_narrow_M-5500_13TeV-madgraph	1.902022e-9 · 0.493370
Zprime_VBF_Zh_Zinvhinc_narrow_M-6000_13TeV-madgraph	5.236990e-10 · 0.489594
Zprime_VBF_Zh_Zlephinc_narrow_M-800_13TeV-madgraph	3.352141e-3 · 0.500874
Zprime_VBF_Zh_Zlephinc_narrow_M-1000_13TeV-madgraph	1.094491e-3 · 0.496030
Zprime_VBF_Zh_Zlephinc_narrow_M-1200_13TeV-madgraph	4.226482e-4 · 0.495921
Zprime_VBF_Zh_Zlephinc_narrow_M-1400_13TeV-madgraph	1.819783e-4 · 0.492476
Zprime_VBF_Zh_Zlephinc_narrow_M-1600_13TeV-madgraph	8.366986e-5 · 0.499822
Zprime_VBF_Zh_Zlephinc_narrow_M-1800_13TeV-madgraph	4.172603e-5 · 0.492498
Zprime_VBF_Zh_Zlephinc_narrow_M-2000_13TeV-madgraph	2.155255e-5 · 0.490429
Zprime_VBF_Zh_Zlephinc_narrow_M-2500_13TeV-madgraph	4.678337e-6 · 0.490559
Zprime_VBF_Zh_Zlephinc_narrow_M-3000_13TeV-madgraph	1.144028e-6 · 0.494481
Zprime_VBF_Zh_Zlephinc_narrow_M-3500_13TeV-madgraph	3.064356e-7 · 0.491457
Zprime_VBF_Zh_Zlephinc_narrow_M-4000_13TeV-madgraph	8.561628e-8 · 0.488809
Zprime_VBF_Zh_Zlephinc_narrow_M-4500_13TeV-madgraph	2.411154e-8 · 0.491466
Zprime_VBF_Zh_Zlephinc_narrow_M-5000_13TeV-madgraph	6.836269e-9 · 0.492081
Zprime_VBF_Zh_Zlephinc_narrow_M-5500_13TeV-madgraph	1.902022e-9 · 0.493370
Zprime_VBF_Zh_Zlephinc_narrow_M-6000_13TeV-madgraph	5.236990e-10 · 0.489594

Table 2: $Z' \rightarrow ZH$ signal samples and production cross sections in HVT model C with VBF production. The cross section for each relative sample is obtained by multiplying the production cross section by the vector boson branching fractions ($\mathcal{B}(Z \rightarrow \ell\ell) = 0.101$ and $\mathcal{B}(Z \rightarrow \nu\nu) = 0.200$)

161 **2.2 Background samples**

162 All physics processes yielding final states with two leptons and a large missing transverse mo-
 163 mentum in association with two jets have to be considered as possible sources of background
 164 for the analysis. The complete list of background datasets considered is presented in Table 3-
 165 4 for 2016, Table 5- 6 for 2017 and Table 7- 8 for 2018. The cross section used to normalize
 166 SM backgrounds are derived from the generators or calculations with dedicated softwares re-
 167 ported in Ref. [28], and/or calculated at (N)NLO by the Standard Model Cross Section Working
 168 Group [29].

- 169 • **Z + jets:** this process represents the main irreducible background for the signal in
 170 the 0- and 2-lepton final states given the large missing transverse momentum or the
 171 presence of two resonating leptons in the final state respectively. The production of
 172 single Z/ γ^* bosons in association with one or more partons or gluons in the final
 173 state is topologically similar to the searched signal, but its final state quarks fea-
 174 ture a generally softer p_T spectrum, a non-resonant and rapidly falling di-jet mass
 175 distribution, and other less distinctive characteristics (effective spin and color radia-
 176 tion) that should theoretically distinguish it from the signal. Before b-quark tagging,
 177 the contribution from *udscg* (light) partons dominates, while after the application
 178 of b-tagging the primary contribution in the signal region is from Z + b(b). This
 179 Z +jets background is produced with the MADGRAPH5_amc@NLO generator at LO
 180 in QCD and normalized to the next-to-next-to-leading-order (NNLO) cross section,
 181 computed using FEWZ v3.1 [30]. The V boson p_T spectra are corrected to account
 182 for next-to-leading-order (NLO) QCD and EWK and next-to-next-to-leading order
 183 (NNLO) QCD contributions. [31]. Figure 4 shows the used scale factors. Exclusive
 184 samples are produced in several bins of HT (the sum of the p_T of the hadrons at LHE
 185 level) starting from 100 GeV.
- 186 • **W + jets:** the leptonic decay of a W boson can be an irreducible background in the
 187 zero-lepton channel in the case the charged lepton escapes undetected (e.g. outside
 188 the detector acceptance) or fails the lepton identification requirements. The produc-
 189 tion of a W boson has a cross section larger by an order of magnitude with respect to
 190 the Z, and this makes the W +jets a relevant background also when a lepton veto is
 191 applied. Analogously to the Z +jets samples, an inclusive W($\rightarrow \ell\nu$) sample has been
 192 produced with MADGRAPH5_amc@NLO at LO in QCD in HT-binned samples and
 193 normalized to NNLO inclusive. The same p_T dependent QCD and EWK corrections
 194 as for the Z+jets were applied.
- 195 • **t̄t:** production of t̄t pairs represents a particularly challenging background at the
 196 LHC, given its large production cross section. These events always contain two en-
 197 ergetic b-jets and two W bosons which may decay to high p_T , isolated leptons. The
 198 primary handles to reduce the t̄t background are topological, such as its larger jet
 199 multiplicity and the azimuthal opening angle between the vector boson and the di-
 200 jet system, which is more broadly distributed in top pair production than in signal
 201 events. In the dilepton final state, the most important cut to reduce t̄t is the candi-
 202 date Z p_T . In t̄t production the dilepton p_T spectrum is sharply falling, given the
 203 absence of a dilepton resonance. The main sample considered is generated at NLO
 204 in QCD with the POWHEG 2.0 generator [32–34], and the cross section is computed
 205 with TOP++ v2.0 [35] at next-to-next-to-leading order.
- 206 • **single-top:** Inclusive S_T samples have been produced at NLO in QCD with the
 207 MADGRAPH5_amc@NLOAMC@NLO generator, including all the possible decays
 208 of the W bosons. The s-channel and t-channel single-top samples are produced in

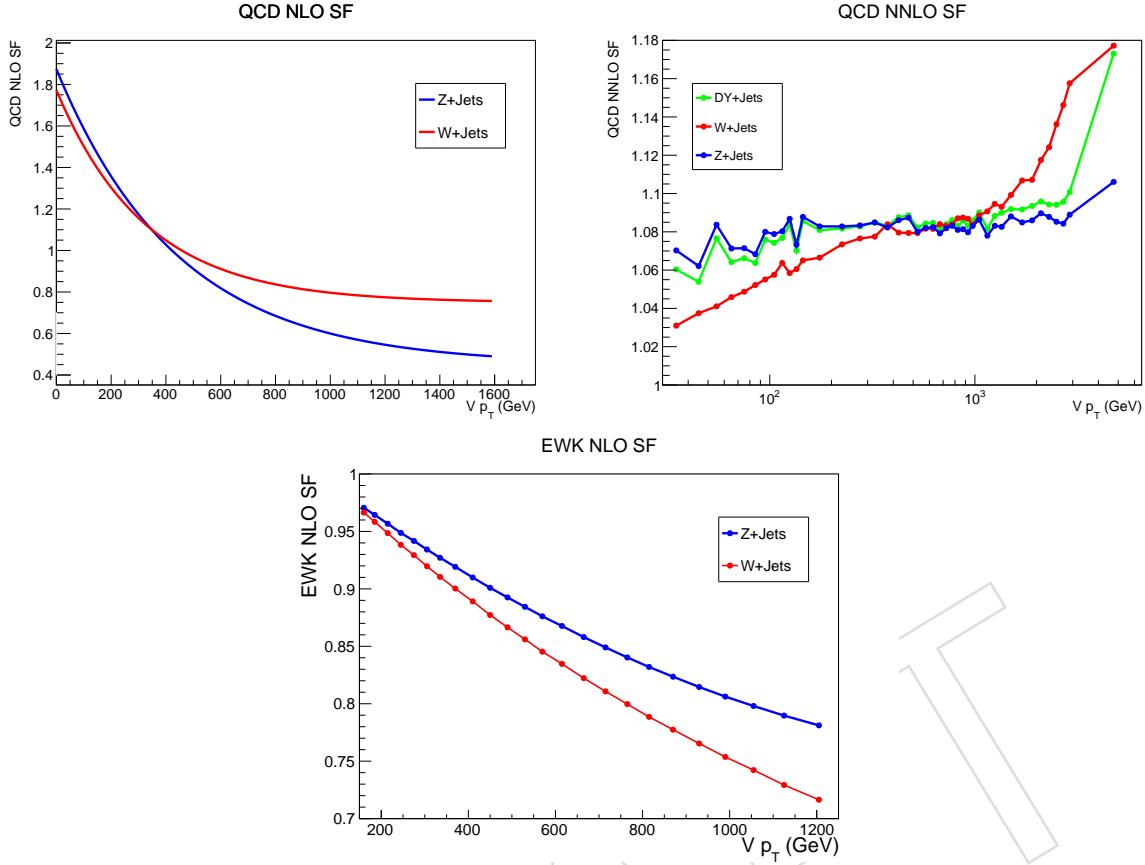


Figure 4: Scale factors for QCD NLO (top left), for QCD NNLO (top right) and for EWK NLO (bottom).[31]

the 4-flavor scheme, while tW-channel is produced in the 5-flavor scheme.

- **Diboson:** the production of two vector bosons in the SM is a rare process, with a similar kinematics to that of the signal. Furthermore, the boost of the bosons could be large. The main handle to discriminate against V V backgrounds is a tight cut on the jet mass. The SM Higgs boson production (V H), instead, is virtually indistinguishable from the signal except for the mass resonance itself. However, the SM Higgs production cross section is much smaller than the one of the other diboson processes. All the diboson production processes (W W, WZ, ZZ, W H, Z H) and their corresponding (semi)-leptonic decay modes are considered, including those involving one or more neutrinos. These backgrounds are simulated at NLO in QCD with the MADGRAPH5_aMC@NLO generator.

Table 3: Z , $W + \text{jets}$ simulated samples for 2016. The cross section \times branching ratio is shown in pb. SM boson branching fractions are taken from Ref. [27].

Dataset	$\sigma \times \mathcal{B}$ (pb)
DYJetsToLL_M-50_HT-100to200_TuneCUETP8M1_13TeV-madgraphMLM-pythia8	147.4
DYJetsToLL_M-50_HT-200to400_TuneCUETP8M1_13TeV-madgraphMLM-pythia8	40.99
DYJetsToLL_M-50_HT-400to600_TuneCUETP8M1_13TeV-madgraphMLM-pythia8	5.678
DYJetsToLL_M-50_HT-600to800_TuneCUETP8M1_13TeV-madgraphMLM-pythia8	1.367
DYJetsToLL_M-50_HT-800to1200_TuneCUETP8M1_13TeV-madgraphMLM-pythia8	0.6304
DYJetsToLL_M-50_HT-1200to2500_TuneCUETP8M1_13TeV-madgraphMLM-pythia8	0.1514
DYJetsToLL_M-50_HT-2500toInf_TuneCUETP8M1_13TeV-madgraphMLM-pythia8	0.003565
ZJetsToNuNu_HT-100To200_13TeV-madgraph	280.35
ZJetsToNuNu_HT-200To400_13TeV-madgraph	77.67
ZJetsToNuNu_HT-400To600_13TeV-madgraph	10.73
ZJetsToNuNu_HT-600To800_13TeV-madgraph	2.559
ZJetsToNuNu_HT-800To1200_13TeV-madgraph	1.1796
ZJetsToNuNu_HT-1200To2500_13TeV-madgraph	0.28833
ZJetsToNuNu_HT-2500ToInf_13TeV-madgraph	0.006945
WJetsToLNu_HT-100To200_TuneCUETP8M1_13TeV-madgraphMLM-pythia8	1345
WJetsToLNu_HT-200To400_TuneCUETP8M1_13TeV-madgraphMLM-pythia8	359.7
WJetsToLNu_HT-400To600_TuneCUETP8M1_13TeV-madgraphMLM-pythia8	48.91
WJetsToLNu_HT-600To800_TuneCUETP8M1_13TeV-madgraphMLM-pythia8	12.05
WJetsToLNu_HT-800To1200_TuneCUETP8M1_13TeV-madgraphMLM-pythia8	5.501
WJetsToLNu_HT-1200To2500_TuneCUETP8M1_13TeV-madgraphMLM-pythia8	1.329
WJetsToLNu_HT-2500ToInf_TuneCUETP8M1_13TeV-madgraphMLM-pythia8	0.03216

Table 4: $t\bar{t}$, dibosons and multijet simulated samples for 2016. The cross section \times branching ratio is shown in pb. SM boson branching fractions are taken from Ref. [27].

Dataset	$\sigma \times \mathcal{B}$ (pb)
TTo2LNu_TuneCUETP8M2_ttHtranche3_13TeV-powheg-pythia8	87.31
TToSemiLepton_TuneCUETP8M2_ttHtranche3_13TeV-powheg-pythia8	364.35
TTWJetsToLNu_TuneCP5_13TeV-amcatnloFXFX-madspin-pythia8	0.2043
TTZToLLNuNu_M-10_TuneCP5_13TeV-amcatnlo-pythia8	0.2529
ST_s-channel_4f_leptonDecays_13TeV-amcatnlo-pythia8_TuneCUETP8M1	3.36
ST_t-channel_top_4f_inclusiveDecays_13TeV-powhegV2-madspin-pythia8_TuneCUETP8M1	136.02
ST_t-channel_antitop_4f_inclusiveDecays_13TeV-powhegV2-madspin-pythia8_TuneCUETP8M1	80.95
ST_tW_top_5f_inclusiveDecays_13TeV-powheg-pythia8_TuneCUETP8M2T4	35.85
ST_tW_antitop_5f_inclusiveDecays_13TeV-powheg-pythia8_TuneCUETP8M2T4	35.85
WWTo4Q_13TeV-powheg	51.723
WWTo2L2Nu_13TeV-powheg	12.178
WWTo1L1Nu2Q_13TeV_amcatnloFXFX_madspin-pythia8	49.997
WZTo1L1Nu2Q_13TeV_amcatnloFXFX_madspin_pythia8	10.71
WZTo2L2Q_13TeV_amcatnloFXFX_madspin_pythia8	5.595
ZZTo2L2Q_13TeV_amcatnloFXFX_madspin_pythia8	3.22
ZZTo2L2Nu_13TeV_powheg-pythia8	0.564
ZZTo2Q2Nu_13TeV_amcatnloFXFX_madspin-pythia8	4.04
ZZTo4L_13TeV_powheg-pythia8	1.212
GluGluHTobb_M125_13TeV_amcatnloFXFX_pythia8	43.92 · 0.5824
ZH_HToBB_ZToNuNu_M125_13TeV_powheg-pythia8	$0.7612 \cdot 0.5824 \cdot 0.201$
ZH_HToBB_ZToLL_M125_13TeV_powheg-pythia8	$0.7612 \cdot 0.5824 \cdot 0.1097$
WplusH_HToBB_WToLNu_M125_13TeV_powheg-pythia8	$0.84 \cdot 0.5824 \cdot 0.1085$
WminusH_HToBB_WToBB_WToLNu_M125_13TeV_powheg_pythia8	$0.533 \cdot 0.5824 \cdot 0.1085$

Table 5: $Z, W + \text{jets}$ simulated samples for 2017. The cross section \times branching ratio is shown in pb. SM boson branching fractions are taken from Ref. [27].

Dataset	$\sigma \times \mathcal{B}$ (pb)
DYjetsToLL_M-50_HT-100to200_TuneCP5_13TeV-madgraphMLM-pythia8	147.4
DYjetsToLL_M-50_HT-200to400_TuneCP5_13TeV-madgraphMLM-pythia8	40.99
DYjetsToLL_M-50_HT-400to600_TuneCP5_13TeV-madgraphMLM-pythia8	5.678
DYjetsToLL_M-50_HT-600to800_TuneCP5_13TeV-madgraphMLM-pythia8	1.367
DYjetsToLL_M-50_HT-800to1200_TuneCP5_13TeV-madgraphMLM-pythia8	0.6304
DYjetsToLL_M-50_HT-1200to2500_TuneCP5_13TeV-madgraphMLM-pythia8	0.1514
DYjetsToLL_M-50_HT-2500toInf_TuneCP5_13TeV-madgraphMLM-pythia8	0.003565
ZjetsToNuNu_HT-100To200_13TeV-madgraph	280.35
ZjetsToNuNu_HT-200To400_13TeV-madgraph	77.67
ZjetsToNuNu_HT-400To600_13TeV-madgraph	10.73
ZjetsToNuNu_HT-600To800_13TeV-madgraph	2.559
ZjetsToNuNu_HT-800To1200_13TeV-madgraph	1.1796
ZjetsToNuNu_HT-1200To2500_13TeV-madgraph	0.28833
ZjetsToNuNu_HT-2500ToInf_13TeV-madgraph	0.006945
WjetsToLNu_IHT-100To200_TuneCP5_13TeV-madgraphMLM-pythia8	1345
WjetsToLNu_IHT-200To400_TuneCP5_13TeV-madgraphMLM-pythia8	359.7
WjetsToLNu_IHT-400To600_TuneCP5_13TeV-madgraphMLM-pythia8	48.91
WjetsToLNu_IHT-600To800_TuneCP5_13TeV-madgraphMLM-pythia8	12.05
WjetsToLNu_IHT-800To1200_TuneCP5_13TeV-madgraphMLM-pythia8	5.501
WjetsToLNu_IHT-1200To2500_TuneCP5_13TeV-madgraphMLM-pythia8	1.329
WjetsToLNu_IHT-2500ToInf_TuneCP5_13TeV-madgraphMLM-pythia8	0.03216

Table 6: $t\bar{t}$, dibosons and multijet simulated samples for 2017. The cross section \times branching ratio is shown in pb. SM boson branching fractions are taken from Ref. [27].

Dataset	$\sigma \times \mathcal{B}$ (pb)
TTTo2LNu_TuneCP5_13TeV-powheg-pythia8	87.31
TTToSemiLeptonic_TuneCP5_13TeV-powheg-pythia8	364.35
TTWJetsToLNu_TuneCP5_13TeV-amcatnloFXFX-madspin-pythia8	0.2043
TTZToLLNuNu_M-10_TuneCP5_13TeV-amcatnlo-pythia8	0.2529
ST_s-channel_4f_leptonDecays_TuneCP5_13TeV-amcatnlo-pythia8	3.36
ST_t-channel_top_4f_inclusiveDecays_TuneCP5_13TeV-powhegV2-madspin-pythia8	136.02
ST_t-channel_antitop_4f_inclusiveDecays_TuneCP5_13TeV-powhegV2-madspin-pythia8	80.95
ST_tW_top_5f_inclusiveDecays_TuneCP5_13TeV-powheg-pythia8	35.85
ST_tW_antitop_5f_inclusiveDecays_TuneCP5_13TeV-powheg-pythia8	35.85
WWToLNuQQ_NNPDF31_TuneCP5_13TeV-powheg-pythia8	49.997
WWTo2L2Nu_NNPDF31_TuneCP5_13TeV-powheg-pythia8	12.178
WWTo4Q_NNPDF31_TuneCP5_13TeV-powheg-pythia8	51.723
WZToII1Nu2Q_13TeV_amcatnloFXFX_madspin_pythia8	10.71
ZZTo2L2Q_13TeV_amcatnloFXFX_madspin_pythia8	5.595
ZZTo2L2Q_13TeV_amcatnloFXFX_madspin_pythia8	3.22
ZZTo2Q2Nu_TuneCP5_13TeV_amcatnloFXFX_madspin_pythia8	4.04
ZZTo2L2Nu_13TeV_powheg-pythia8	0.564
ZZTo4L_13TeV_powheg-pythia8	1.212
GluGluHToBB_M125_13TeV_amcatnloFXFX_pythia8	43.92 . 0.5824
ZH_HToBB_ZToNuNu_M125_13TeV_powheg_pythia8	0.7612 . 0.5824 . 0.201
ZH_HToBB_ZToLL_M125_13TeV_powheg_pythia8	0.7612 . 0.5824 . 0.1097
WplusH_HToBB_WToLNu_M125_13TeV_powheg_pythia8	0.84 . 0.5824 . 0.1085
WminusH_HToBB_WToLNu_M125_13TeV_powheg_pythia8	0.533 . 0.5824 . 0.1085

Table 7: $Z, W + \text{jets}$ simulated samples for 2018. The cross section \times branching ratio is shown in pb. SM boson branching fractions are taken from Ref. [27].

Dataset	$\sigma \times \mathcal{B}$ (pb)
DYjetsToLL_M-50 HT-100to200_TuneCP5_PSweights_13TeV-madgraphMLM-pythia8	147.4
DYjetsToLL_M-50 HT-200to400_TuneCP5_PSweights_13TeV-madgraphMLM-pythia8	40.99
DYjetsToLL_M-50 HT-400to600_TuneCP5_PSweights_13TeV-madgraphMLM-pythia8	5.678
DYjetsToLL_M-50 HT-600to800_TuneCP5_PSweights_13TeV-madgraphMLM-pythia8	1.367
DYjetsToLL_M-50 HT-800to1200_TuneCP5_PSweights_13TeV-madgraphMLM-pythia8	0.6304
DYjetsToLL_M-50 HT-1200to2500_TuneCP5_PSweights_13TeV-madgraphMLM-pythia8	0.1514
DYjetsToLL_M-50 HT-2500toInf_TuneCP5_PSweights_13TeV-madgraphMLM-pythia8	0.003565
ZjetsToNuNu_HT-100To200_13TeV-madgraph	280.35
ZjetsToNuNu_HT-200To400_13TeV-madgraph	77.67
ZjetsToNuNu_HT-400To600_13TeV-madgraph	10.73
ZjetsToNuNu_HT-600To800_13TeV-madgraph	2.559
ZjetsToNuNu_HT-800To1200_13TeV-madgraph	1.1796
ZjetsToNuNu_HT-1200To2500_13TeV-madgraph	0.28833
ZjetsToNuNu_HT-2500ToInf_13TeV-madgraph	0.006945
WjetsToLNu_HT-100To200_TuneCP5_13TeV-madgraphMLM-pythia8	1345
WjetsToLNu_HT-200To400_TuneCP5_13TeV-madgraphMLM-pythia8	359.7
WjetsToLNu_HT-400To600_TuneCP5_13TeV-madgraphMLM-pythia8	48.91
WjetsToLNu_HT-600To800_TuneCP5_13TeV-madgraphMLM-pythia8	12.05
WjetsToLNu_HT-800To1200_TuneCP5_13TeV-madgraphMLM-pythia8	5.501
WjetsToLNu_HT-1200To2500_TuneCP5_13TeV-madgraphMLM-pythia8	1.329
WjetsToLNu_HT-2500ToInf_TuneCP5_13TeV-madgraphMLM-pythia8	0.03216

Table 8: $t\bar{t}$, dibosons and multijet simulated samples for 2018. The cross section \times branching ratio is shown in pb. SM boson branching fractions are taken from Ref. [27].

Dataset	$\sigma \times \mathcal{B}$ (pb)
TTTo2L2Nu_TuneCP5_13TeV-powheg-pythia8	87.31
TTToSemiLeptonic_TuneCP5_13TeV-powheg-pythia8	364.35
TTWJetsToLNu_TuneCP5_13TeV-amcatnloFXFX-madspin-pythia8	0.2043
TTZToLLNuNu_M-10_TuneCP5_13TeV-amcatnlo-pythia8	0.2529
ST_s-channel_4f_leptonDecays_TuneCP5_13TeV-madgraph-pythia8	3.36
ST_t-channel_top_4f_InclusiveDecays_TuneCP5_13TeV-powheg-madspin-pythia8	136.02
ST_t-channel_antitop_4f_InclusiveDecays_TuneCP5_13TeV-powheg-madspin-pythia8	80.95
ST_tW_top_5f_inclusiveDecays_TuneCP5_13TeV-powheg-pythia8	35.85
ST_tW_antitop_5f_inclusiveDecays_TuneCP5_13TeV-powheg-pythia8	35.85
WWTo1L1Nu2Q_13TeV_amcatnloFXFX_madspin-pythia8	49.997
WWTo2L2Nu_NNPDF31_TuneCP5_13TeV-powheg-pythia8	12.178
WWTo4Q_NNPDF31_TuneCP5_13TeV-powheg-pythia8	51.723
WZTo2L2Q_13TeV_amcatnloFXFX_madspin-pythia8	5.595
ZZTo2Q2Nu_TuneCP5_13TeV_amcatnloFXFX_madspin-pythia8	4.04
ZZTo2L2Q_13TeV_amcatnloFXFX_madspin-pythia8	3.22
ZZTo2L2Nu_TuneCP5_13TeV_powheg-pythia8	0.564
ZZTo4L_TuneCP5_13TeV_powheg-pythia8	1.212
GluGluHToBB_M125_13TeV_amcatnloFXFX_pythia8	43.92 · 0.5824
ZH_HToBB_ZToNuNu_M125_13TeV_powheg_pythia8	0.7612 · 0.5824 · 0.201
ZH_HToBB_ZToLL_M125_13TeV_powheg_pythia8	0.7612 · 0.5824 · 0.1097
WplusH_HToBB_WToLNu_M125_13TeV_powheg_pythia8	0.84 · 0.5824 · 0.1085
WminusH_HToBB_WToLNu_M125_13TeV_powheg_pythia8	0.533 · 0.5824 · 0.1085

220 2.3 Data

221 Data events have been collected during the 2016, 2017 and 2018 data taking, at a center-of-
 222 mass energy of 13 TeV, with Lepton, Photon and E_T^{miss} triggers. The MET primary dataset is
 223 used when requiring missing energy triggers, the SingleMuon is used for data selected with
 224 a single muon trigger, and SingleElectron and SinglePhoton are used for data selected
 225 with an electron or photon trigger.
 226 The full list of datasets used is shown in Table 9 for 2016, in Table 10 for 2017 and Table 11 for
 227 2018. Data belong to the 25Oct2019 NanoAOD campaign and is processed with a CMSSW_10_2_15
 228 release. Runs and lumisections are taken into account according to the Golden JSON files (Cert_271036-284044_13TeV_PromptReco_Collisions16_JSON,
 229 Cert_294927-306462_13TeV_PromptReco_Collisions17_JSON,
 230 Cert_314472-325175_13TeV_PromptReco_Collisions18_JSON) that includes all the runs
 231 certified as valid for all CMS subsystems. The integrated luminosity amounts to 35.920 fb^{-1}
 232 for 2016, 41.530 fb^{-1} for 2017 and 59.740 fb^{-1} for 2018, which gives a combined integrated
 233 luminosity of 137.19 fb^{-1} (Fig. 5).
 234

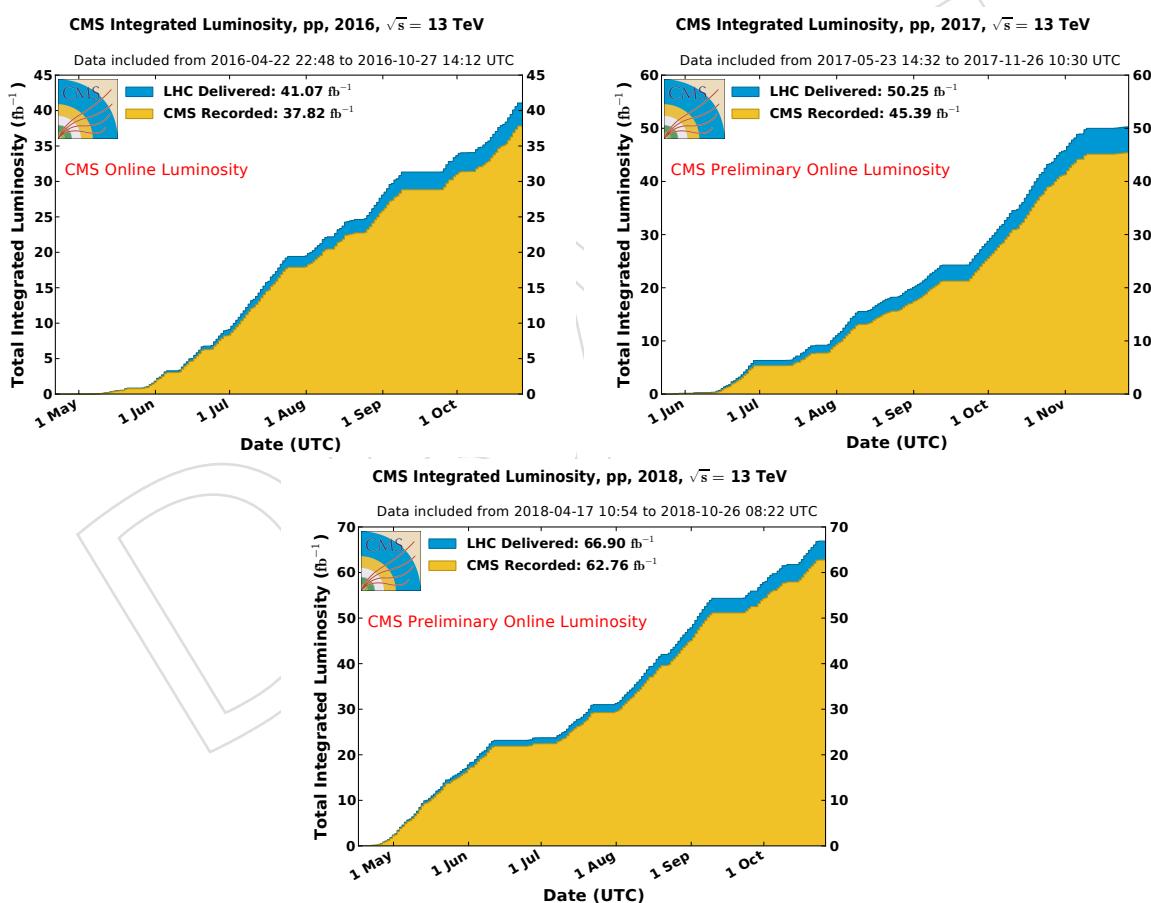


Figure 5: Cumulative luminosity versus day delivered to (blue), and recorded by CMS (orange) during stable beams and for pp collisions at 13 TeV centre-of-mass energy in 2016 (Top left), 2017 (Top right) and 2018 (Bottom). The delivered luminosity accounts for the luminosity delivered from the start of stable beams until the LHC requests CMS to turn off the sensitive detectors to allow a beam dump or beam studies. Given is the luminosity as determined from counting rates measured by the luminosity detectors.

235 In order to remove problematic or noise-dominated events, the following list of filters sug-
 236 gested by the JETMET POG [36] have been applied on both data and simulation (except `EEBadScFilter`
 237 which is applied on data only and `EcalBadCalibFilterV2` only for 2017/2018):

- 238 • `GoodVertices`
- 239 • `HBHENoiseFilter`
- 240 • `HBHENoiseIsoFilter`
- 241 • `EEBadScFilter`
- 242 • `GlobalSuperTightHalo2016Filter`
- 243 • `EcalDeadCellTriggerPrimitiveFilter`
- 244 • `BadPFMuonFilter`
- 245 • `EcalBadCalibFilterV2`

Table 9: 2016 Datasets.

Dataset	Int. lumi (fb^{-1})
MET/Run2016B_ver1-Nano25Oct2019_ver1-v1	5.9
MET/Run2016B_ver2-Nano25Oct2019_ver2-v1	
MET/Run2016C-Nano25Oct2019-v1	2.6
MET/Run2016D-Nano25Oct2019-v1	4.4
MET/Run2016E-Nano25Oct2019-v1	4.1
MET/Run2016F-Nano25Oct2019-v1	3.2
MET/Run2016G-Nano25Oct2019-v1	7.7
MET/Run2016H-Nano25Oct2019-v1	8.9
SingleMuon/Run2016B_ver1-Nano25Oct2019_ver1-v1	5.9
SingleMuon/Run2016B_ver2-Nano25Oct2019_ver2-v1	
SingleMuon/Run2016C-Nano25Oct2019-v1	2.6
SingleMuon/Run2016D-Nano25Oct2019-v1	4.4
SingleMuon/Run2016E-Nano25Oct2019-v1	4.1
SingleMuon/Run2016F-Nano25Oct2019-v1	3.2
SingleMuon/Run2016G-Nano25Oct2019-v1	7.7
SingleMuon/Run2016H-Nano25Oct2019-v1	8.9
SingleElectron/Run2016B_ver1-Nano25Oct2019_ver1-v1	5.9
SingleElectron/Run2016B_ver2-Nano25Oct2019_ver2-v1	
SingleElectron/Run2016C-Nano25Oct2019-v1	2.6
SingleElectron/Run2016D-Nano25Oct2019-v1	4.4
SingleElectron/Run2016E-Nano25Oct2019-v1	4.1
SingleElectron/Run2016F-Nano25Oct2019-v1	3.2
SingleElectron/Run2016G-Nano25Oct2019-v1	7.7
SingleElectron/Run2016H-Nano25Oct2019-v1	8.9

246 2.4 Trigger

247 Events are selected on-line by a two-stage trigger. The Level 1 (L1) trigger consists of hardware
 248 processors that perform a very basic selection and counting of physics objects, and reduce the
 249 rate from 40 MHz down to 100 kHz. Events passing the L1 decision are acquired by the DAQ
 250 system, and a complete and more accurate reconstruction is performed by the High Level Trig-
 251 ger (HLT), which exploits similar but faster variations of the same algorithms used in the offline
 252 event reconstruction. A trigger path is a string that identifies a list of selections performed at
 253 HLT.

Table 10: 2017 Datasets.

Dataset	Int. lumi (fb^{-1})
MET/Run2017B-Nano25Oct2019-v1	4.8
MET/Run2017C-Nano25Oct2019-v1	9.7
MET/Run2017D-Nano25Oct2019-v1	4.3
MET/Run2017E-Nano25Oct2019-v1	9.3
MET/Run2017F-Nano25Oct2019-v1	13.6
SingleMuon/Run2017B-Nano25Oct2019-v1	4.8
SingleMuon/Run2017C-Nano25Oct2019-v1	9.7
SingleMuon/Run2017D-Nano25Oct2019-v1	4.3
SingleMuon/Run2017E-Nano25Oct2019-v1	9.3
SingleMuon/Run2017F-Nano25Oct2019-v1	13.6
SingleElectron/Run2017B-Nano25Oct2019-v1	4.8
SingleElectron/Run2017C-Nano25Oct2019-v1	9.7
SingleElectron/Run2017D-Nano25Oct2019-v1	4.3
SingleElectron/Run2017E-Nano25Oct2019-v1	9.3
SingleElectron/Run2017F-Nano25Oct2019-v1	13.6

Table 11: 2018 Datasets.

Dataset	Int. lumi (fb^{-1})
MET/Run2018A-Nano25Oct2019-v1	14.0
MET/Run2018B-Nano25Oct2019-v1	7.1
MET/Run2018C-Nano25Oct2019-v1	6.9
MET/Run2018D-Nano25Oct2019_ver2-v1	31.9
SingleMuon/Run2018A-Nano25Oct2019-v1	14.0
SingleMuon/Run2018B-Nano25Oct2019-v1	7.1
SingleMuon/Run2018C-Nano25Oct2019-v1	6.9
SingleMuon/Run2018D-Nano25Oct2019-v1	31.9
EGamma/Run2018A-Nano25Oct2019-v1	14.0
EGamma/Run2018B-Nano25Oct2019-v1	7.1
EGamma/Run2018C-Nano25Oct2019-v1	6.9
EGamma/Run2018D-Nano25Oct2019-v1	31.9

Events are considered if they fire a specific set of triggers, in both data and Monte Carlo. Single lepton triggers, requiring at least one, non-isolated lepton, have been used to select events. The efficiencies are derived separately in both data and MC, and scale factors, defined as $SF = \varepsilon_{\text{data}} / \varepsilon_{MC}$, are applied consistently to simulated events in order to correct for potential discrepancies. We assume that the higher p_T lepton fires the trigger.

Events with no genuine leptons, characterized by large missing transverse momentum final states, pure E_T^{miss} triggers or E_T^{miss} triggers combined with other event requirements are used.

2.4.1 Electron triggers

Electrons are selected by requiring two types of electron trigger to ensure an optimal efficiency over the whole p_T range. Due to the relatively high threshold of the single electron, non-isolated triggers (115 GeV), the most efficient way to collect events with low boost is to use a single electron, isolated trigger, with a logical OR with the usual non-isolated triggers to maintain the efficiency in the boosted regime. The single electron triggers are reported in Tab. 12. The single electron trigger efficiencies are derived using a tag and probe method on $Z \rightarrow \ell\ell$ event and

268 are approved by the EGamma POG [37]. The electron trigger scale factors are applied to all the
 269 MC samples used in the analysis and are shown for each year in figure 6.

270 The trigger `HLT_Ele27_WPTight_Gsf` is used for Run2016, `HLT_Ele35_WPTight_Gsf` for Run2017
 271 and `HLT_Ele32_WPTight_Gsf` for Run2018. The trigger
 272 `HLT_Ele115_CaloIdVT_GsfTrkIdT` is not available in Run2017B.

Table 12: Single electron HLT trigger paths used in the analysis.

HLT paths
<code>HLT_Ele115_CaloIdVT_GsfTrkIdT</code>
<code>HLT_Ele35_WPTight_Gsf</code>
<code>HLT_Ele32_WPTight_Gsf</code>
<code>HLT_Ele27_WPTight_Gsf</code>

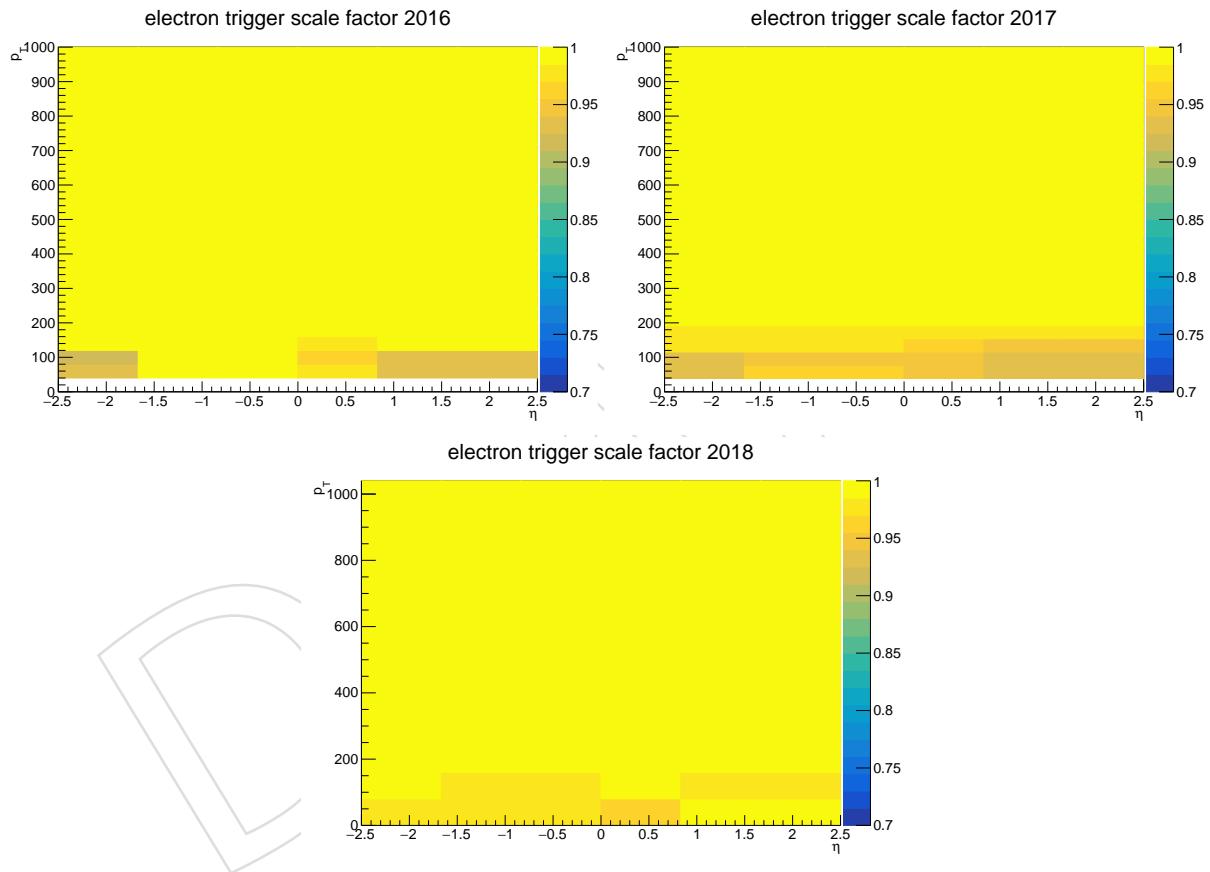


Figure 6: `HLT_Ele27_WPTight` OR `HLT_Ele115` OR `HLT_Photon175` scale factors for 2016, (top left), `HLT_Ele35_WPTight` OR `HLT_Ele115` OR `HLT_Photon200` scale factors for 2017 (top right) and `HLT_Ele32_WPTight` OR `HLT_Ele115` OR `HLT_Photon200` scale factors for 2018 (bottom) as a function of the η and p_T of the electron.

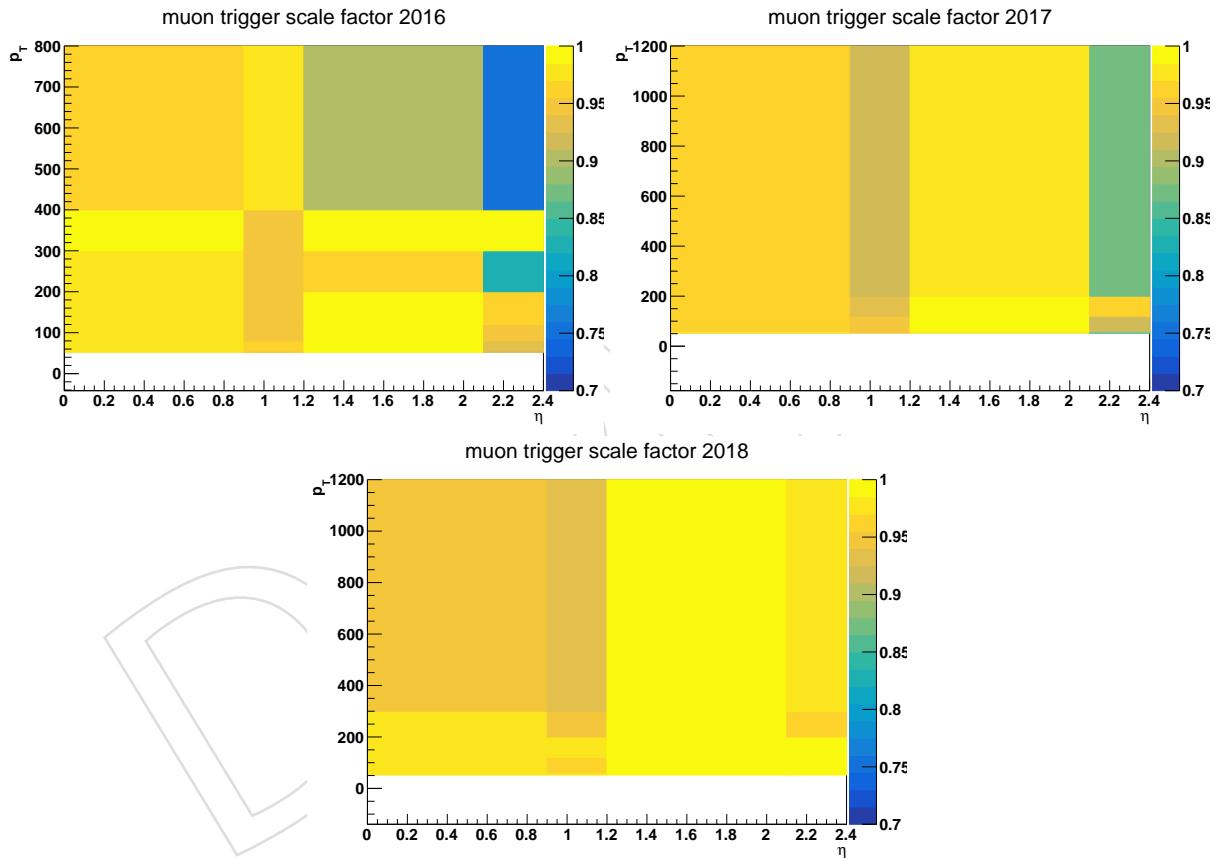
273 2.4.2 Muon triggers

274 Events with muons are selected with single muon triggers that require no isolation, in order
 275 to avoid efficiency losses in case of very boosted $Z \rightarrow \mu\mu$ events, when the two muons are
 276 close to each other. The trigger used is shown in Tab. 13. `HLT_TkMu50` is only used for 2016,
 277 `HLT_TkMu100` and `HLT_OldMu100` only for 2017 and 2018.

Table 13: Single muon HLT trigger path used in the analysis.

HLT paths
HLT_Mu50
HLT_TkMu50
HLT_TkMu100
HLT_OldMu100

278 The efficiencies of the single muon triggers are provided centrally by the Muon POG [38] with
 279 a tag and probe procedure by selecting $Z \rightarrow ll$ events. Tight lepton identification requirements
 280 are applied to the *probes*. The trigger efficiency is then evaluated studying the *tag* lepton effi-
 281 ciency as a function of both p_T and η for both data and MC. The muon trigger scale factors
 282 are applied consistently to the simulated events passing the trigger requirements to match the
 283 trigger efficiency measured in data. The scale factors for each year are shown in figure 7.

Figure 7: HLT_Mu50 scale factor for 2016 (top left), 2017 (top right) and 2018 (bottom) as a function of the η and p_T of the muon. The scale factor are provided by the Muon POG.

284 2.4.3 Missing energy triggers

285 The E_T^{miss} triggers are the logic OR of different trigger quantities, with thresholds on both the
 286 MET and the MHT computed using particle flow objects. The list of triggers used is reported
 287 in Table 14 for 2016 and in Table 15 for 2017 and 2018.
 288 The efficiency of the 2016 E_T^{miss} triggers is measured selecting $W \rightarrow ev$ events in the SingleElec-
 289 tron primary dataset, on events that trigger the HLT_Ele27_WPTight_Gsf_v* OR HLT_Ele32_WPTight_Gsf_v
 290 path. These events have to have exactly one electron with $p_T > 30 \text{ GeV}$, lying in the central re-

Table 14: 2016 Missing energy HLT trigger paths used in the analysis.

HLT paths
HLT_PFMETNoMu110_PFMHTNoMu110_IDTight
HLT_PFMETNoMu120_PFMHTNoMu120_IDTight
HLT_MonoCentralPFJet80_PFMETNoMu120_PFMHTNoMu120_IDTight
HLT_PFMET110_PFMHT110_IDTight
HLT_PFMET120_PFMHT120_IDTight
HLT_PFMET170_NotCleaned
HLT_PFMET170_HBHECleaned

Table 15: 2017 and 2018 Missing energy HLT trigger paths used in the analysis. The triggers HLT_PFMETNoMu130_PFMHTNoMu130_IDTight, HLT_PFMETNoMu140_PFMHTNoMu140_IDTight, HLT_PFMET200_NotCleaned, HLT_PFMET200_HBHECleaned, HLT_PFMET200_HBHE_BeamHaloCleaned, HLT_PFMET250_HBHECleaned are not available in Run2017B.

HLT paths
HLT_PFMETNoMu110_PFMHTNoMu110_IDTight
HLT_PFMETNoMu120_PFMHTNoMu120_IDTight
HLT_PFMETNoMu130_PFMHTNoMu130_IDTight
HLT_PFMETNoMu140_PFMHTNoMu140_IDTight
HLT_MonoCentralPFJet80_PFMETNoMu120_PFMHTNoMu120_IDTight
HLT_PFMET110_PFMHT110_IDTight
HLT_PFMET120_PFMHT120_IDTight
HLT_PFMET130_PFMHT130_IDTight
HLT_PFMET140_PFMHT140_IDTight
HLT_PFMETTypeOne110_PFMHT110_IDTight
HLT_PFMETTypeOne120_PFMHT120_IDTight
HLT_PFMETTypeOne130_PFMHT130_IDTight
HLT_PFMETTypeOne140_PFMHT140_IDTight
HLT_PFMET200_NotCleaned
HLT_PFMET200_HBHECleaned
HLT_PFMET200_HBHE_BeamHaloCleaned
HLT_PFMET250_HBHECleaned

gion $|\eta| < 2.1$, passing tight identification and isolation requirements, and with a minimum separation in the azimuthal angle $\Delta\phi(e, E_T^{\text{miss}}) > 0.5$. These events represent the denominator, and the numerator events are also required to fire at least one of the E_T^{miss} HLT trigger paths. The efficiency of the trigger is almost 1 for E_T^{miss} above the threshold, therefore the value was fixed at 1.

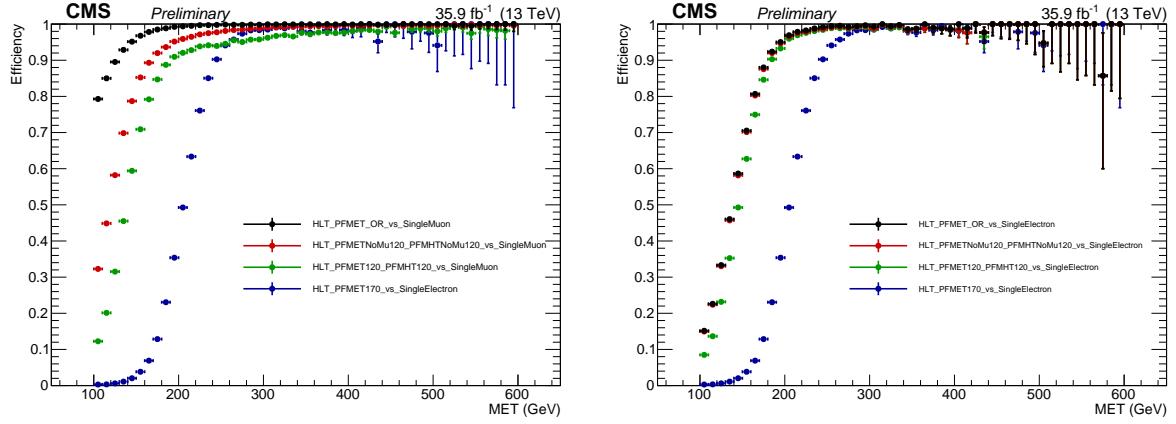


Figure 8: 2016 Trigger efficiency for the OR of the `HLT_PFMETNoMu*_PFMHTNoMu*_IDTight`, `HLT_PFMET*_PFMHT*_IDTight`, and `HLT_PFMET170_*` HLT paths as function of the minimum value between the offline reconstructed E_T^{miss} and H_T^{miss} . The efficiencies are calculated from the SingleElectron (left) and SingleMuon (right) primary dataset.

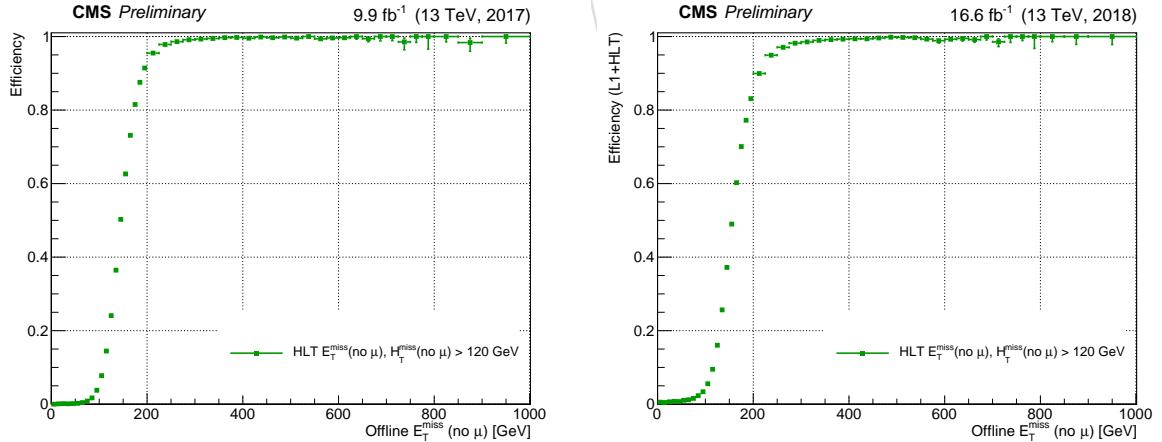


Figure 9: 2017 (left) and 2018 (right) Trigger efficiency for the `HLT_PFMETNoMu120_PFMHTNoMu120_IDTight` trigger path as function of the offline reconstructed E_T^{miss} . The efficiencies are calculated from the SingleMuon dataset[39][40].

296 3 Physics objects

297 In this section, a list of the physics objects used in the analysis is presented, with performance
 298 and validation plots. The objects are selected according to the standard Run2 recommendations
 299 provided by the various POGs for the Summer16, Fall17 and Autumn18 MC generation cam-
 300 paign (25ns). Except for the b-tagging and VBF tag all object are directly taken from NanoAOD.

301 3.1 Vertex and Pile-up

302 Due to pileup, several primary vertices are typically reconstructed in an event. The primary
 303 vertex of the events is chosen as the one with the highest sum of the p_T^2 of the associated clus-
 304 tered particles, identified leptons, and missing transverse momentum [41]. It has to fulfill the
 305 following conditions:

- 306 • number of associated tracks > 0
- 307 • number of degrees of freedom $N_{DoF} > 4$
- 308 • vertex position along the beampipe $|z_{vtx}| < 24\text{ cm}$
- 309 • vertex distance with respect the beam pipe $d_0 < 2\text{ cm}$

310 where z_{vtx} and d_0 are the distance along and perpendicular to the beam line of the vertex with
 311 respect the nominal interaction point $(0, 0, 0)$.

312 The data sample contains a significant number of additional interactions per bunch crossing,
 313 an effect known as pileup (PU), as described in Sec. 2. Nevertheless, the MC PU description
 314 do not match exactly the conditions in data, and there is therefore the need to reweight the
 315 simulated events in order to improve the agreement with the data.

316 The MC samples are reweighted using the standard CMS PU reweighting technique [42, 43]
 317 assuming a total inelastic cross section of $\sigma_{in} = 69\,200\mu\text{b}$.

318 3.2 Electrons

319 Electrons are reconstructed from energy deposits in the ECAL matched to tracks reconstructed
 320 in the silicon tracker. The electron trajectories are reconstructed using a dedicated modeling of
 321 the electron energy loss and fitted with a Gaussian sum filter. Electrons used in this analysis
 322 are required to pass the Particle Flow criteria, and to fall in the ECAL pseudorapidity fiducial
 323 range ($|\eta| < 2.5$).

324 The electron identification used in this analysis is based on the “cut-based” Id defined by the
 325 EGamma POG tuned for the campaigns Summer16, Fall17, Autumn18 and 94X releases [44].
 326 Isolation cuts are already applied within the cut-based Id definitions, therefore no additional
 327 Isolation cut is required. In the isolation definition the effect of PU is considered by taking into
 328 account the energy deposits in the calorimeter, estimated through the so-called ρ -area method,
 329 by subtracting the median energy density in the event ρ multiplied by electron effective area.
 330 The isolation value is computed in a ΔR cone of 0.3 centered along the lepton direction. The
 331 loose cut-based id is applied to both electrons.

332 The detailed set of cuts are reported in the Table 16. $\Delta\eta_{in}^{seed}$ and $\Delta\varphi_{in}$ are the difference in η
 333 and φ between the track position as measured in the inner layer, extrapolated to the interaction
 334 vertex and then extrapolated to the calorimeter and the η of the seed cluster or the φ of the
 335 supercluster, H/E is the ratio of the hadronic energy of the CaloTowers in a cone of radius
 336 0.15 centred on the electron’s position in the calorimeter to the electromagnetic energy of the
 337 electron’s supercluster, $\sigma_{i\eta i\eta}$ is the spread in eta in units of crystals of the electrons energy in 5x5

block centred on the seed crystal, and $1/E - 1/p$ is the difference of the inverse of the energy and the momentum. The relative isolation is defined as the ratio of the p_T sum of all charged and neutral particle-flow candidates (excluding other PF electrons and muons) in the event within a cone with a radius of $\Delta R = 0.3$ centered along the electron direction. Corrections in order to reduce the PU contamination are also applied, using the effective area method.

Table 16: Fall17 cut-based selection for 94X releases [44]. EB: barrel cuts ($|\eta_{\text{supercluster}}| \leq 1.479$); EE: endcap cuts ($|\eta_{\text{supercluster}}| > 1.479$)

Electrons loose	EB	EE
$\sigma_{i\eta i\eta}$	< 0.0112	0.0425
$\Delta\eta_{in}^{\text{seed}}$	< 0.00377	0.00674
$\Delta\varphi_{in}$	< 0.0884	0.169
H/E	< $0.05 + 1.16/E_{SC} + 0.0324\rho/E_{SC}$	$0.0441 + 2.54/E_{SC} + 0.183\rho/E_{SC}$
relIso (EA)	< $0.112 + 0.506/p_T$	$0.108 + 0.963/p_T$
$1/E - 1/p$	< 0.193	0.111
missing hits	≤ 1	1
conversion veto	yes	yes
$ d_0 $	< 0.05	0.10
$ d_z $	< 0.10	0.20

Electrons in the present analysis are identified with the standard cut-based identification methods and the *loose* working point. A sufficiently loose selection criterion is needed in order to select leptons arising from a boosted Z , potentially close in ΔR . The electron isolation does not represent a problem, because the PF algorithm does not sum the contribution of other nearby electrons. These selections are tested on simulation using very boosted events, in order to check that no loss of efficiency is introduced by the reconstruction algorithms when the two electrons are close to each other. The efficiency as a function of the ΔR and p_T of the two leptons is shown in Fig. 10. The HEEP Id represents a valid alternative for electron identification, but it is not then used in the analysis, and kept only as a cross-check.

Scale factors for the electron reconstruction, identification, isolation are derived by the EGAMMA POG through the tag-and-probe method on the $Z \rightarrow ee$ mass peak for all the working points separately, as a function of the p_T and η of the electrons, and are applied consistently in the analysis to account for the small data/simulation difference in the efficiencies of these selections.

Validation of the electron object is performed with an inclusive $Z \rightarrow e^+e^-$ selection, for events passing the electron triggers (Sec. 2.4), and the leading (sub-leading) electron passing the *loose* Id, and a p_T threshold of 55 GeV (20 GeV).

The data/simulation comparison, after the application of all scale factors, is shown in Figure 11 for 2016, Figure 12 for 2017 and Figure 13 for 2018.

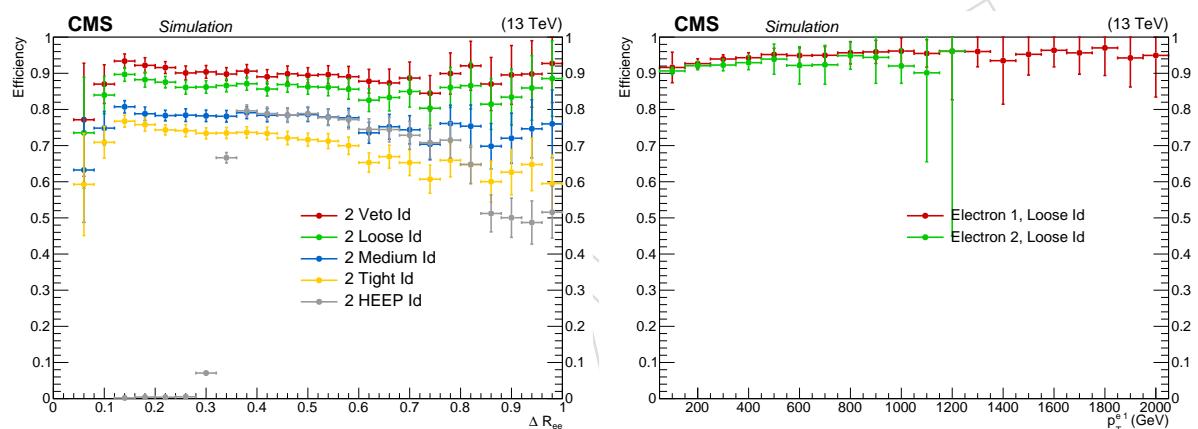


Figure 10: Electron identification efficiency as a function of the ΔR between the two electrons at generation level (left) and p_T (right), after matching and p_T selections. Events from different signal samples are considered together.

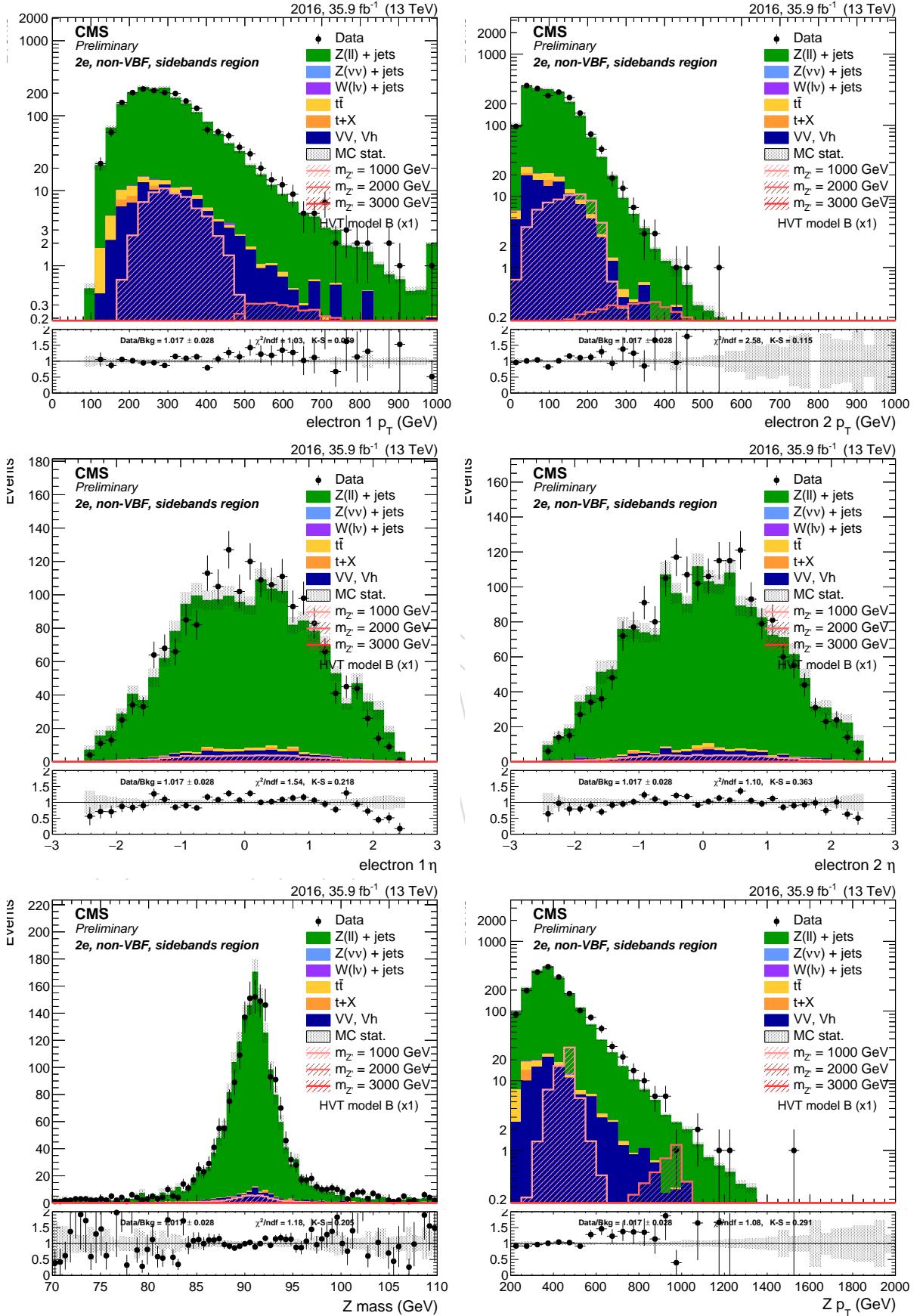


Figure 11: Top: Leading (left) and sub-leading (right) electron p_T spectra. Center: Leading (left) and sub-leading (right) electron η distribution. Bottom: Reconstructed Z mass (left) and Z p_T (right). Each after the inclusive $Z \rightarrow ee$ selections for 2016.

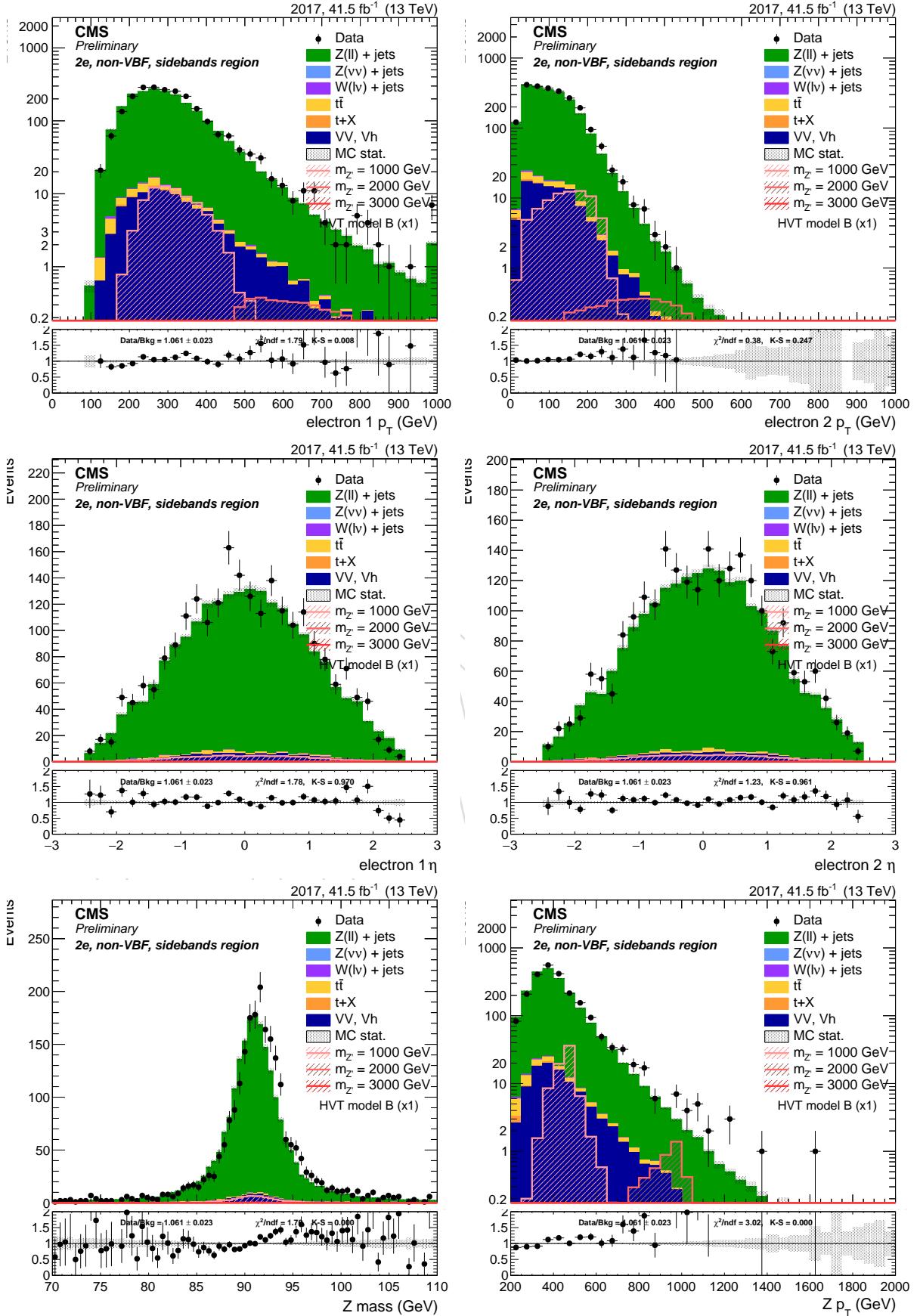


Figure 12: Top: Leading (left) and sub-leading (right) electron p_T spectra. Center: Leading (left) and sub-leading (right) electron η distribution. Bottom: Reconstructed Z mass (left) and Z p_T (right). Each after the inclusive $Z \rightarrow ee$ selections for 2017.

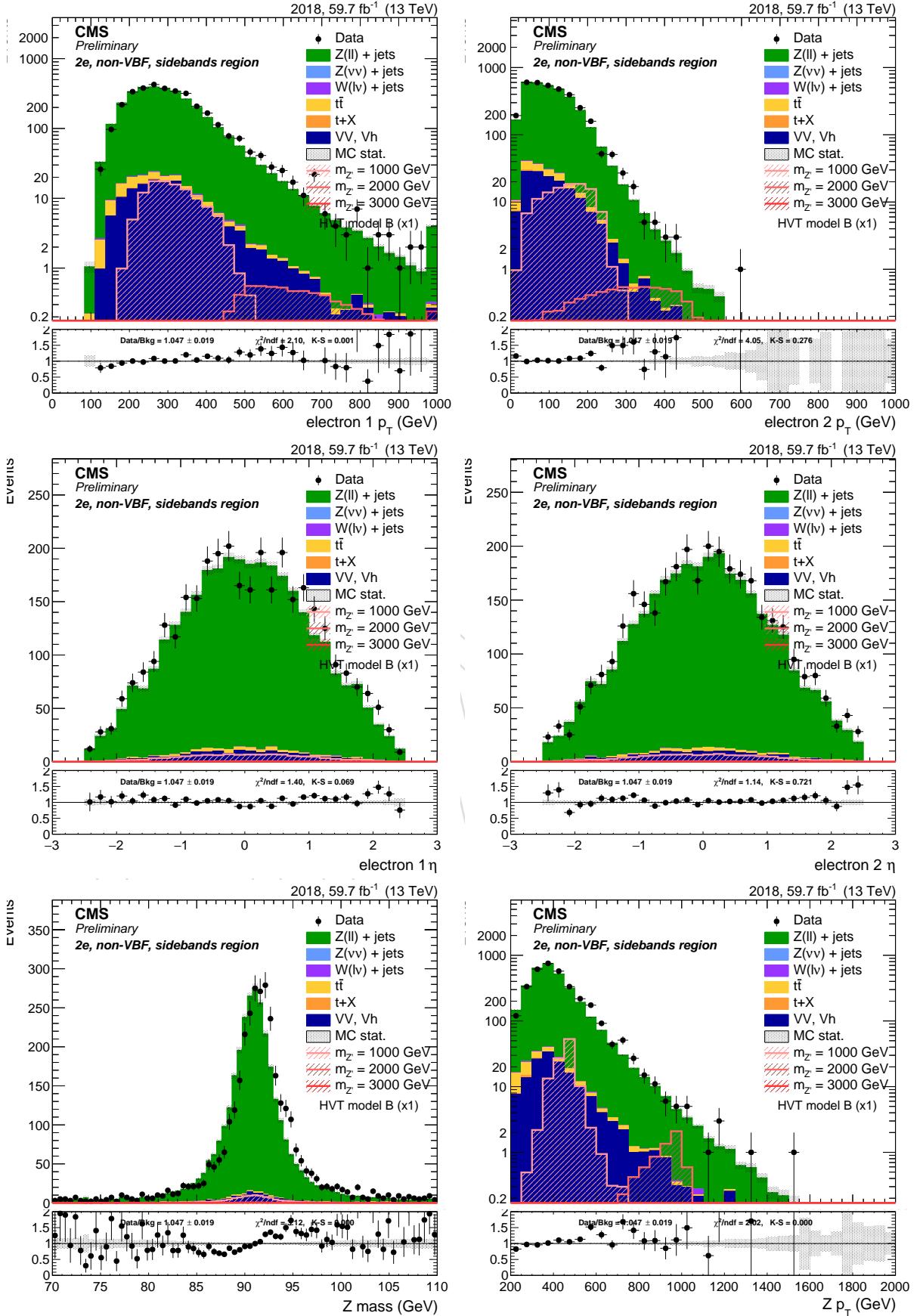


Figure 13: Top: Leading (left) and sub-leading (right) electron p_T spectra. Center: Leading (left) and sub-leading (right) electron η distribution. Bottom: Reconstructed Z mass (left) and Z p_T (right). Each after the inclusive $Z \rightarrow ee$ selections for 2018.

362 3.3 Muons

363 In the standard CMS reconstruction for pp collisions, muon tracks are first reconstructed in-
 364 dependently in the inner tracker (tracker track) and in the muon system (standalone-muon
 365 track) [45].

366 Muons are usually based on the *Particle Flow Muon* selection, considering Global Muon or a
 367 Tracker Muon candidates and by applying minimal requirements on the track components
 368 in the muon system and taking into account a matching with small energy deposits in the
 369 calorimeters. However, in the boosted $Z \rightarrow \mu\mu$ regimes, muons have similar problems to
 370 electrons. The Global muon reconstruction suffers a drop in efficiency as the ΔR between the
 371 muon decreases. This is a consequence of the seeding algorithm, which includes in the seed
 372 some segments of the other muon, and after the final muon trajectory builder, a cleaning is
 373 applied based on the number of segments and the χ^2 of the muon track. After the cleaning,
 374 only one muon track is selected among the group of tracks that share segments, and this effect
 375 avoids the reconstruction of the other muon.

376 The reconstruction of muons very close in ΔR is also a problem for the PF algorithm, which is
 377 based on the hypothesis that the muon is a minimum-ionizing particle. Another high- p_T track
 378 close to a reconstructed muon can also fail to pass the PF identification of the nearby muon,
 379 further lowering the efficiency at small angles. The adopted compromise between efficiency
 380 and fake-muons rejection is then to require that *at least* one of the two muons (not necessarily
 381 the highest- p_T) fulfills both the PF and the HighPt, while the other has to satisfy a looser
 382 selection. This asymmetric selections ensures a high efficiency ($\gtrsim 95\%$) in the whole p_T , η and
 383 ΔR ranges. The HighPt Id is a set of cuts specifically designed for high-momentum muons
 384 from the Muon POG [46]:

- 385 • to be reconstructed also as Global muon
- 386 • at least one muon chamber hit included in the global-muon track fit
- 387 • muon segments in at least two muon stations
- 388 • the track used to obtain the muon momentum needs to pass $\delta p_T / p_T < 0.3$
- 389 • tracker track transverse impact parameter $d_{xy} < 2\text{mm}$ w.r.t. the primary vertex
- 390 • longitudinal impact parameter $d_z < 5\text{mm}$ w.r.t. the primary vertex
- 391 • number of pixel hits > 0
- 392 • number of tracker layers with hits > 5 .

393 The other muons in the event, if present, should be identified with a tracker-only selection. A
 394 tight *TrackerHighPt* Id is defined using the same quality cuts on the muon track as the HighPt,
 395 but dropping the requirements that force the muon to be Global or PF:

- 396 • to be reconstructed as a standard Tracker muon (was Global muon in HightPt Id)
- 397 • at least one muon chamber hit included in the global-muon track fit
- 398 • muon segments in at least two muon stations
- 399 • the track used to obtain the muon momentum needs to pass $\delta p_T / p_T < 0.3$.
- 400 • tracker track transverse impact parameter $d_{xy} < 2\text{mm}$ w.r.t. the primary vertex
- 401 • longitudinal impact parameter $d_z < 5\text{mm}$ w.r.t. the primary vertex
- 402 • number of pixel hits > 0
- 403 • number of tracker layers with hits > 5 .

404 For muons reconstructed using the PF algorithm, the standard muon isolation is defined as
 405 the ratio of the p_T sum of all charged and neutral particle-flow candidates in the event within
 406 a cone with a radius of $\Delta R = 0.3$ centred along the lepton direction. Corrections in order to
 407 reduce the PU contamination are also applied, using the $\Delta\beta$ method. Muons with $p_T > 10$ GeV
 408 reconstructed with the PF algorithm, identified with the *loose* PFI σ lution id and either the
 409 HighPt or the TrackerHighPt id are used for muon counting and vetoed in the 0-lepton
 410 category.

411 Scale factors for the muon *HighPt* and *TrackerHighPt* identification and tracker isolation, are
 412 centrally provided as a function of the muon p_T and η by the Muon POG [38], and applied
 413 consistently in the analysis.

414 The muon selection efficiency in the signal is defined in the same way as the electrons. Figure
 415 show the muon selection efficiency as a function of the different Id selections applied
 416 as a function of the distance between the two muons, and confirms that no loss of efficiency is
 417 expected at low ΔR with the selections described. Figure 15 shows the data/simulation com-
 418 parison for the muons after the inclusive selection for 2016, Figure 16 for 2017 and Figure 17
 419 for 2018.

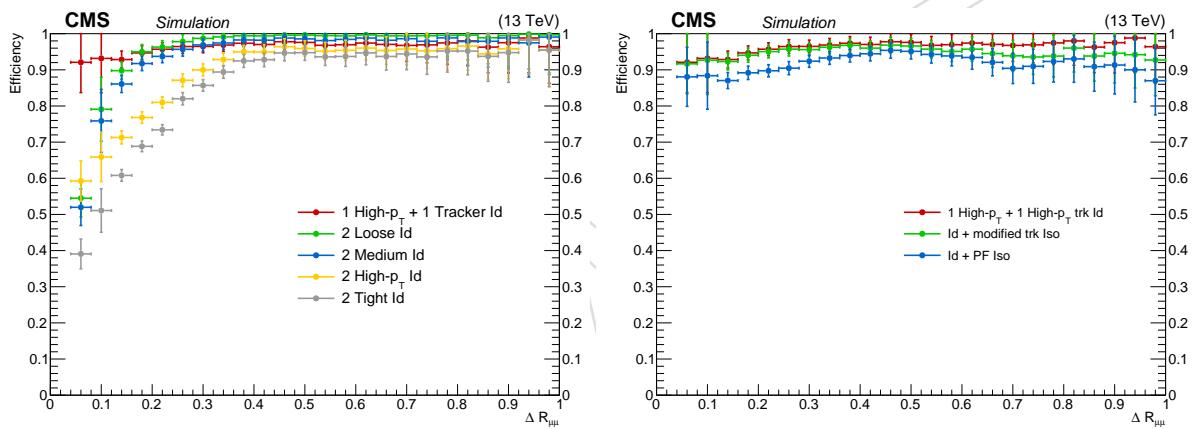


Figure 14: Identification (left) and combined identification and isolation (right) efficiency as a function of the ΔR at generation level, after matching and p_T selections, when muons are required to pass different identification and isolation requirements. Events from all the generated mass points are considered together.

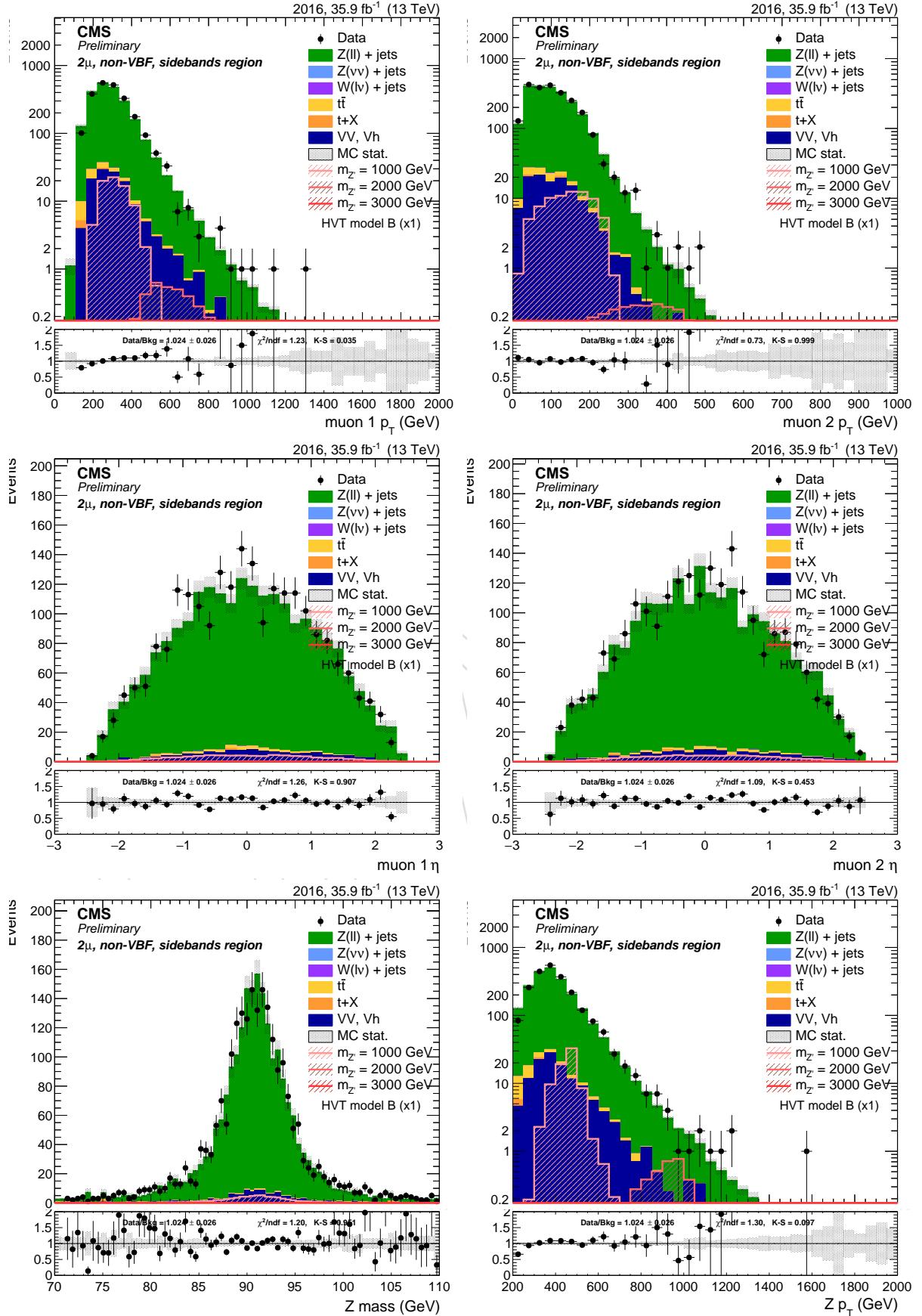


Figure 15: Top: Leading (left) and sub-leading (right) muon p_T spectra. Center: Leading (left) and sub-leading (right) muon η distribution. Bottom: Reconstructed Z mass (left) and Z p_T (right). Each after the inclusive $Z \rightarrow \mu\mu$ selections for 2016.

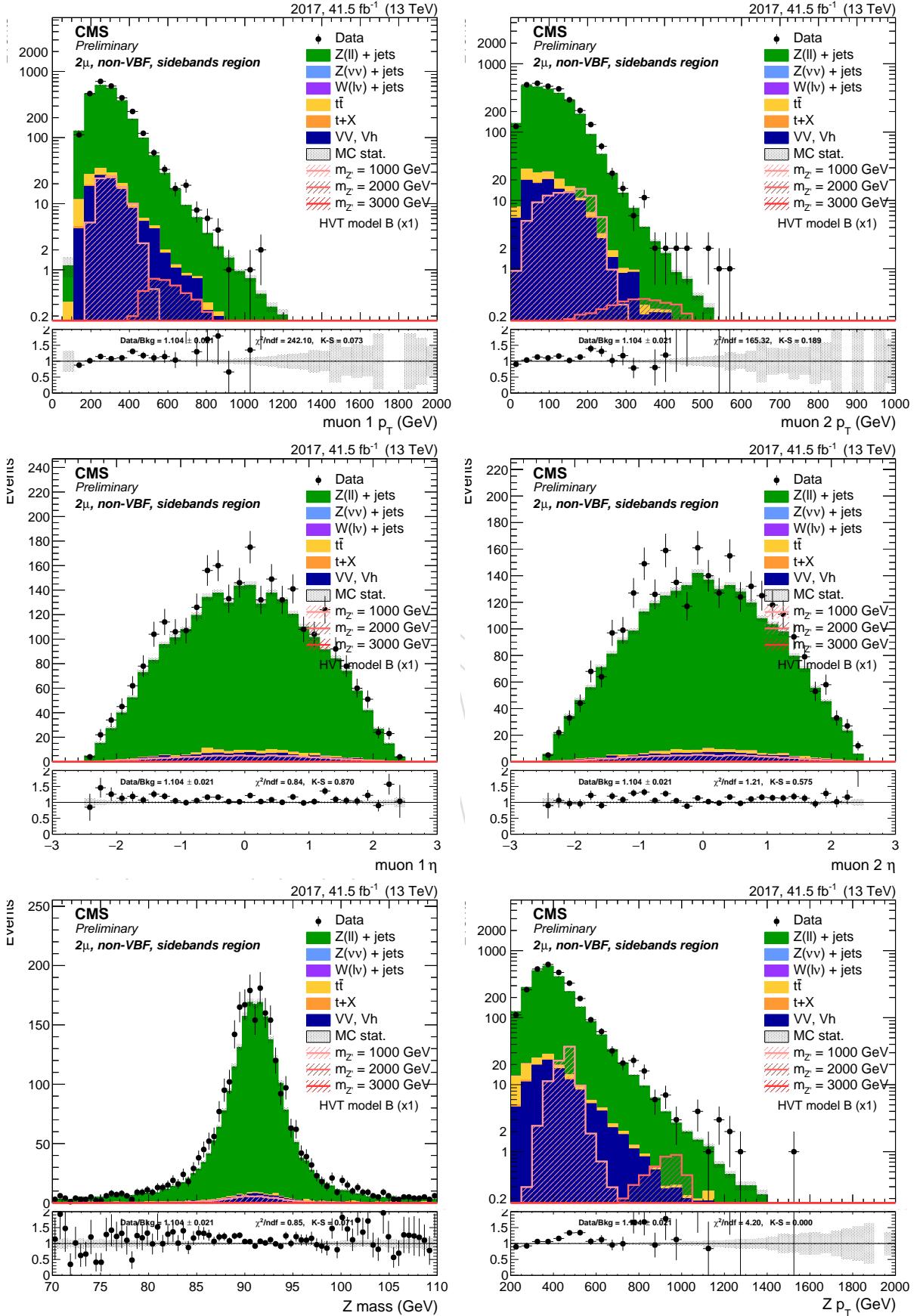


Figure 16: Top: Leading (left) and sub-leading (right) muon p_T spectra. Center: Leading (left) and sub-leading (right) muon η distribution. Bottom: Reconstructed Z mass (left) and Z p_T (right). Each after the inclusive $Z \rightarrow \mu\mu$ selections for 2017.

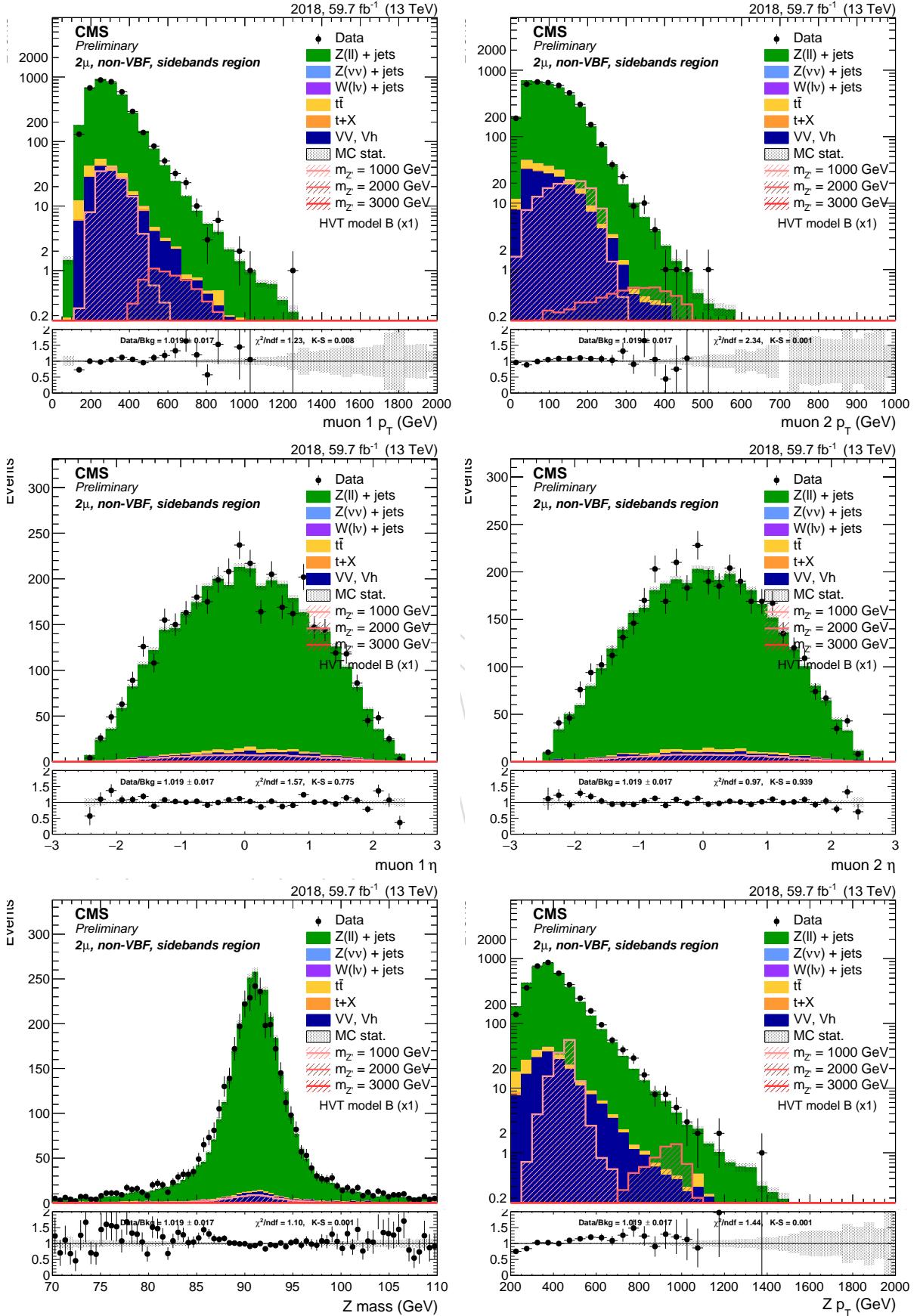


Figure 17: Top: Leading (left) and sub-leading (right) muon p_T spectra. Center: Leading (left) and sub-leading (right) muon η distribution. Bottom: Reconstructed Z mass (left) and Z p_T (right). Each after the inclusive $Z \rightarrow \mu\mu$ selections for 2018.

420 3.4 Taus

421 The presence of hadronically-decaying taus may be an indication of other electroweak bosons
 422 in the events, for instance from $t\bar{t}$ decays. Since hadronic tau decays are not targeted in this
 423 analysis, they only act as veto for the events both in the signal and in the control regions. The
 424 selection criteria for taus are $p_T > 18$ GeV and $|\eta| < 2.3$, and being at least $\Delta R > 0.4$ afar from
 425 other isolated electrons and muons.

426 3.5 Jets

427 Events in the CMS detector are reconstructed using the the particle-flow algorithm [47, 48],
 428 which combines information from all sub-detectors in order to reconstruct stable particles
 429 (muons, electrons, photons, neutral and charged hadrons). Two different methods to remove
 430 contributions from pileup are used. For the small conesize jets with $R = 0.4$ (AK4 jets) the
 431 charged hadron subtraction algorithm (CHS) [49] and for jets with $R = 0.8$ (AK8 jets) the
 432 pileup per particle identification (PUPPI) [50] algorithm are applied. The remaining particles
 433 are used as input to jet clustering algorithms to reconstruct particle-flow jets. The jets are clus-
 434 tered using the FASTJET package [51] with the anti- k_T jet clustering algorithm [52] with two
 435 different clustering parameters, $R = 0.4$ (AK4 jets) or $R = 0.8$ (AK8 jets).

436 In this analysis, AK4 jets are considered if the p_T is larger than 30 GeV, lie in the tracker ac-
 437 ceptance ($|\eta| < 2.4$), pass the tight JetID and being at least $\Delta R > 0.4$ afar from other isolated
 438 electrons and muons. For AK8 jets a p_T of larger than 200 GeV and $|\eta| < 2.4$ is required.

439
 440 For the identification of a VBF production we are looking for AK4 jets which satisfy $|\eta| < 5.$,
 441 pass the tight JetID, being at least $\Delta R > 1.2$ afar from the Higgs candidate and $\Delta R > 0.4$ afar
 442 from other isolated leptons. Pileup is reduced by requiring the tight Pileup Jet Id. The two jets
 443 with the largest transverse momentum must have opposite η , an η separation of larger than
 444 4 ($\Delta\eta(jet_1, jet_2) > 4$) and a di-jet mass of larger than 500 GeV to be considered as jets coming
 445 from a VBF production.

446 3.6 Jet pile-up mitigation

447 The algorithm chosen to mitigate the effect of pileup on AK8 jets and E_T^{miss} is the *pileup per*
 448 *particle identification* (PUPPI) [50].

449 This method uses local shape information, event pileup properties and tracking information
 450 together in order to compute a weight describing the degree to which a particle is pileup-like.
 451 A local variable α is computed which contrasts the collinear structure of QCD with the soft
 452 diffuse radiation coming from pileup. The distribution of α for charged pileup, assumed as a
 453 proxy for all pileup, is then used to calculate a weight for each particle on an event-by-event
 454 basis.

455 Different definitions are used for particles in the central ($|\eta| < 2.5$) and forward region ($|\eta| >$
 456 2.5) of the detector, where tracking information is not available. For a given particle i in the
 457 central region, α is defined as

$$\alpha_i = \log \sum_{\substack{j \in Ch, PV \\ j \neq i}} \left(\frac{p_{T,j}}{\Delta R_{ij}} \right)^2 \Theta(R_{min} < \Delta R_{ij} < R_0)$$

458 where Θ is the step function, i refers to the particle in question and j refers to the neighbouring
 459 charged particles from the primary vertex within a cone of radius R_0 and a minimum radial

460 difference of R_{min} . In the forward region, outside of the tracker coverage, the sum is taken over
461 all the particles.

462 A χ^2 approximation

$$\chi_i^2 = \frac{(\alpha_i - \bar{\alpha}_{PU})^2}{RMS_{PU}^2}$$

463 where $\bar{\alpha}_{PU}$ is the median value of the α_i distribution for pileup particles in the event and RMS_{PU}
464 is the corresponding RMS, is used to determine the probability of a particle to be from pileup.
465 In the tracker region, $\bar{\alpha}_{PU}$ and RMS_{PU} are calculated using all charged pileup particles, while
466 in the forward region they are calculated using all the particles in the event. In the forward
467 region the corresponding χ^2 are summed. Particles are then assigned a weight given by $w_i =$
468 $F_{\chi^2, NDF=1}(\chi_i^2)$ where $F_{\chi^2, NDF=1}$ is the cumulative distribution function of the χ^2 distribution
469 with one degree of freedom.

470 The algorithm parameter choices are similar to what is recommended in Ref. [50]. No additional
471 pileup corrections are applied to jets clustered from these weighted inputs.

472 3.6.1 Jet mass

473 The jet mass is the main observable in distinguishing a H-jet from a QCD jet. Jet grooming
474 consists in the suppression of uncorrelated UE/PU (underlying event and pile-up) radiation
475 from the target jet and improves the discrimination pushing the jet mass for QCD jets towards
476 lower values while maintaining the jet mass for V(H)-jets around the boson-mass.

The grooming algorithm chosen for this analysis is the *Soft Drop*, applied on top of the PUPPI particle candidates for pile-up mitigation [50]. The “soft drop declustering” is a jet substructure technique which recursively removes soft wide-angle radiation from a jet [53]. It depends on two parameters: a soft threshold z_{cut} and an angular exponent β . Like any grooming method, soft drop declustering removes wide-angle soft radiation from a jet in order to mitigate the effects of contamination from initial state radiation (ISR), underlying event (UE), and multiple hadron scattering (pileup). Given a jet of radius R_0 with only two constituents, the soft drop procedure removes the softer constituent unless:

$$\frac{\min(p_T^1, p_T^2)}{p_T^1 + p_T^2} > z_{cut} \left(\frac{\Delta R_{12}}{R_0} \right)^\beta$$

477 By construction, this condition fail for wide-angle soft radiation. The degree of jet grooming
478 is controlled by z_{cut} and β , with $\beta \rightarrow \infty$ returning back an ungroomed jet. The $\beta = 0$ limit
479 of the energy loss is particularly interesting, since it is largely insensitive to the value of the
480 strong coupling constant. The default parameters used by CMS are $\beta = 0$ and $z_{cut} = 1$. In the
481 NanoAOD samples the jet energy corrections are applied on the jet mass by default.

482 3.7 b-tagging

483 3.7.1 Baseline tagger: subjet DEEPCSV

484 Several algorithms have been developed to tag jets from b-quarks. One of best-performing
485 algorithms, used throughout this analysis is DeepCSV. It is based on the pfCombinedInclusiveSecondaryVertexV2BJetTags, often shortened to *combined secondary vertex* (CSV), but with
486 the extension to use more charged particle tracks. This algorithm involves the use of secondary
487 vertices, together with other lifetime information, like the IP significance or decay lengths.

489 Secondary vertices are reconstructed with the inclusive vertex finder algorithm, that does not
 490 require jets (and thus is independent on the jet size) and uses all tracks to reconstruct secondary
 491 vertices [54]. In order to provide discrimination even when no secondary vertices are found, so
 492 the maximum possible b-tagging efficiency is not limited by the secondary vertex reconstruc-
 493 tion efficiency ($50 \sim 60\%$). In many cases, tracks with an IP significance > 2 can be combined in
 494 a so-called pseudo vertex, allowing for the computation of a subset of secondary vertex based
 495 quantities even without an actual vertex fit. When even this is not possible, a no vertex cate-
 496 gory reverts simply to track based variables similarly to the jet probability algorithm. The list
 497 of variables feeded as input to an Artificial Neural Network is:

- 498 • the vertex category (real, pseudo, or no vertex)
- 499 • 2D flight distance significance
- 500 • vertex mass
- 501 • number of tracks at the vertex
- 502 • ratio of the energy carried by tracks at the vertex with respect to all tracks in the jet
- 503 • the pseudo-rapidity of the tracks at the vertex with respect to the jet axis
- 504 • 2D IP significance of the first track that raises the invariant mass above the charm
 505 threshold of 1.5 GeV when subsequently summing up tracks ordered by decreasing
 506 IP significance
- 507 • 3D signed IP significances for all tracks in the jet
- 508 • number of tracks in the jet
- 509 • ΔR between the secondary vertex flight direction and the jet axis
- 510 • number of secondary vertices associated to the jet or sub-jet

511 Thanks to the explicit jet-to-track association, b-tagging algorithms can be applied to both the
 512 fat-jet and the sub-jets, independently. The DeepCSV is applied on the same charged particle-
 513 flow candidate list that compose the AK8 subjets. The jet or sub-jet is considered as tagged if
 514 the discriminator value is above some threshold value, often referred to as the cut value, and
 515 the efficiency is defined as the number of jets which have a discriminator value that is above
 516 that cut divided by the total number of jets (of the same flavor). Three working points are
 517 usually defined for each algorithm, defining cuts in the discriminators based on the level of
 518 mis-tagging. The cut values and the corresponding mis-tagging for light-flavor jets relative to
 519 the DeepCSV algorithm are reported in Tables 17, 18 and 19.

Working point	Cut	ϵ_{light}
Loose	0.2217	$\sim 10\%$
Medium	0.6321	$\sim 1\%$
Tight	0.8953	$\sim 0.1\%$

Table 17: 2016 DeepCSV official working points.

Working point	Cut	ϵ_{light}
Loose	0.1522	$\sim 10\%$
Medium	0.4941	$\sim 1\%$
Tight	0.8001	$\sim 0.1\%$

Table 18: 2017 DeepCSV official working points.

Working point	Cut	ϵ_{light}
Loose	0.1241	$\sim 10\%$
Medium	0.4184	$\sim 1\%$
Tight	0.7527	$\sim 0.1\%$

Table 19: 2018 DeepCSV official working points.

520 It is known that b-tagging efficiency is not the same in data and MC. In order to take into
 521 account this shortcoming, the BTV POG provides collections of b-tagging scale factors for b-jets
 522 and mistagged light jets, measured for different physics processes, for the supported tagging
 523 algorithms and the three standard working points [55]. A weight is calculated on a per-event
 524 basis as a function of the b-tagging status and the flavour of the hadron that initiated the jet in
 525 the event, according to method 1a in Ref. [56].

526 3.7.2 Choice of the b-tagging algorithm

527 The subjet b-tagging, the double-b tagger and the DeepTagMD tagger are different Higgs tag-
 528 ging method, and only one can be adopted in the analysis. In order to test the algorithm perfor-
 529 mances, ROC curves have been built by deriving the Higgs b-tagging efficiency and non-Higgs
 530 mis-tagging efficiency on simulation, by using the information at generator level. In this case,
 531 the “tag” is represented by the events in signal samples (the leading AK8 jet is the Higgs bo-
 532 son candidate), and as a “mistag” all other AK8 jets in SM backgrounds. Both the “tag” and
 533 “mistag” events have to pass the selections of the analysis, including the jet mass.

534 Fig. 18 shows the ROC curves for the CSV, DeepCSV, double-b tagger and DeepTagMD tag-
 535 gers. CVS1 and DeepCSV1 correspond to the maximal tagger value of both sub-jets, CSV2 and
 536 DeepCSV2 to the minimal value. CSV shows the mean of CSV1 and CSV2, DeepCSV the mean
 537 of DeepCSV1 and DeepCSV2. DeepTagMD_ZHbbvsQCD would show the best performance,
 538 but because of the mass sculpting effect DeepCSV2 was chosen to be used for this analysis.
 539 The markers show the different combinations of loose and medium work points for DeepCSV
 540 sub-jets.

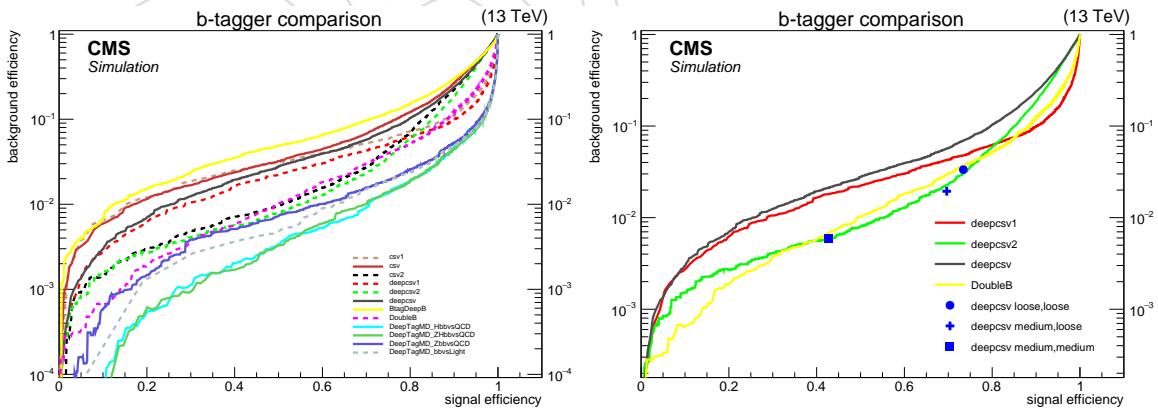


Figure 18: ROC curves for the considered b-tagging algorithms. The background is repre-
 sented by the weighted sum of the SM backgrounds in the channel, after all analysis selections
 (including a m_j cut on the Higgs mass, and excluding other b-tagging selections). The signal is
 represented by HVT model B signal events after passing the same selections as the background.

541 Taggers who cause a masssculpting effect should be avoided, as they could lead to a bump in
 542 the signal region of the background, which then could be mistaken for a signal. The masssculpt-

543 ing effect can be revealed by comparing the normalized sum of the background distribution for
 544 the jet mass with different cuts applied on the tagger and is shown in Figure 19 for a combined
 545 sample. In order to have a similar efficiency for both taggers, the range of the cuts are differ-
 546 ent. The tagger DeepTagMD_ZHbbvsQCD shows a large masssculpting effect, therefore the
 547 DeepCSV2 tagger was chosen.

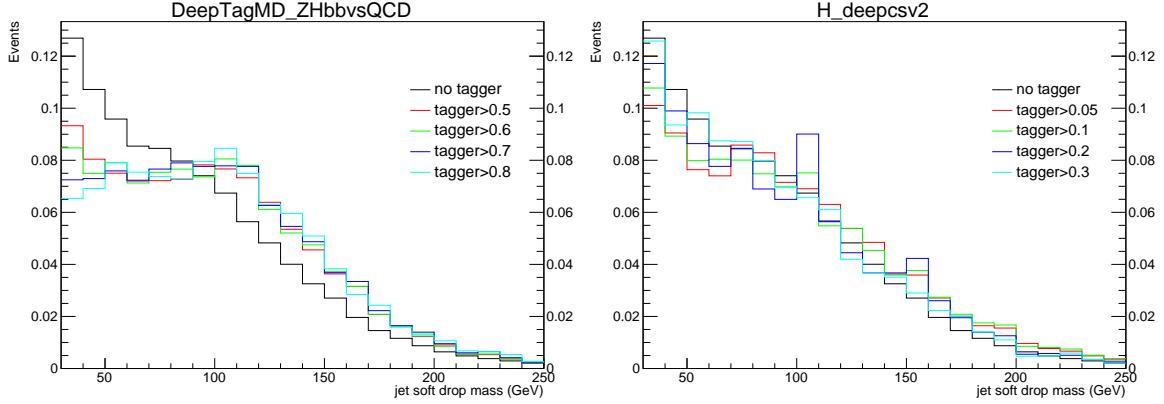


Figure 19: Masssculpting effect for the taggers DeepTagMD_ZHbbvsQCD (left) and DeepCSV2 (right).

548 3.8 Missing Energy

549 The E_T^{miss} is defined as the imbalance in the transverse energy of all visible particles, and it is
 550 reconstructed with the particle flow algorithm [47]. The raw E_T^{miss} is defined as the inverse vec-
 551 torial sum of the transverse momentum of all the reconstructed charged and neutral particle
 552 flow candidates: $E_T^{\text{miss}} = -\sum_{i=0}^{\text{all}} \vec{p}_{T,i}$. The raw E_T^{miss} is systematically different from true E_T^{miss} ,
 553 for many reasons including the non-compensating nature of the calorimeters and detector mis-
 554 alignment. To better estimate the true E_T^{miss} , jet energy corrections are propagated to the Puppi
 555 MET. Figure 20 shows the Puppi E_T^{miss} distribution for data and Monte Carlo for each year.

556 3.9 VBF

557 The VBF production channel is identified by looking for jets which pass the tight Jet Id, the
 558 tight Pileup jet ID and satisfy $|\eta| < 5$, $\Delta R(H, \text{jet}) > 1.2$ and $\Delta R(\ell, \text{jet}) > 0.4$. The two jets
 559 with the largest transverse momentum must have opposite η , an η separation of larger than 4
 560 ($\Delta\eta(jet_1, jet_2) > 4$) and a di-jet mass of larger than 500 GeV to be considered as VBF jets. The
 561 VBF production channel has different spin correlations than the $q\bar{q}$ production. This results
 562 in a different distribution of the Higgs rapidity, showing a double-peaked structure at +1 and
 563 -1, which is also true for the Z boson. In the 0 lepton channels the X mass cannot be fully
 564 reconstructed, therefore the transverse mass is used. The events at large Higgs η usually have
 565 a naturally lower m_T^X , because the longitudinal component of the $Z \rightarrow \nu\nu$ is lost. Since these
 566 events contribute less in the fit, this region of the phase space is cut away by requiring $|\eta| < 1.1$
 567 for the Higgs in the 0 lepton VBF channels. This selection sculpts the mass by removing the
 568 low- m_T^X tails, making the signal look like a peak again, with a modest impact on the signal
 569 efficiency. In figures 21-26 the data/MC comparison is shown for all the years.

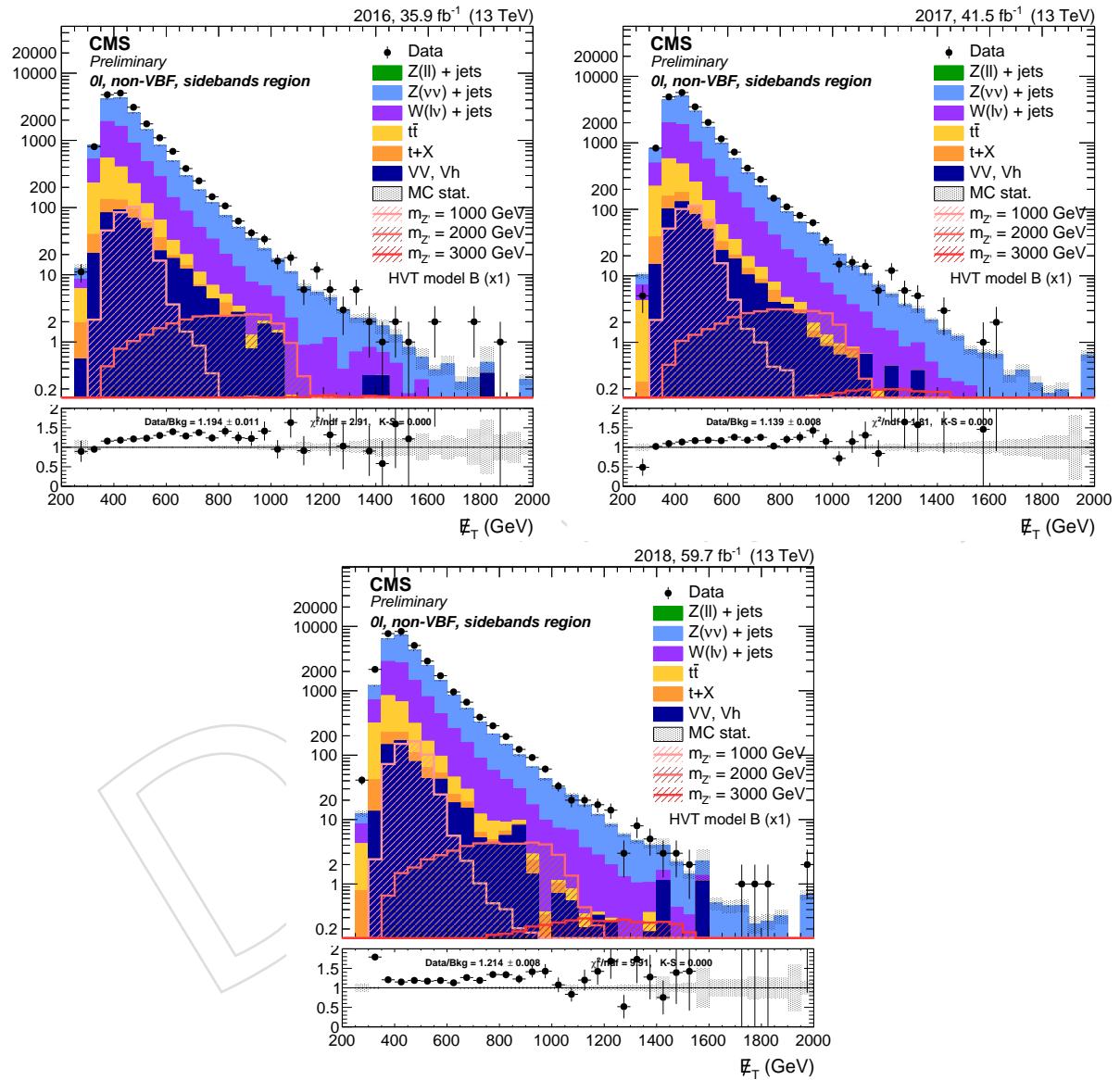


Figure 20: E_T^{miss} in $Z \rightarrow \nu\nu$ for 2016 (top left), 2017 (top right) and 2018 (bottom)

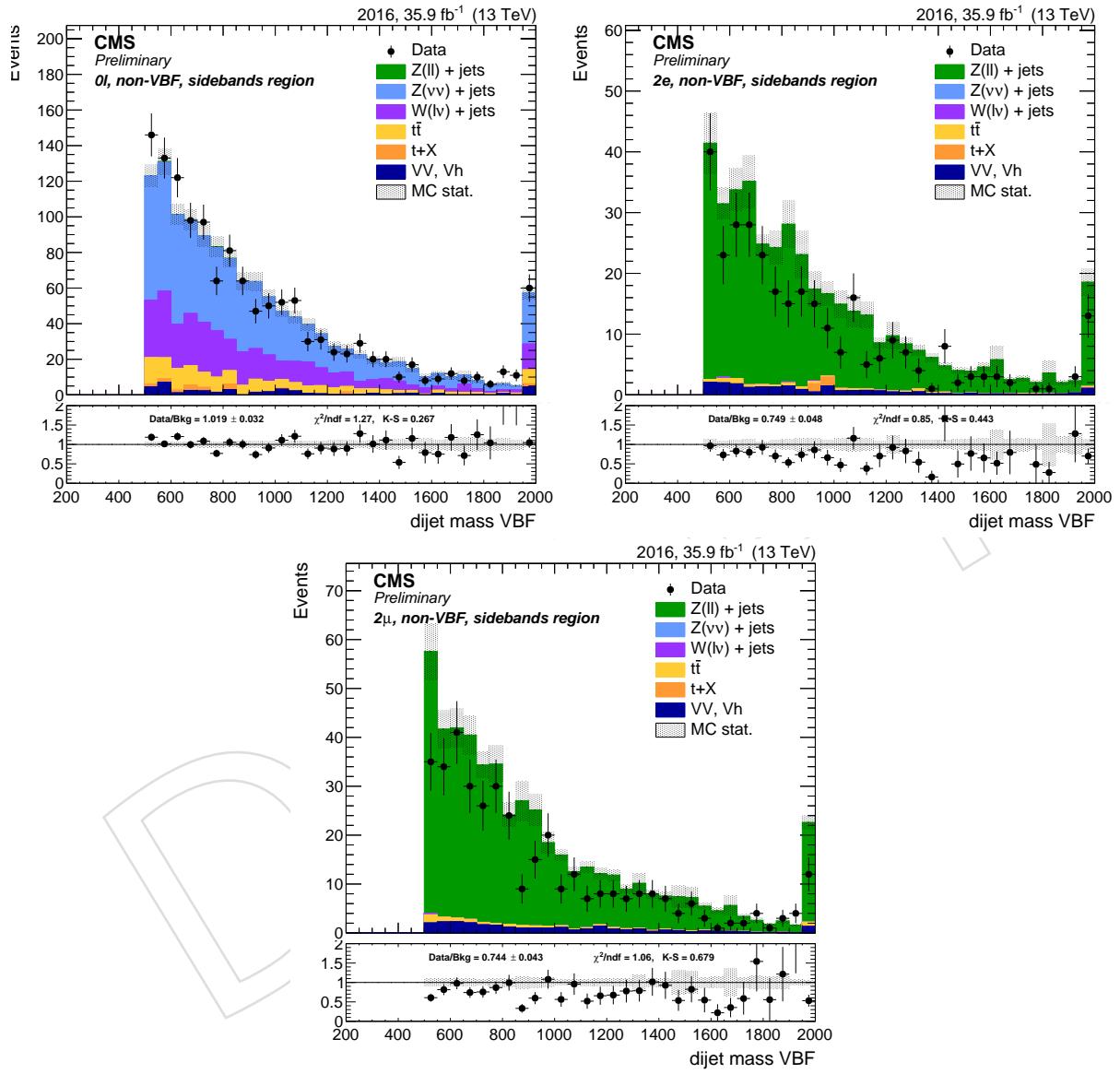


Figure 21: Dijet mass of VBF jets for 2016 $Z \rightarrow \nu\nu$ (Top Left), $Z \rightarrow ee$ (Top Right) and $Z \rightarrow \mu\mu$ (Bottom).

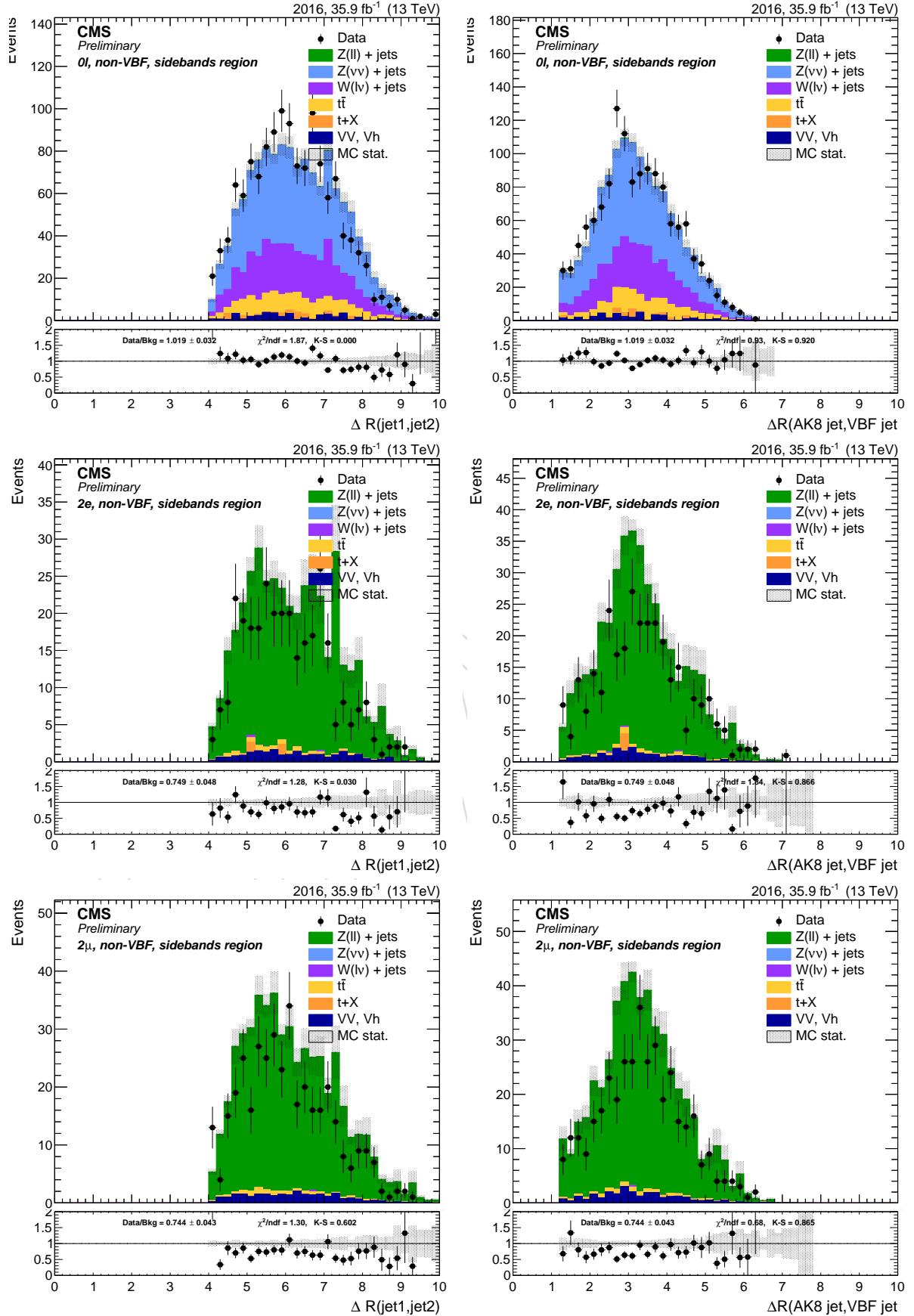


Figure 22: ΔR between VBF jets (left) and ΔR between VBF jets and Higgs (right) with inclusive selection for 2016 $Z \rightarrow \nu\nu$ (Top), $Z \rightarrow ee$ (Center) and $Z \rightarrow \mu\mu$ (Bottom).

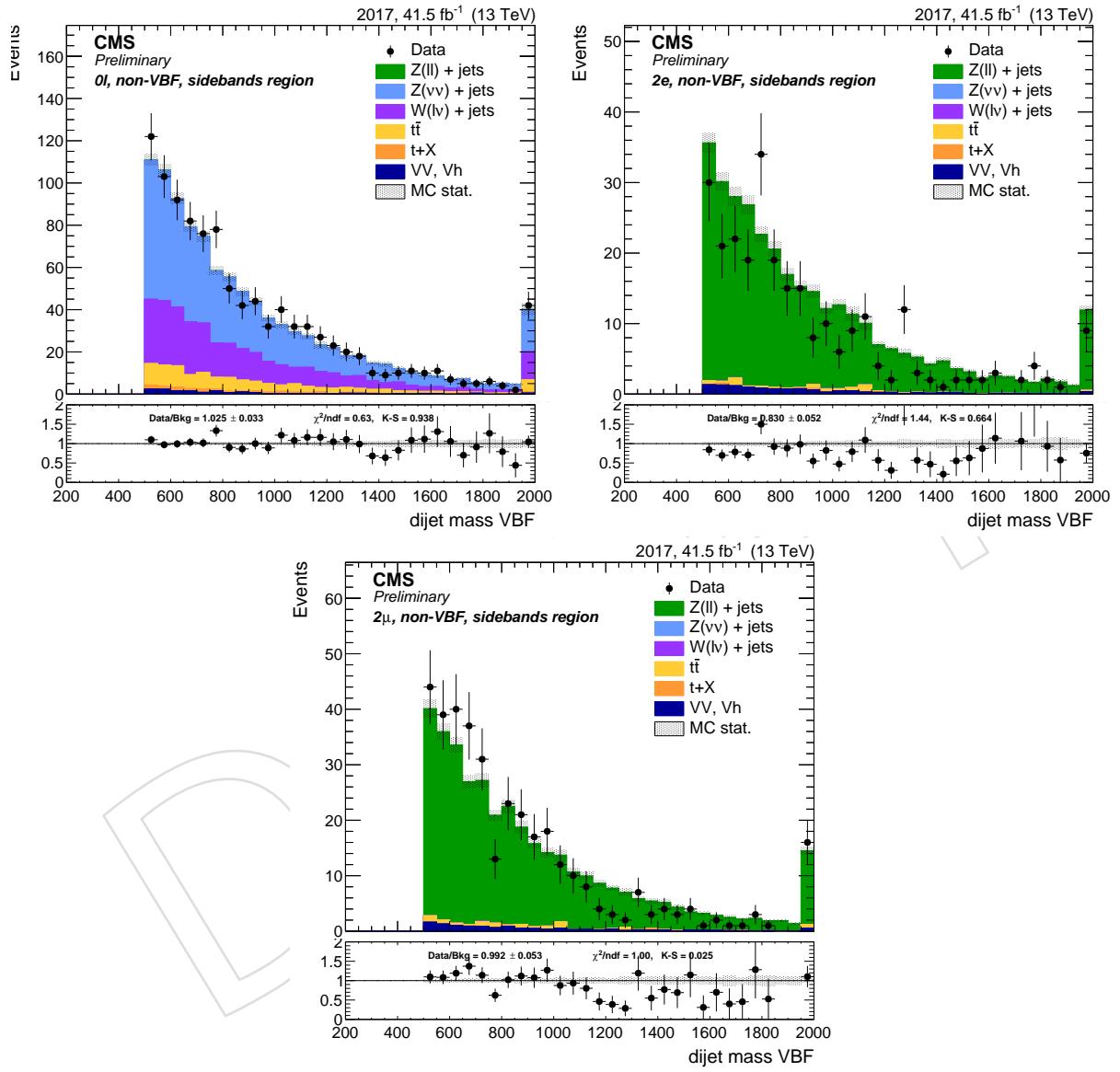


Figure 23: Dijet mass of VBF jets for 2017 $Z \rightarrow \nu\nu$ (Top Left), $Z \rightarrow ee$ (Top Right) and $Z \rightarrow \mu\mu$ (Bottom).

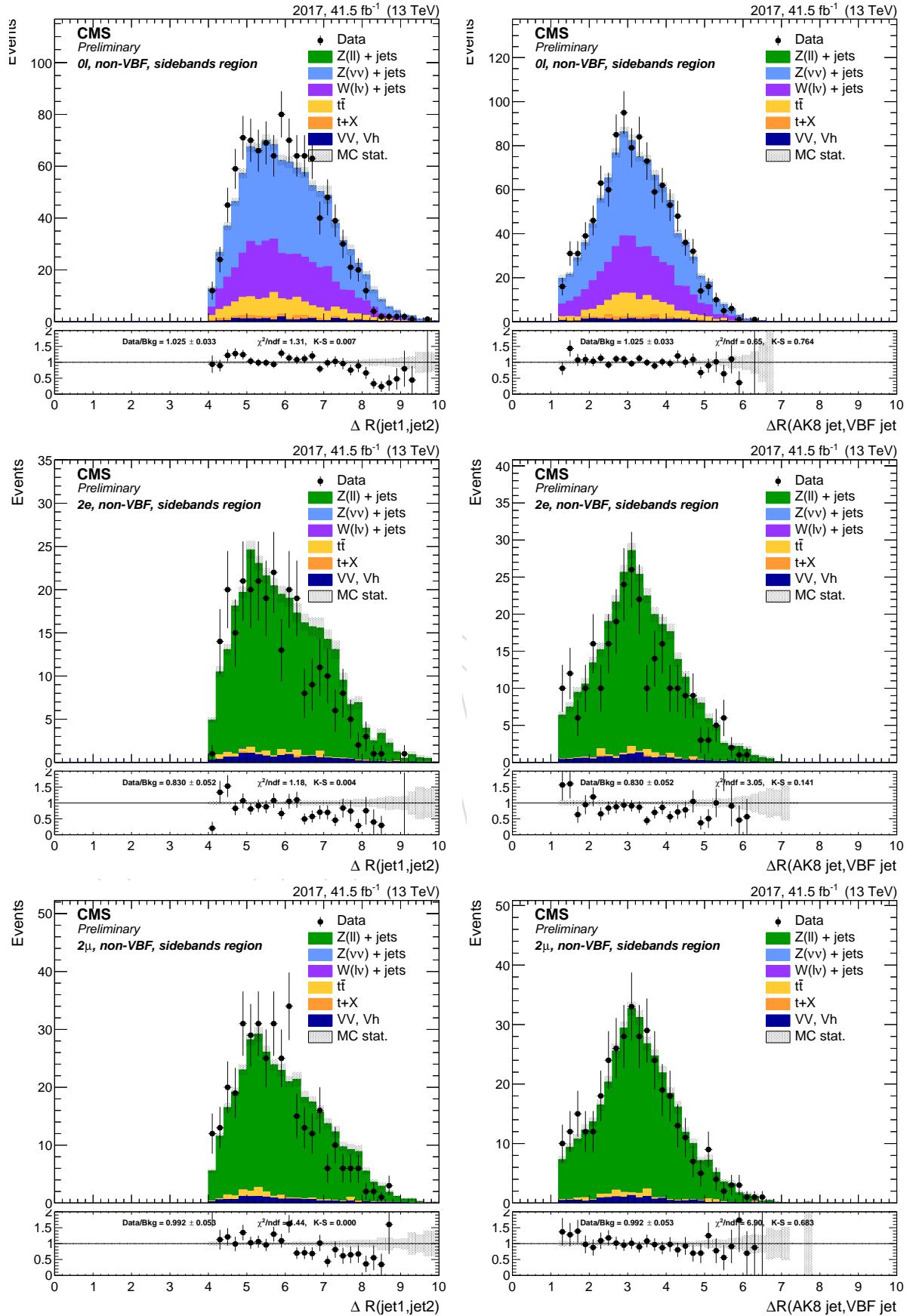


Figure 24: ΔR between VBF jets (left) and ΔR between VBF jets and Higgs (right) with inclusive selection for 2017 $Z \rightarrow \nu\nu$ (Top), $Z \rightarrow ee$ (Center) and $Z \rightarrow \mu\mu$ (Bottom).

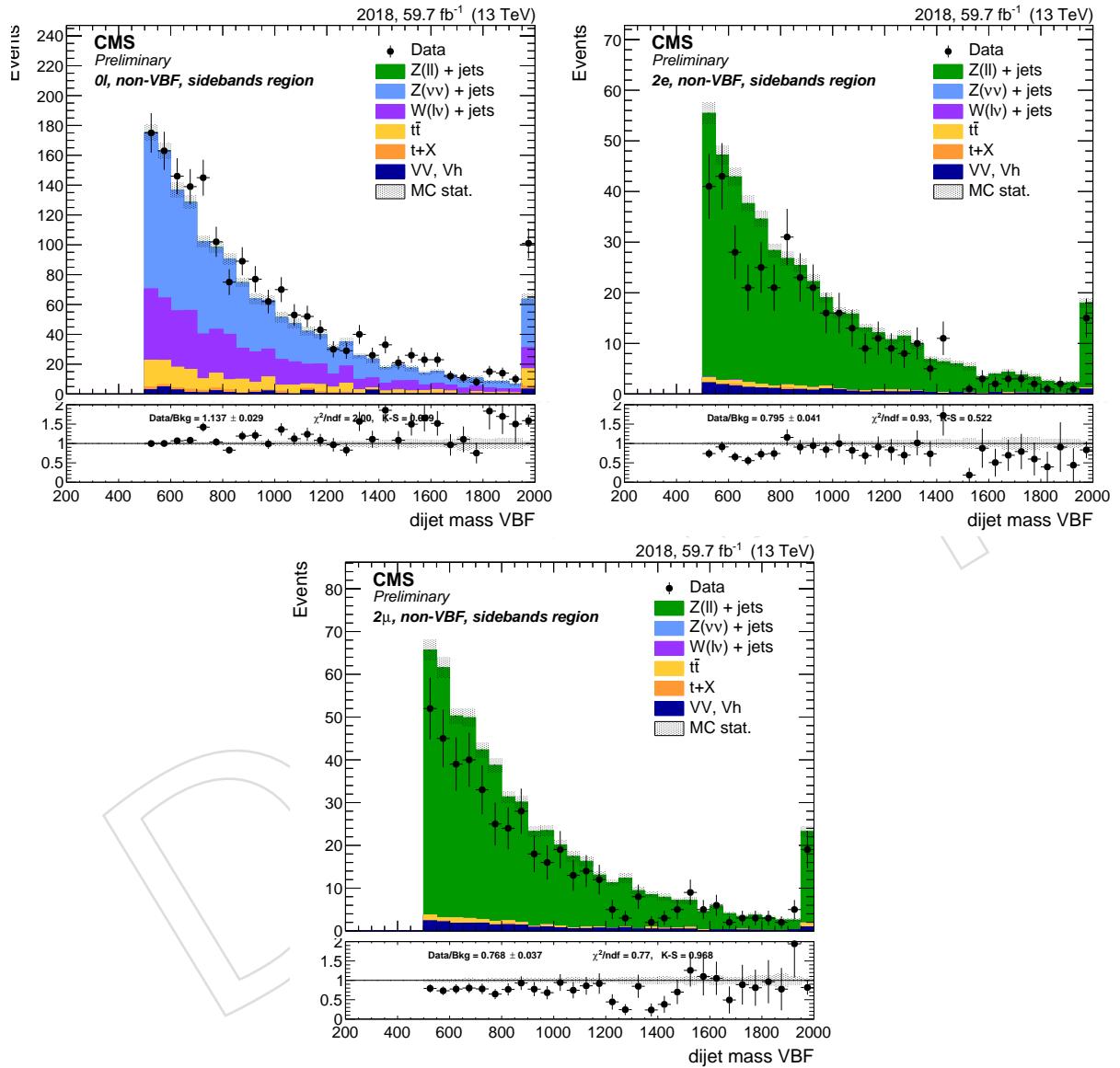


Figure 25: Dijet mass of VBF jets for 2018 $Z \rightarrow \nu\nu$ (Top Left), $Z \rightarrow ee$ (Top Right) and $Z \rightarrow \mu\mu$ (Bottom).

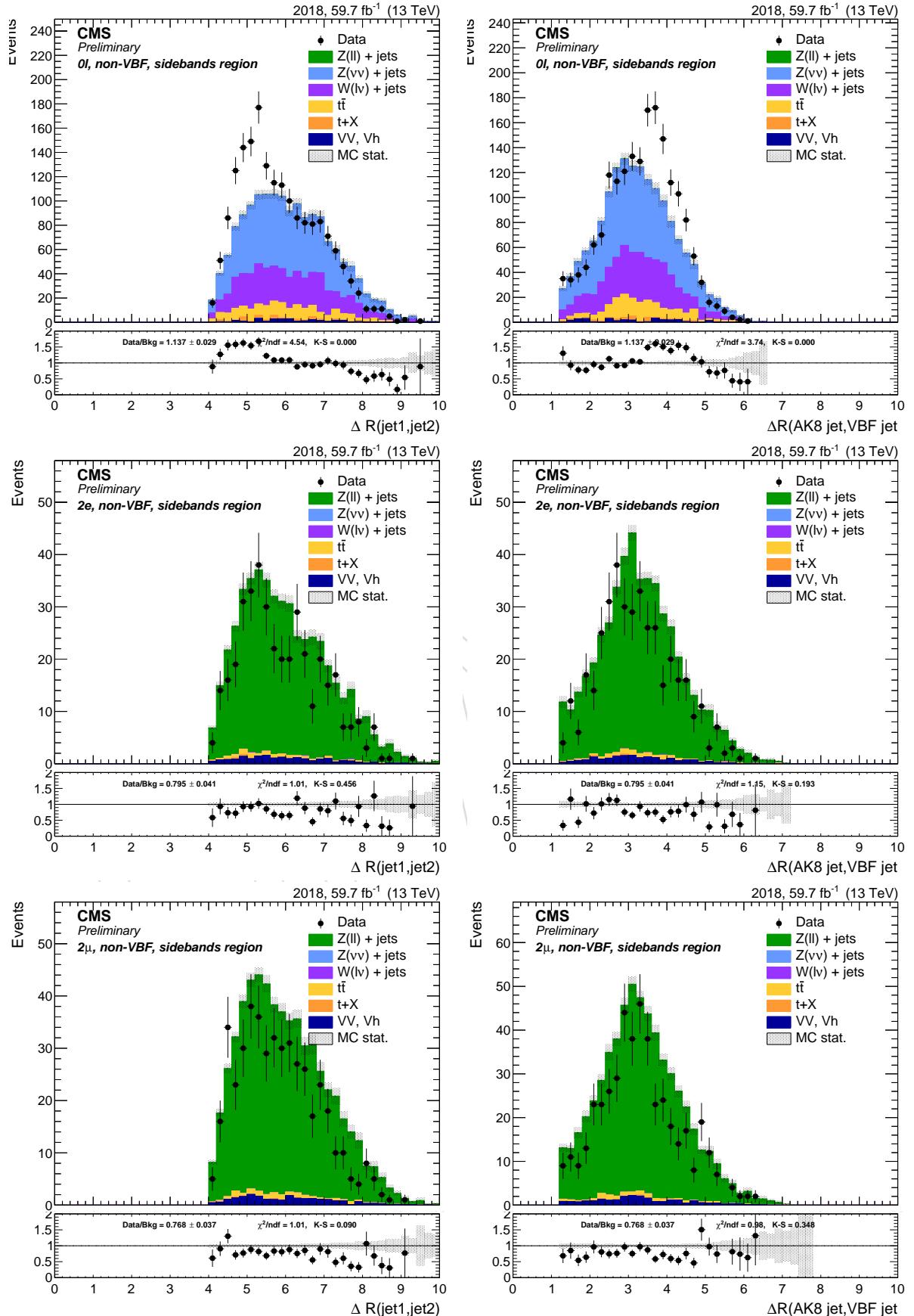


Figure 26: ΔR between VBF jets (left) and ΔR between VBF jets and Higgs (right) with inclusive selection for 2018 $Z \rightarrow \nu\nu$ (Top), $Z \rightarrow ee$ (Center) and $Z \rightarrow \mu\mu$ (Bottom).

570 4 Boson reconstruction

571 4.1 Z boson to neutrinos

572 If the Z boson decays into a pair of neutrinos, no products are visible in the detector. A simple
 573 and effective solution, adopted in this analysis, is to consider the transverse mass of the X
 574 candidate using the jet and E_T^{miss} kinematics defined by the following formula:

$$m_{\nu\nu bb}^T = \sqrt{2E_T^j E_T^{\text{miss}} \cdot (1 - \cos \Delta\varphi(j, E_T^{\text{miss}}))}$$

575 4.2 Z boson to leptons

576 In leptonic channels ($X \rightarrow ZH \rightarrow ee jj$ and $X \rightarrow ZH \rightarrow \mu\mu jj$) the candidate Z boson is re-
 577 constructed from the pair of selected leptons. The two leptons are chosen as the pair of same
 578 flavor and opposite sign lepton pair with the highest combined p_T in the event. Additional
 579 requirements are applied to the Z candidate:

580 **Mass:** $70 \leq m_{\ell\ell} \leq 110 \text{ GeV}$

581 **p_T :** $p_T^Z > 200 \text{ GeV}$

582 4.3 Higgs reconstruction

583 The Higgs candidate is built upon the leading- p_T AK8 jet in the event. The identification of jets
 584 produced by Higgs decay is based on two ideas:

585 **Jet mass:** jets produced by the decay of a massive particle should have the invariant mass
 586 around the nominal mass of the original particle. Oppositely, jets originated by
 587 QCD radiation are produced by the emission of quarks or gluons and typically have
 588 smaller invariant mass. The Higgs candidate has to have a jet groomed mass com-
 589 patible with the Higgs boson mass.

590 **Sub-jet b-tagging:** one of the most characteristic features to distinguish jets originating
 591 from $H \rightarrow bb$ from V+jets backgrounds is to check for the presence of two b-quarks
 592 inside the jet.

593 The jet mass selection has the twofold purpose to reject the background and make the Higgs
 594 analyses orthogonal with respect to the other diboson searches, which target hadronically-
 595 decaying vector bosons (W and Z). The jet mass observables are derived after the application
 596 of the grooming algorithm. The selected one is **soft drop**, in conjunction with **PUPPI** for pile-up
 597 mitigation. Both are used for the jet mass, while the b-tagging is still applied to the PF CHS
 598 sub-jets. For the AK8 jet and Higgs kinematic selections, as well as the reconstruction of the
 599 mass of the heavy resonance m_X , the four momentum of the PUPPI jet is used instead.

600 **p_T :** $p_T^H > 200 \text{ GeV}$

601 **Mass:** $105 \leq \text{soft drop PUPPI corrected mass} \leq 135 \text{ GeV}$

602 **b-tagging:** < 2 or 2 subjets b-tagged with the *loose* working point depending on the cate-
 603 gory

604 5 Event selection

605 Events considered in this analysis have to pass a certain number of selections before being
 606 considered as suitable signal candidates, identically in both data and simulation. The selections
 607 are reported below and in Table 20.

608 5.1 Leptonic selection

609 The leptonic *pre-selection* cuts are different by the final state, selected physics objects and candi-
 610 date reconstruction:

611 **Neutrino channel:** ($X \rightarrow ZH \rightarrow \nu\nu jj$)

612 **Trigger:** E_T^{miss} triggers (Sec. 2.4.3)

613 **MET:** Missing energy $E_T^{\text{miss}} > 250 \text{ GeV}$

614 **leptons:** electrons, muons, and τ are vetoed

615 **Di-electron channel:** ($X \rightarrow ZH \rightarrow ee jj$)

616 **Trigger:** electron triggers OR photon triggers (Sec. 2.4.1)

617 **p_T :** at least two PF electrons with $p_T > 55 \text{ GeV}$ and 20 GeV for leading and
 618 sub-leading, respectively

619 **J:** $|\eta_{SC}| < 2.5$

620 **Id:** both electrons identified with the *loose* working point

621 **Iso:** included in Id requirement

622 **Z mass:** $70 \leq m_{ee} \leq 110 \text{ GeV}$

623 **Z p_T :** $p_T^Z > 200 \text{ GeV}$

624 **Di-muon channel:** ($X \rightarrow ZH \rightarrow \mu\mu jj$)

625 **Trigger:** muon triggers (Sec. 2.4.2)

626 **p_T :** at least two muons with $p_T > 55 \text{ GeV}$ and 20 GeV for leading and sub-
 627 leading muon, respectively

628 **J:** $|\eta| < 2.4$

629 **Id:** at least one muon identified as `HighPt`, the other with the *tracker HighPt*
 630 Id (Section 3.3)

631 **Iso:** tracker-isolation < 0.1

632 **Z mass:** $70 \leq m_{\mu\mu} \leq 110 \text{ GeV}$

633 **Z p_T :** $p_T^Z > 200 \text{ GeV}$

634 5.2 Hadronic selection

635 The selections of the hadronic part are exactly the same for all the three lepton categories.

636 **Hadronic selection:** (all categories)

637 **p_T :** at least one AK8 PFJet with $p_T > 200 \text{ GeV}$

638 **J:** $|\eta| < 2.4$

639 **Lepton cleaning:** minimal separation between jet and isolated leptons $\Delta R_{jet-\ell} >$
 640 0.8

641 **Mass:** soft drop PUPPI mass (Section 3.6.1)

642 **b-tagging:** **less than two or two** sub-jets b-tagged with Deepcsv, *loose* work-
 643 ing point depending on the category

644 **VBF:** VBF id depending on the category

645 **5.3 Topology and event cleaning**

646 The following additional selections are applied to reject noisy events, reject multijet or $t\bar{t}$ back-
647 grounds, and assure orthogonality between all channels:

648 **Neutrino channel:** ($X \rightarrow ZH \rightarrow \nu\nu jj$)

649 **Isolated e, μ :** veto

650 **Hadronic taus:** veto

651 **Cleaning:** $\Delta\phi(jet, E_T^{\text{miss}}) > 2$

652 **Top rejection:** anti b-tag *loose* on other AK4 jets

653 **QCD rejection:** $\min \Delta\phi(jet, E_T^{\text{miss}}) > 0.5$ between E_T^{miss} and all AK4 jets

654 **Correction:** charged hadron fraction > 0.1 , $MET/H_{p_T} > 0.6$

655 **η (only VBF):** $|\eta| < 1.1$

656 **Di-electron and di-muon channel:** ($X \rightarrow ZH \rightarrow ee jj$ and $X \rightarrow ZH \rightarrow \mu\mu jj$)

657 **Bkg rejection (only noVBF):** $\Delta\eta(Z, jet) < 1.7$

658 **Separation:** minimal separation between jet and Z boson $\Delta R_{jet-Z} > 2$

	$Z \rightarrow ee$	$Z \rightarrow \mu\mu$	$Z \rightarrow \nu\nu$
Trigger	HLT_Ele(115) HLT_Ele(35) or HLT_Pho(200)	HLT_Mu50 HLT_TkMu100	HLT_PFMET or HLT_PFMETNoMu
Lept Id	2e <i>loose</i> WP	1 μ HighPt, 1 μ tracker HighPt	e, μ, τ veto
Lept Iso	inc. in Id	$tkIso < 0.1$	-
Lept p_T	$p_T > 55, 20 \text{ GeV}$	$p_T > 55, 20 \text{ GeV}$	-
Z boson p_T		$p_T^V > 200 \text{ GeV}$	$E_T^{\text{miss}} > 250 \text{ GeV}$
Z boson mass		$70 < m_{\ell\ell} < 110 \text{ GeV}$	-
H-jet		AK8 PFJet, $p_T > 200 \text{ GeV}$	
H mass	$105 < m_j < 135 \text{ GeV}$ (SR), $30 < m_j < 65 \text{ GeV}$, $m_j > 135 \text{ GeV}$ (SB)		
H b-tag		< 2 or 2 subjets b-tagged <i>loose</i>	
Top rejection	-	-	veto max b-tag <i>loose</i> AK4 jets
QCD rejection	-	-	$\min \Delta\phi_{j, E_T^{\text{miss}}} > 0.5$
Noise cleaning	-	-	$\Delta\phi_{jet, E_T^{\text{miss}}} > 2$
Separation		$ \Delta\eta(Z, jet) < 1.7$	-
MET Correction	-	-	$\text{chf} > 0.1, MET/H_{p_T} > 0.6$

Table 20: Summary of the selection cuts.

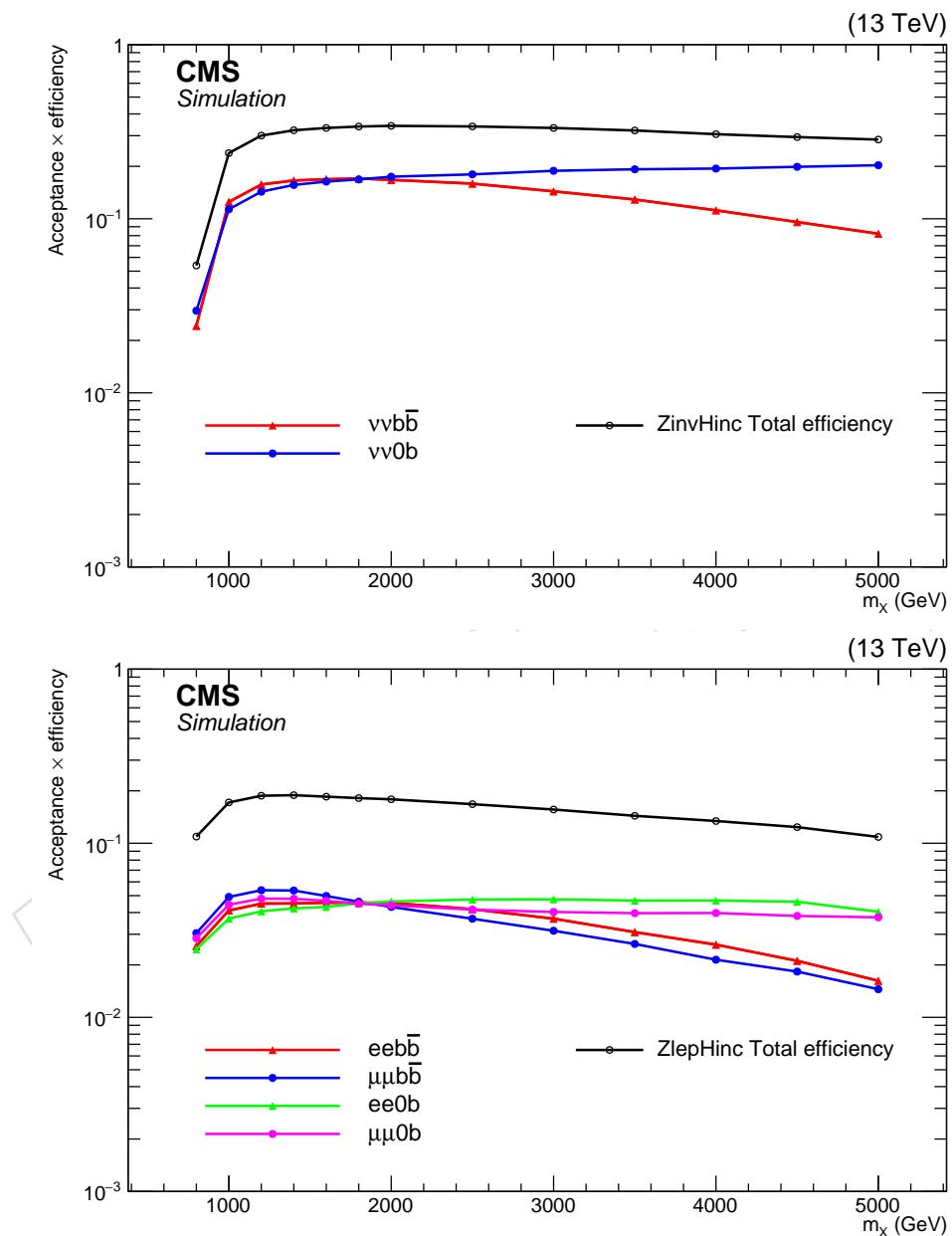


Figure 27: Signal efficiency for all channels. Top: ZinvHinc. Bottom: ZlepHinc.

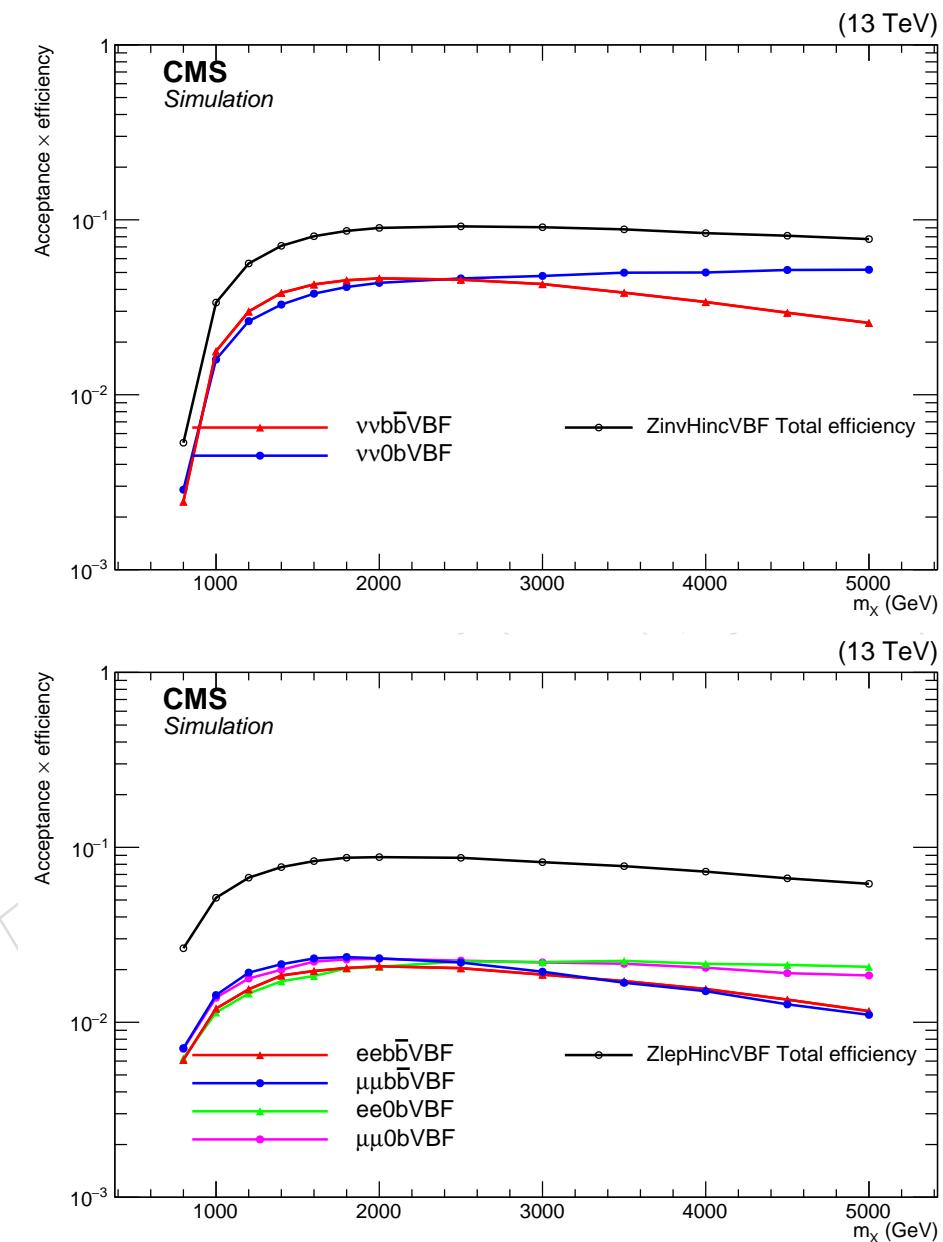


Figure 28: VBF Signal efficiency for all channels. Top: ZinvHincVBF. Bottom: ZlepHincVBF.

6 Data-simulation comparison

In this section, a comparison between data and simulation is reported for various kinematic observables. It can be seen that the dominant background contribution comes from the Z+jets production, while sub-leading contributions from $t\bar{t}$ and dibosons can be non-negligible especially in the zero lepton channel.

In the following plots, the comparison is performed in three different regions. On top of the preselections defined in Section 5, additional regions are defined for each category:

Inclusive: on top of the preselection the cleaning cuts are applied

Sidebands (SB): Only events in the sidebands, defined the interval between $30 < m_j < 105 \text{ GeV}$ and $m_j > 135 \text{ GeV}$ are considered. This region can be considered as signal-depleted. The main difference with the previous regions is that the bulk of the jet mass distribution, peaking at $m_j \sim 20 \text{ GeV}$, is not included. The region selected is thus much closer kinematically to the signal region.

Signal region (SR): Represents the phase space where signal is expected. The signal region is considered **blind**, so data is not shown in these plots.

6.1 2016

6.1.1 Zero lepton channel

Sample	Events	Entries	%
data_obs	18406.00	18405	119.37
TTbarSL	1124.88	23774	7.30
DYJetsToNuNu_HT	9298.48	225596	60.31
DYJetsToLL_HT	37.09	1596	0.24
ST	157.89	580	1.02
VV	386.89	17321	2.51
WJetsToLNu_HT	4413.50	15808	28.62
BkgSum	15418.72	284680	100.00
XZH_M1000	325.61	17138	0.00
XZH_M2000	27.63	28642	0.00
XZH_M3000	2.65	30000	0.00

Figure 29: Number of events in the inclusive region of the 0-lepton channel.

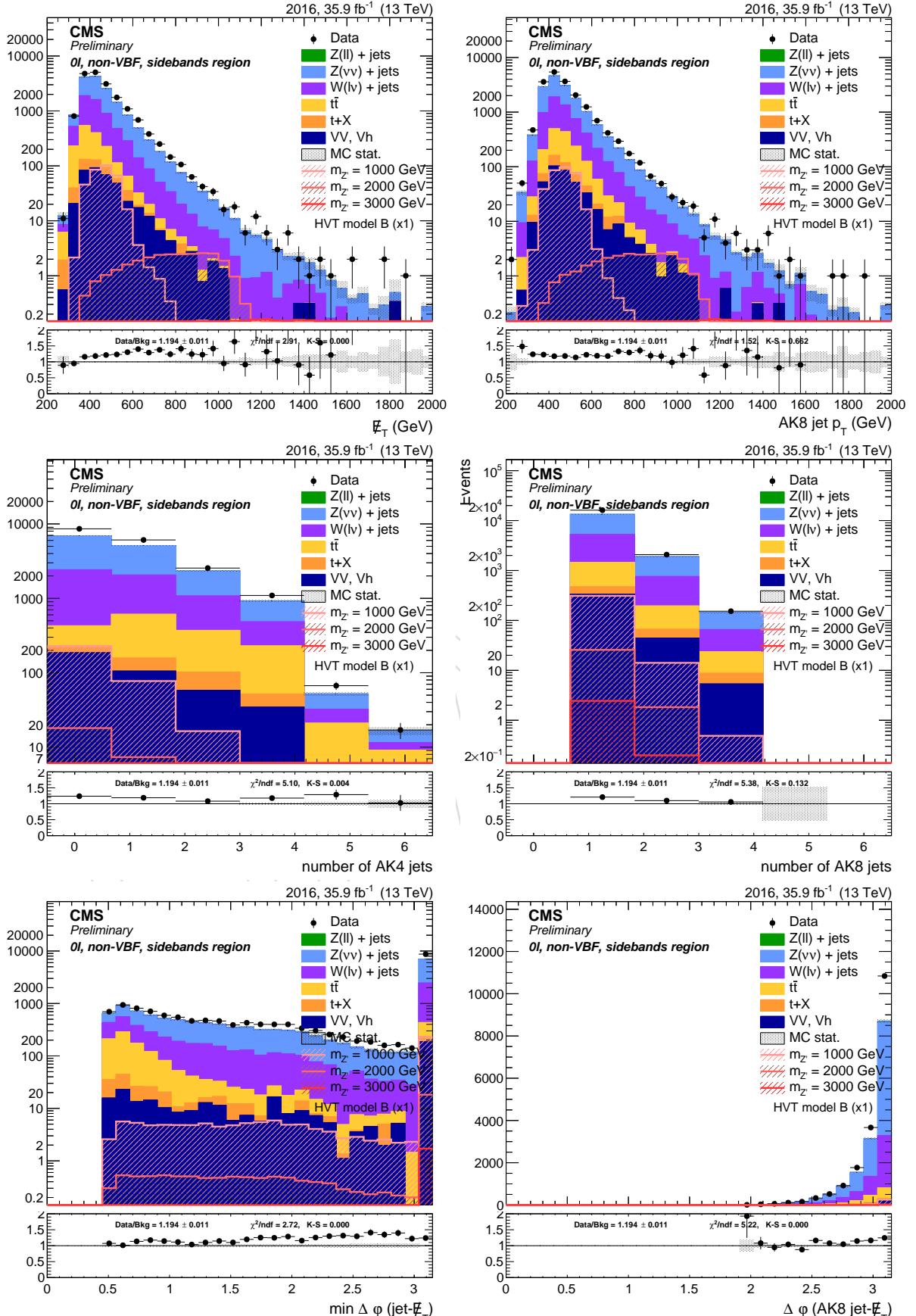


Figure 30: Top: E_T^{miss} (left) and leading AK8 jet p_T (right). Center: number of AK4 jets (left) and AK8 jets (right). Bottom: minimum $\Delta\phi$ between the AK4 jets and AK8 jet in the event (left) and $\Delta\phi$ between the AK8 jet and the E_T^{miss} (right). Events are selected with the *inclusive* selection, and simulated backgrounds are normalized to luminosity.

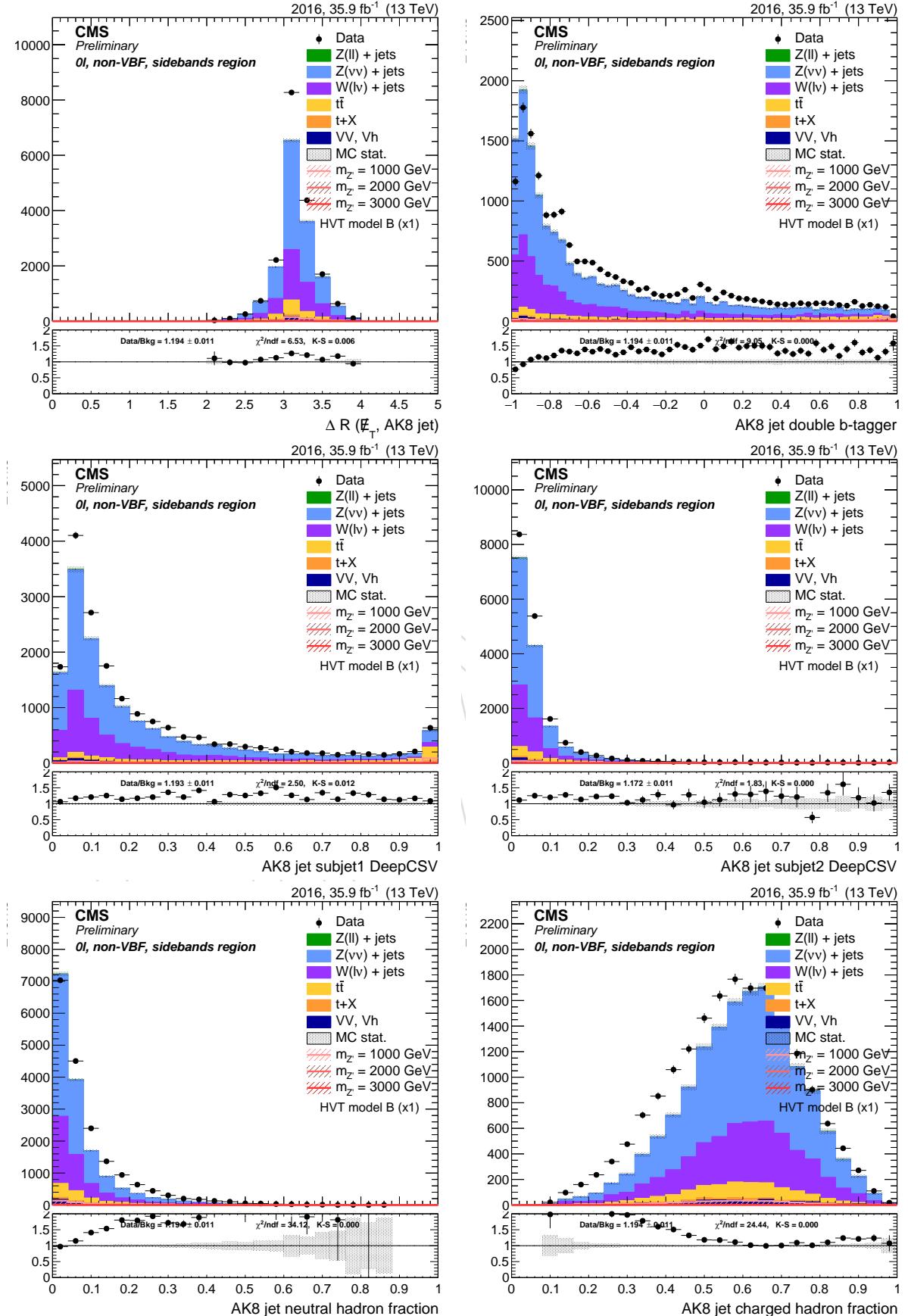


Figure 31: Top: ΔR between Z boson and leading AK8 jet (left), AK8 double-b tagger discriminator (right). Center: DeepCSV distribution of the AK8 sub-jets. Bottom: leading AK8 jet neutral hadron fraction (left) and charged hadron fraction (right). Events are selected with the *inclusive* selection, and simulated backgrounds are normalized to luminosity.

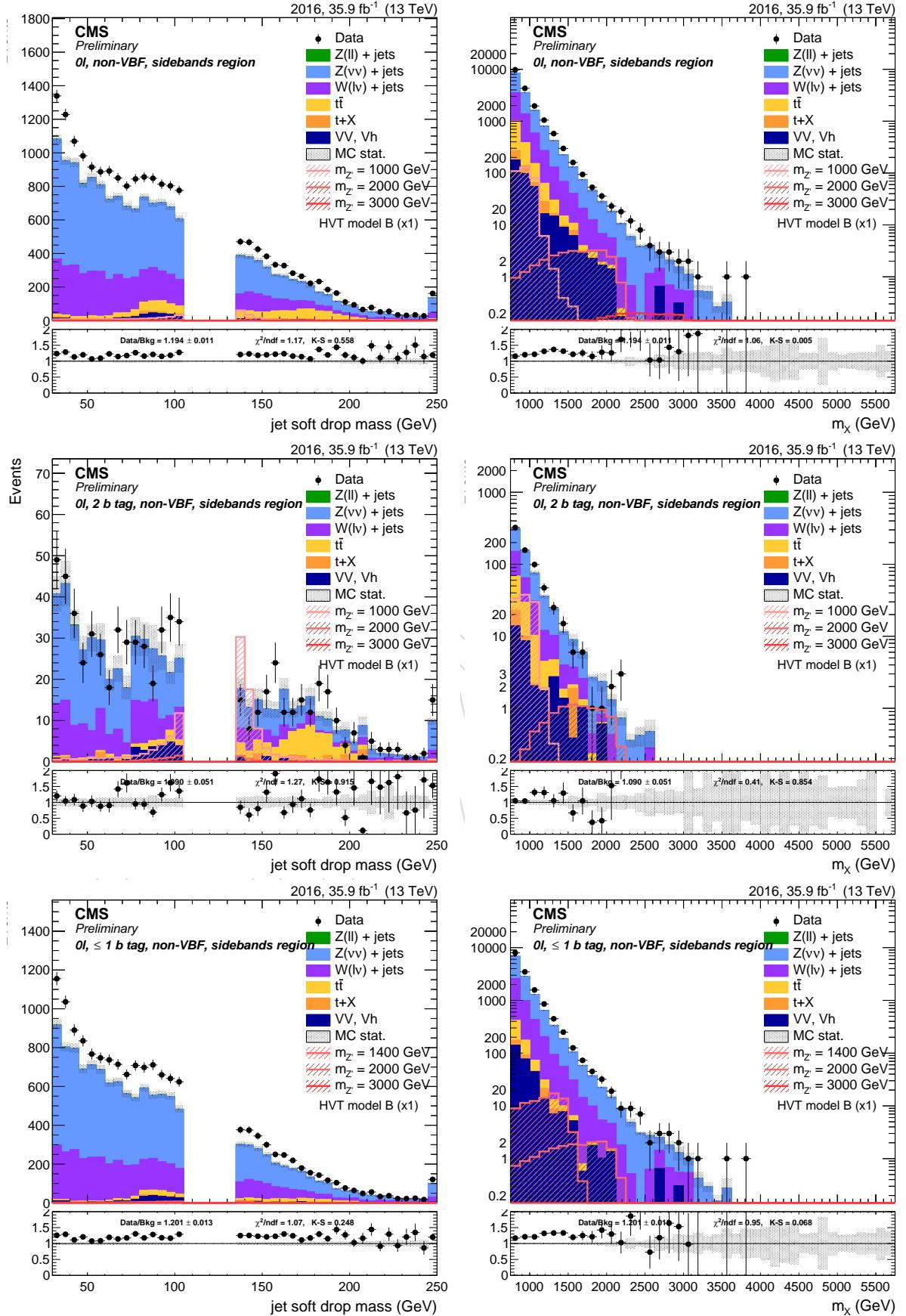


Figure 32: Leading AK8 jet soft drop PUPPI mass (left) and resonance transverse mass (right). Top: inclusive region. Center: mass sidebands and b-tag category. Bottom: mass sidebands and no b-tag category

676 6.1.2 Zero lepton channel VBF

Sample	Events	Entries	%
data_obs	1348.00	1347	101.87
TTbarSL	145.53	3739	11.00
DYJetsToNuNu_HT	750.19	27000	56.70
DYJetsToLL_HT	3.39	261	0.26
ST	19.42	77	1.47
VV	38.97	1489	2.95
WJetsToLNu_HT	365.69	1894	27.64
BkgSum	1323.20	34465	100.00
XZHVB_M1000	0.12	3041	0.00
XZHVB_M2000	0.01	7861	0.00
XZHVB_M3000	0.00	9272	0.00

Figure 33: Number of events in the inclusive region of the 0-lepton channel.

DRAFT

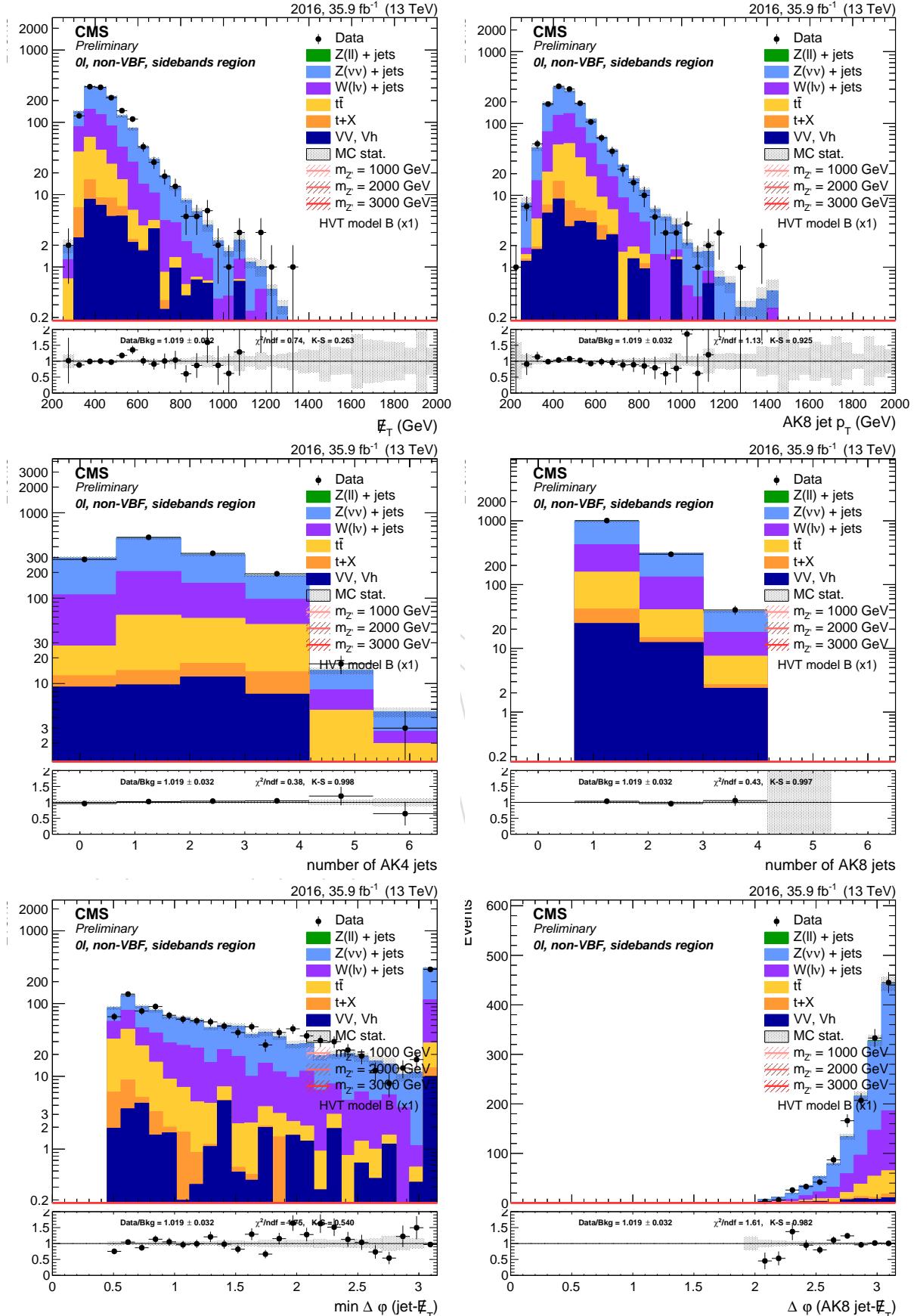


Figure 34: Top: E_T^{miss} (left) and leading AK8 jet p_T (right). Center: number of AK4 jets (left) and AK8 jets (right). Bottom: minimum $\Delta\phi$ between the AK4 jets and AK8 jet in the event (left) and $\Delta\phi$ between the AK8 jet and the E_T^{miss} (right). Events are selected with the *inclusive* selection, and simulated backgrounds are normalized to luminosity.

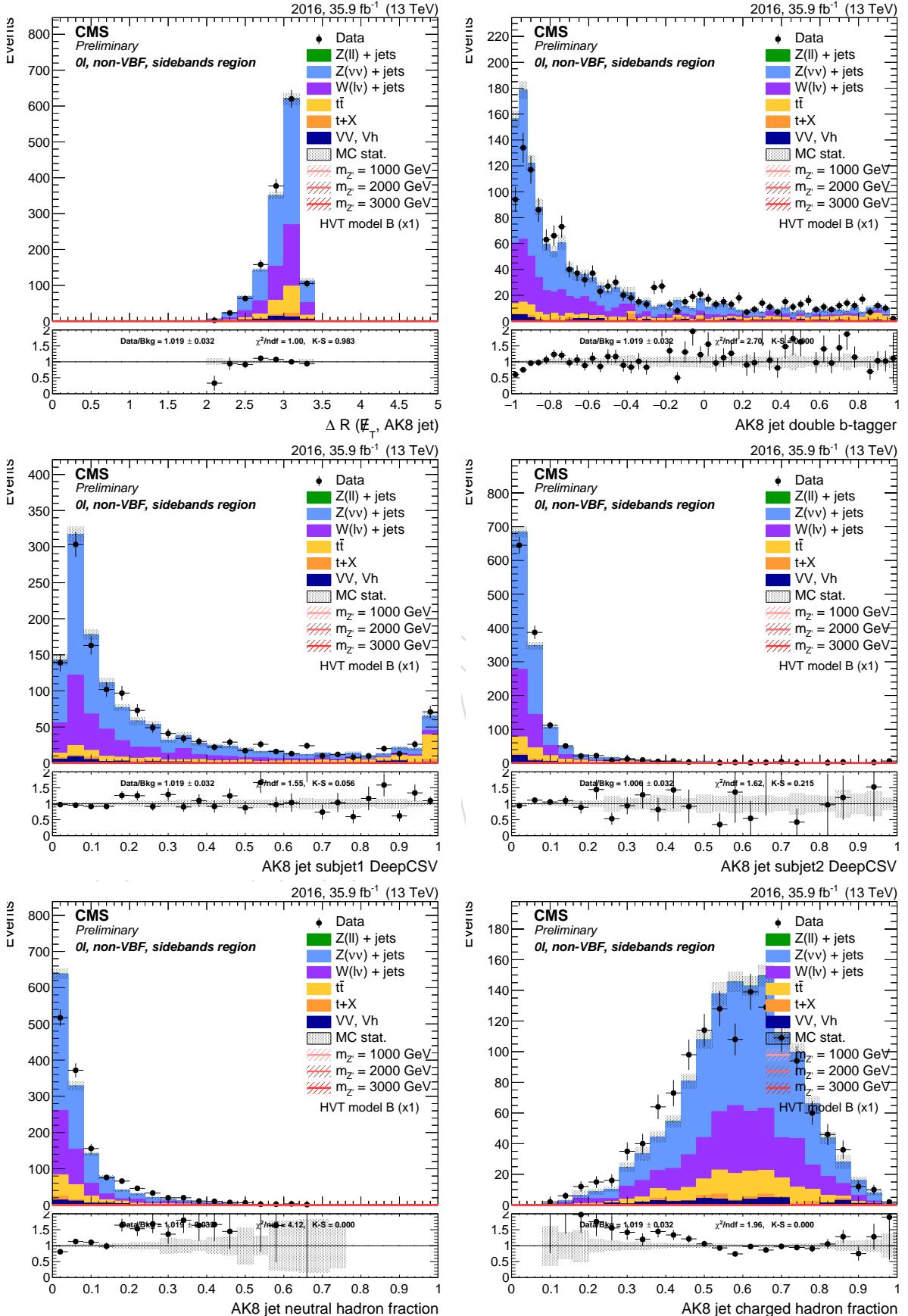


Figure 35: Top: ΔR between Z boson and leading AK8 jet (left), AK8 double-b tagger discriminator (right). Center: DeepCSV distribution of the AK8 sub-jets. Bottom: leading AK8 jet neutral hadron fraction (left) and charged hadron fraction (right). Events are selected with the *inclusive* selection, and simulated backgrounds are normalized to luminosity.

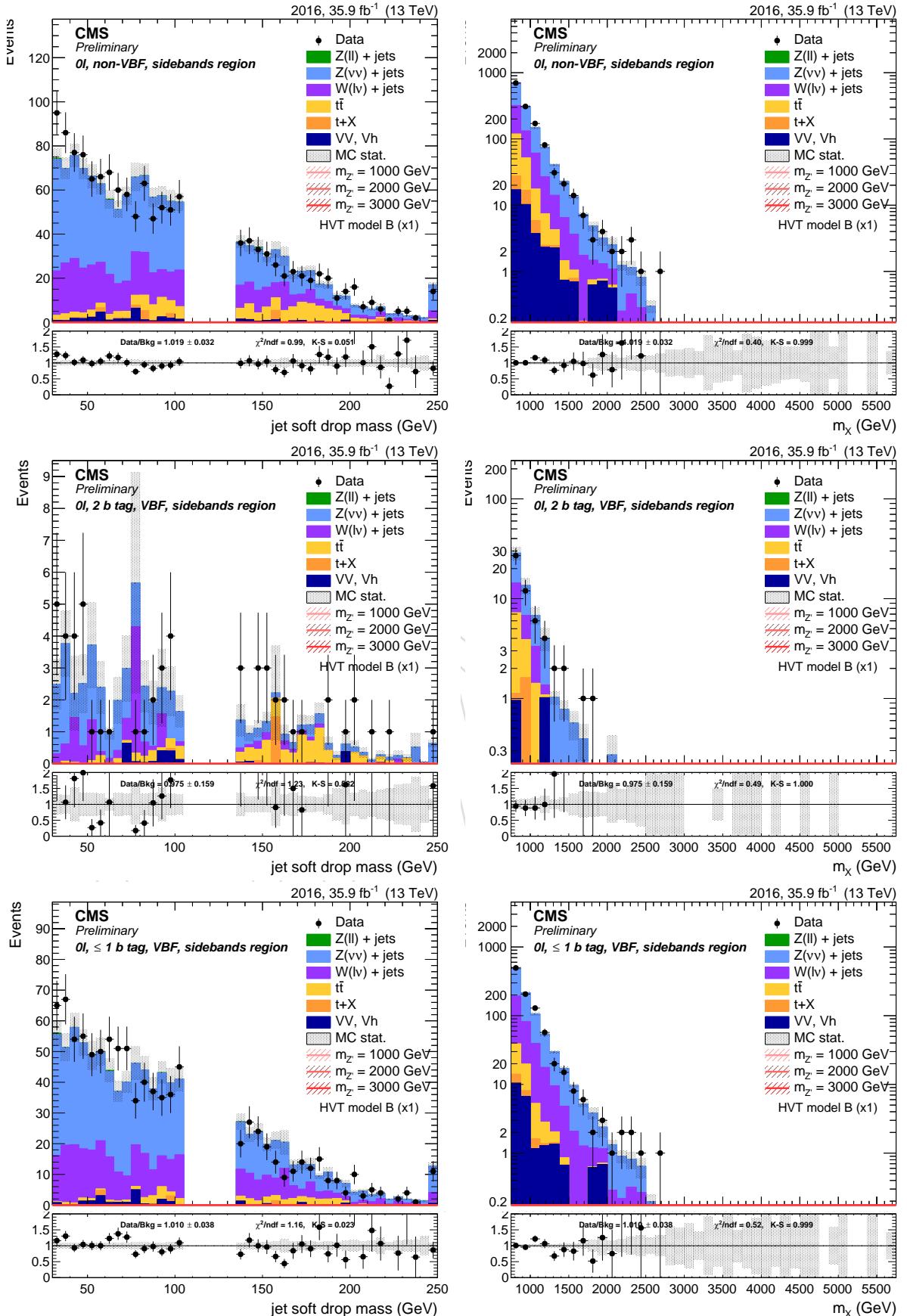


Figure 36: Leading AK8 jet soft drop PUPPI mass (left) and resonance transverse mass (right). Top: inclusive region. Center: mass sidebands and b-tag category. Bottom: mass sidebands and no b-tag category

677 6.1.3 Dilepton channel

Sample	Events	Entries	%	Sample	Events	Entries	%
data_obs	1898.00	1897	101.69	data_obs	2263.00	2262	102.40
TTbarSL	20.97	2996	1.12	TTbarSL	27.70	3529	1.25
DYJetsToNuNu_HT	0.00	-1	0.00	DYJetsToNuNu_HT	0.00	-1	0.00
DYJetsToLL_HT	1740.60	103806	93.25	DYJetsToLL_HT	2056.29	127554	93.04
ST	4.16	2	0.22	ST	2.46	1	0.11
VV	99.46	22639	5.33	VV	123.07	27152	5.57
WWJetsToLNu_HT	1.33	8	0.07	WWJetsToLNu_HT	0.50	1	0.02
BkgSum	1866.51	129455	100.00	BkgSum	2210.02	158241	100.00
XZH_M1000	63.25	6410	0.00	XZH_M1000	75.40	7773	0.00
XZH_M2000	3.72	7780	0.00	XZH_M2000	3.48	7566	0.00
XZH_M3000	0.32	7387	0.00	XZH_M3000	0.26	6293	0.00

678

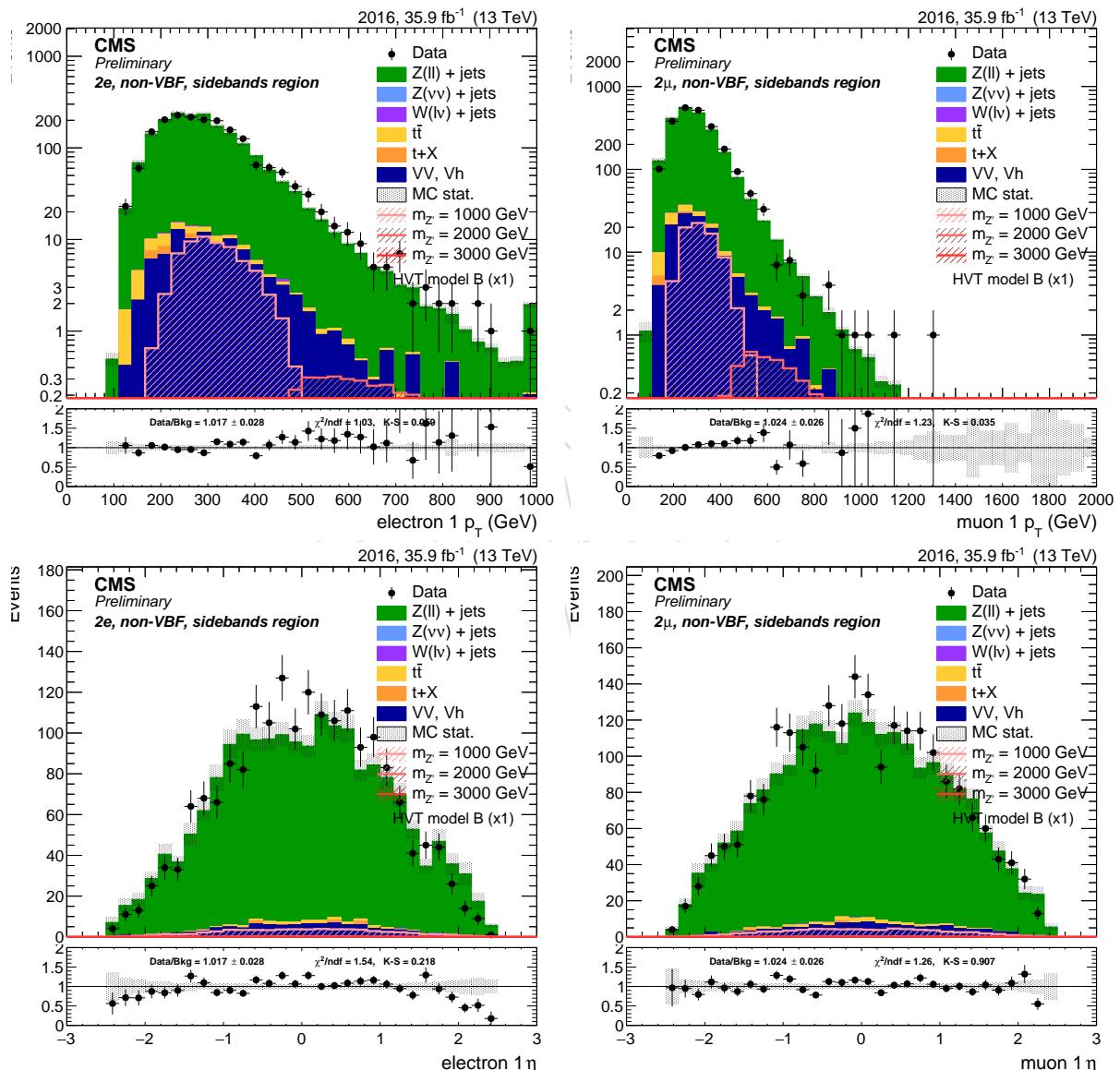


Figure 37: Leading lepton p_T (top) and η (bottom) for di-electron (left) and di-muon (right) channel. Events are selected with the *inclusive* selection, and simulated backgrounds are normalized to luminosity.

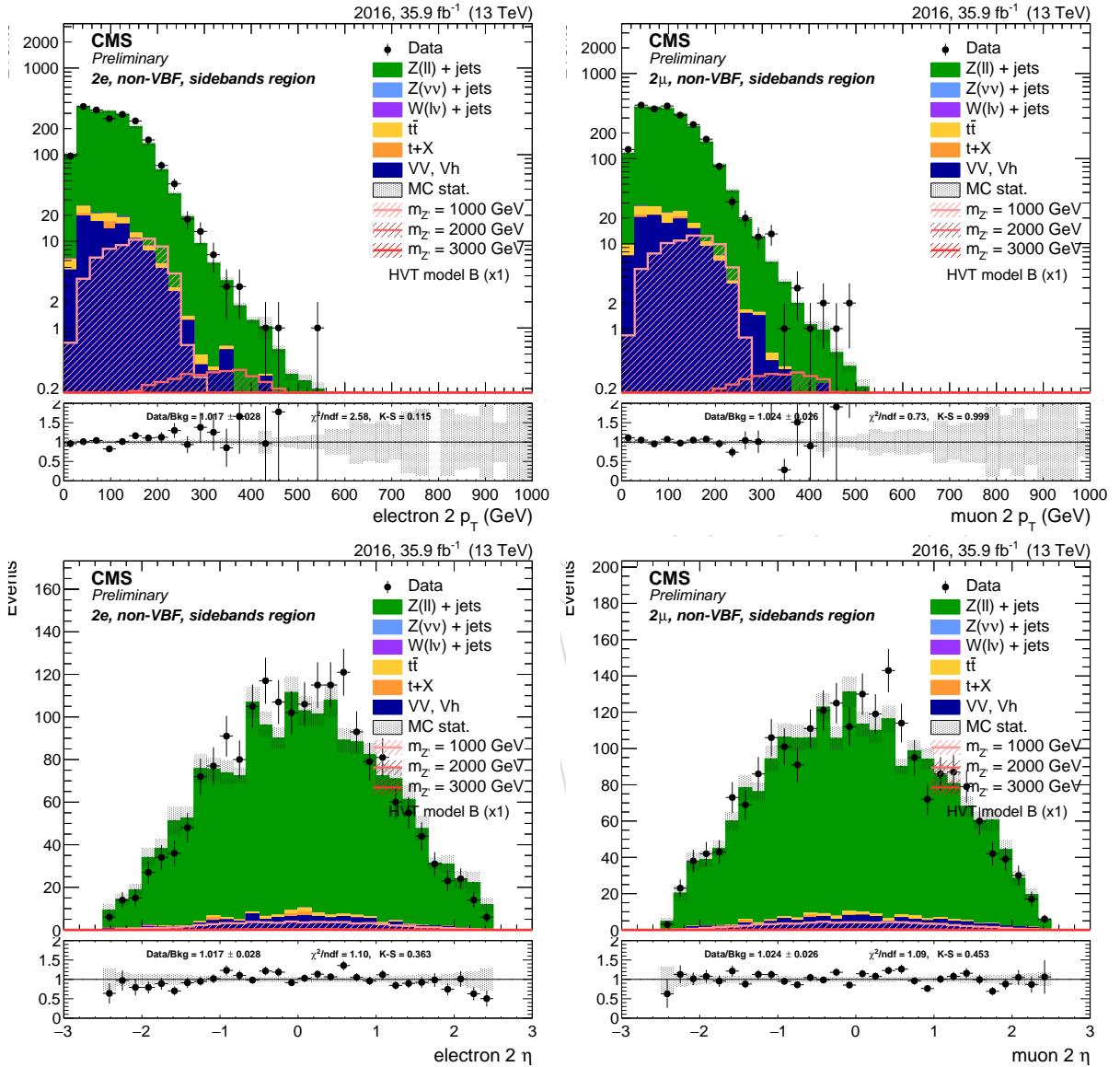


Figure 38: Sub-leading lepton p_T (top) and η (bottom) for di-electron (left) and di-muon (right) channel. Events are selected with the *inclusive* selection, and simulated backgrounds are normalized to luminosity.

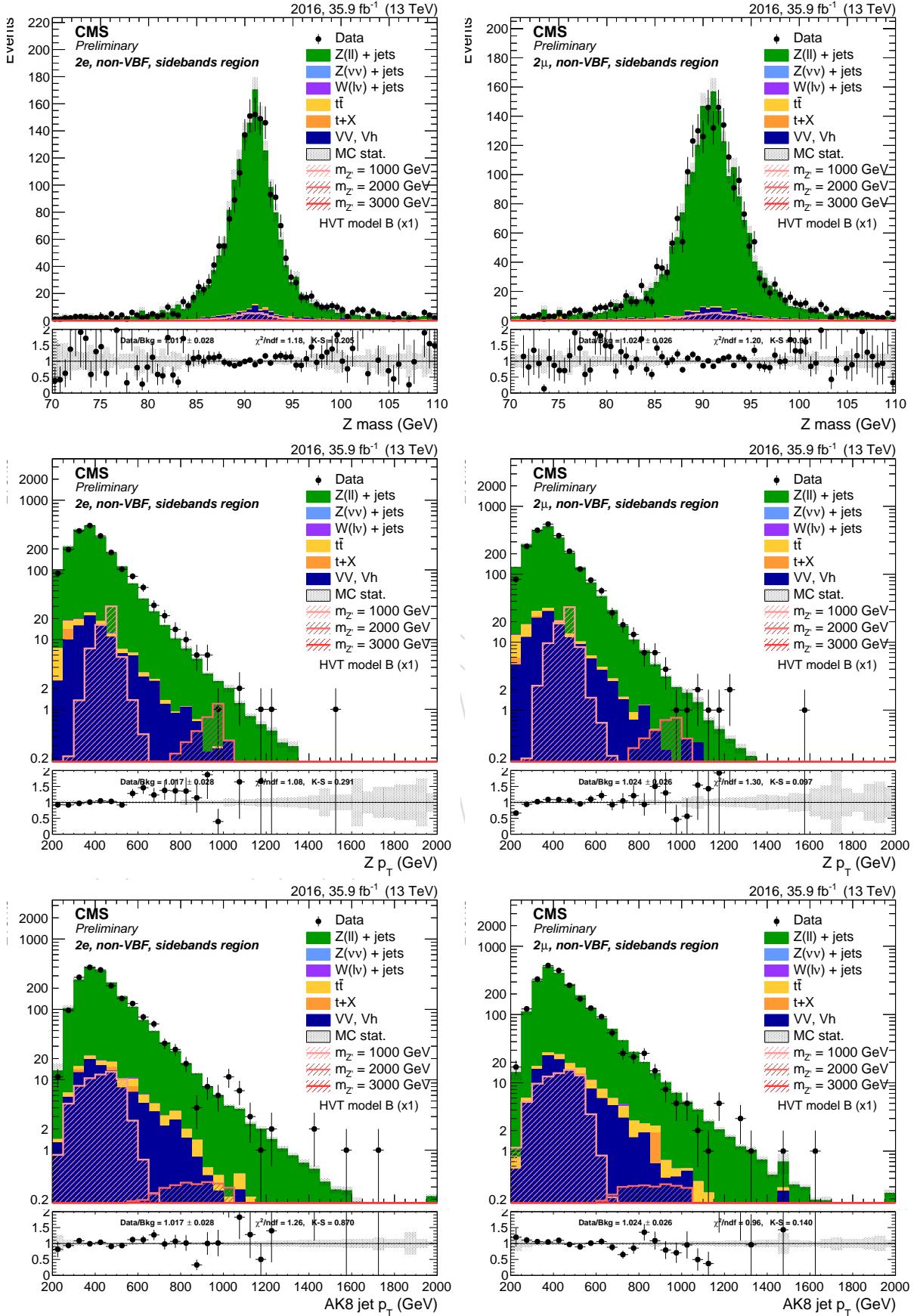


Figure 39: Top: Z candidate mass. Center: Z candidate p_T . Bottom: leading AK8 jet p_T . left: di-electron channel. right: di-muon channel. Events are selected with the *inclusive* selection, and simulated backgrounds are normalized to luminosity.

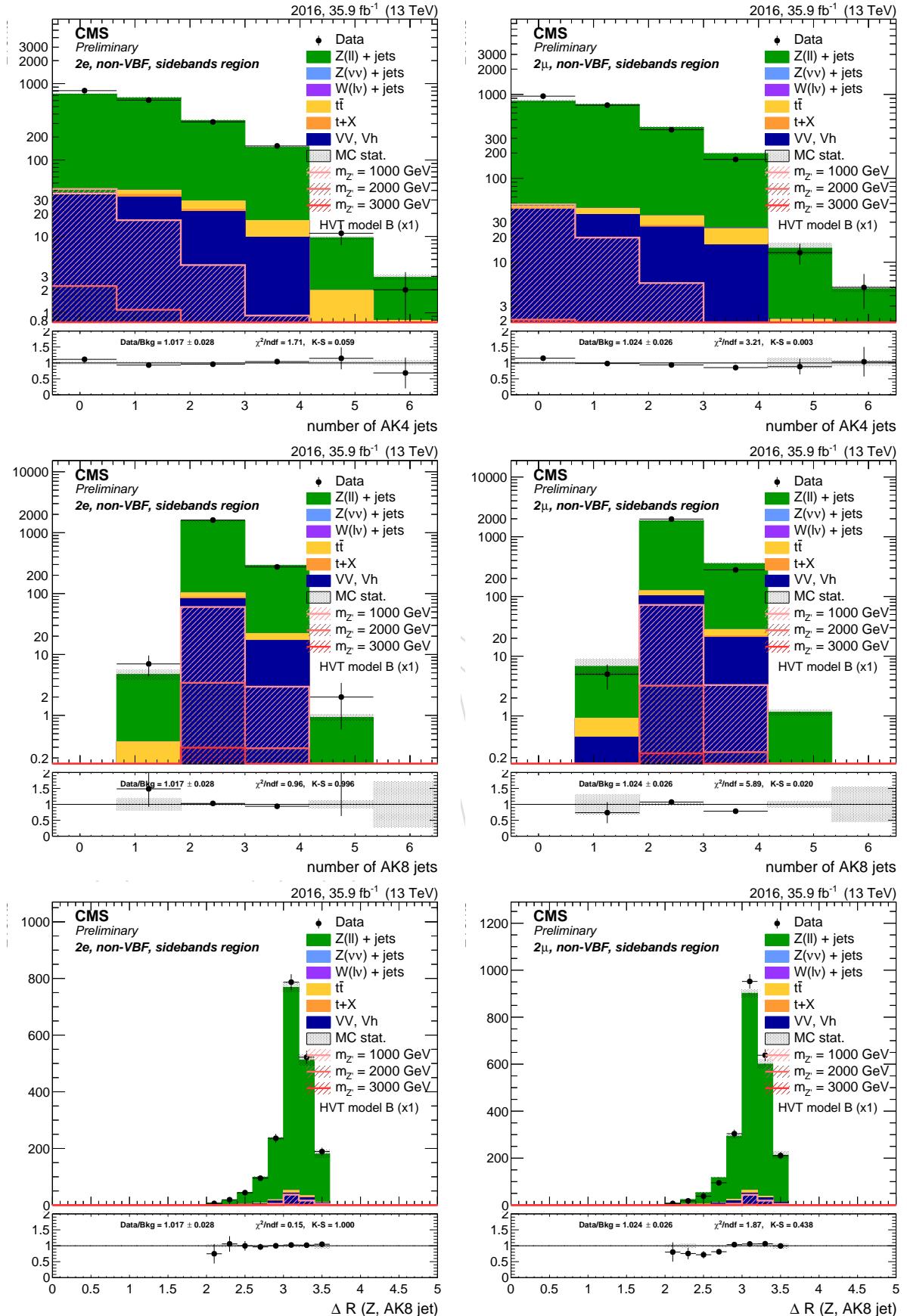


Figure 40: Top: number of AK4 jets. Center: number of AK8 jets. Bottom: ΔR between Z boson and leading AK8 jet. left: di-electron channel. right: di-muon channel. Events are selected with the *inclusive* selection, and simulated backgrounds are normalized to luminosity.

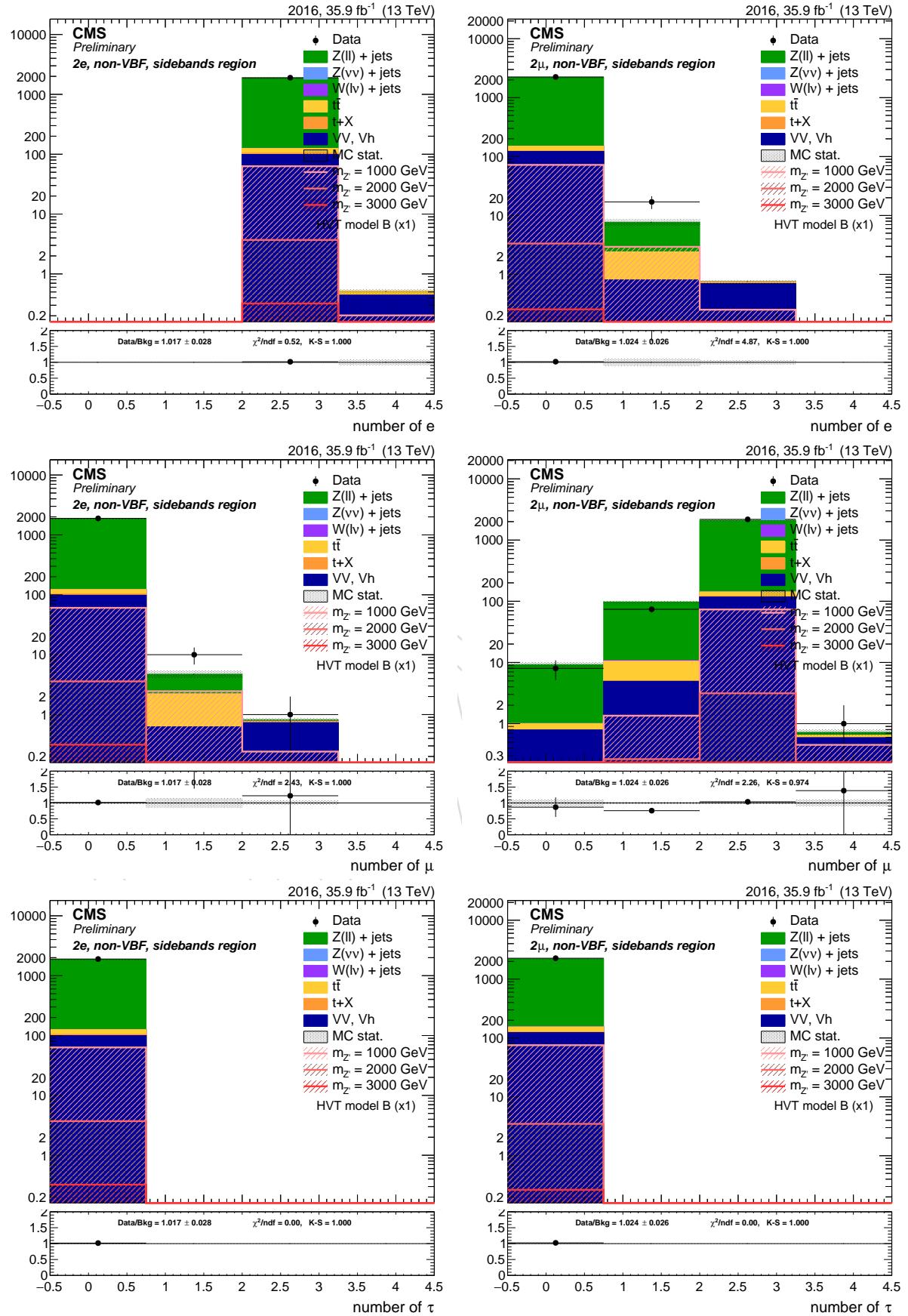


Figure 41: Top: number of electrons. Center: number of muons. Bottom: number of hadronic taus. left: di-electron channel. right: di-muon channel. Events are selected with the *inclusive* selection, and simulated backgrounds are normalized to luminosity.

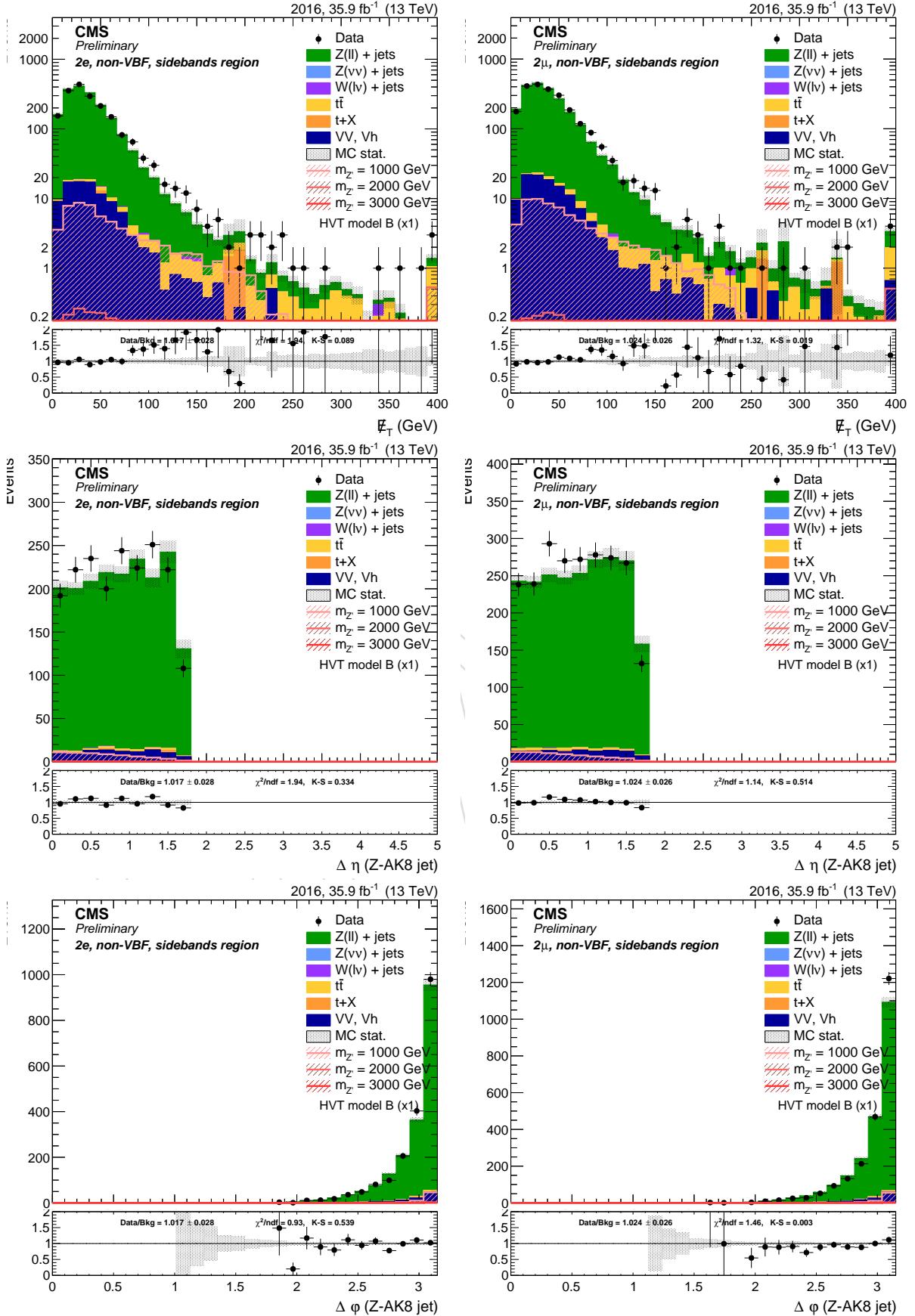


Figure 42: Top: E_T^{miss} . Center: $\Delta\eta$ between the Z and the AK8 jet. Bottom: $\Delta\phi$ between the Z and H candidates. left: di-electron channel. right: di-muon channel. Events are selected with the *inclusive* selection, and simulated backgrounds are normalized to luminosity.

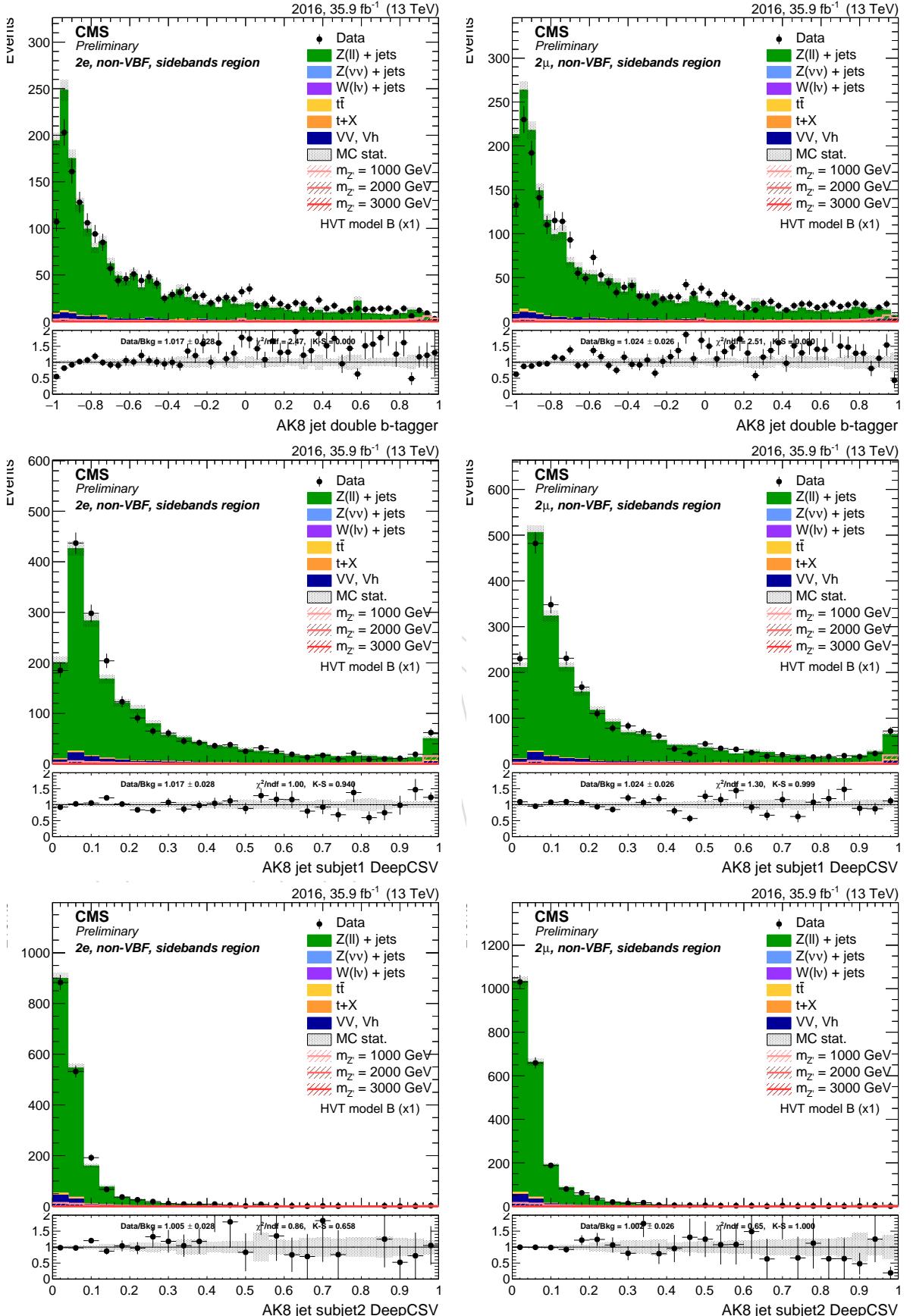


Figure 43: Top: AK8 double-b tagger discriminator . Center: DeepCSV distribution of the leading AK8 sub-jet. Bottom: DeepCSV distribution of the sub-leading AK8 sub-jet. left: di-electron channel. right: di-muon channel. Events are selected with the *inclusive* selection, and simulated backgrounds are normalized to luminosity.

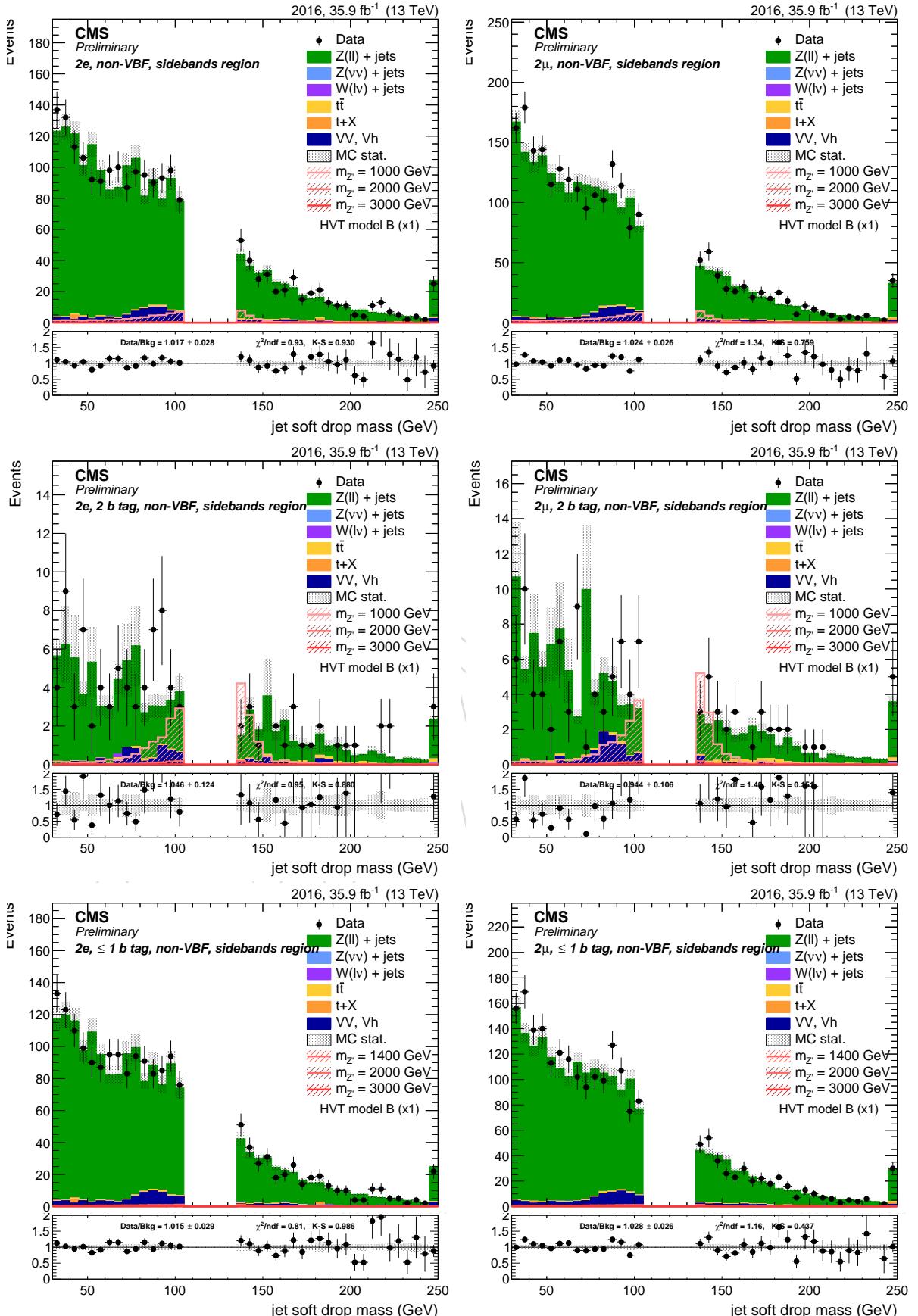


Figure 44: Leading AK8 jet soft drop PUPPI mass. Top: inclusive region. Center: mass sidebands and 2 b-tag category. Bottom: mass sidebands and no b-tag category. left: di-electron channel. right: di-muon channel.

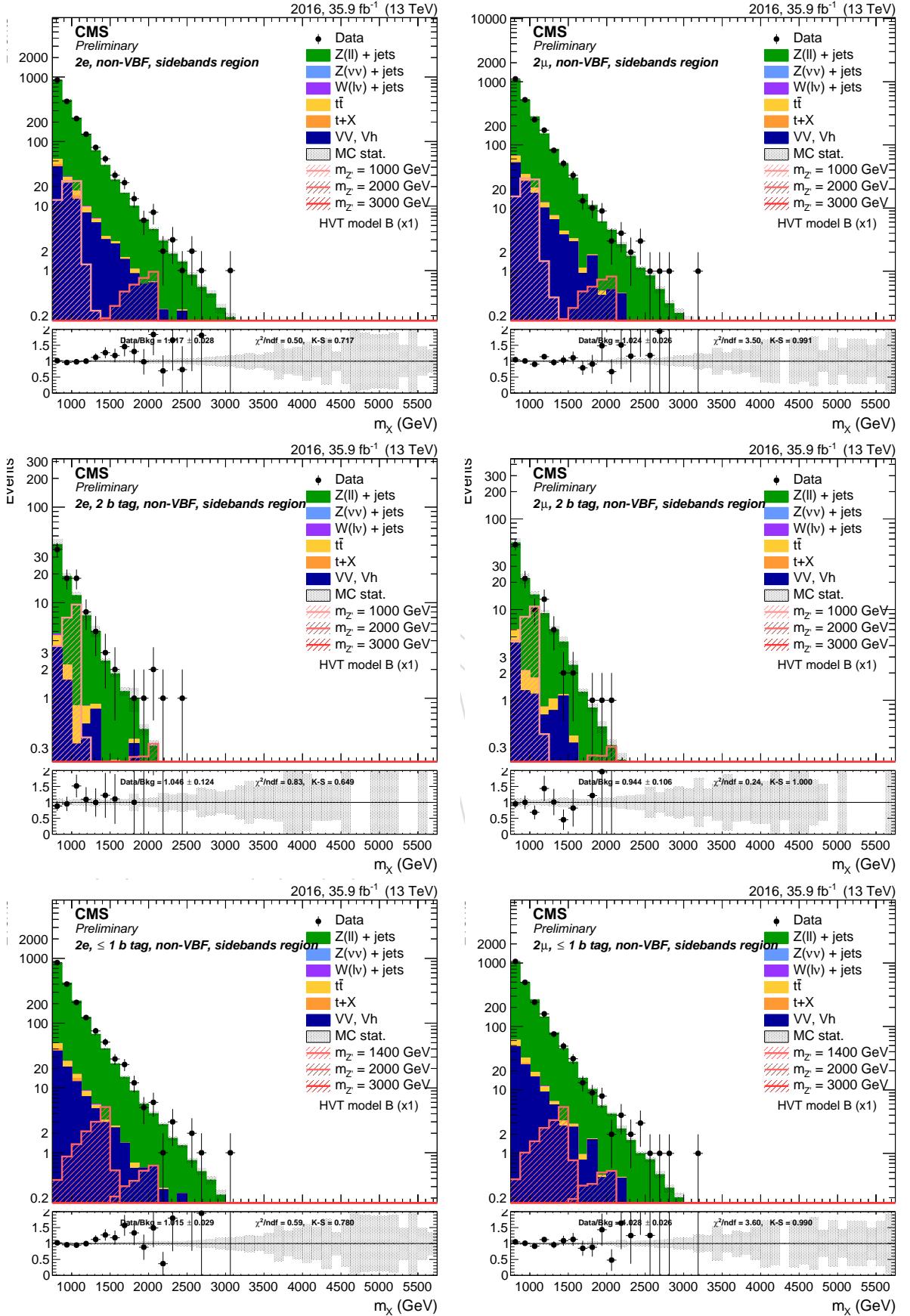


Figure 45: Resonance candidate mass. Top: inclusive region. Center: mass sidebands and 2 b-tag category. Bottom: mass sidebands and no b-tag category. left: di-electron channel. right: di-muon channel.

6.1.4 Dilepton channel VBF

Sample	Events	Entries	%	Sample	Events	Entries	%
data_obs	311.00	310	74.85	data_obs	380.00	379	74.38
TTbarSL	8.10	1310	1.95	TTbarSL	10.75	1542	2.10
DYJetsToNuNu_HT	0.00	-1	0.00	DYJetsToNuNu_HT	0.00	-1	0.00
DYJetsToLL_HT	382.89	26933	92.16	DYJetsToLL_HT	473.31	33678	92.64
ST	2.78	1	0.67	ST	0.00	-1	0.00
VV	21.20	4229	5.10	VV	26.56	5074	5.20
WJetsToLNu_HT	0.51	2	0.12	WJetsToLNu_HT	0.29	0	0.06
BkgSum	415.48	32479	100.00	BkgSum	510.91	40297	100.00
XZHVB_M1000	0.06	2816	0.00	XZHVB_M1000	0.07	3531	0.00
XZHVB_M2000	0.00	4443	0.00	XZHVB_M2000	0.00	5068	0.00
XZHVB_M3000	0.00	4524	0.00	XZHVB_M3000	0.00	4645	0.00

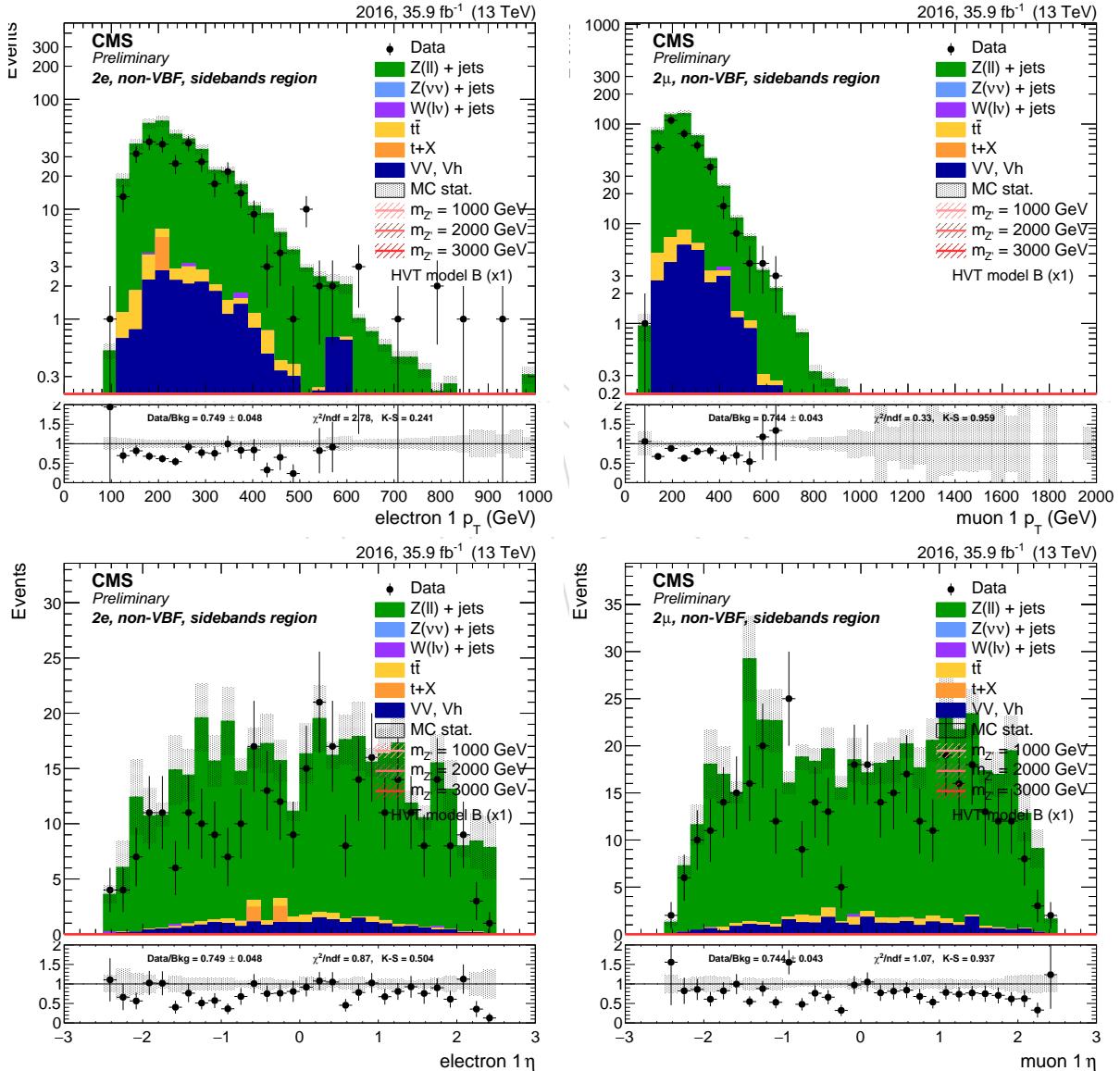


Figure 46: Leading lepton p_T (top) and η (bottom) for di-electron (left) and di-muon (right) channel. Events are selected with the *inclusive* selection, and simulated backgrounds are normalized to luminosity.

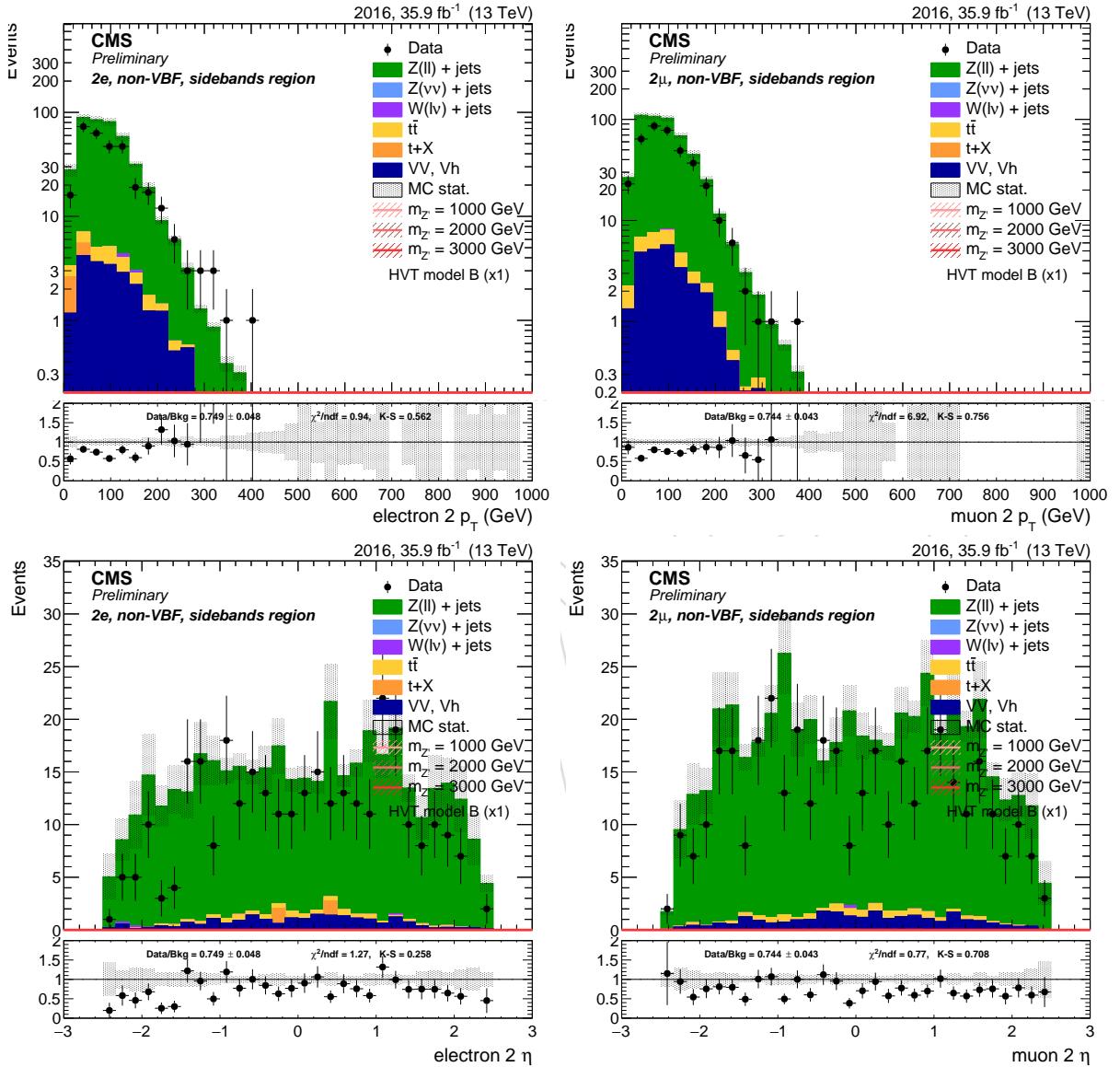


Figure 47: Sub-leading lepton p_T (top) and η (bottom) for di-electron (left) and di-muon (right) channel. Events are selected with the *inclusive* selection, and simulated backgrounds are normalized to luminosity.

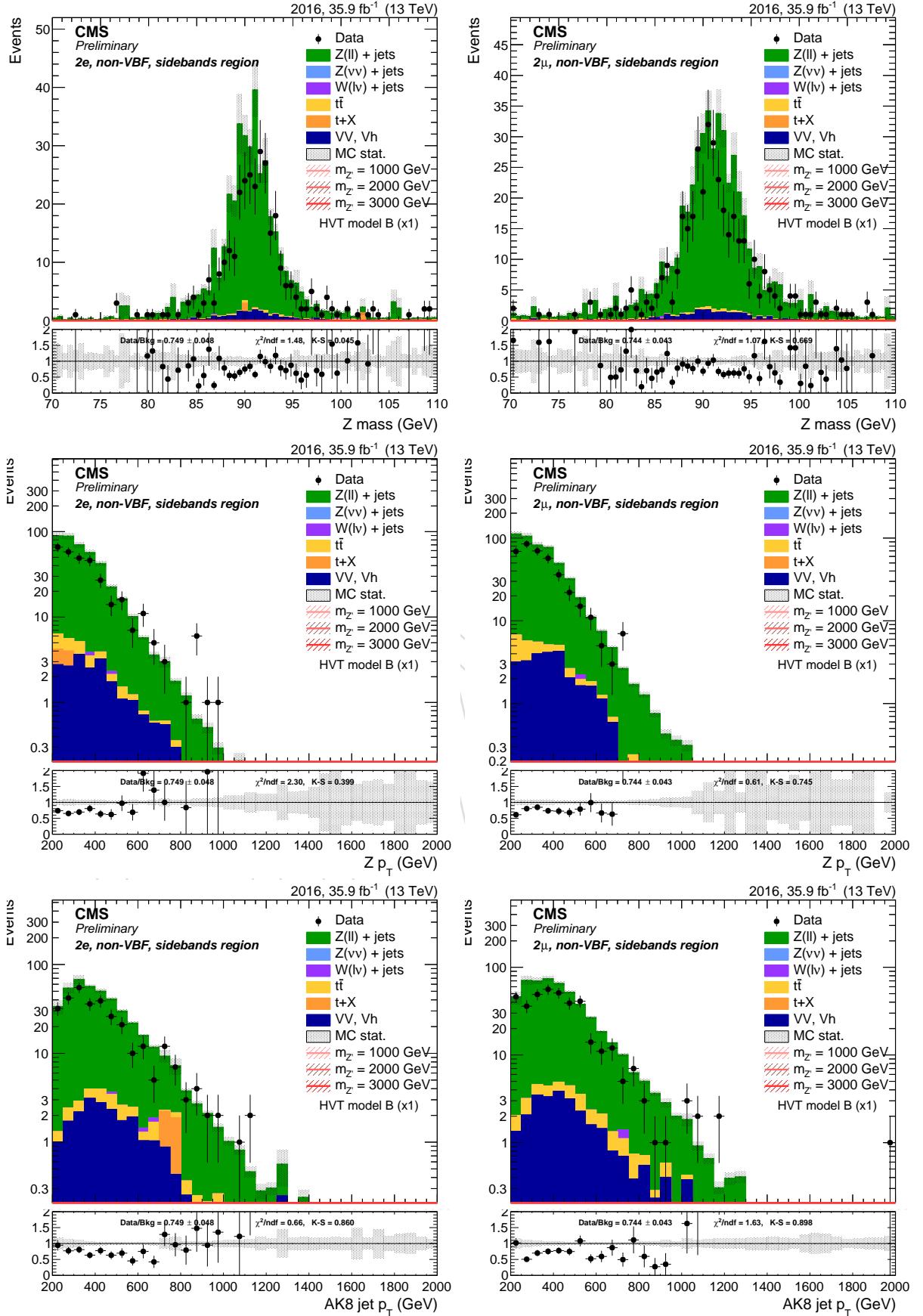


Figure 48: Top: Z candidate mass. Center: Z candidate p_T . Bottom: leading AK8 jet p_T . left: di-electron channel. right: di-muon channel. Events are selected with the *inclusive* selection, and simulated backgrounds are normalized to luminosity.

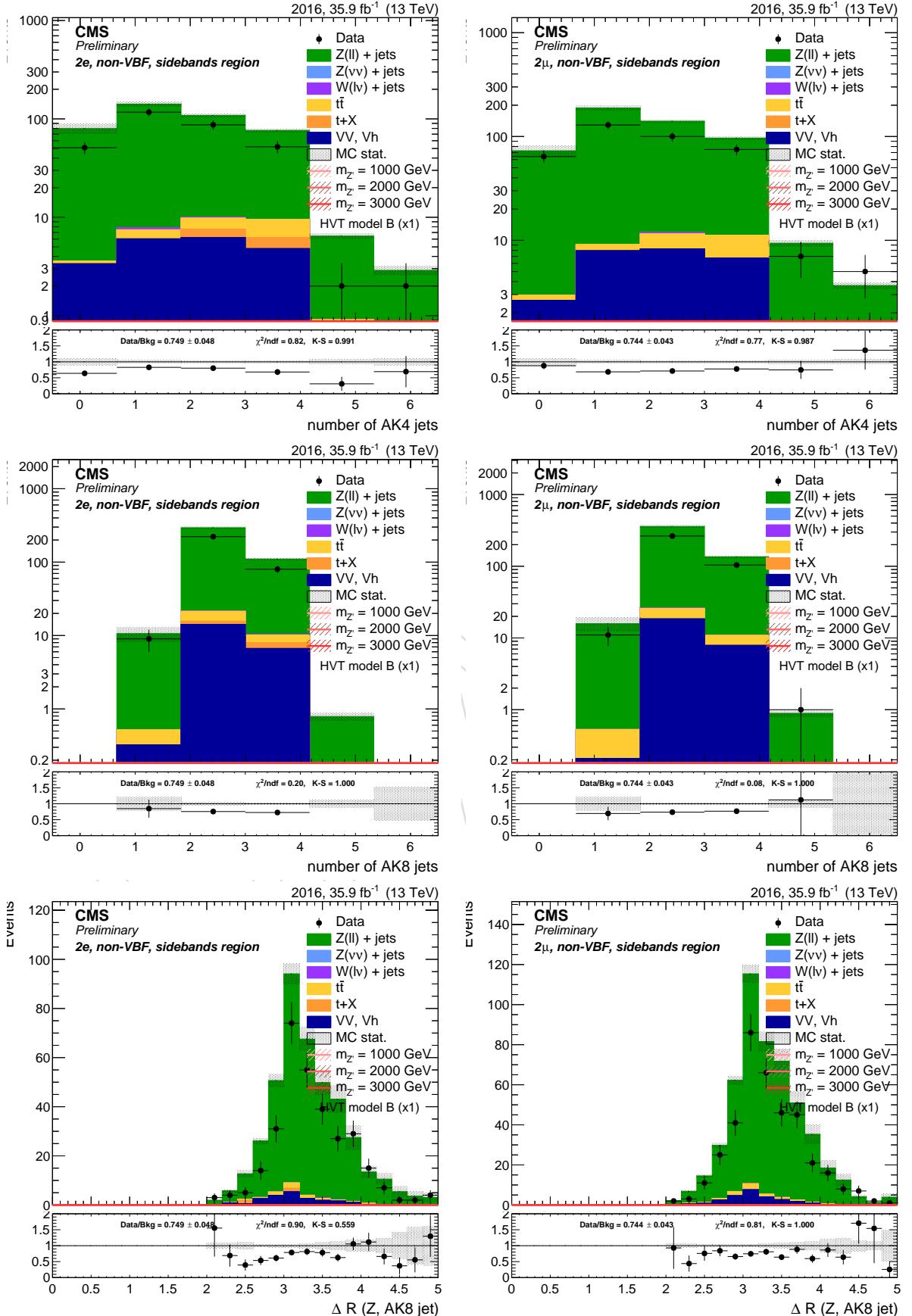


Figure 49: Top: number of AK4 jets. Center: number of AK8 jets. Bottom: ΔR between Z boson and leading AK8 jet. left: di-electron channel. right: di-muon channel. Events are selected with the *inclusive* selection, and simulated backgrounds are normalized to luminosity.

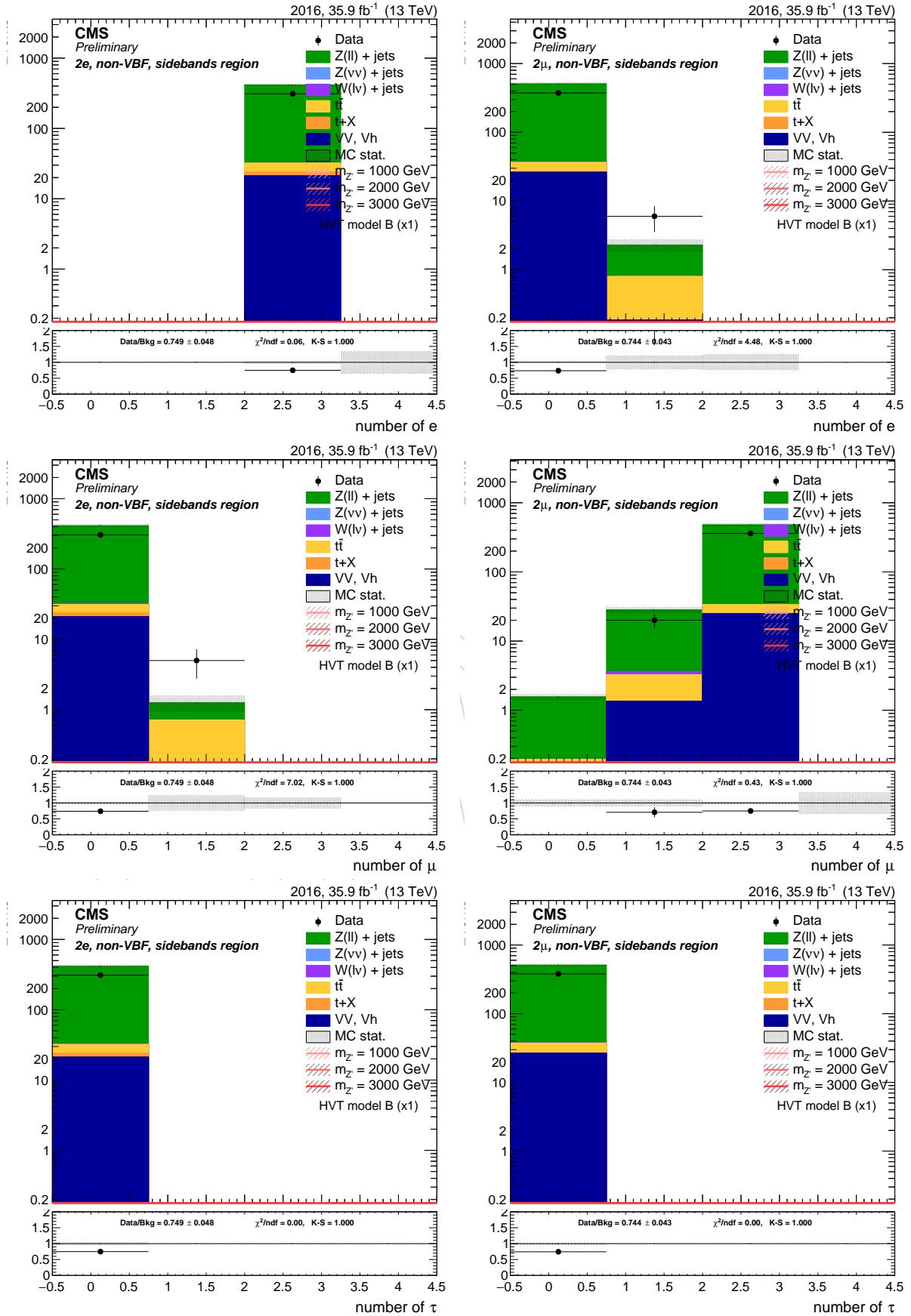


Figure 50: Top: number of electrons. Center: number of muons. Bottom: number of hadronic taus. left: di-electron channel. right: di-muon channel. Events are selected with the *inclusive* selection, and simulated backgrounds are normalized to luminosity.

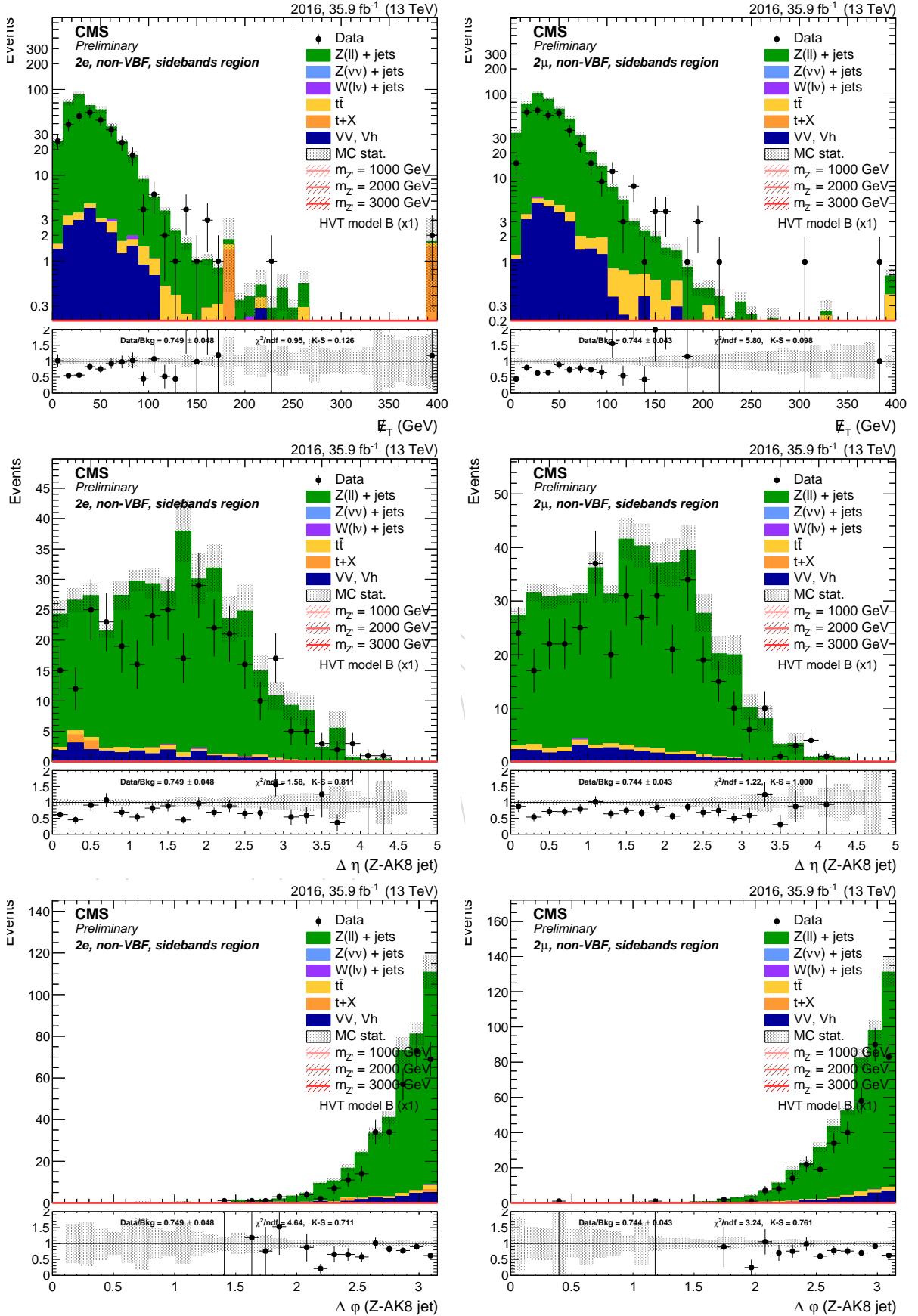


Figure 51: Top: E_T^{miss} . Center: $\Delta\eta$ between the Z and the AK8 jet. Bottom: $\Delta\phi$ between the Z and H candidates. left: di-electron channel. right: di-muon channel. Events are selected with the *inclusive* selection, and simulated backgrounds are normalized to luminosity.

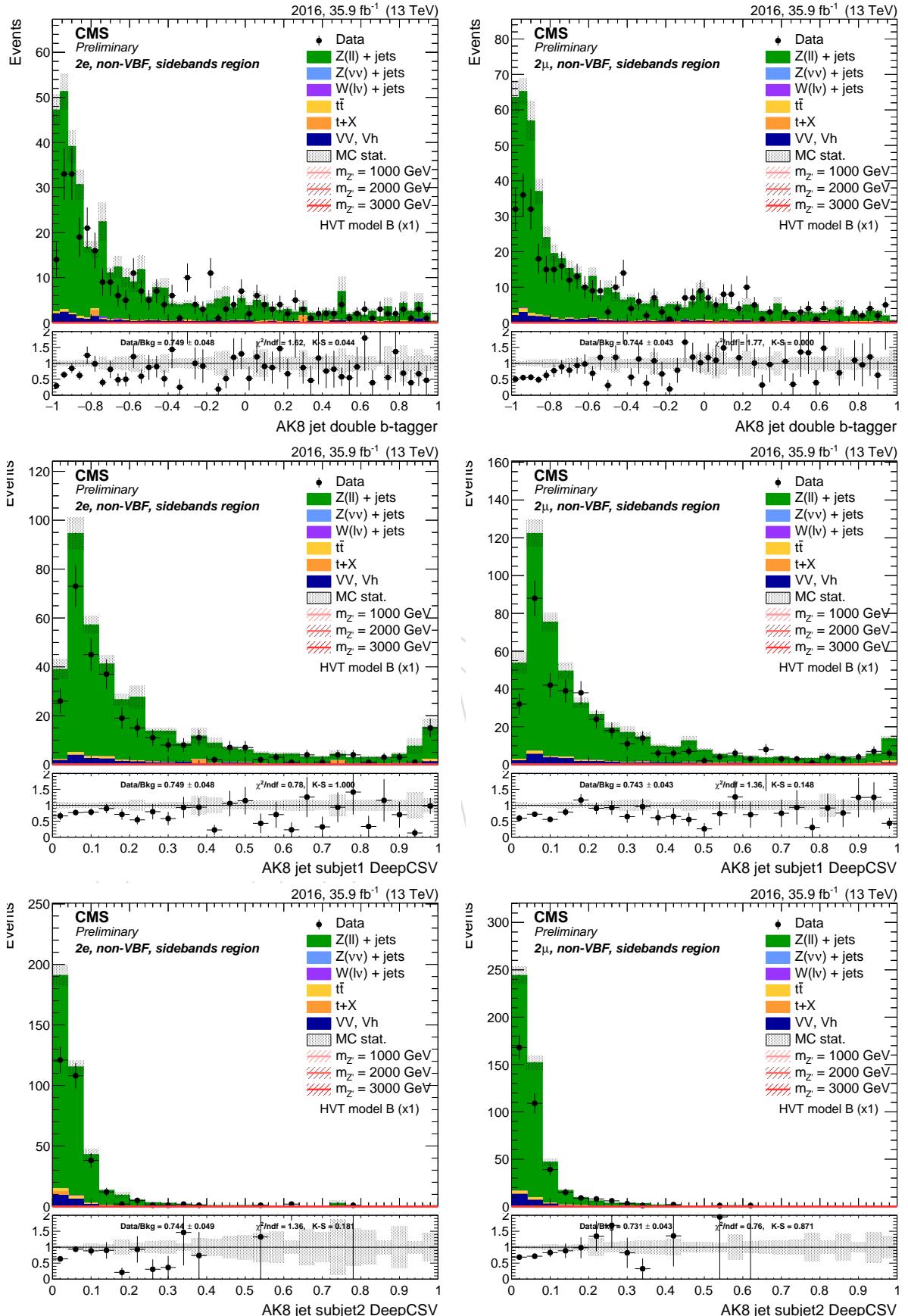


Figure 52: Top: AK8 double-b tagger discriminator . Center: DeepCSV distribution of the leading AK8 sub-jet. Bottom: DeepCSV distribution of the sub-leading AK8 sub-jet. left: di-electron channel. right: di-muon channel. Events are selected with the *inclusive* selection, and simulated backgrounds are normalized to luminosity.

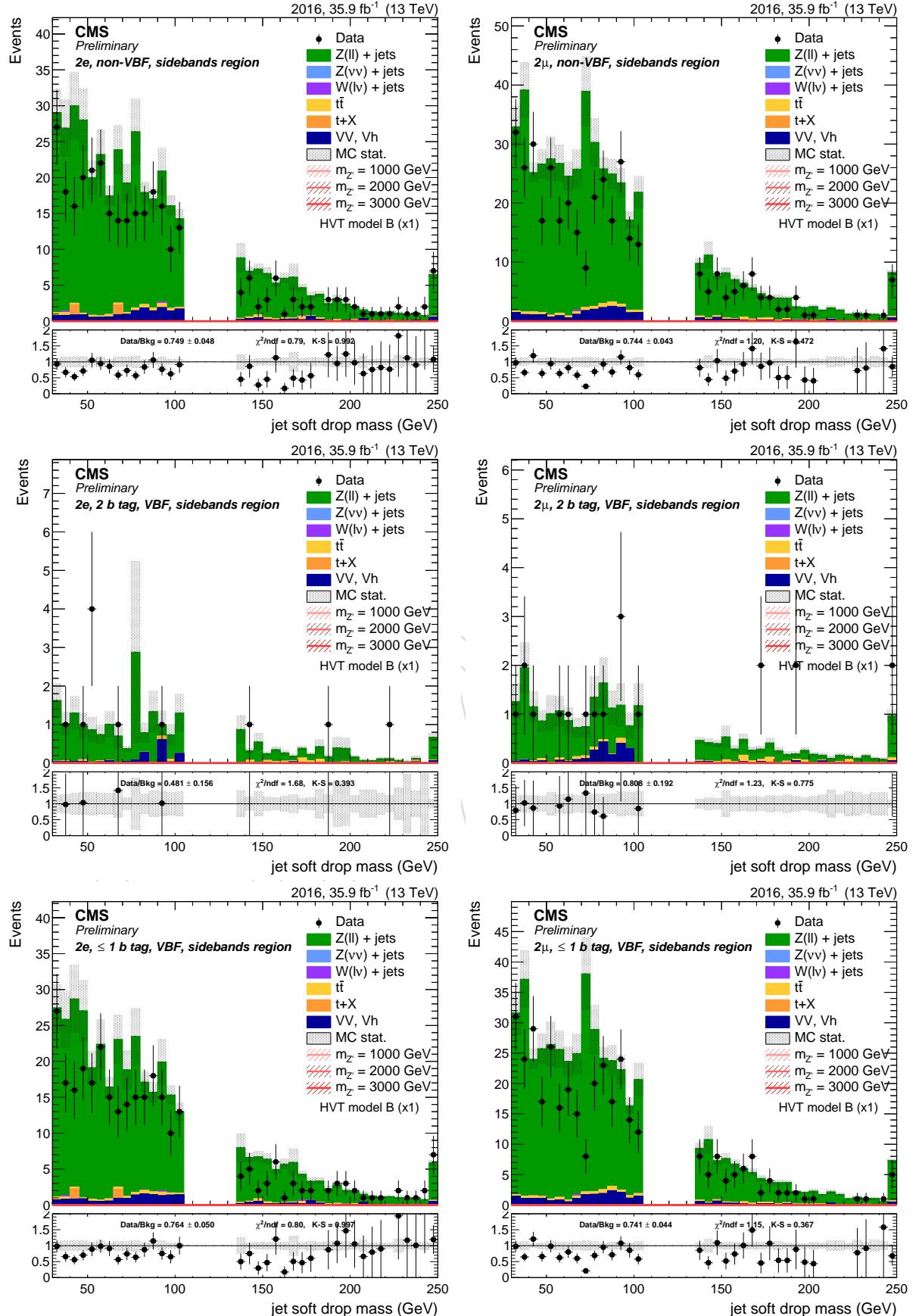


Figure 53: Leading AK8 jet soft drop PUPPI mass. Top: inclusive region. Center: mass sidebands and 2 b-tag category. Bottom: mass sidebands and no b-tag category. left: di-electron channel. right: di-muon channel.

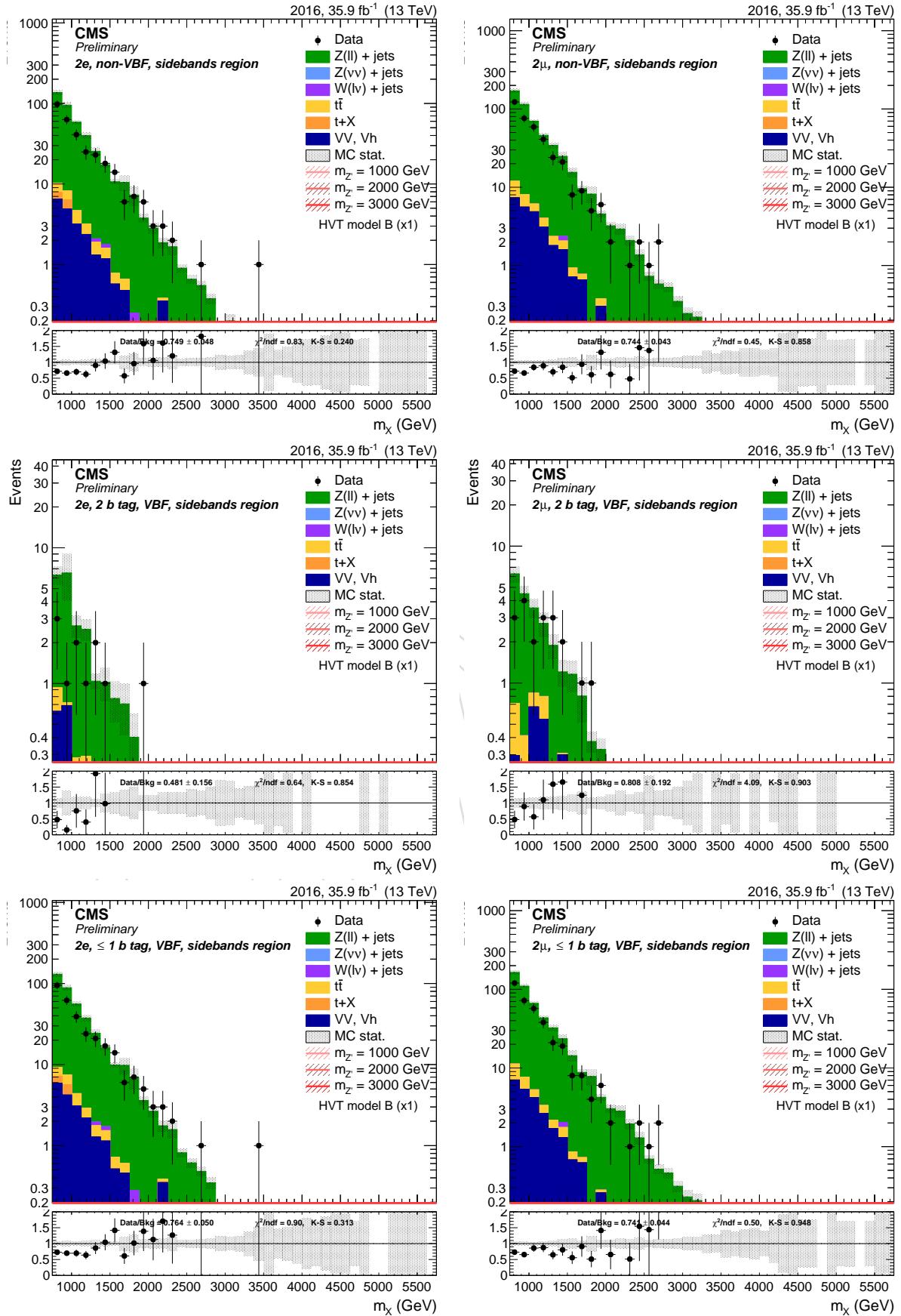


Figure 54: Resonance candidate mass. Top: inclusive region. Center: mass sidebands and 2 b-tag category. Bottom: mass sidebands and no b-tag category. left: di-electron channel. right: di-muon channel.

681 **6.2 2017**682 **6.2.1 Zero lepton channel**

Sample	Events	Entries	%
data_obs	20040.00	20039	113.92
TTbarSL	1178.15	45143	6.70
DYJetsToNuNu_HT	10843.57	350013	61.64
DYJetsToLL_HT	30.99	2367	0.18
ST	188.54	1857	1.07
VV	452.18	89697	2.57
WJetsToLNu_HT	4897.92	152111	27.84
BkgSum	17591.35	641193	100.00
XZH_M1000	361.56	16359	0.00
XZH_M2000	32.57	29061	0.00
XZH_M3000	3.14	30750	0.00

Figure 55: Number of events in the inclusive region of the 0-lepton channel.

DRAFT

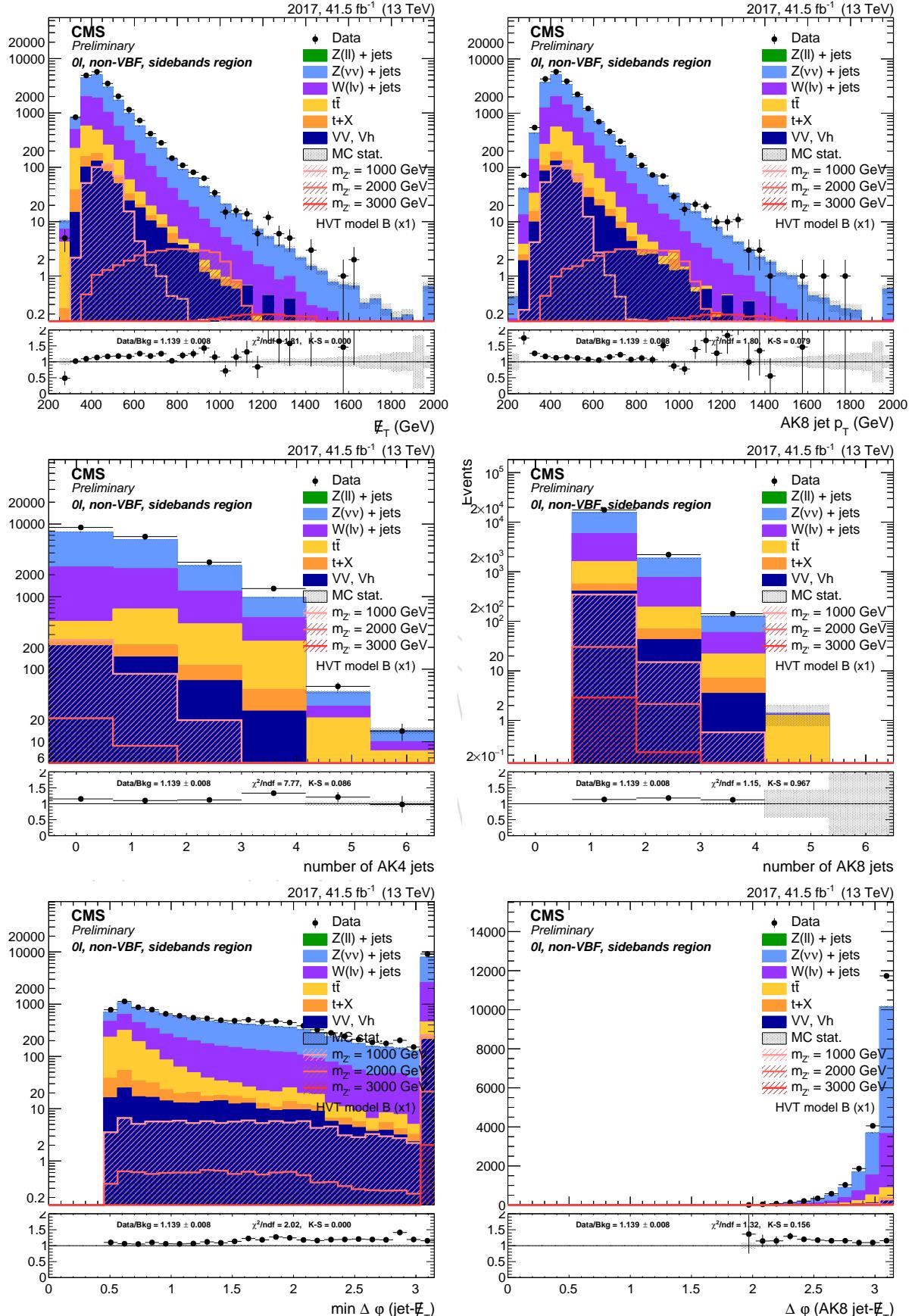


Figure 56: Top: E_T^{miss} (left) and leading AK8 jet p_T (right). Center: number of AK4 jets (left) and AK8 jets (right). Bottom: minimum $\Delta\phi$ between the AK4 jets and AK8 jet in the event (left) and $\Delta\phi$ between the AK8 jet and the E_T^{miss} (right). Events are selected with the *inclusive* selection, and simulated backgrounds are normalized to luminosity.

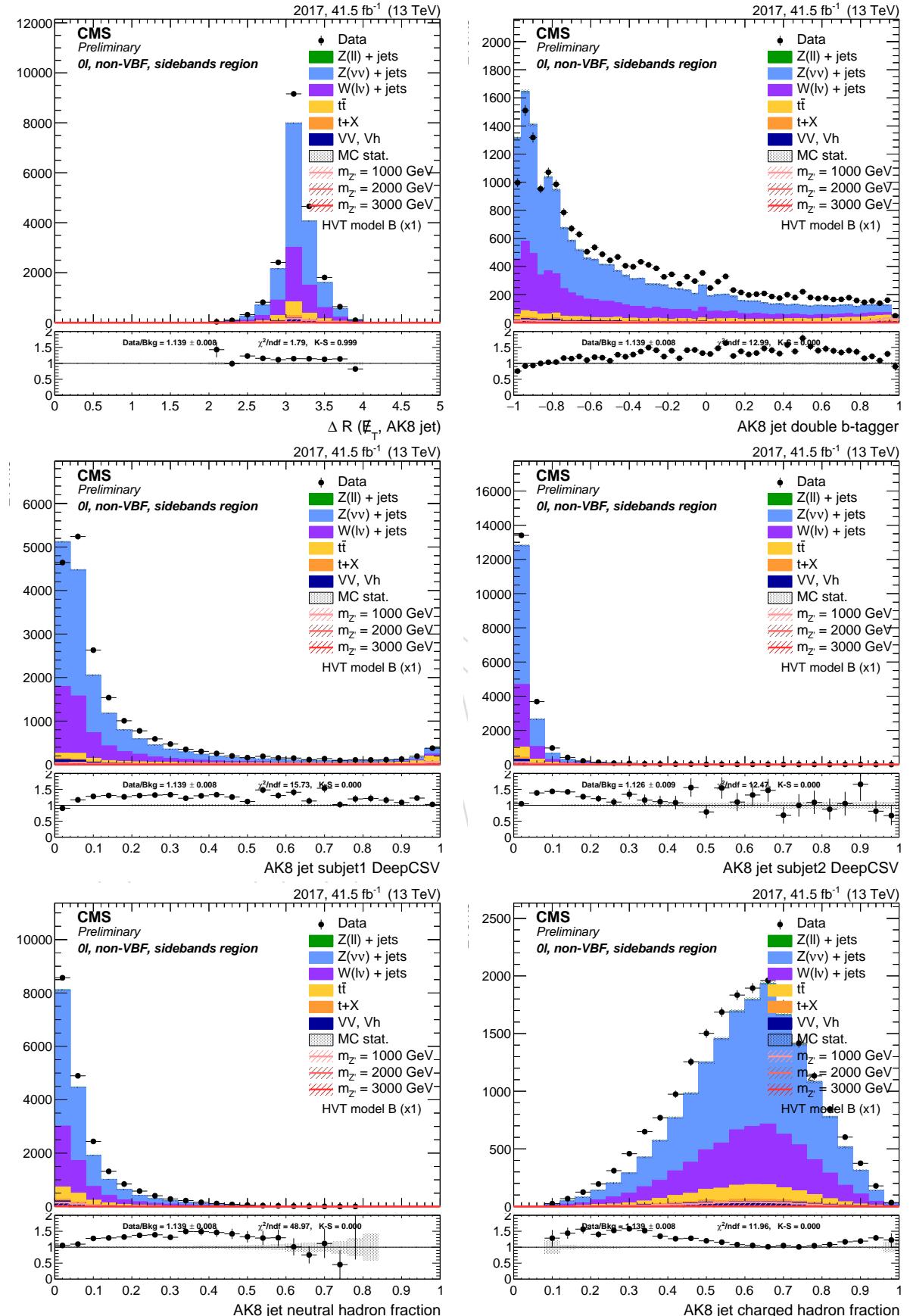


Figure 57: Top: ΔR between Z boson and leading AK8 jet (left), AK8 double-b tagger discriminator (right). Center: DeepCSV distribution of the AK8 sub-jets. Bottom: leading AK8 jet neutral hadron fraction (left) and charged hadron fraction (right). Events are selected with the *inclusive* selection, and simulated backgrounds are normalized to luminosity.

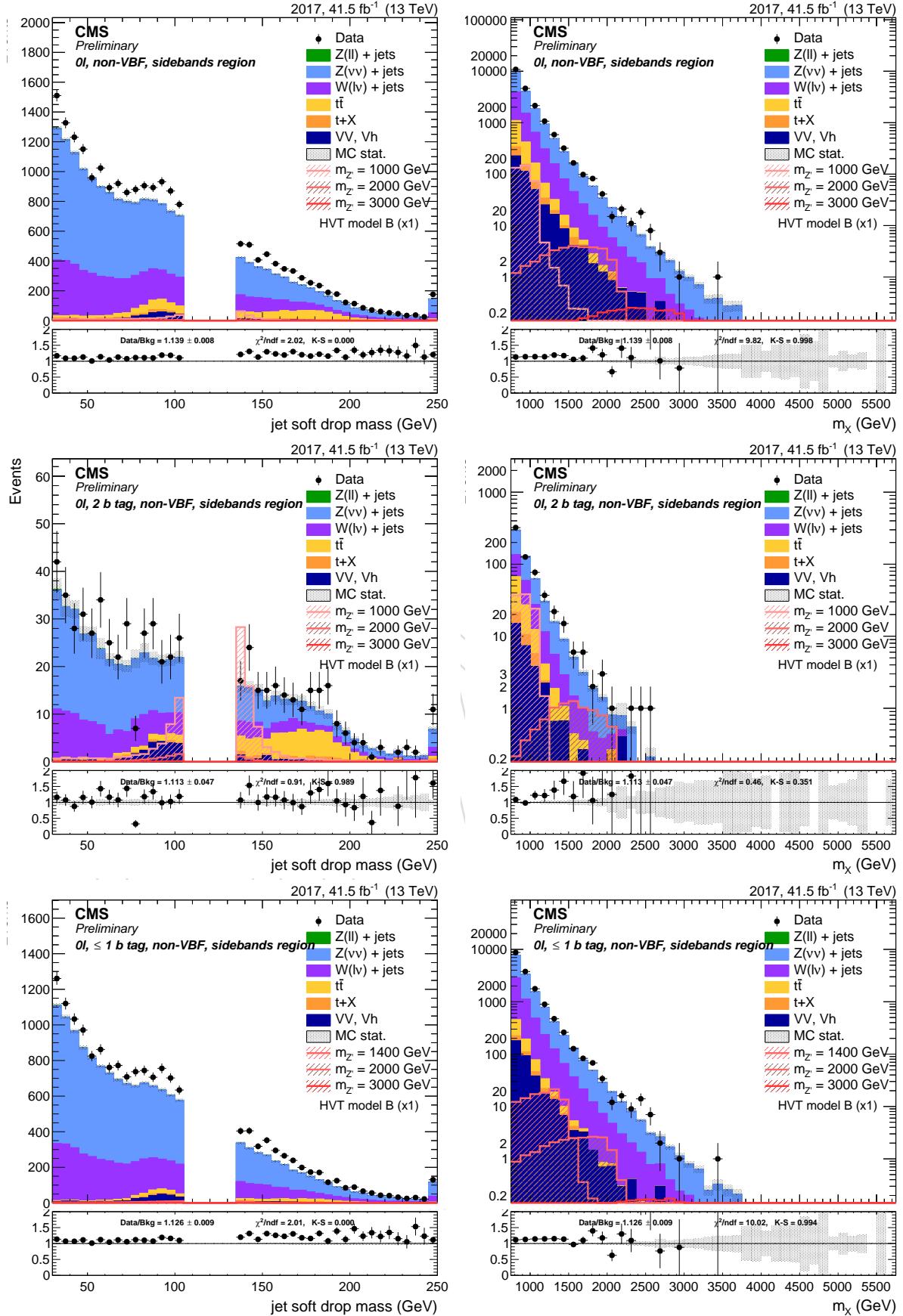


Figure 58: Leading AK8 jet soft drop PUPPI mass (left) and resonance transverse mass (right). Top: inclusive region. Center: mass sidebands and 2 b-tag category. Bottom: mass sidebands and no b-tag category

683 **6.2.2 Zero lepton channel VBF**

Sample	Events	Entries	%
data_obs	1045.00	1044	102.48
TTbarSL	105.77	5310	10.37
DYJetsToNuNu_HT	573.77	21757	56.27
DYJetsToLL_HT	1.72	183	0.17
ST	17.78	141	1.74
VV	17.82	3518	1.75
WJetsToLNu_HT	302.88	15262	29.70
BkgSum	1019.74	46176	100.00
XZHVBFA_M1000	0.11	2288	0.00
XZHVBFA_M2000	0.01	6082	0.00
XZHVBFA_M3000	0.00	6750	0.00

Figure 59: Number of events in the inclusive region of the 0-lepton channel.

DRAFT

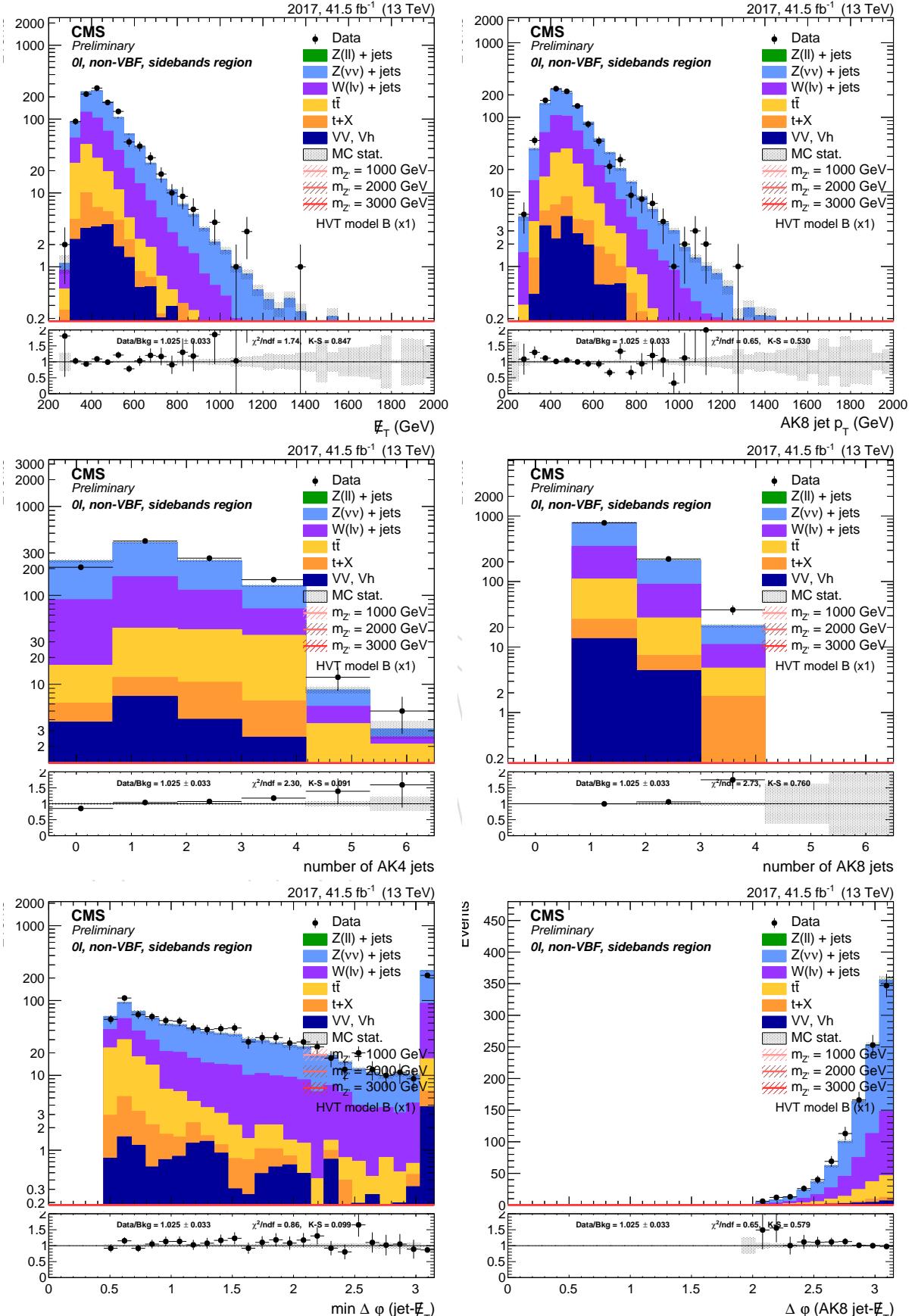


Figure 60: Top: E_T^{miss} (left) and leading AK8 jet p_T (right). Center: number of AK4 jets (left) and AK8 jets (right). Bottom: minimum $\Delta\phi$ between the AK4 jets and AK8 jet in the event (left) and $\Delta\phi$ between the AK8 jet and the E_T^{miss} (right). Events are selected with the *inclusive* selection, and simulated backgrounds are normalized to luminosity.

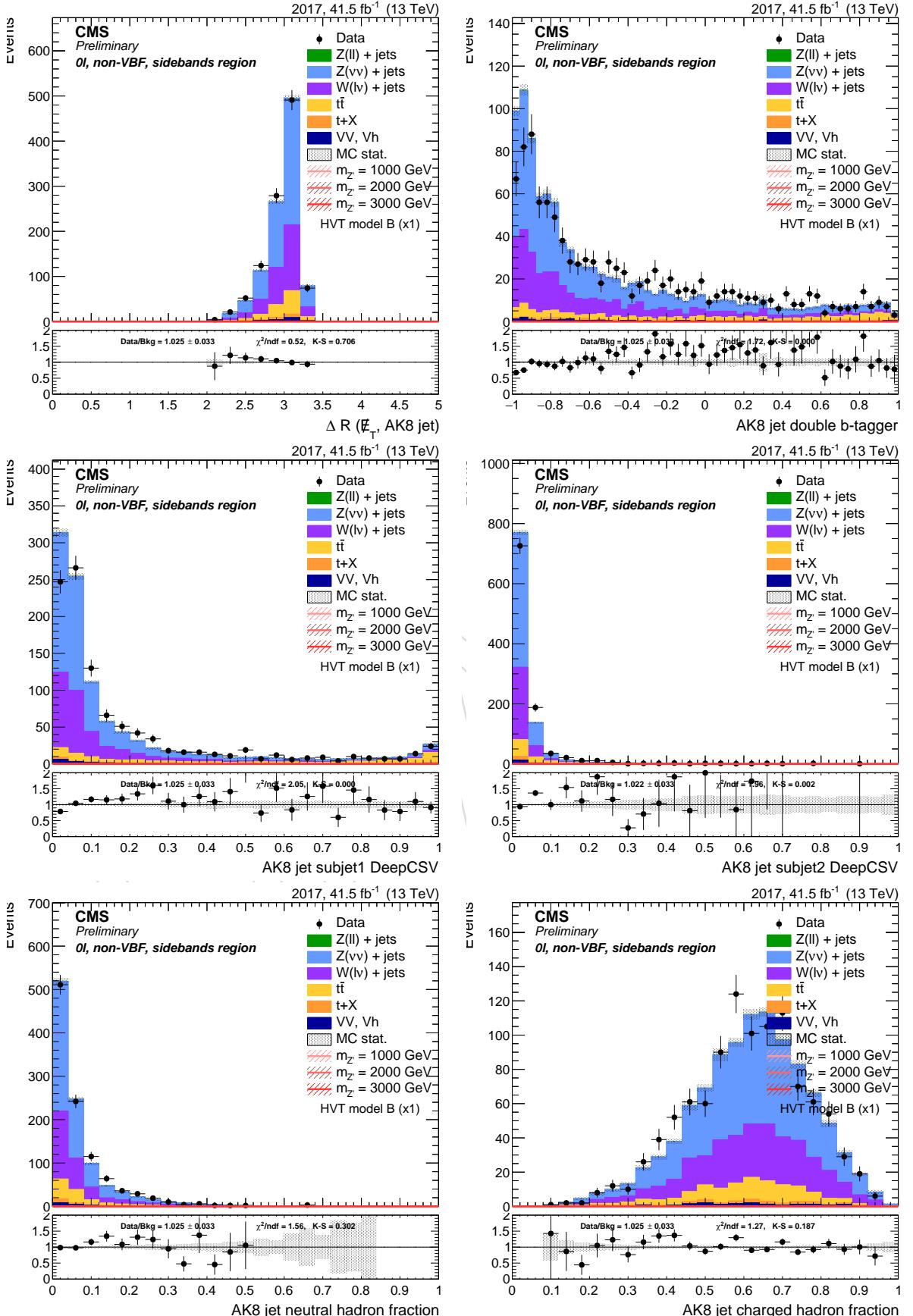


Figure 61: Top: ΔR between Z boson and leading AK8 jet (left), AK8 double-b tagger discriminator (right). Center: DeepCSV distribution of the AK8 sub-jets. Bottom: leading AK8 jet neutral hadron fraction (left) and charged hadron fraction (right). Events are selected with the *inclusive* selection, and simulated backgrounds are normalized to luminosity.

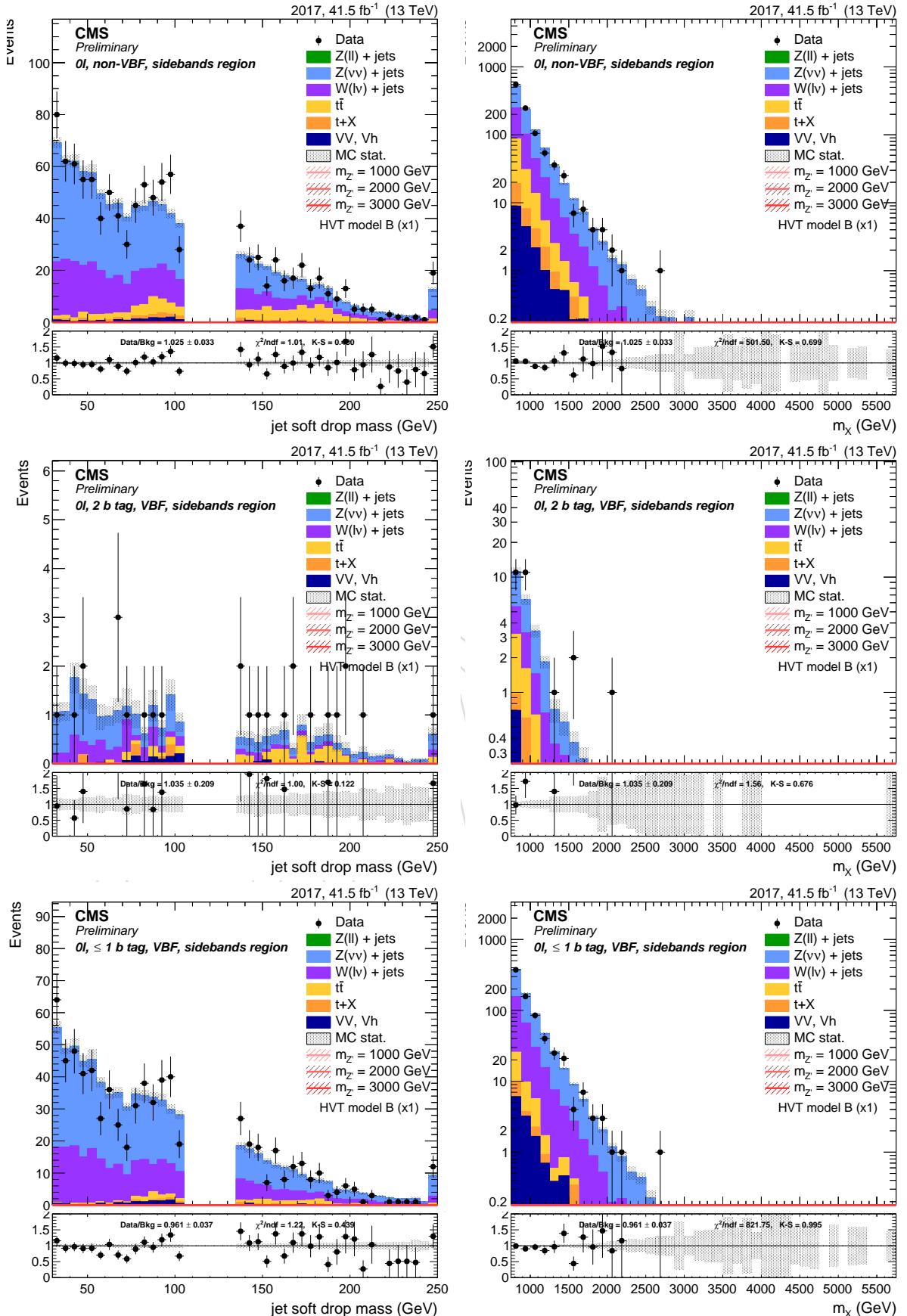


Figure 62: Leading AK8 jet soft drop PUPPI mass (left) and resonance transverse mass (right). Top: inclusive region. Center: mass sidebands and 2 b-tag category. Bottom: mass sidebands and no b-tag category

684 6.2.3 Dilepton channel

Sample	Events	Entries	%
data_obs	2315.00	2314	106.11
TTbarSL	20.60	11222	0.94
DYJetsToNuNu_HT	0.00	-1	0.00
DYJetsToLL_HT	2058.04	158016	94.34
ST	2.30	15	0.11
VV	97.69	23085	4.48
WJetsToLNu_HT	2.98	272	0.14
BkgSum	2181.61	192614	100.00
XZH_M1000	75.26	7126	0.00
XZH_M2000	4.37	8118	0.00
XZH_M3000	0.36	7916	0.00

Sample	Events	Entries	%
data_obs	2794.00	2793	110.41
TTbarSL	34.94	12989	1.38
DYJetsToNuNu_HT	0.00	-1	0.00
DYJetsToLL_HT	2380.18	183053	94.06
ST	2.22	14	0.09
VV	112.70	26677	4.45
WJetsToLNu_HT	0.44	146	0.02
BkgSum	2530.47	222883	100.00
XZH_M1000	86.89	8398	0.00
XZH_M2000	4.11	7762	0.00
XZH_M3000	0.32	6633	0.00

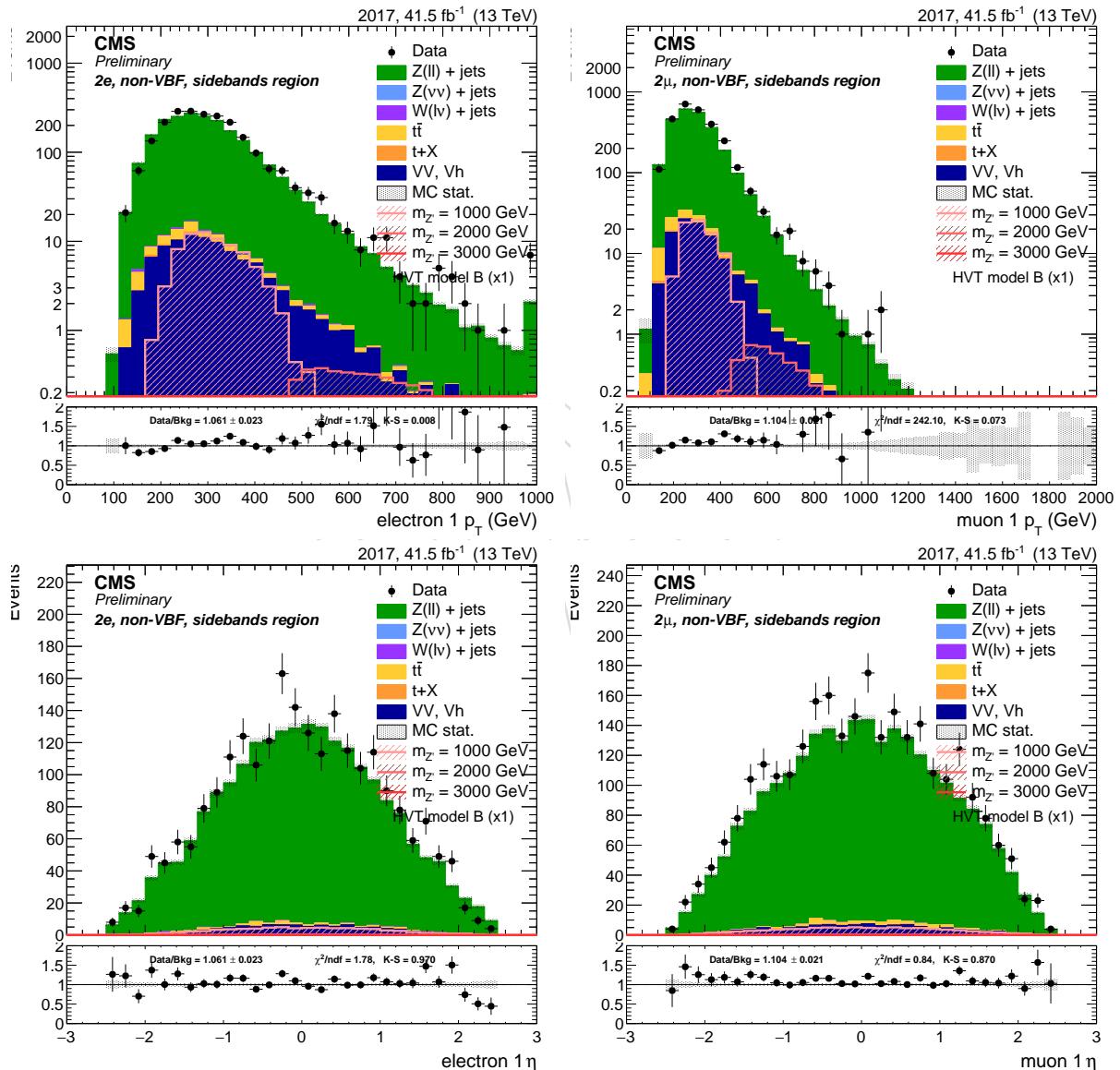


Figure 63: Leading lepton p_T (top) and η (bottom) for di-electron (left) and di-muon (right) channel. Events are selected with the *inclusive* selection, and simulated backgrounds are normalized to luminosity.

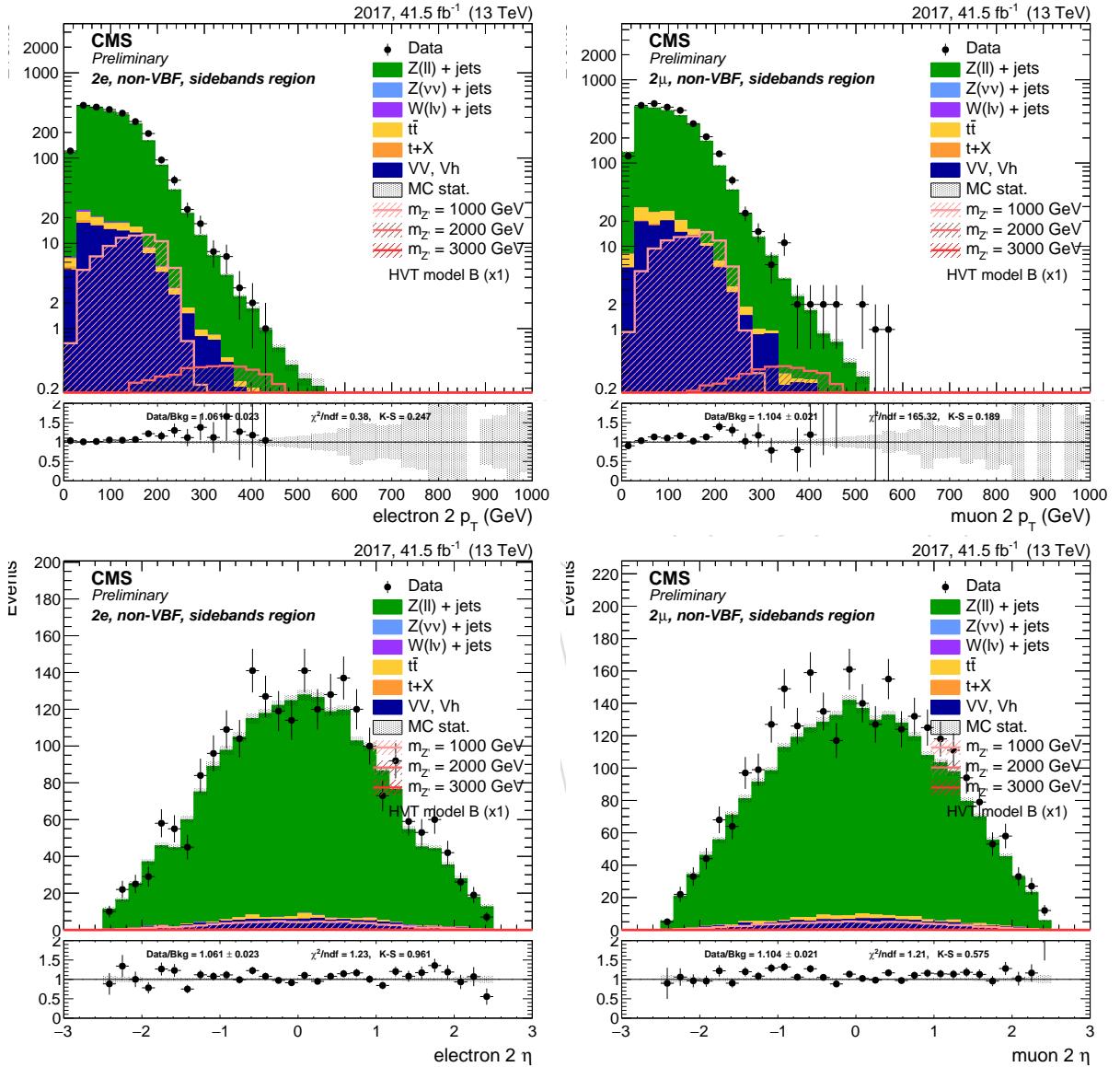


Figure 64: Sub-leading lepton p_T (top) and η (bottom) for di-electron (left) and di-muon (right) channel. Events are selected with the *inclusive* selection, and simulated backgrounds are normalized to luminosity.

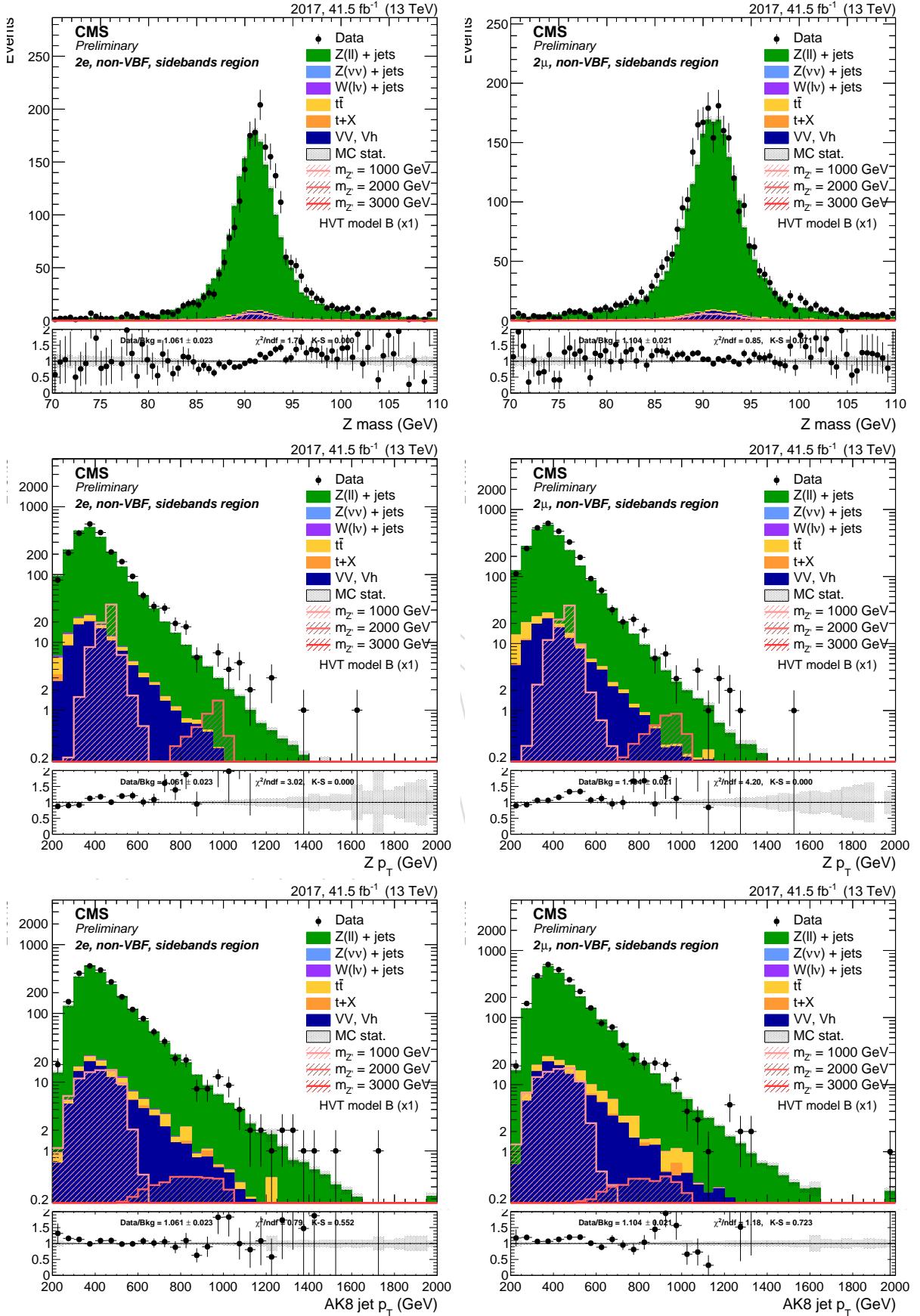


Figure 65: Top: Z candidate mass. Center: Z candidate p_T . Bottom: leading AK8 jet p_T . left: di-electron channel. right: di-muon channel. Events are selected with the *inclusive* selection, and simulated backgrounds are normalized to luminosity.

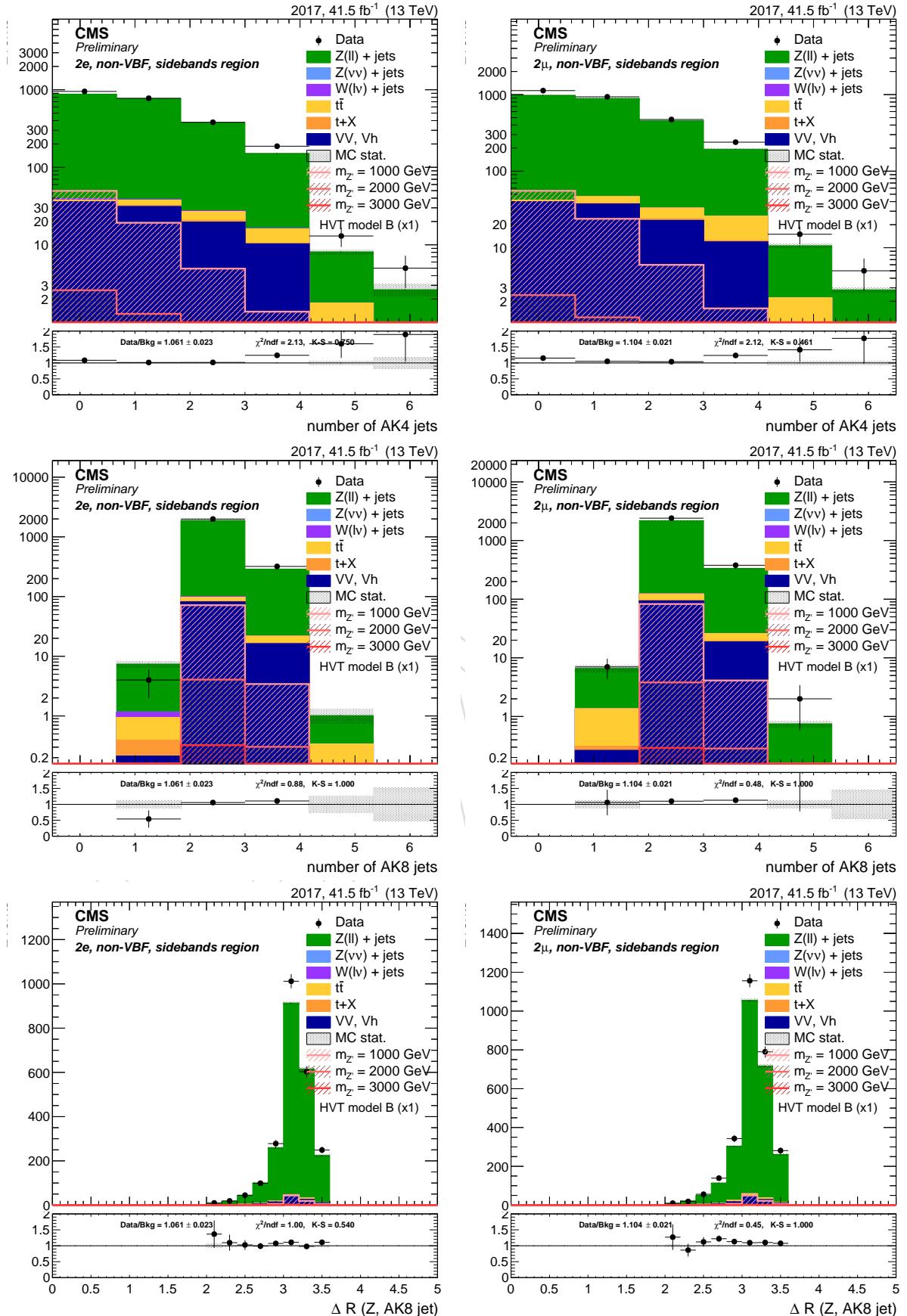


Figure 66: Top: number of AK4 jets. Center: number of AK8 jets. Bottom: ΔR between Z boson and leading AK8 jet. Left: di-electron channel. Right: di-muon channel. Events are selected with the *inclusive* selection, and simulated backgrounds are normalized to luminosity.

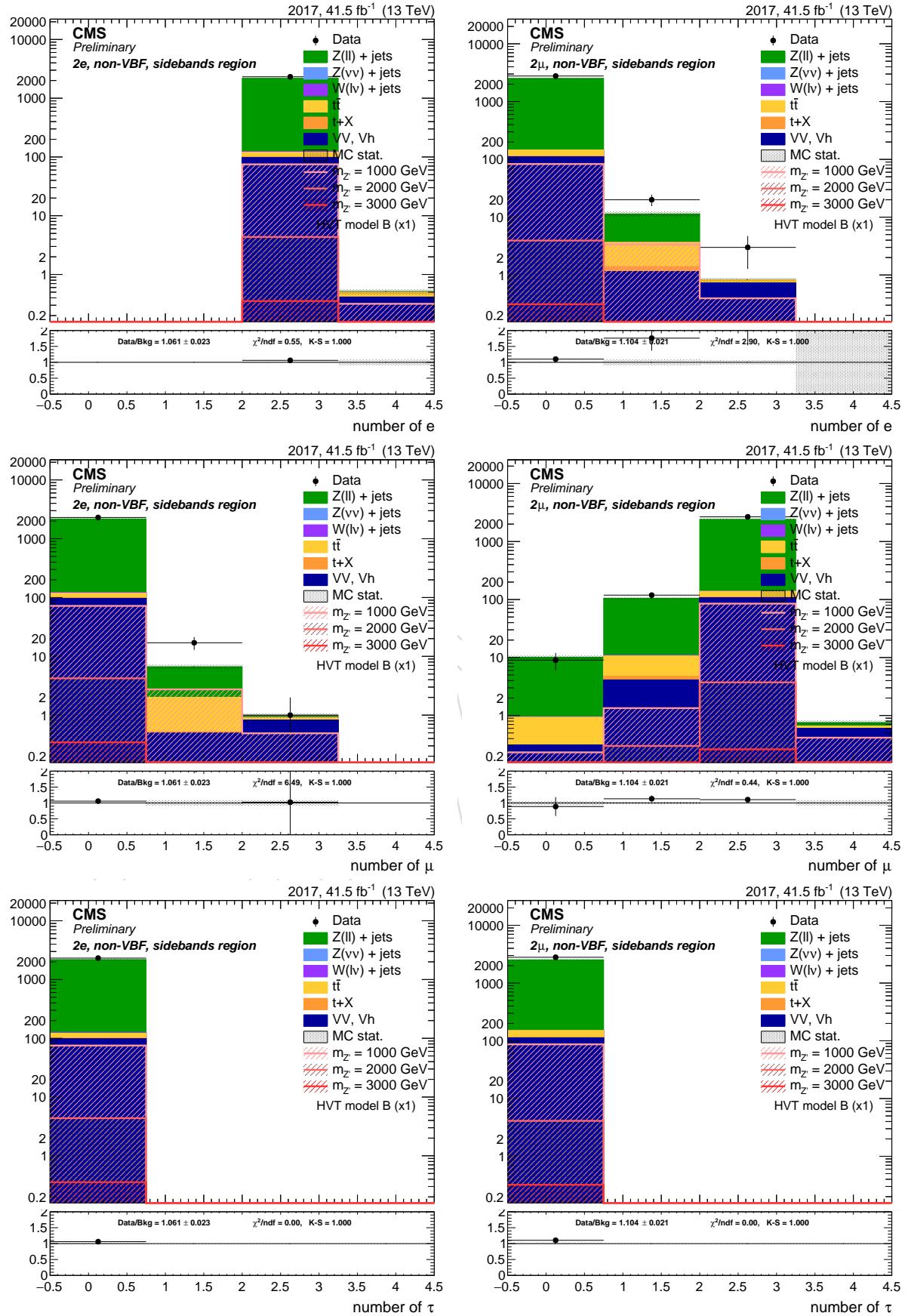


Figure 67: Top: number of electrons. Center: number of muons. Bottom: number of hadronic taus. left: di-electron channel. right: di-muon channel. Events are selected with the *inclusive* selection, and simulated backgrounds are normalized to luminosity.

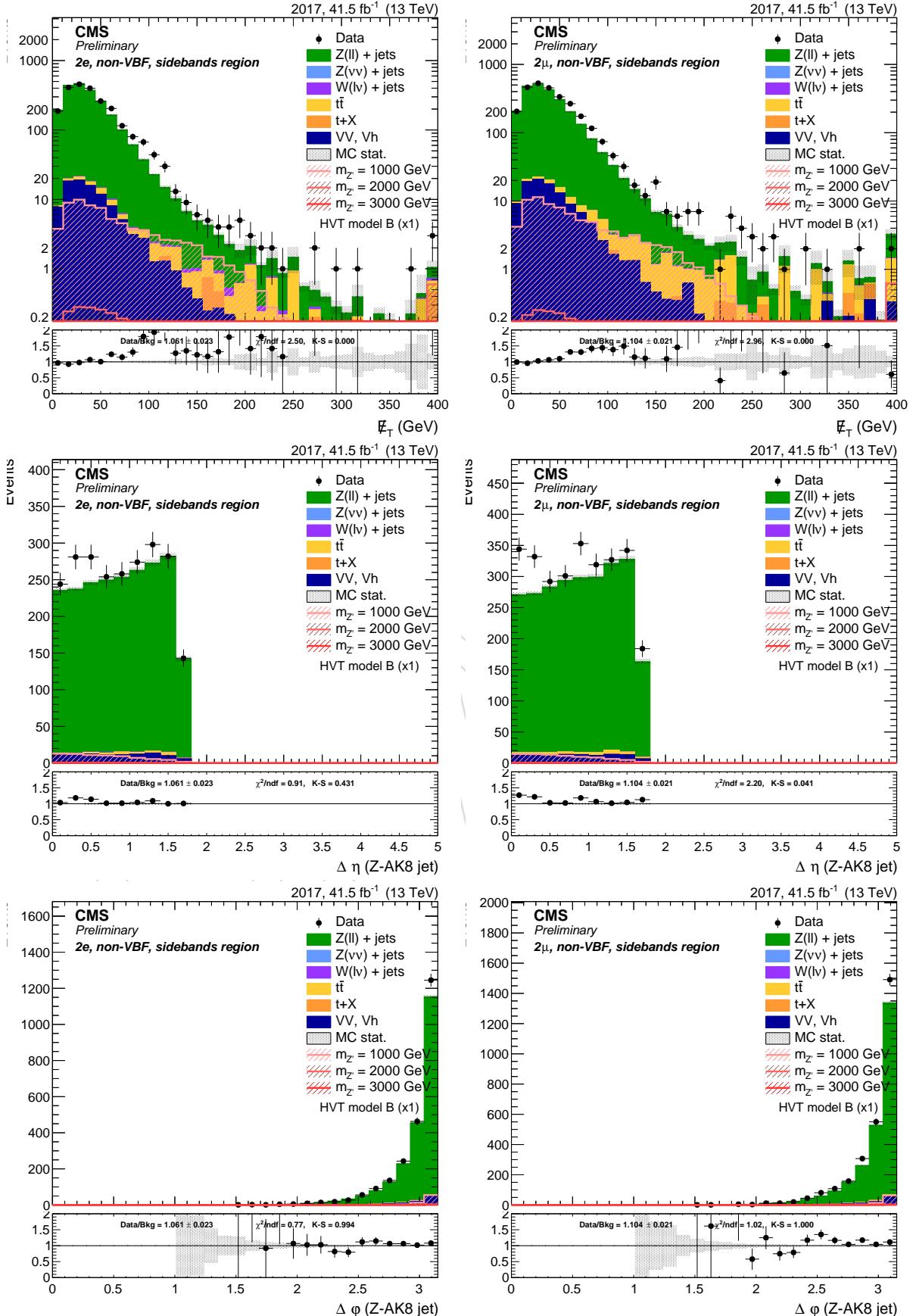


Figure 68: Top: E_T^{miss} . Center: $\Delta\eta$ between the Z and the AK8 jet. Bottom: $\Delta\phi$ between the Z and H candidates. left: di-electron channel. right: di-muon channel. Events are selected with the *inclusive* selection, and simulated backgrounds are normalized to luminosity.

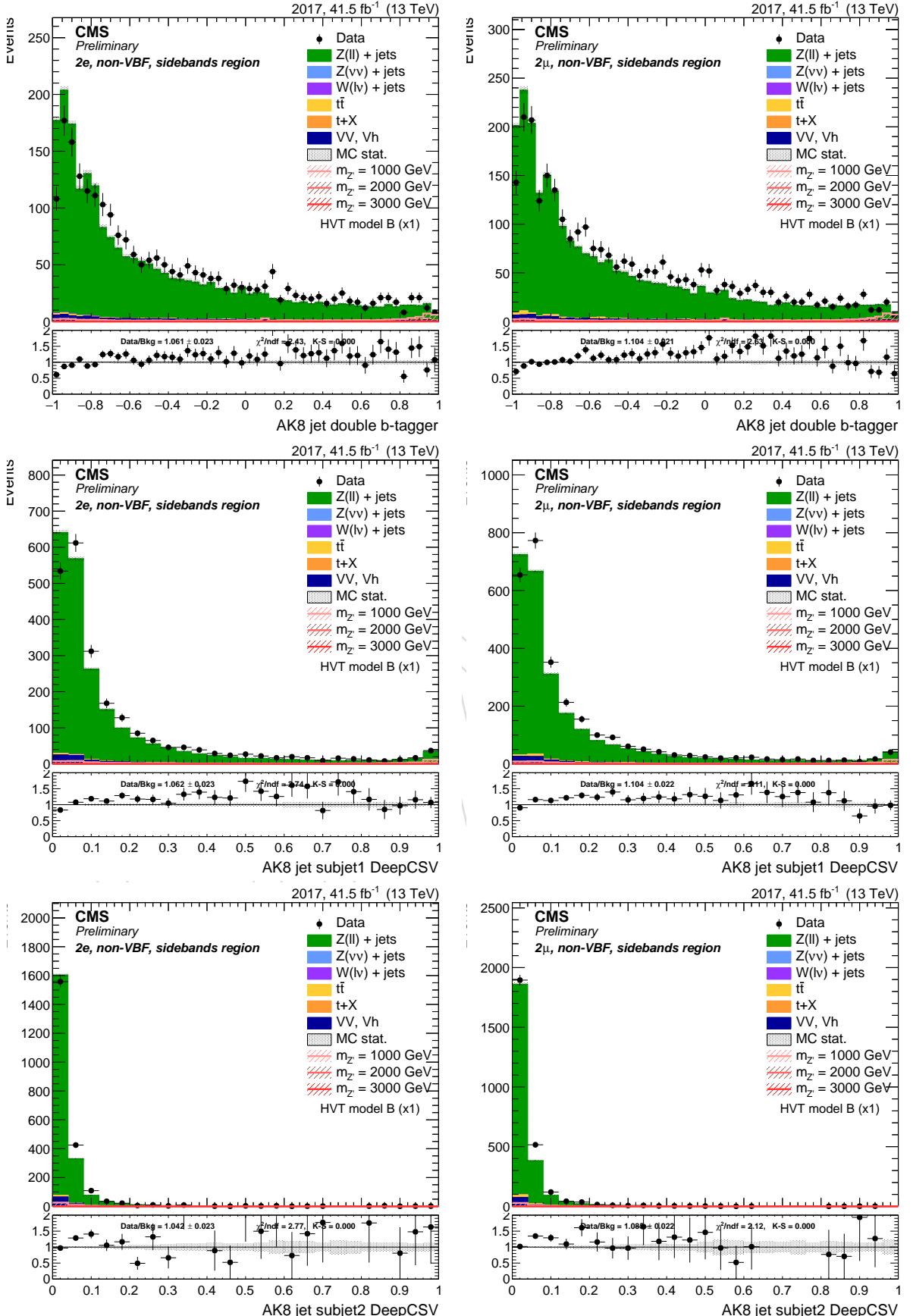


Figure 69: Top: AK8 double-b tagger discriminator . Center: DeepCSV distribution of the leading AK8 sub-jet. Bottom: DeepCSV distribution of the sub-leading AK8 sub-jet. left: di-electron channel. right: di-muon channel. Events are selected with the *inclusive* selection, and simulated backgrounds are normalized to luminosity.

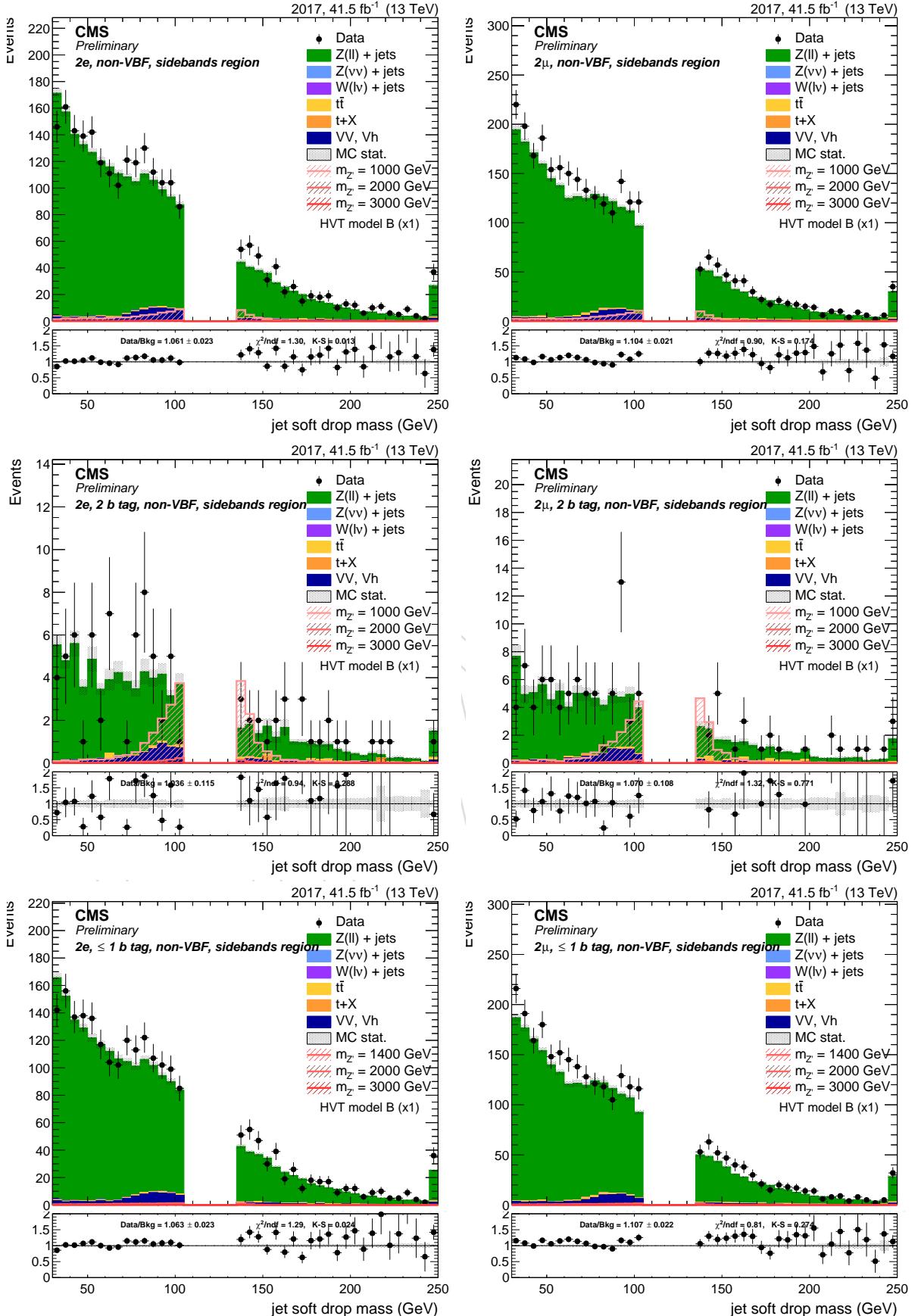


Figure 70: Leading AK8 jet soft drop PUPPI mass. Top: inclusive region. Center: mass sidebands and 2 b-tag category. Bottom: mass sidebands and no b-tag category. left: di-electron channel. right: di-muon channel.

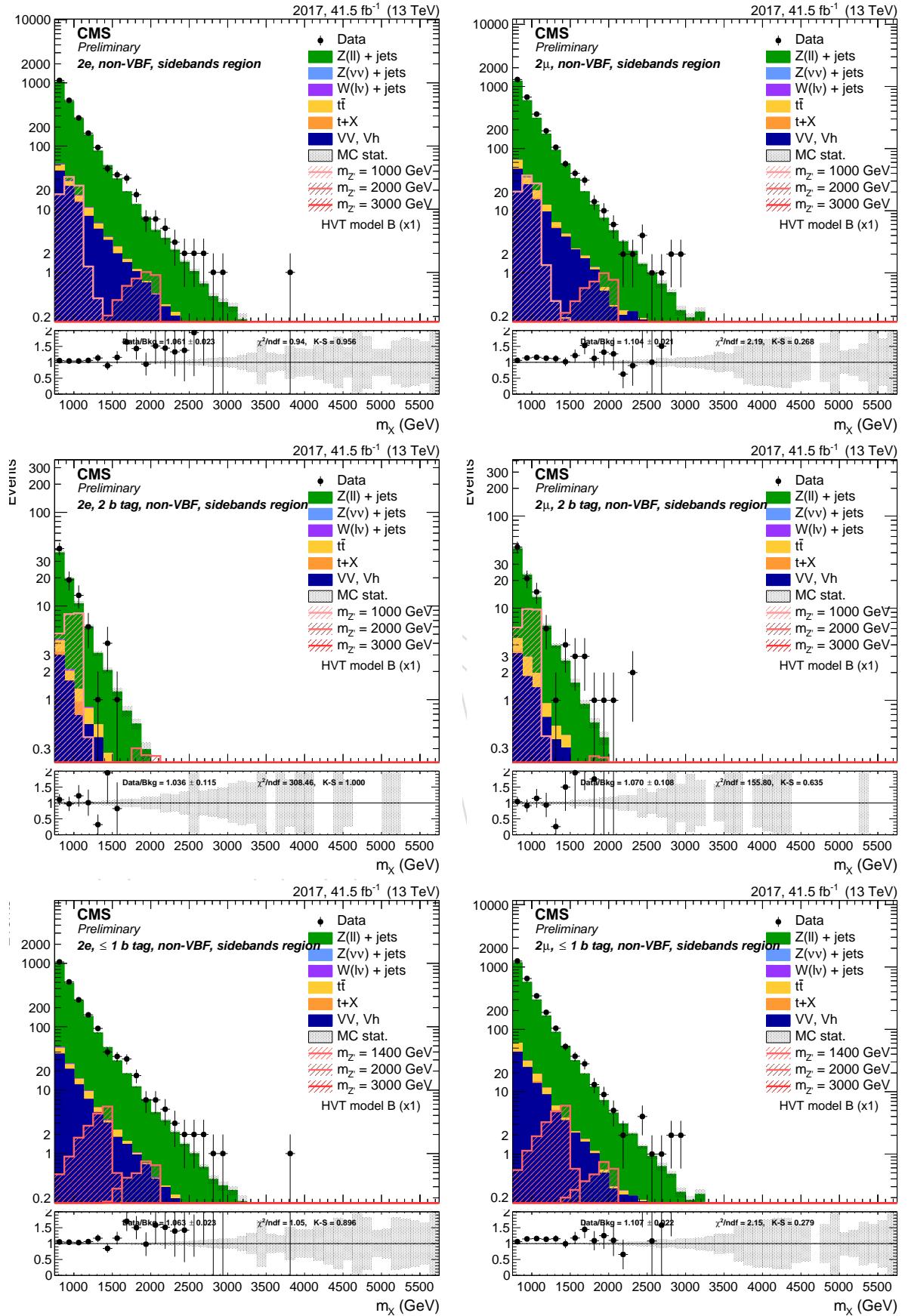


Figure 71: Resonance candidate mass. Top: inclusive region. Center: mass sidebands and 2 b-tag category. Bottom: mass sidebands and no b-tag category. left: di-electron channel. right: di-muon channel.

686 6.2.4 Dilepton channel VBF

Sample	Events	Entries	%	Sample	Events	Entries	%
data_obs	270.00	269	82.98	data_obs	368.00	367	99.21
TTbarSL	6.61	3004	2.03	TTbarSL	9.25	3295	2.49
DYJetsToNuNu_HT	0.00	-1	0.00	DYJetsToNuNu_HT	0.00	-1	0.00
DYJetsToLL_HT	305.51	24095	93.90	DYJetsToLL_HT	348.35	27729	93.91
ST	0.46	2	0.14	ST	0.23	0	0.06
VV	12.52	2359	3.85	VV	13.02	2572	3.51
WJetsToLNu_HT	0.26	35	0.08	WJetsToLNu_HT	0.09	22	0.02
BkgSum	325.36	29499	100.00	BkgSum	370.94	33622	100.00
XZHVB_M1000	0.05	2375	0.00	XZHVB_M1000	0.06	2696	0.00
XZHVB_M2000	0.00	3413	0.00	XZHVB_M2000	0.00	3747	0.00
XZHVB_M3000	0.00	3544	0.00	XZHVB_M3000	0.00	3371	0.00

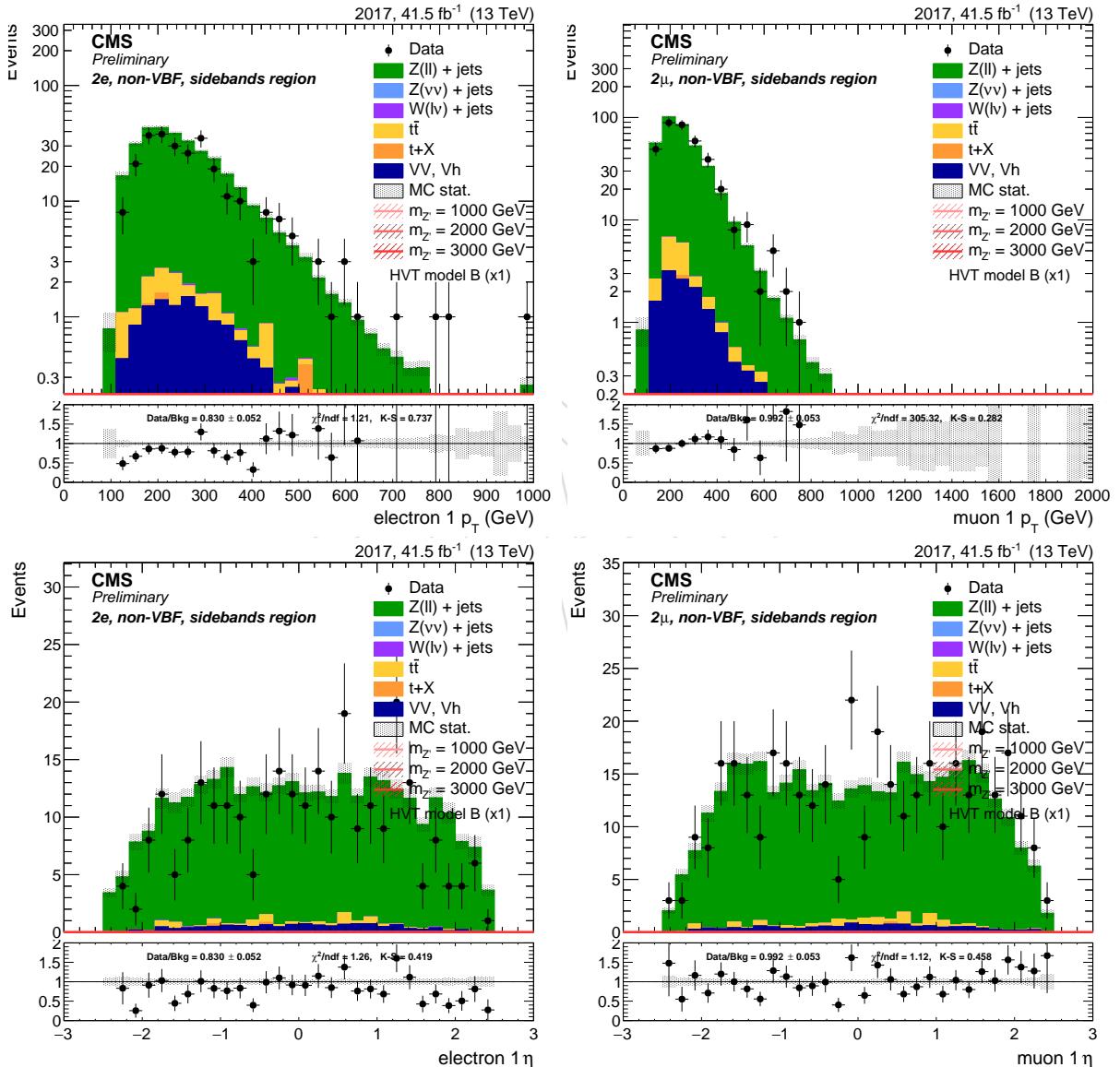


Figure 72: Leading lepton p_T (top) and η (bottom) for di-electron (left) and di-muon (right) channel. Events are selected with the *inclusive* selection, and simulated backgrounds are normalized to luminosity.

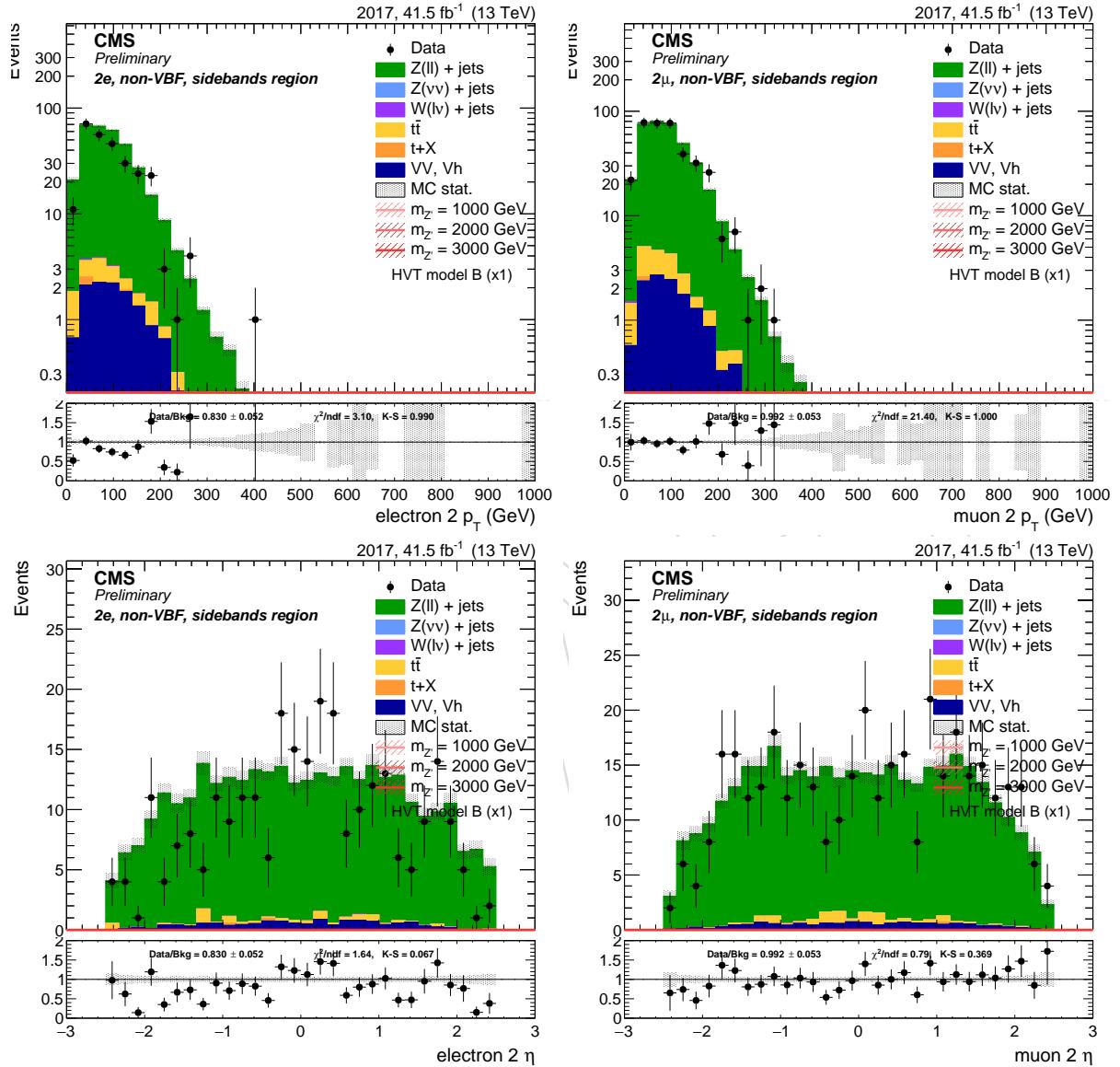


Figure 73: Sub-leading lepton p_T (top) and η (bottom) for di-electron (left) and di-muon (right) channel. Events are selected with the *inclusive* selection, and simulated backgrounds are normalized to luminosity.

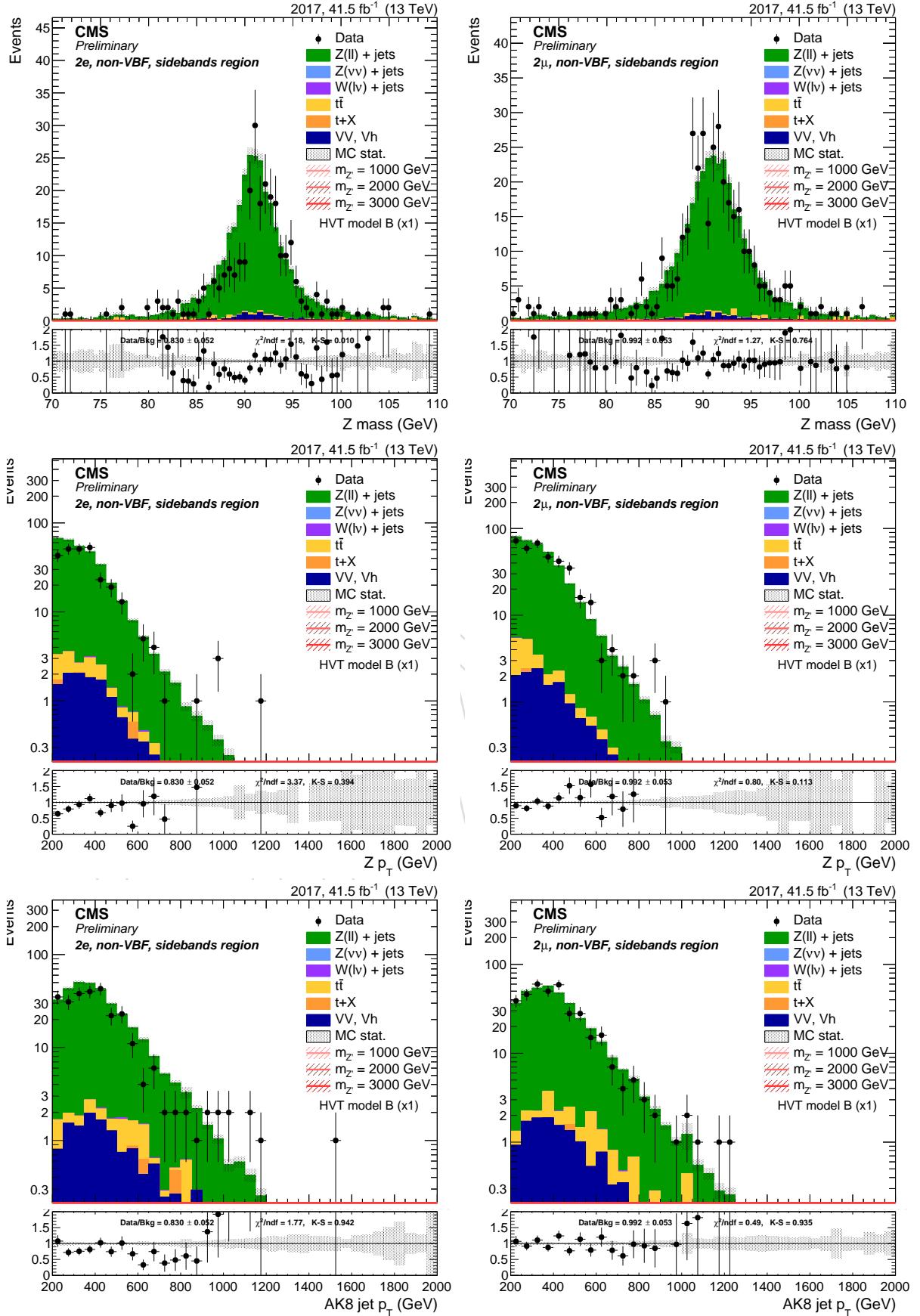


Figure 74: Top: Z candidate mass. Center: Z candidate p_T . Bottom: leading AK8 jet p_T . left: di-electron channel. right: di-muon channel. Events are selected with the *inclusive* selection, and simulated backgrounds are normalized to luminosity.

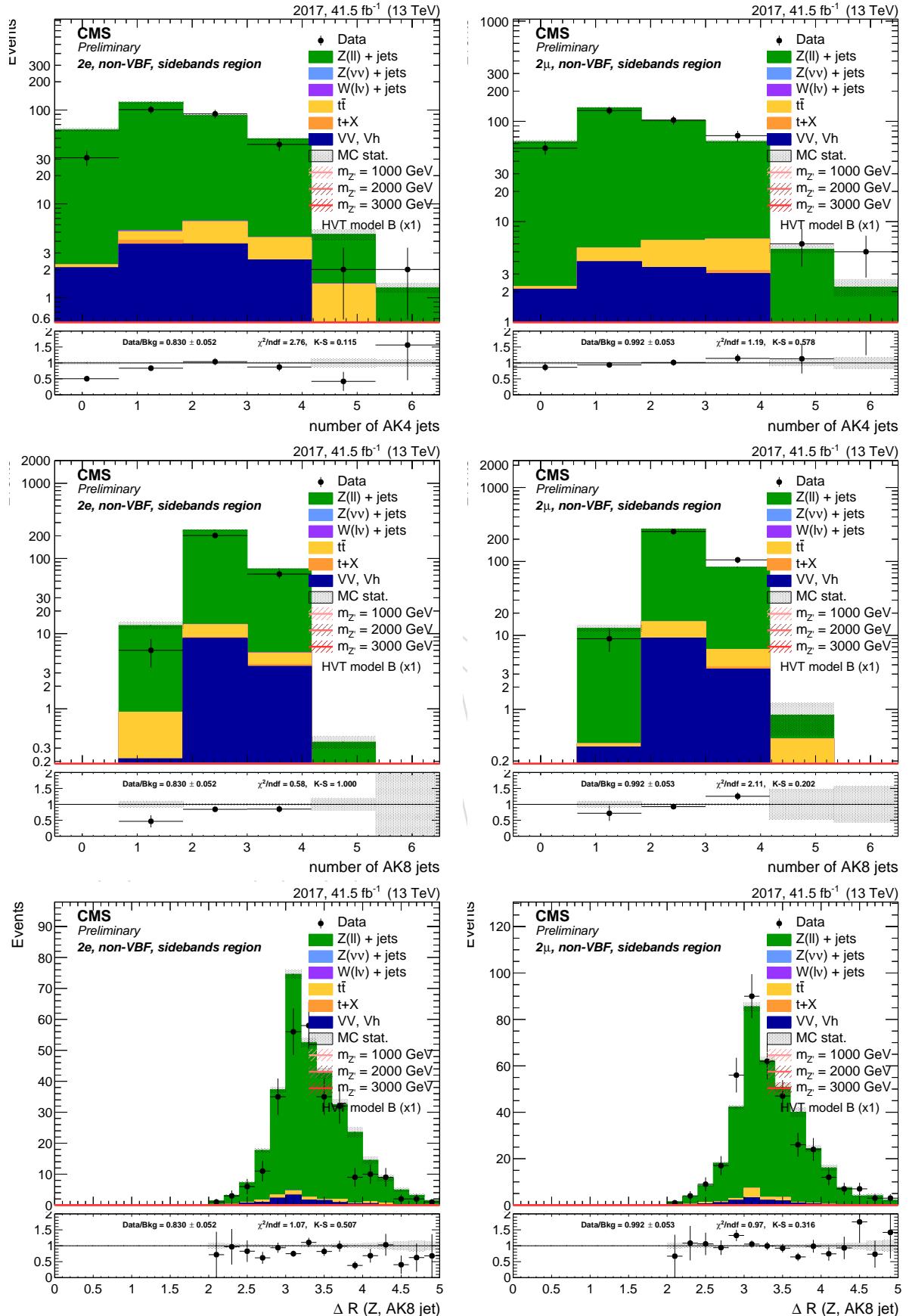


Figure 75: Top: number of AK4 jets. Center: number of AK8 jets. Bottom: ΔR between Z boson and leading AK8 jet. left: di-electron channel. right: di-muon channel. Events are selected with the *inclusive* selection, and simulated backgrounds are normalized to luminosity.

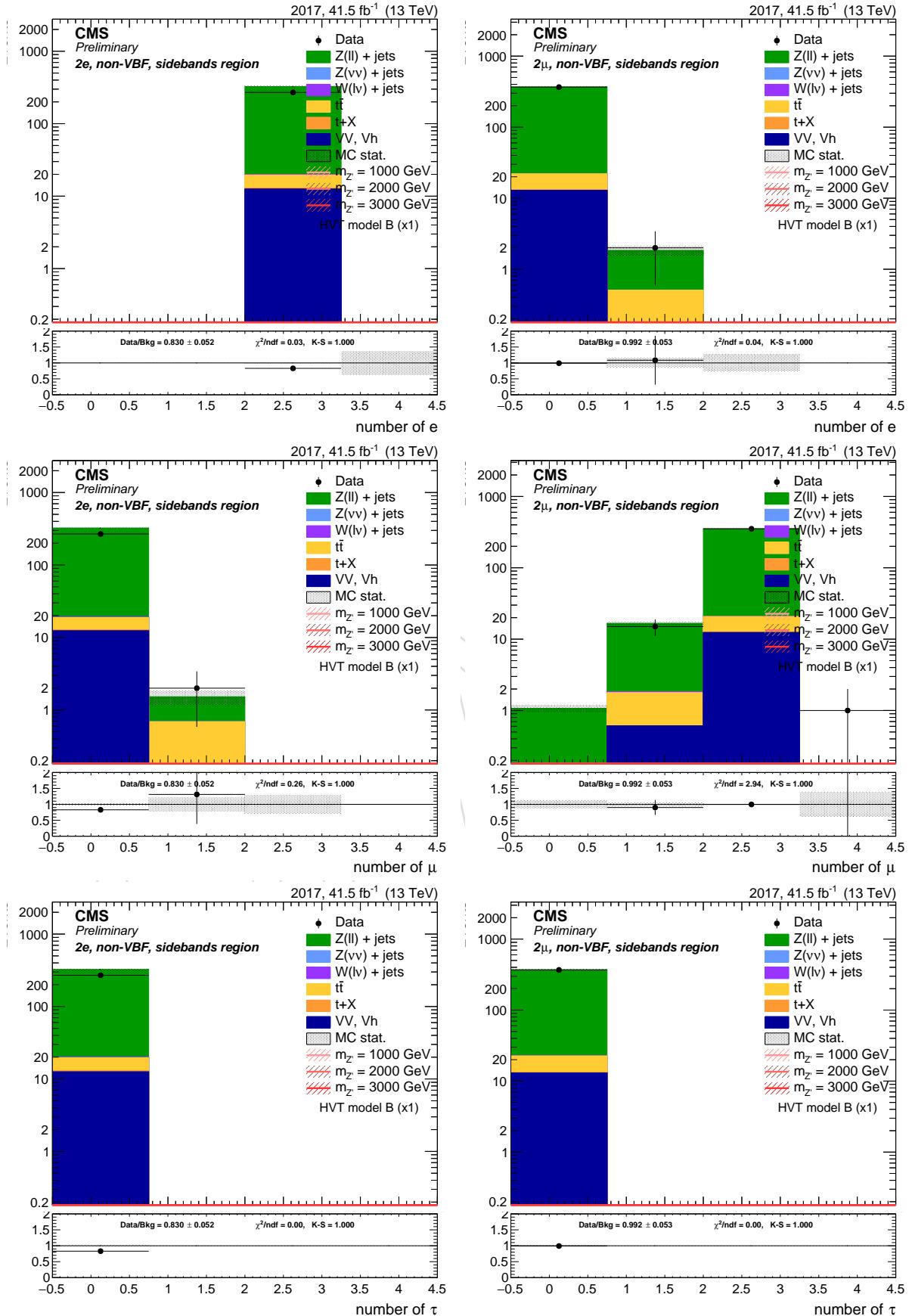


Figure 76: Top: number of electrons. Center: number of muons. Bottom: number of hadronic taus. left: di-electron channel. right: di-muon channel. Events are selected with the *inclusive* selection, and simulated backgrounds are normalized to luminosity.

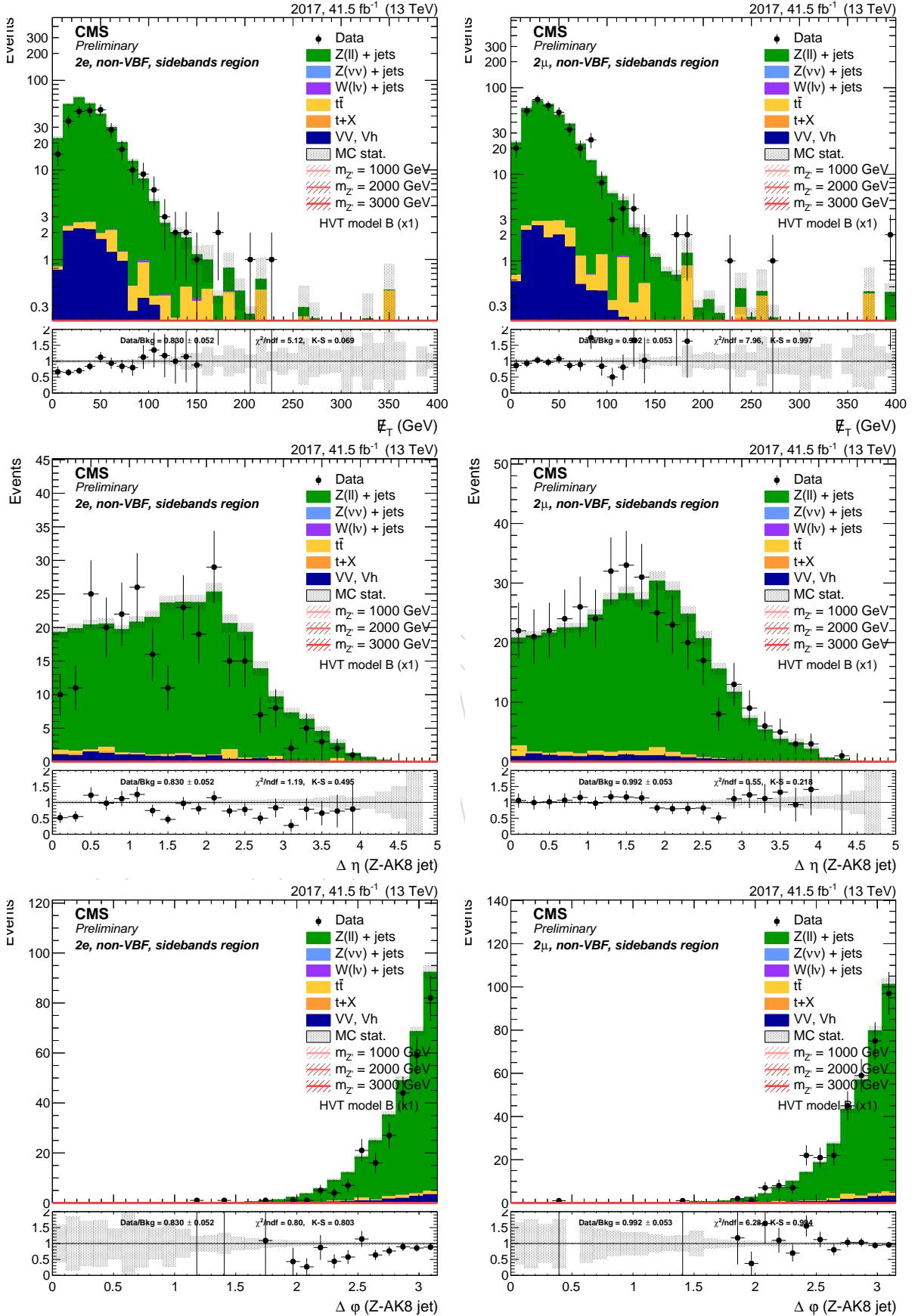


Figure 77: Top: E_T^{miss} . Center: $\Delta\eta$ between the Z and the AK8 jet. Bottom: $\Delta\phi$ between the Z and H candidates. left: di-electron channel. right: di-muon channel. Events are selected with the *inclusive* selection, and simulated backgrounds are normalized to luminosity.

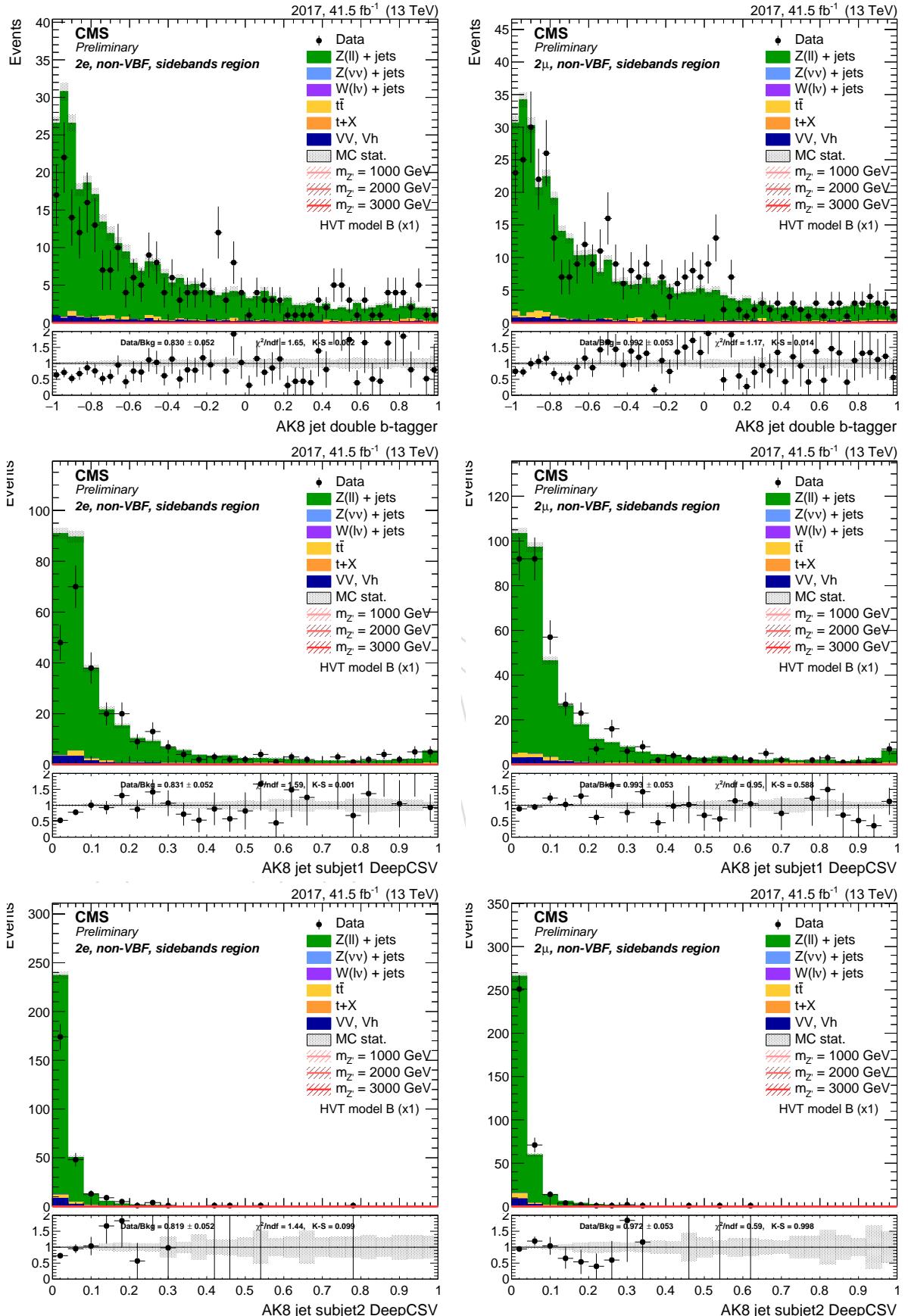


Figure 78: Top: AK8 double-b tagger discriminator . Center: DeepCSV distribution of the leading AK8 sub-jet. Bottom: DeepCSV distribution of the sub-leading AK8 sub-jet. left: di-electron channel. right: di-muon channel. Events are selected with the *inclusive* selection, and simulated backgrounds are normalized to luminosity.

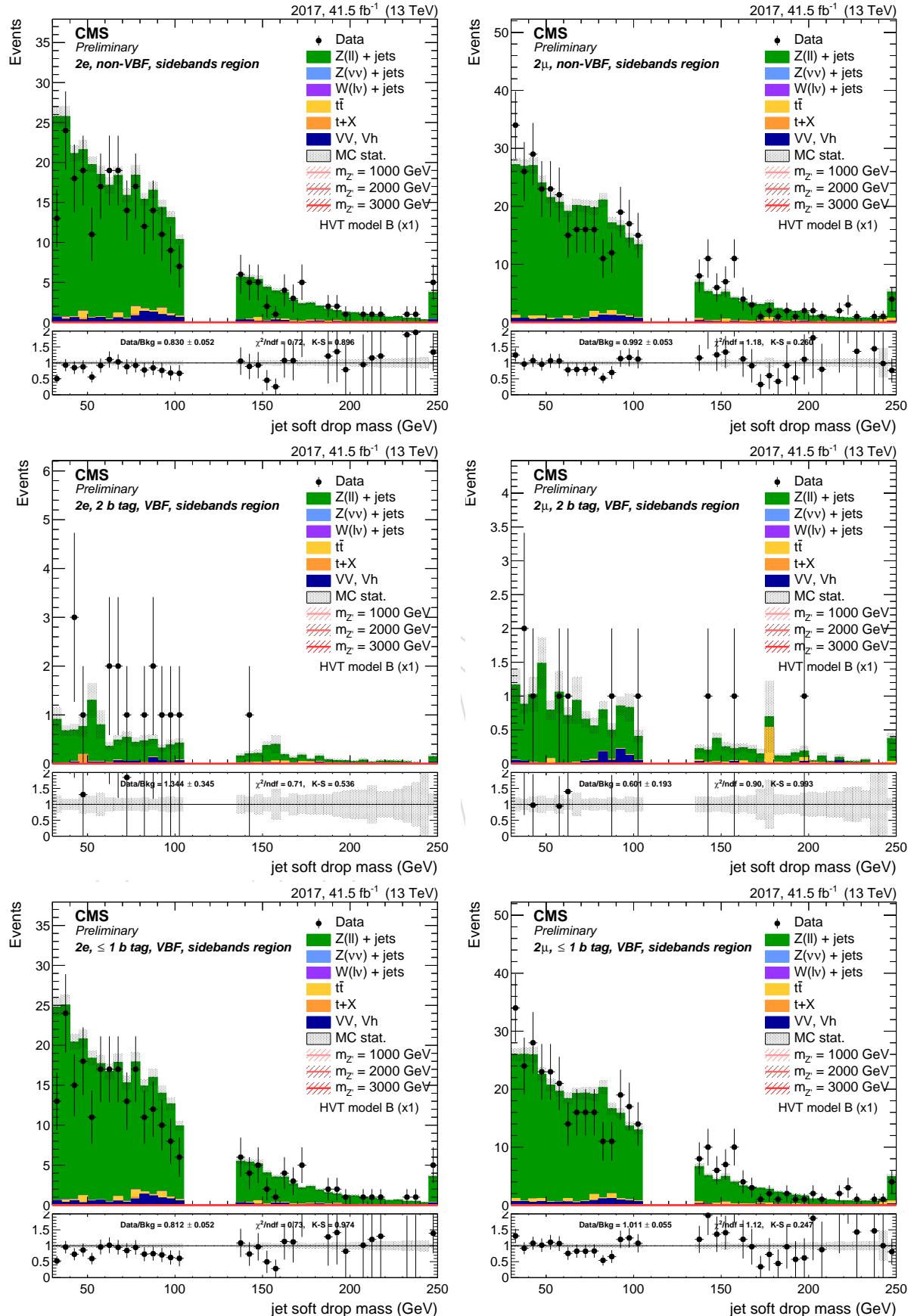


Figure 79: Leading AK8 jet soft drop PUPPI mass. Top: inclusive region. Center: mass sidebands and 2 b-tag category. Bottom: mass sidebands and no b-tag category. left: di-electron channel. right: di-muon channel.

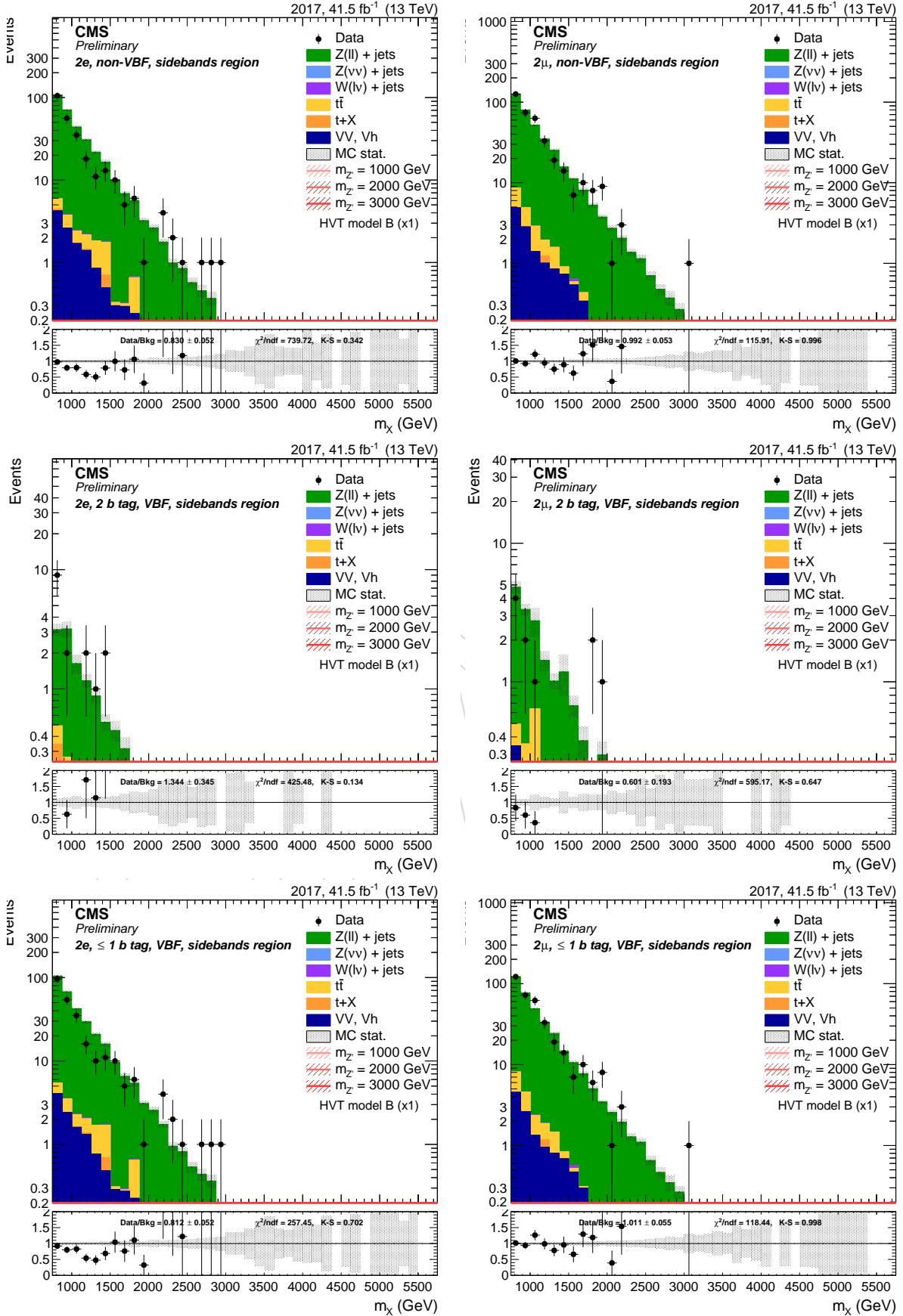


Figure 80: Resonance candidate mass. Top: inclusive region. Center: mass sidebands and 2 b-tag category. Bottom: mass sidebands and no b-tag category. left: di-electron channel. right: di-muon channel.

688 **6.3 2018**689 **6.3.1 Zero lepton channel**

Sample	Events	Entries	%
data_obs	30818.00	30817	121.38
TTbarSL	1727.29	58638	6.80
DYJetsToNuNu_HT	15721.99	360840	61.92
DYJetsToLL_HT	49.10	2399	0.19
ST	242.49	2378	0.96
VV	551.18	83679	2.17
WJetsToLNu_HT	7098.57	90291	27.96
BkgSum	25390.62	598230	100.00
XZH_M1000	526.75	16708	0.00
XZH_M2000	47.14	29398	0.00
XZH_M3000	4.56	31171	0.00

Figure 81: Number of events in the inclusive region of the 0-lepton channel.

DRAFT

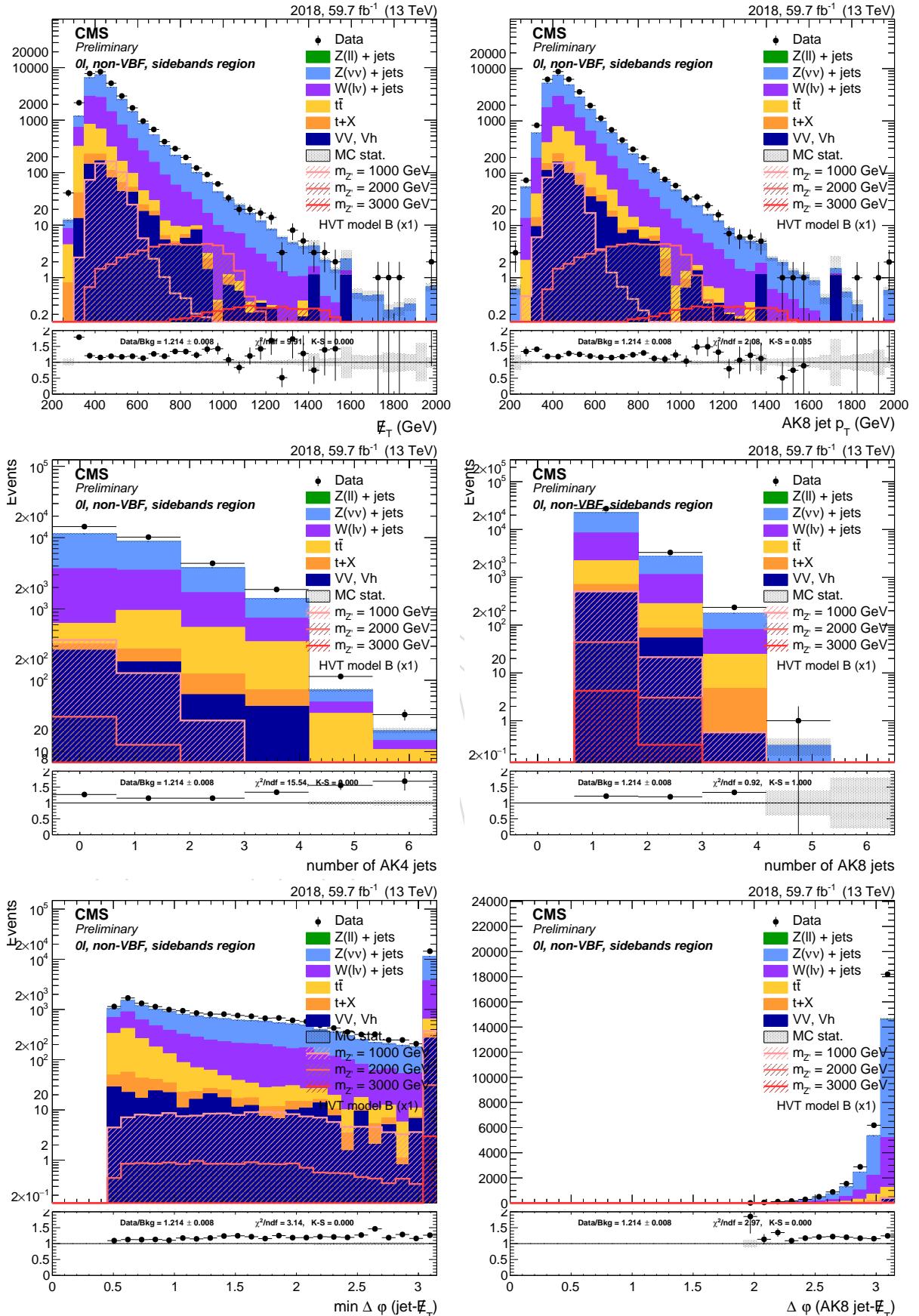


Figure 82: Top: E_T^{miss} (left) and leading AK8 jet p_T (right). Center: number of AK4 jets (left) and AK8 jets (right). Bottom: minimum $\Delta\phi$ between the AK4 jets and E_T^{miss} (left) and $\Delta\phi$ between the AK8 jet and the E_T^{miss} (right). Events are selected with the *inclusive* selection, and simulated backgrounds are normalized to luminosity.

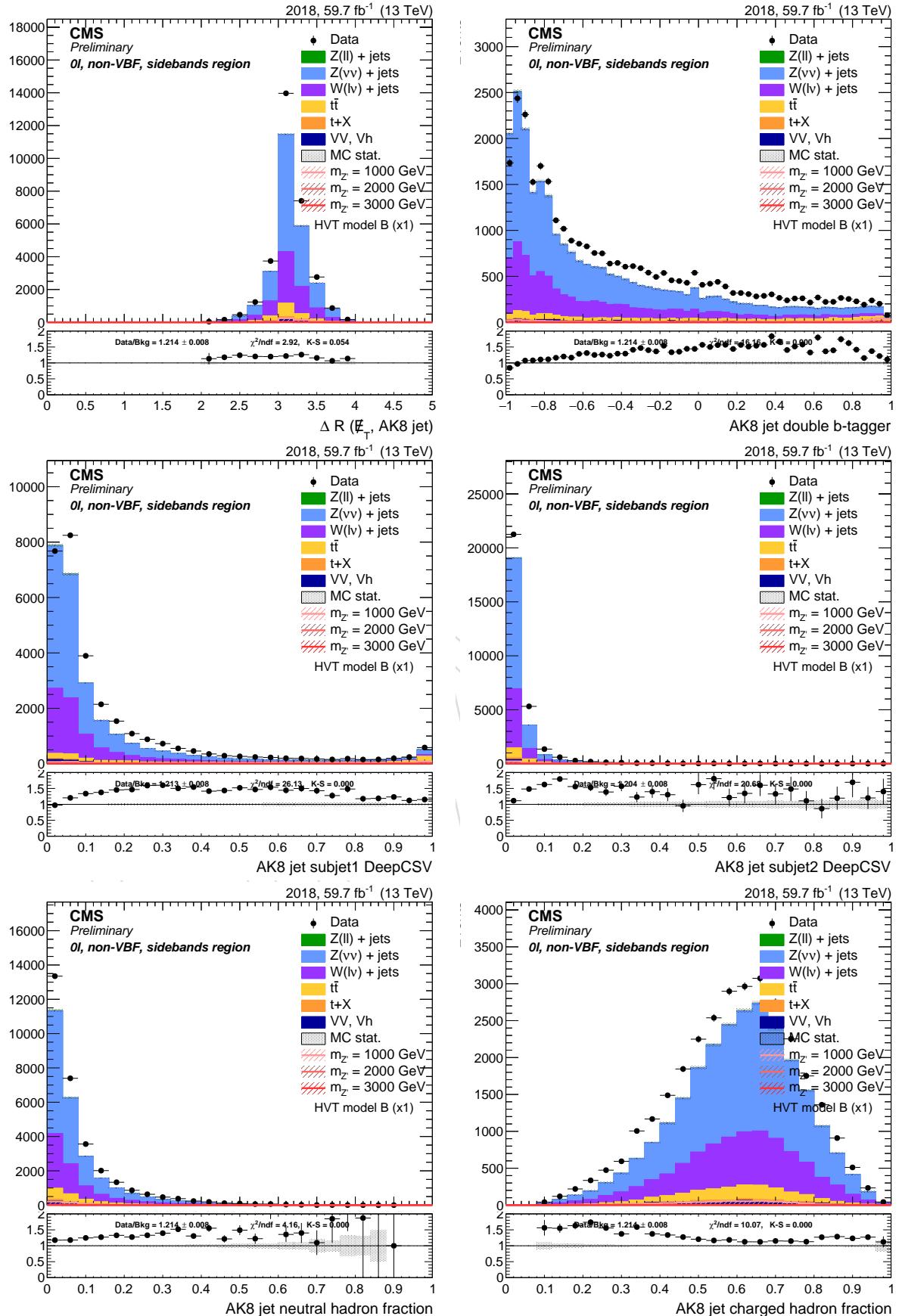


Figure 83: Top: ΔR between Z boson and leading AK8 jet (left), AK8 double-b tagger discriminator (right). Center: DeepCSV distribution of the AK8 sub-jets. Bottom: leading AK8 jet neutral hadron fraction (left) and charged hadron fraction (right). Events are selected with the *inclusive* selection, and simulated backgrounds are normalized to luminosity.

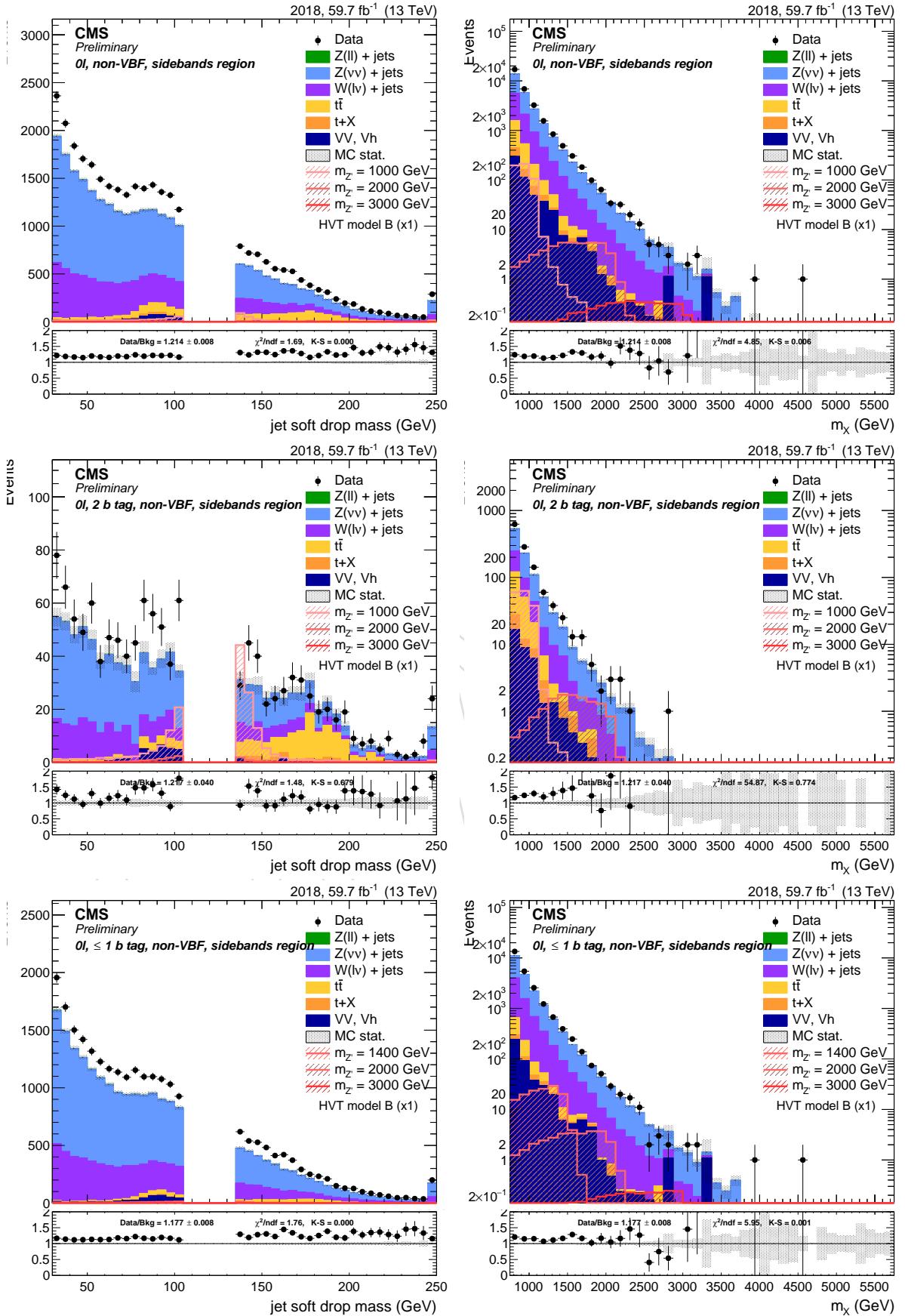


Figure 84: Leading AK8 jet soft drop PUPPI mass (left) and resonance transverse mass (right). Top: inclusive region. Center: mass sidebands and 2 b-tag category. Bottom: mass sidebands and no b-tag category.

690 **6.3.2 Zero lepton channel VBF**

Sample	Events	Entries	%
data_obs	1813.00	1812	113.73
TTbarSL	168.79	7846	10.59
DYJetsToNuNu_HT	899.50	23608	56.42
DYJetsToLL_HT	3.77	222	0.24
ST	25.50	183	1.60
VV	26.41	3420	1.66
WJetsToLNu_HT	470.18	8925	29.49
BkgSum	1594.16	44209	100.00
XZHVBFA_M1000	0.17	2399	0.00
XZHVBFA_M2000	0.01	6768	0.00
XZHVBFA_M3000	0.00	6955	0.00

Figure 85: Number of events in the inclusive region of the 0-lepton channel.

DRAFT

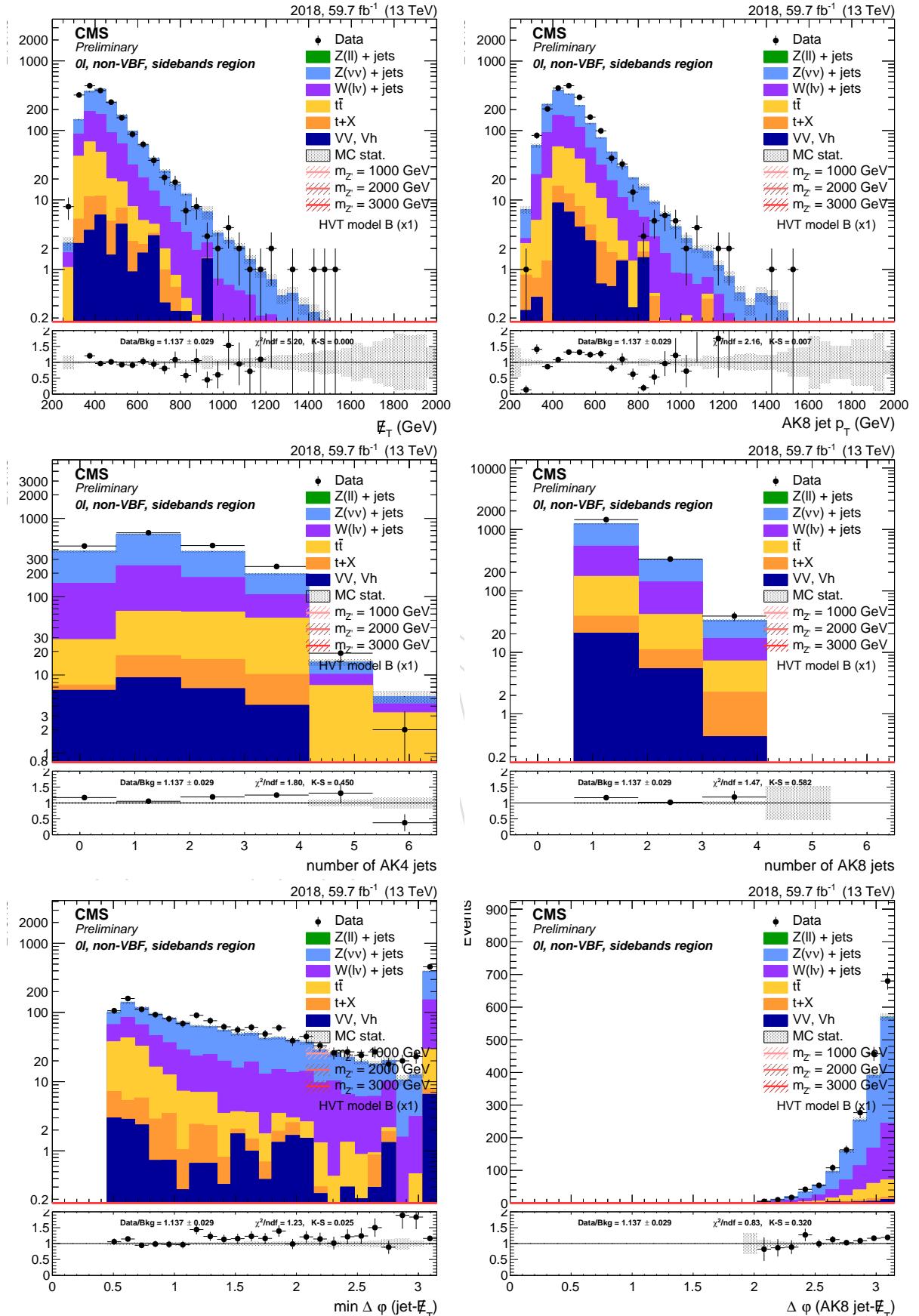


Figure 86: Top: E_T^{miss} (left) and leading AK8 jet p_T (right). Center: number of AK4 jets (left) and AK8 jets (right). Bottom: minimum $\Delta\phi$ between the AK4 jets and AK8 jet in the event (left) and $\Delta\phi$ between the AK8 jet and the E_T^{miss} (right). Events are selected with the *inclusive* selection, and simulated backgrounds are normalized to luminosity.

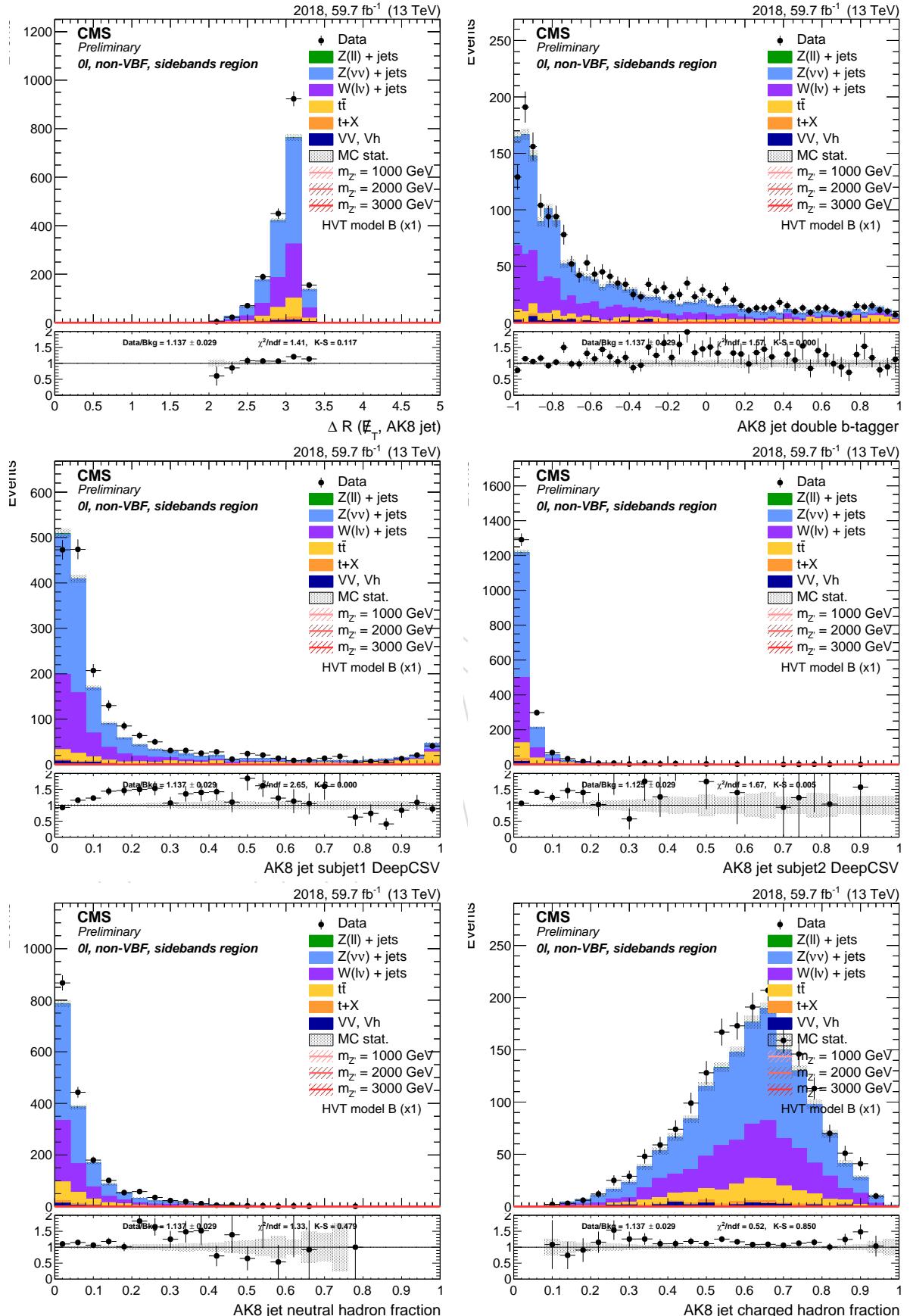


Figure 87: Top: ΔR between Z boson and leading AK8 jet (left), AK8 double-b tagger discriminator (right). Center: DeepCSV distribution of the AK8 sub-jets. Bottom: leading AK8 jet neutral hadron fraction (left) and charged hadron fraction (right). Events are selected with the *inclusive* selection, and simulated backgrounds are normalized to luminosity.

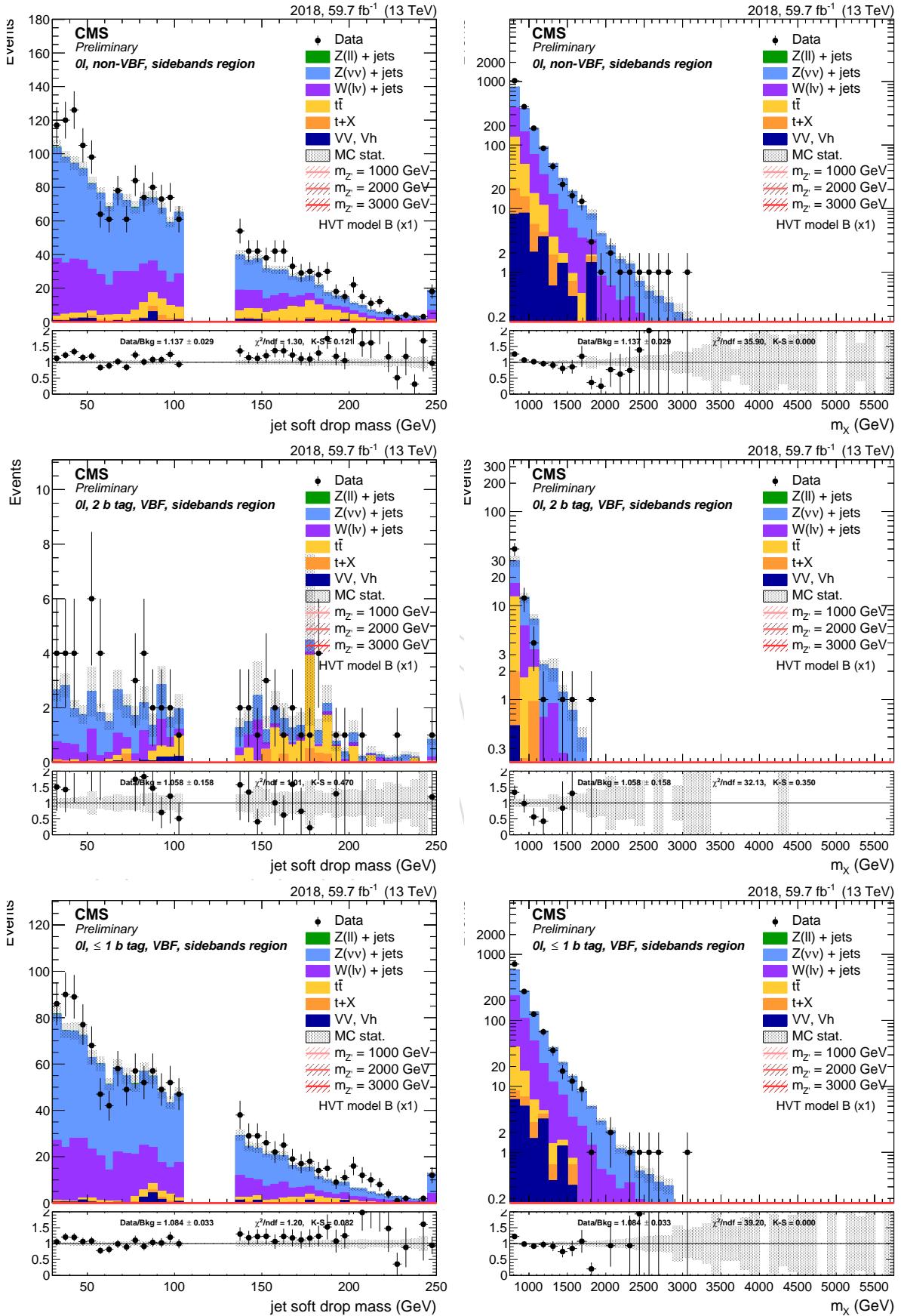


Figure 88: Leading AK8 jet soft drop PUPPI mass (left) and resonance transverse mass (right). Top: inclusive region. Center: mass sidebands and 2 b-tag category. Bottom: mass sidebands and no b-tag category.

691 6.3.3 Dilepton channel

Sample	Events	Entries	%	Sample	Events	Entries	%
data_obs	3379.00	3378	104.75	data_obs	3786.00	3785	101.87
TTbarSL	40.57	18920	1.26	TTbarSL	47.35	22124	1.27
DYJetsToNuNu_HT	0.00	-1	0.00	DYJetsToNuNu_HT	0.00	-1	0.00
DYJetsToLL_HT	3027.14	154946	93.84	DYJetsToLL_HT	3495.44	183938	94.05
ST	2.13	8	0.07	ST	2.36	13	0.06
VV	152.38	22907	4.72	VV	170.71	26771	4.59
WJetsToLNu_HT	3.64	114	0.11	WJetsToLNu_HT	0.72	46	0.02
BkgSum	3225.85	196899	100.00	BkgSum	3716.58	232896	100.00
XZH_M1000	110.45	7058	0.00	XZH_M1000	127.88	8479	0.00
XZH_M2000	6.56	8111	0.00	XZH_M2000	6.00	7904	0.00
XZH_M3000	0.57	7652	0.00	XZH_M3000	0.47	6816	0.00

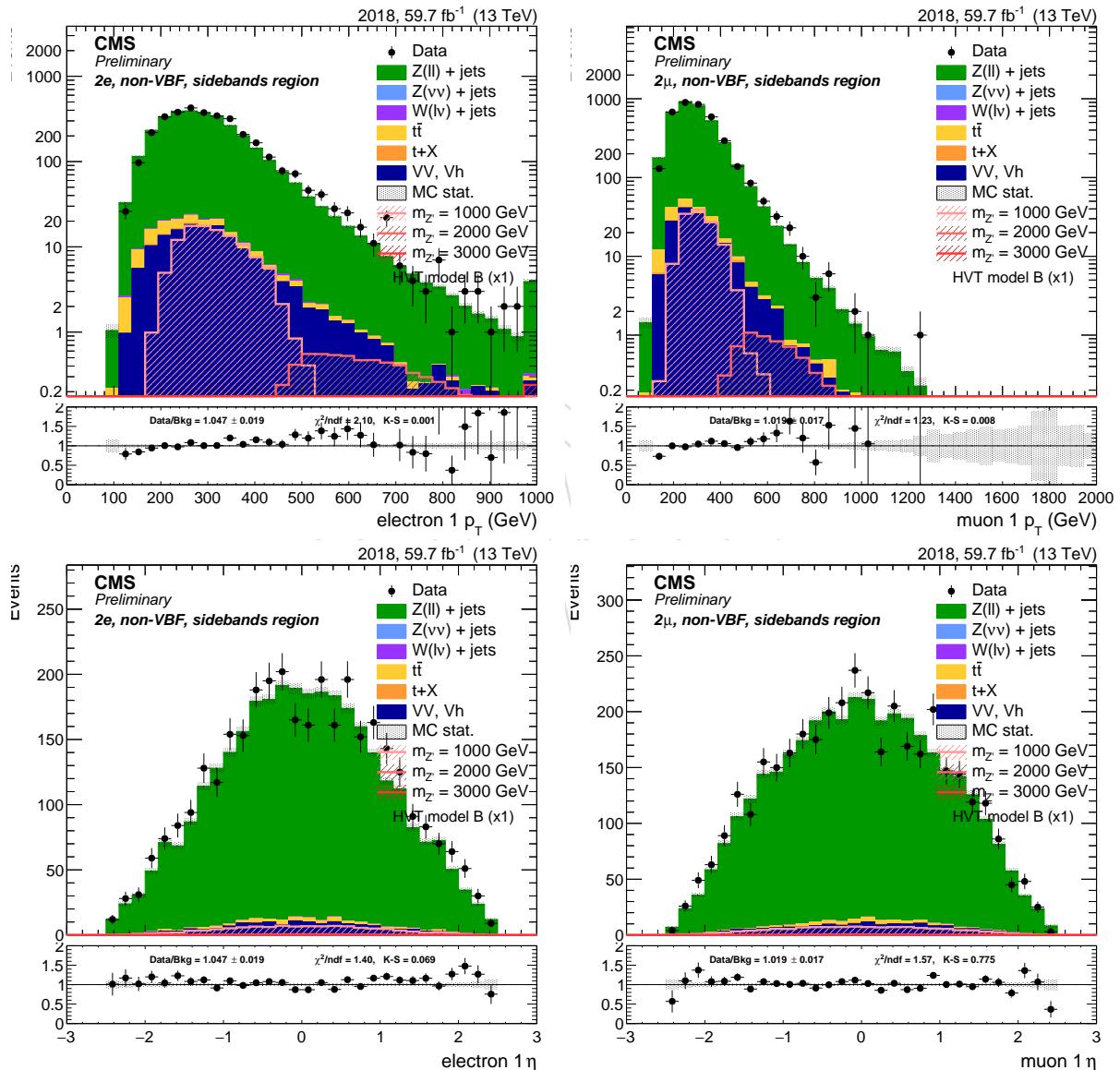


Figure 89: Leading lepton p_T (top) and η (bottom) for di-electron (left) and di-muon (right) channel. Events are selected with the *inclusive* selection, and simulated backgrounds are normalized to luminosity.

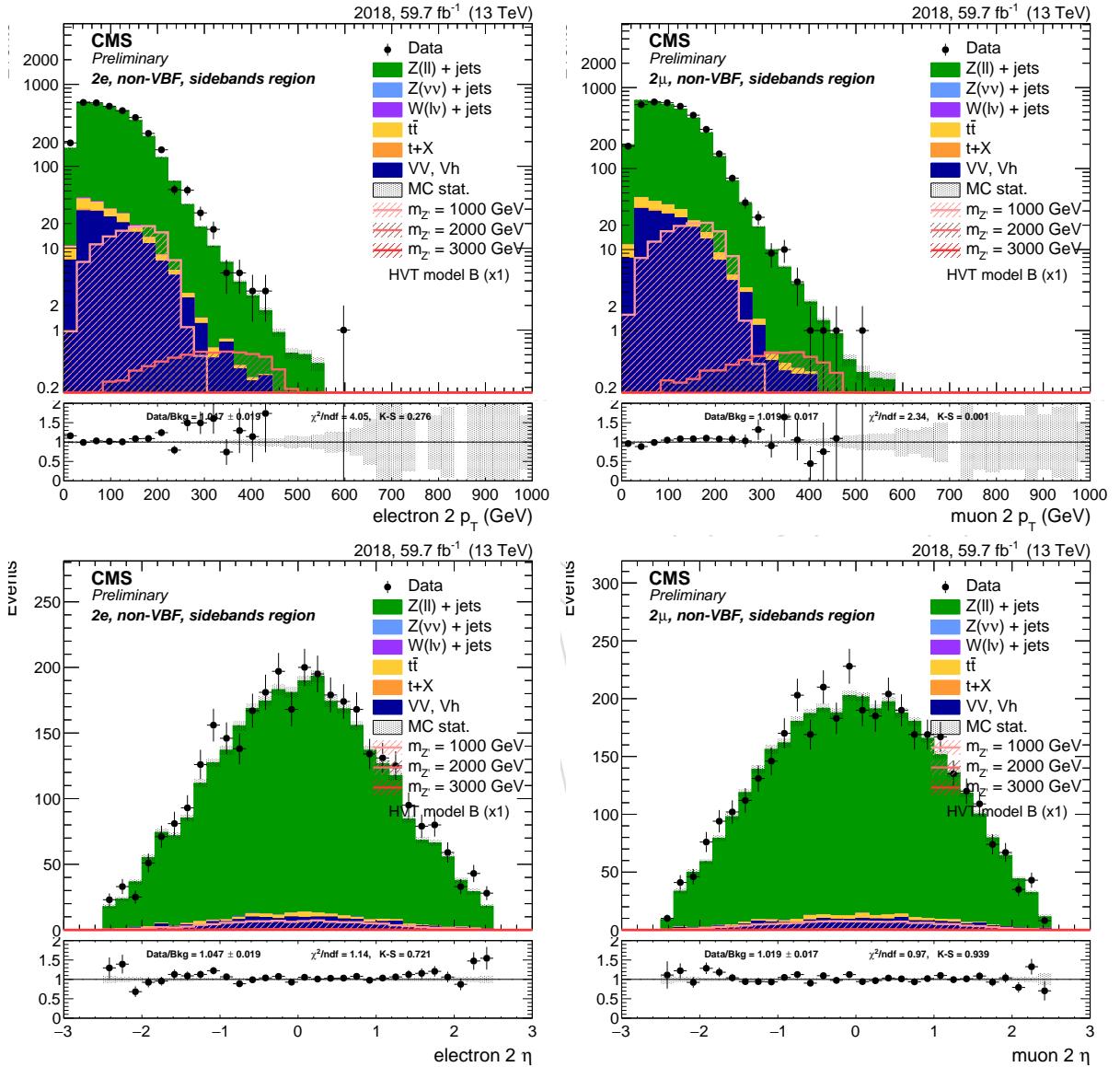


Figure 90: Sub-leading lepton p_T (top) and η (bottom) for di-electron (left) and di-muon (right) channel. Events are selected with the *inclusive* selection, and simulated backgrounds are normalized to luminosity.

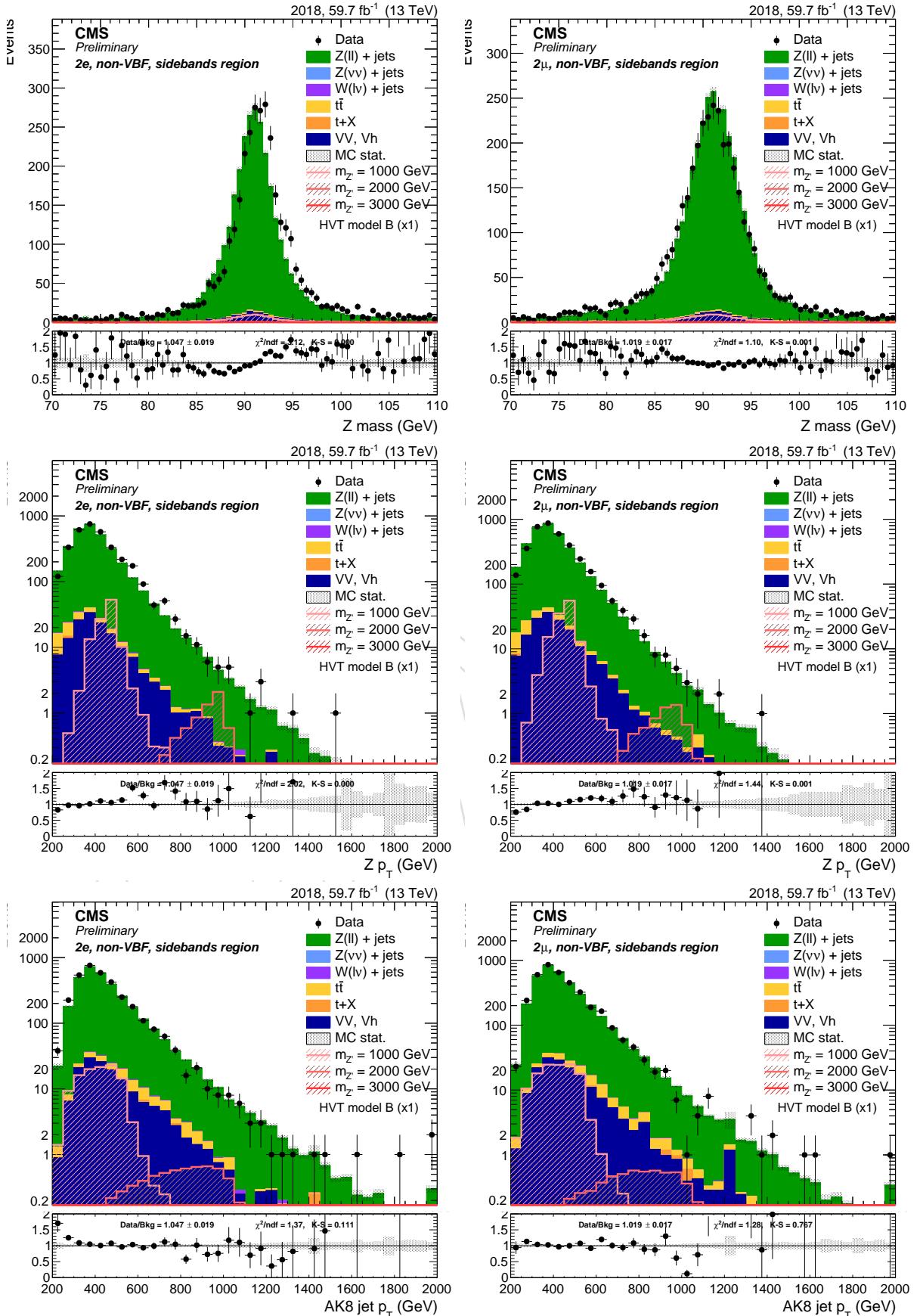


Figure 91: Top: Z candidate mass. Center: Z candidate p_T . Bottom: leading AK8 jet p_T . left: di-electron channel. right: di-muon channel. Events are selected with the *inclusive* selection, and simulated backgrounds are normalized to luminosity.

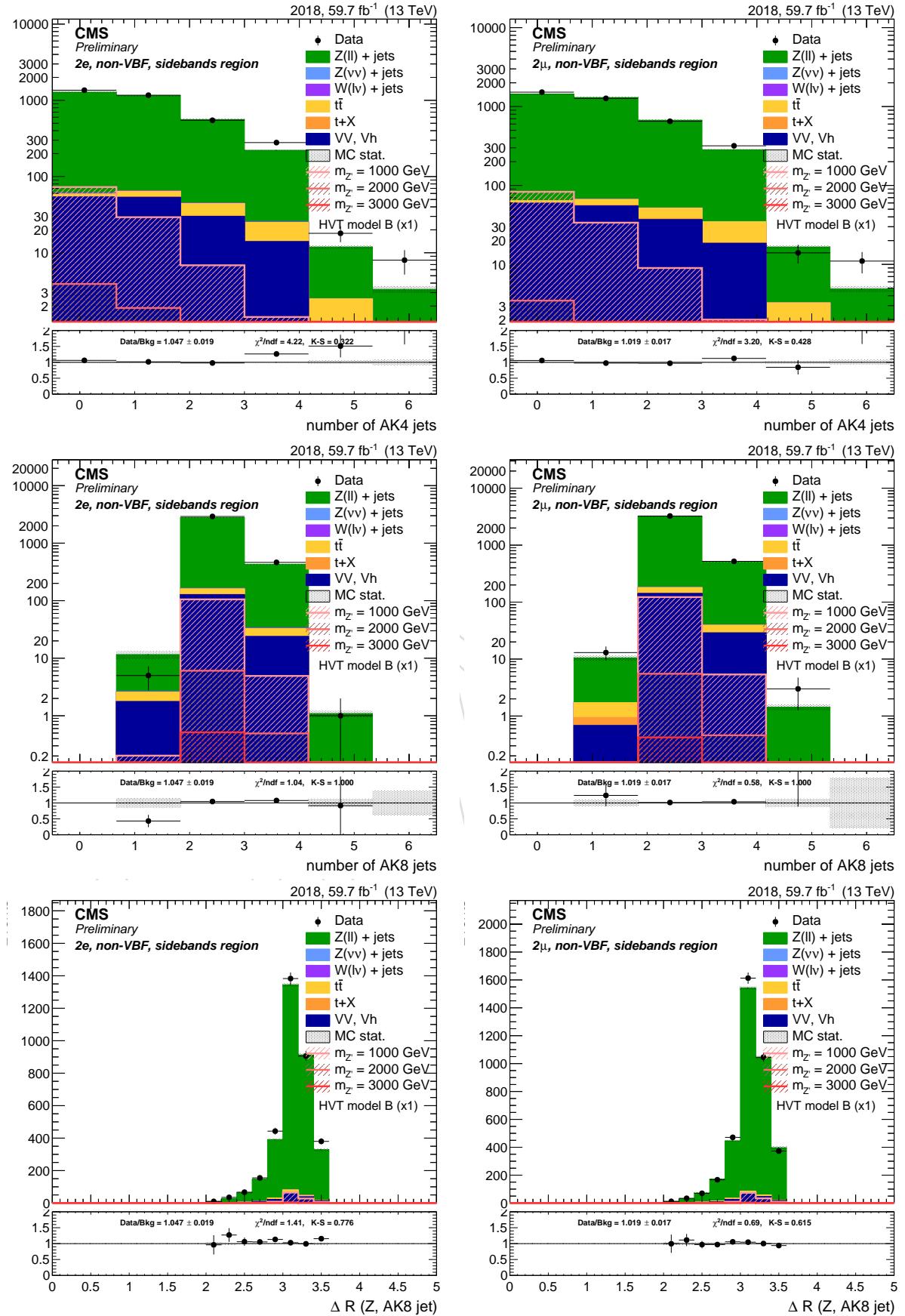


Figure 92: Top: number of AK4 jets. Center: number of AK8 jets. Bottom: ΔR between Z boson and leading AK8 jet. left: di-electron channel. right: di-muon channel. Events are selected with the *inclusive* selection, and simulated backgrounds are normalized to luminosity.

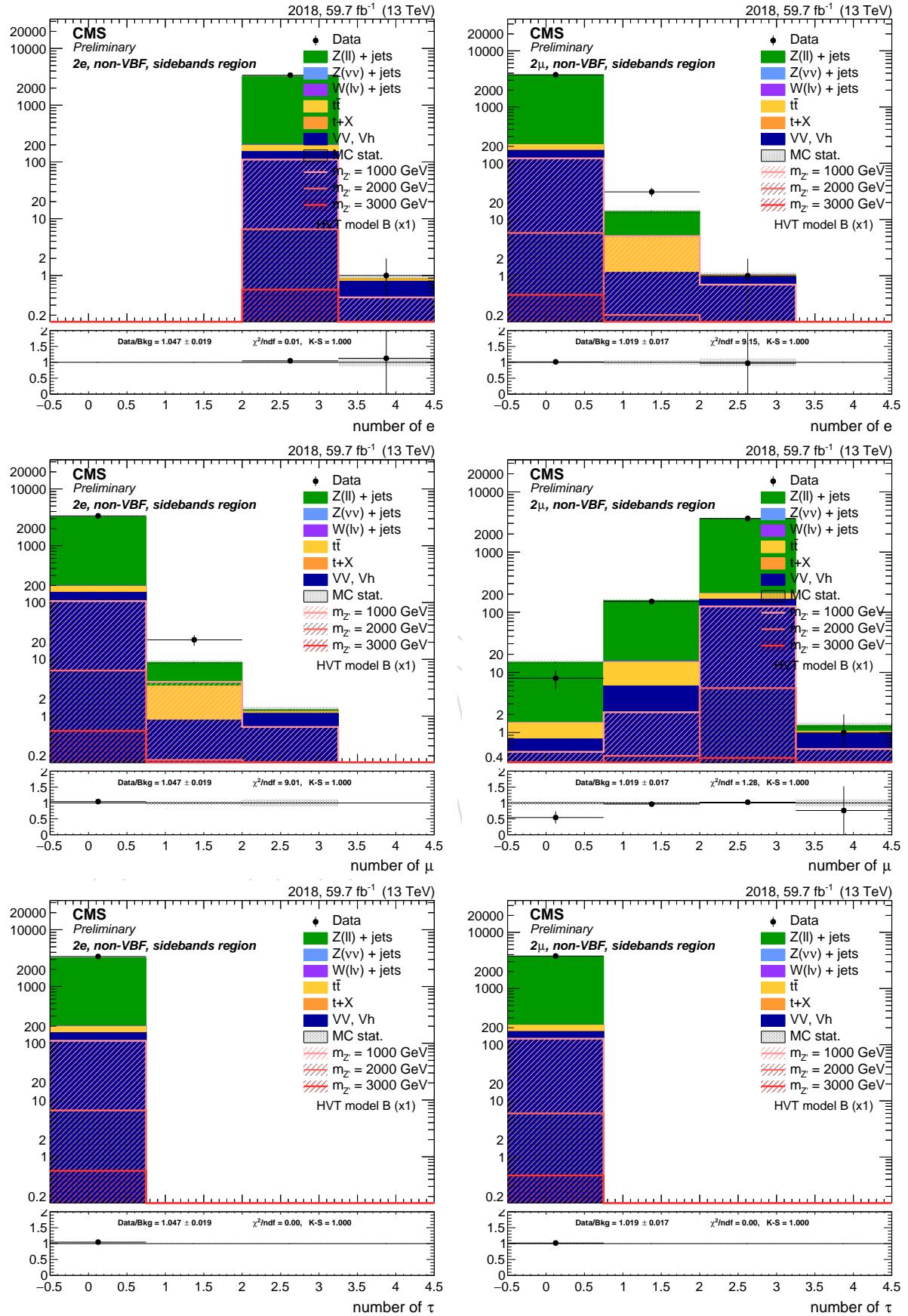


Figure 93: Top: number of electrons. Center: number of muons. Bottom: number of hadronic taus. left: di-electron channel. right: di-muon channel. Events are selected with the *inclusive* selection, and simulated backgrounds are normalized to luminosity.

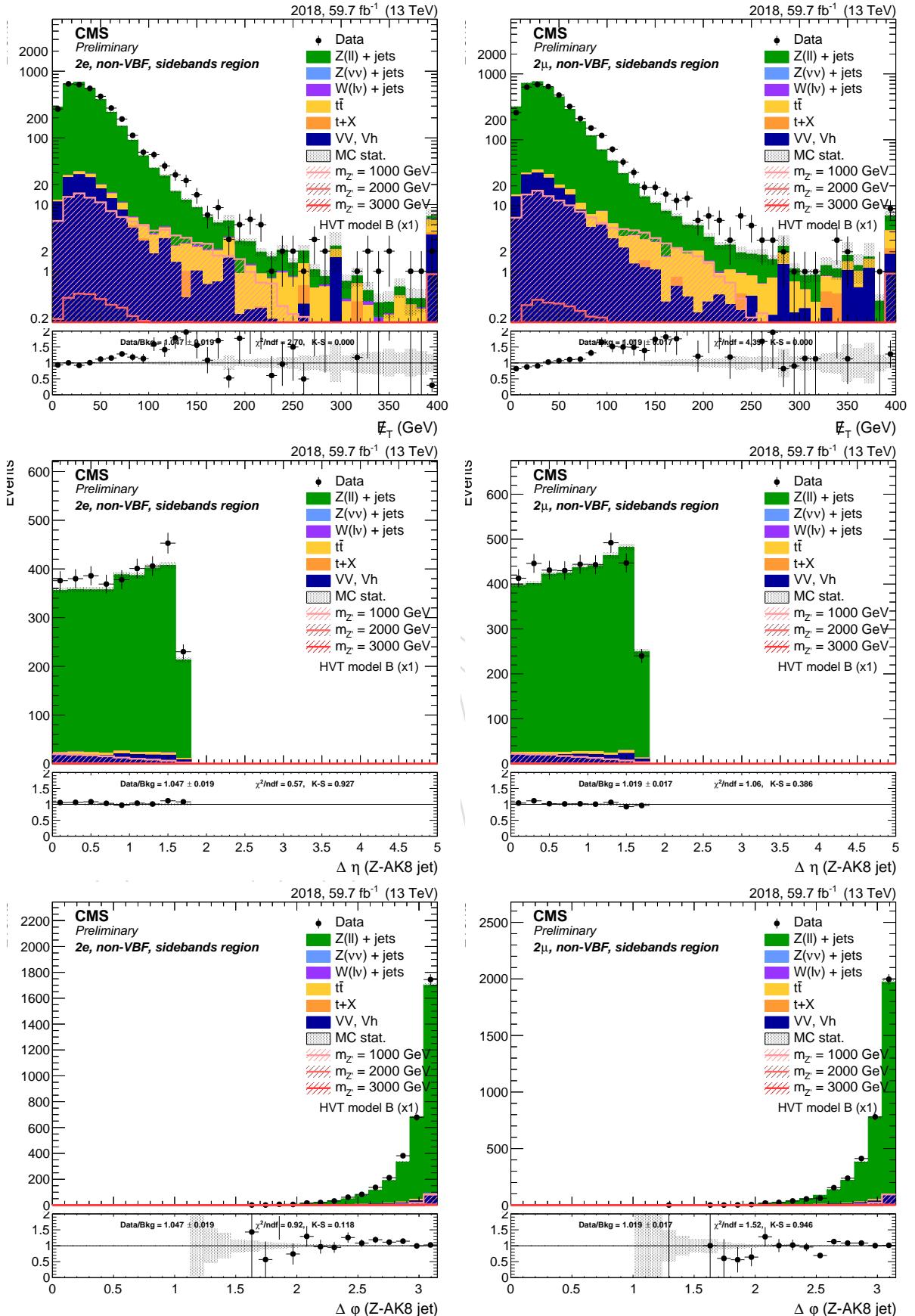


Figure 94: Top: E_T^{miss} . Center: $\Delta\eta$ between the Z and the AK8 jet. Bottom: $\Delta\phi$ between the Z and H candidates. left: di-electron channel. right: di-muon channel. Events are selected with the *inclusive* selection, and simulated backgrounds are normalized to luminosity.

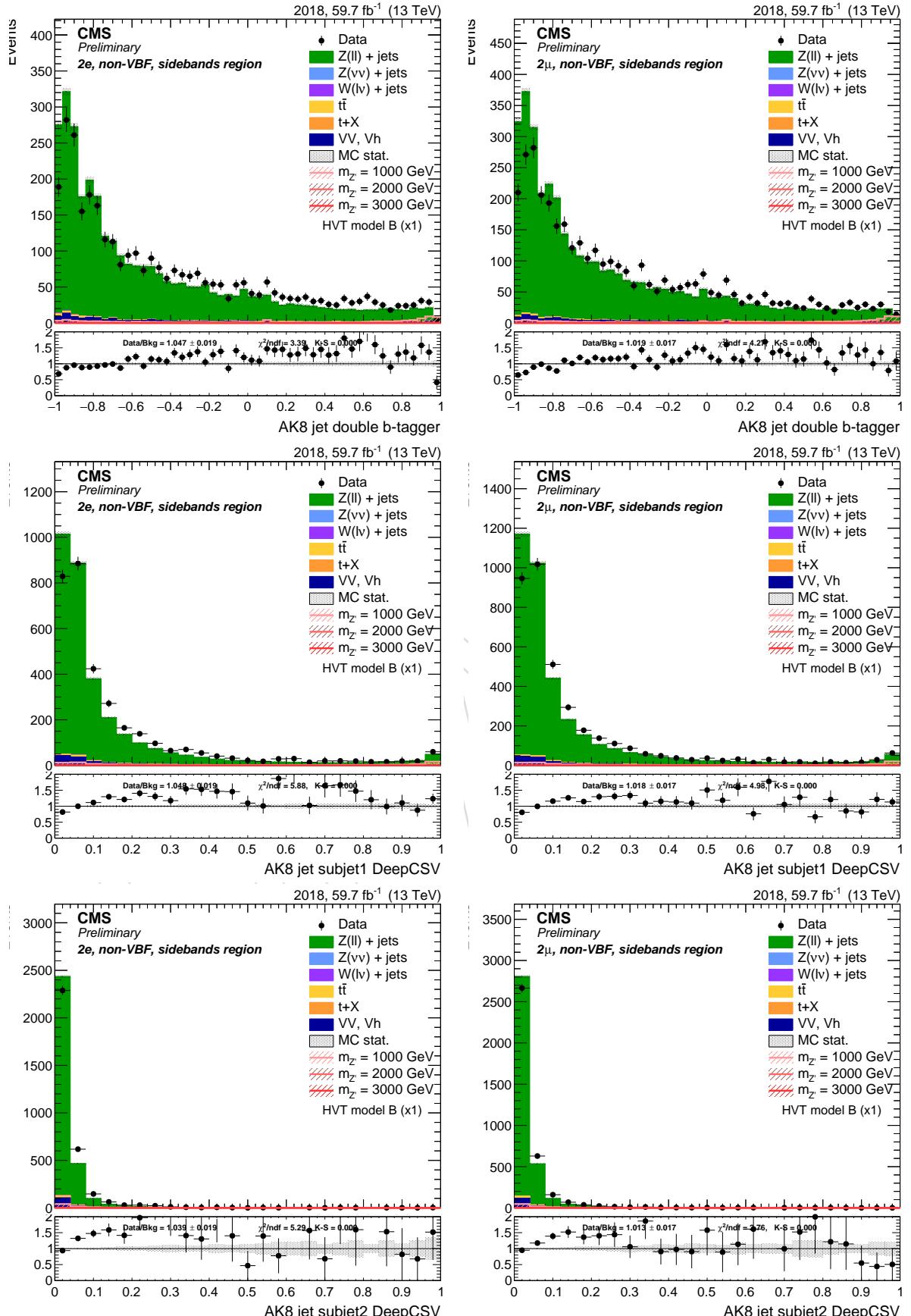


Figure 95: Top: AK8 double-b tagger discriminator . Center: DeepCSV distribution of the leading AK8 sub-jet. Bottom: DeepCSV distribution of the sub-leading AK8 sub-jet. left: di-electron channel. right: di-muon channel. Events are selected with the *inclusive* selection, and simulated backgrounds are normalized to luminosity.

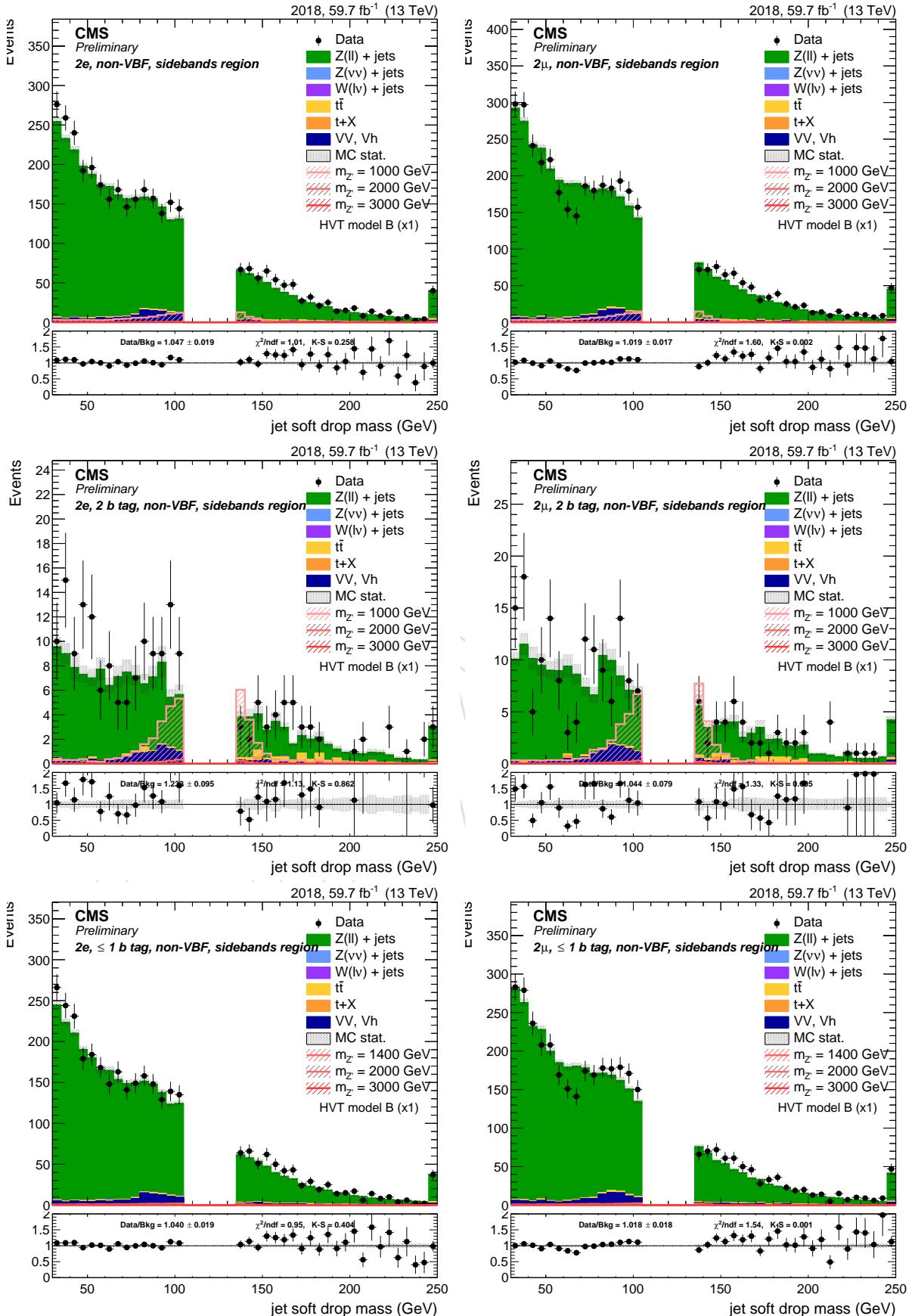


Figure 96: Leading AK8 jet soft drop PUPPI mass. Top: inclusive region. Center: mass sidebands and 2 b-tag category. Bottom: mass sidebands and no b-tag category. left: di-electron channel. right: di-muon channel.

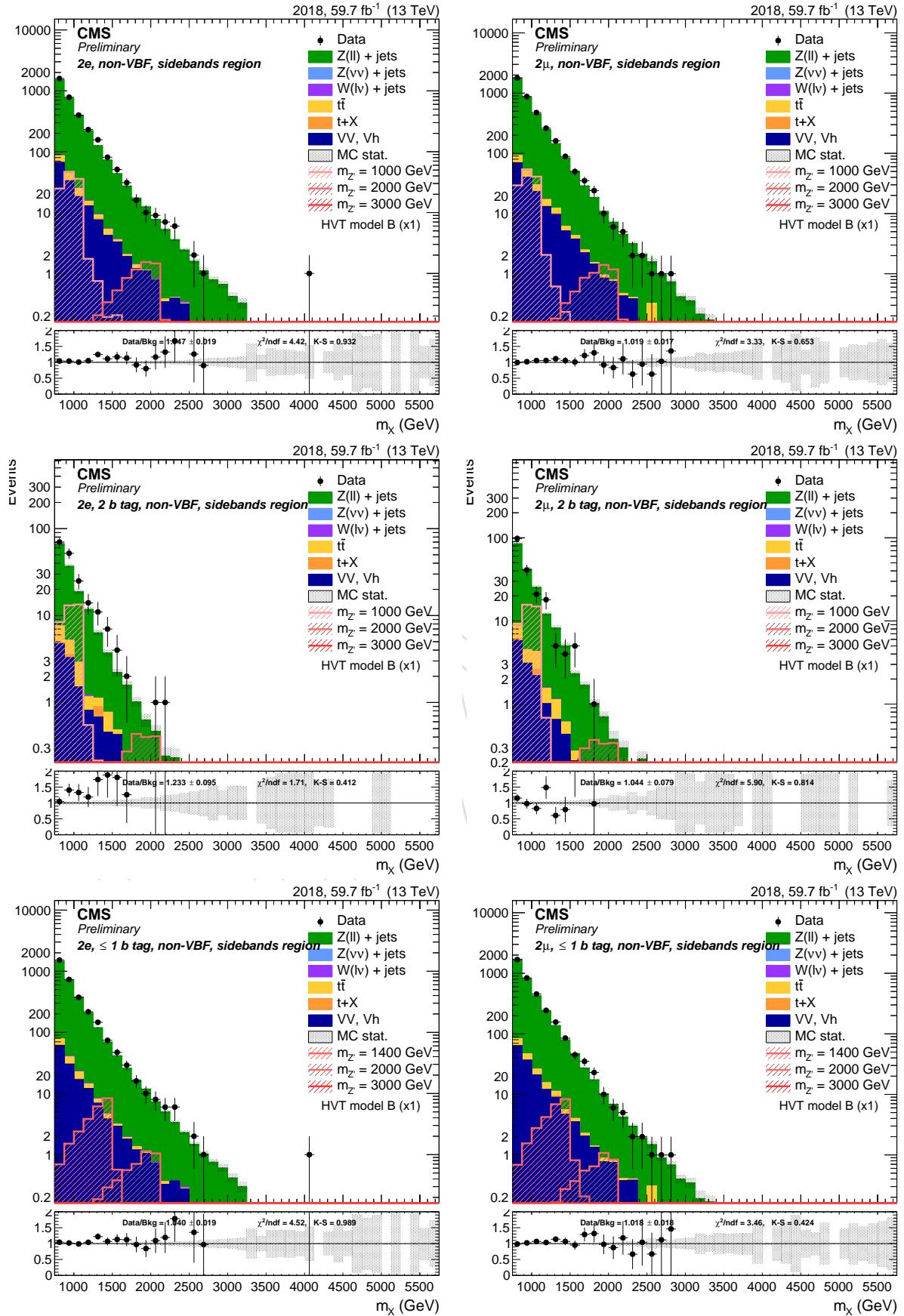


Figure 97: Resonance candidate mass. Top: inclusive region. Center: mass sidebands and 2 b-tag category. Bottom: mass sidebands and no b-tag category. left: di-electron channel. right: di-muon channel.

6.3.4 Dilepton channel VBF

Sample	Events	Entries	%
data_obs	395.00	394	79.45
TTbarSL	9.80	4997	1.97
DYJetsToNuNu_HT	0.00	-1	0.00
DYJetsToLL_HT	467.51	24815	94.04
ST	0.71	3	0.14
VV	18.67	2395	3.75
WJetsToLNu_HT	0.47	13	0.10
BkgSum	497.16	32227	100.00
XZHVBFA_M1000	0.09	2467	0.00
XZHVBFA_M2000	0.00	3693	0.00
XZHVBFA_M3000	0.00	3670	0.00

Sample	Events	Entries	%
data_obs	461.00	460	76.79
TTbarSL	12.85	6004	2.14
DYJetsToNuNu_HT	0.00	-1	0.00
DYJetsToLL_HT	563.55	29981	93.87
ST	0.43	1	0.07
VV	23.52	2863	3.92
WJetsToLNu_HT	0.02	3	0.00
BkgSum	600.37	38856	100.00
XZHVBFA_M1000	0.10	2860	0.00
XZHVBFA_M2000	0.00	4195	0.00
XZHVBFA_M3000	0.00	3621	0.00

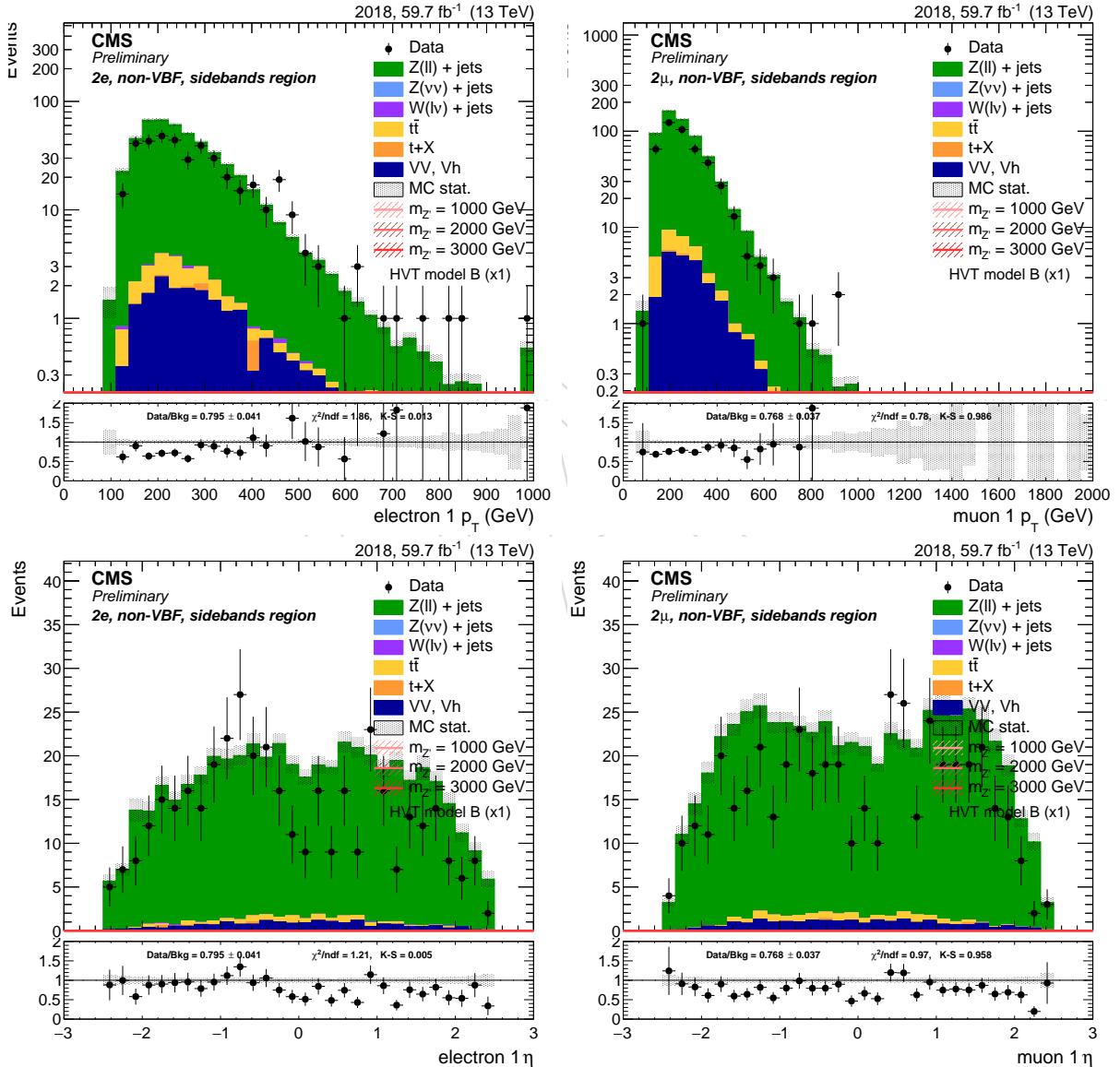


Figure 98: Leading lepton p_T (top) and η (bottom) for di-electron (left) and di-muon (right) channel. Events are selected with the *inclusive* selection, and simulated backgrounds are normalized to luminosity.

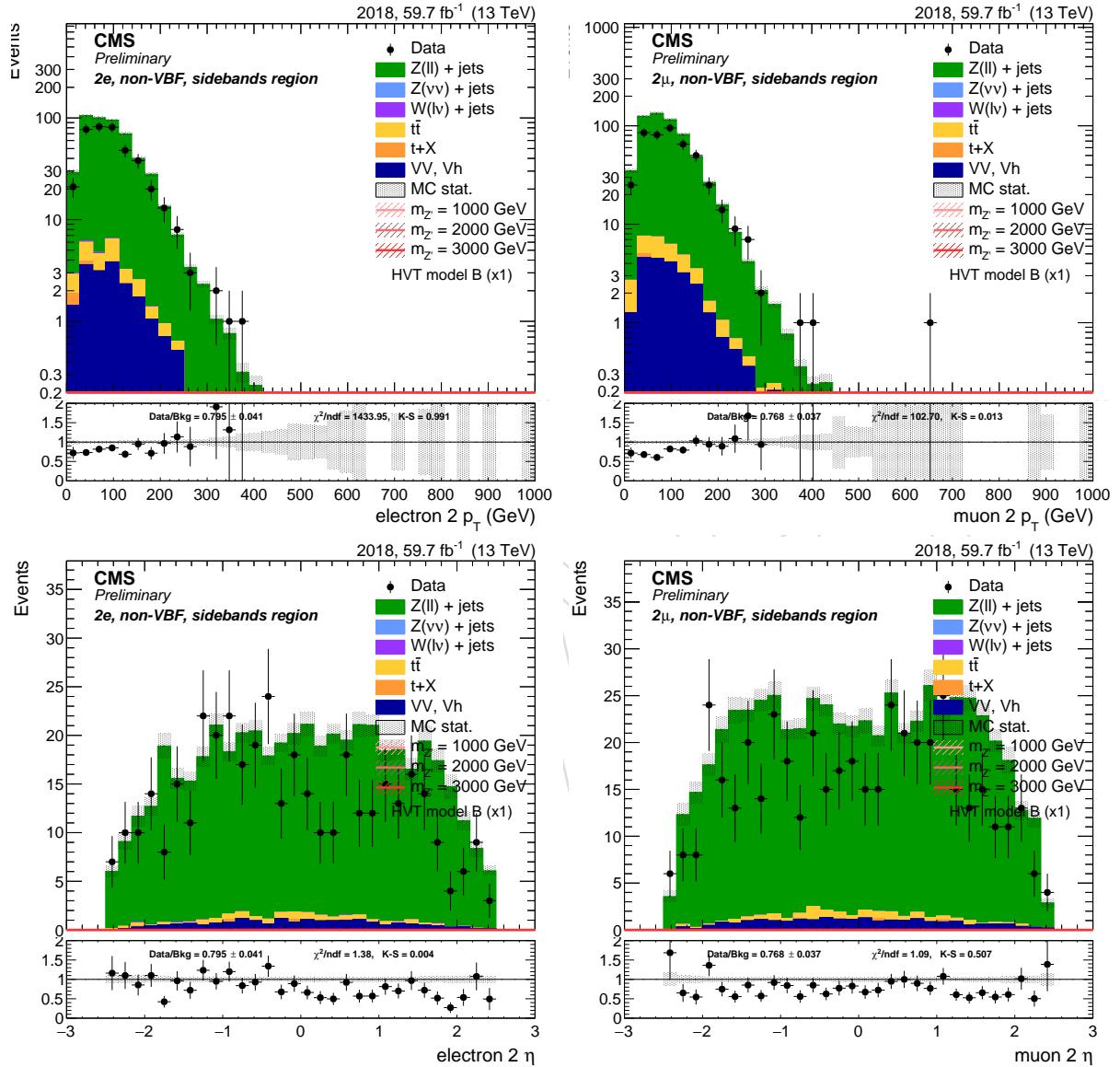


Figure 99: Sub-leading lepton p_T (top) and η (bottom) for di-electron (left) and di-muon (right) channel. Events are selected with the *inclusive* selection, and simulated backgrounds are normalized to luminosity.

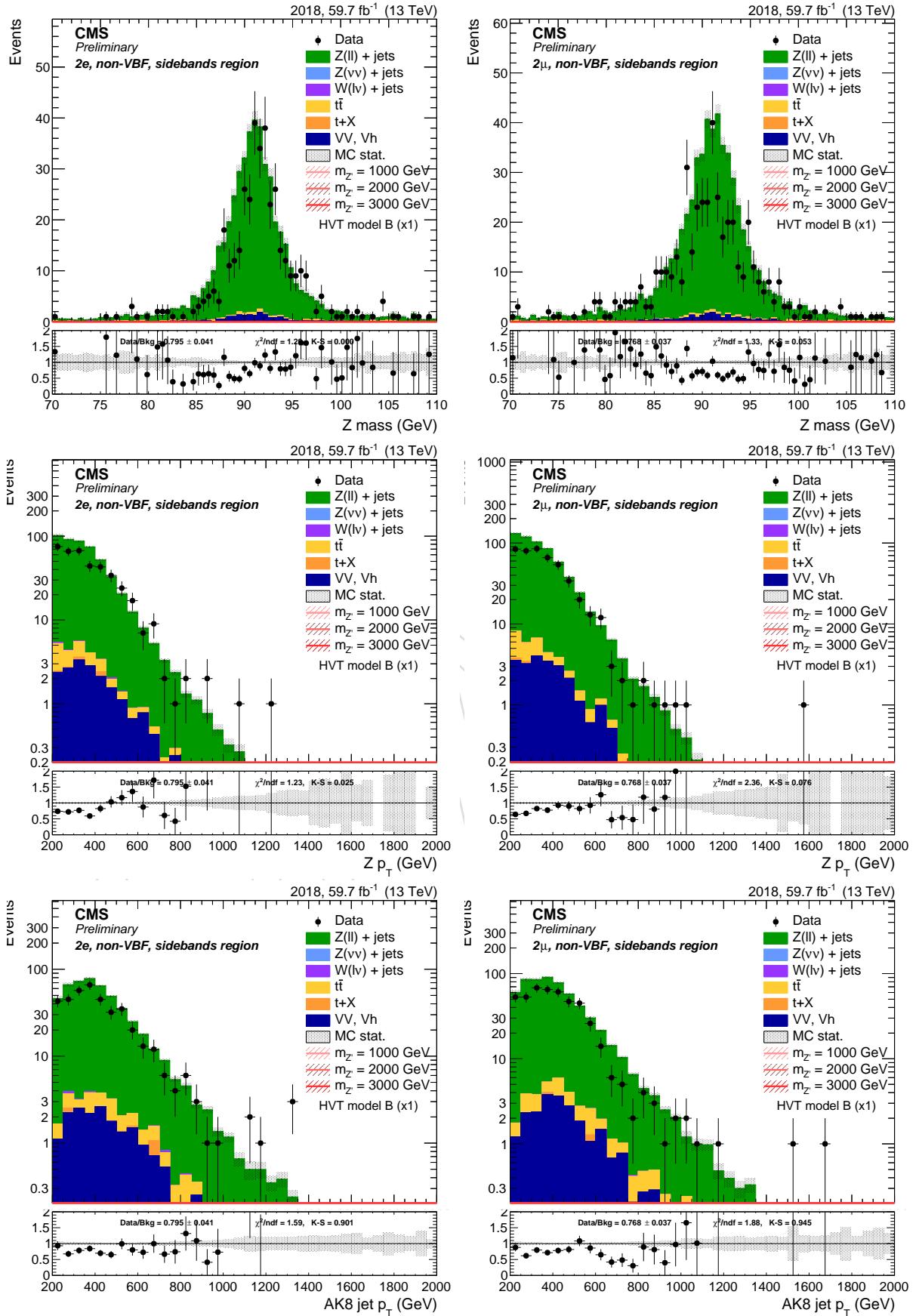


Figure 100: Top: Z candidate mass. Center: Z candidate p_T . Bottom: leading AK8 jet p_T . left: di-electron channel. right: di-muon channel. Events are selected with the *inclusive* selection, and simulated backgrounds are normalized to luminosity.

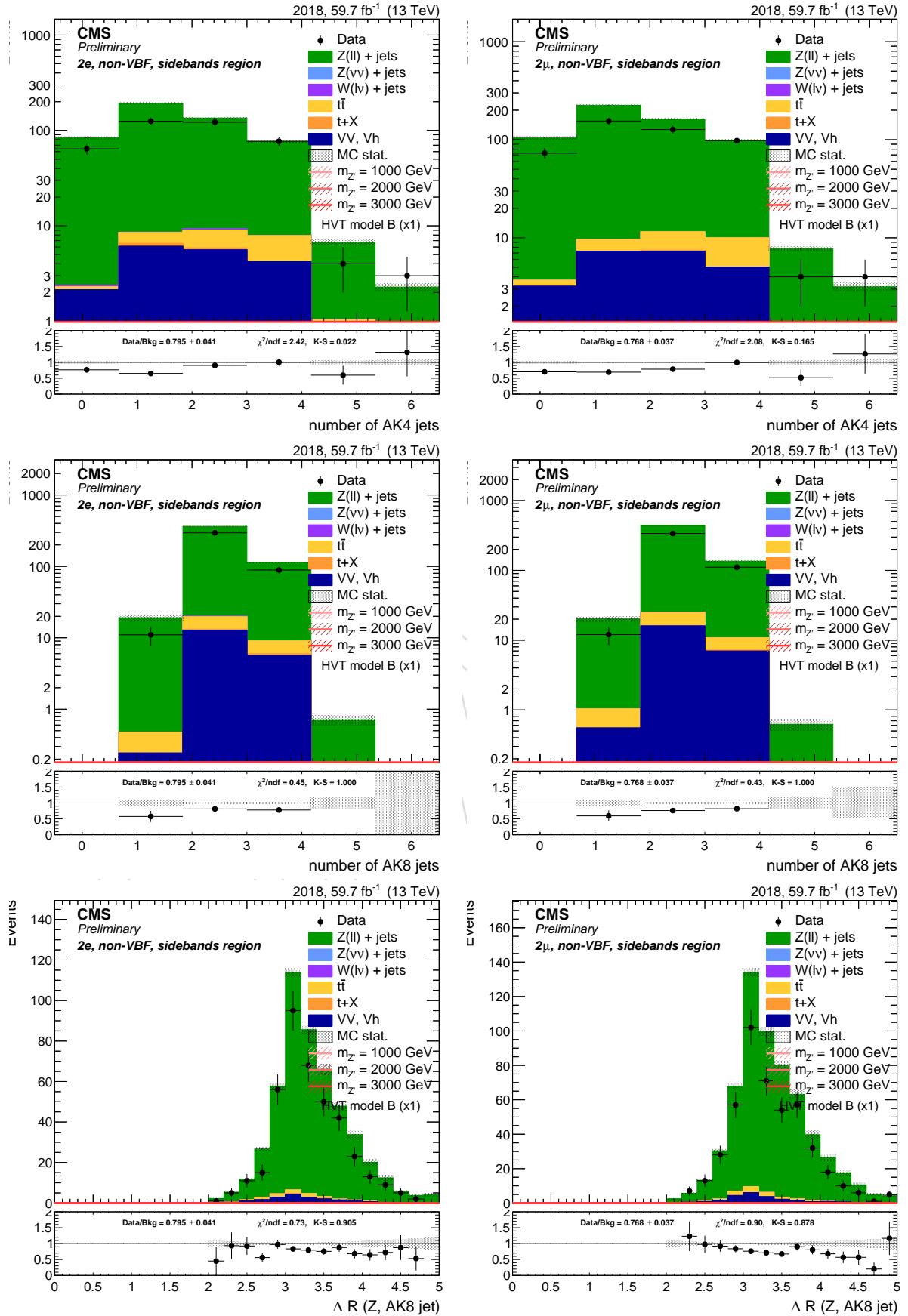


Figure 101: Top: number of AK4 jets. Center: number of AK8 jets. Bottom: ΔR between Z boson and leading AK8 jet. left: di-electron channel. right: di-muon channel. Events are selected with the *inclusive* selection, and simulated backgrounds are normalized to luminosity.

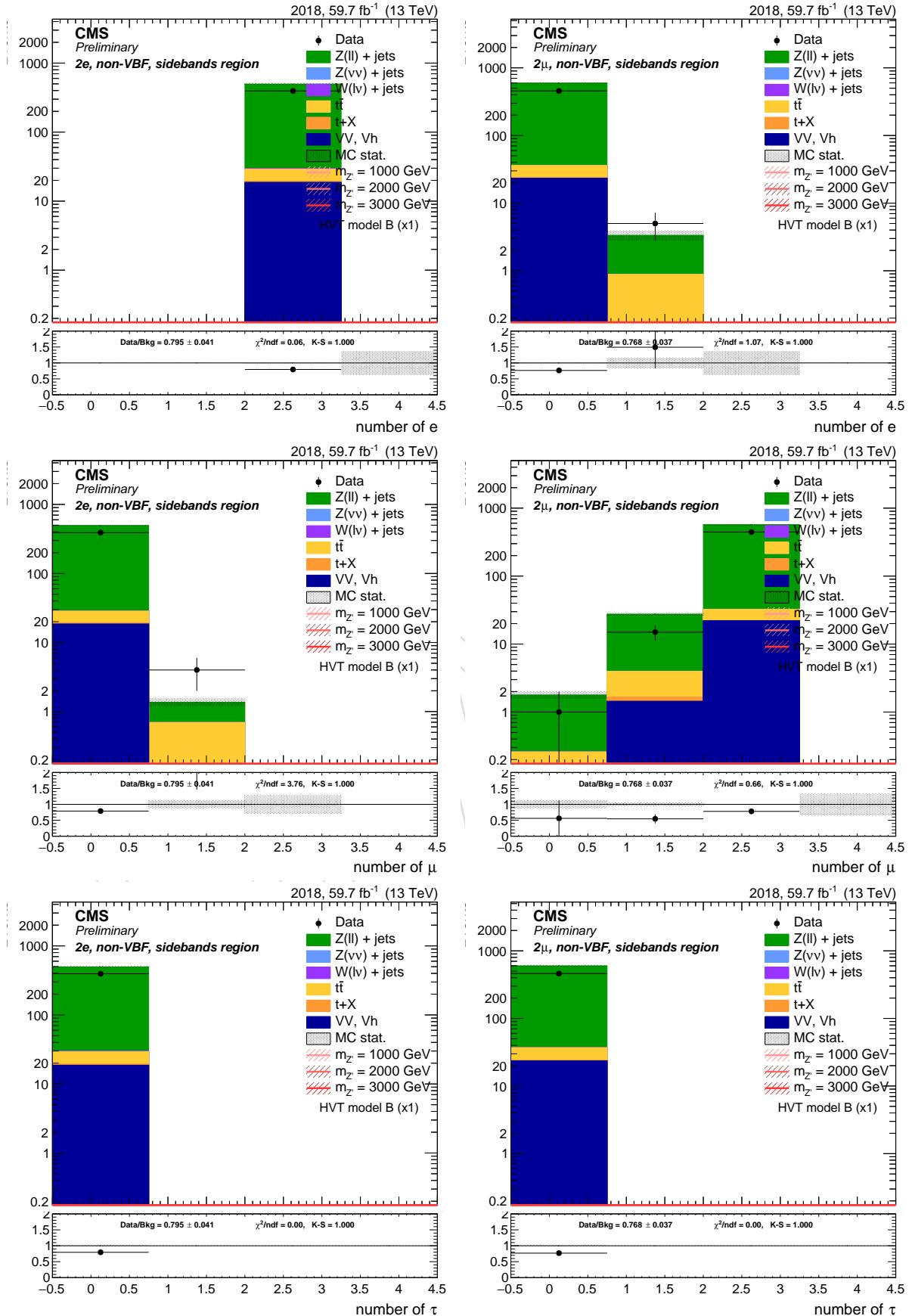


Figure 102: Top: number of electrons. Center: number of muons. Bottom: number of hadronic taus. left: di-electron channel. right: di-muon channel. Events are selected with the *inclusive* selection, and simulated backgrounds are normalized to luminosity.

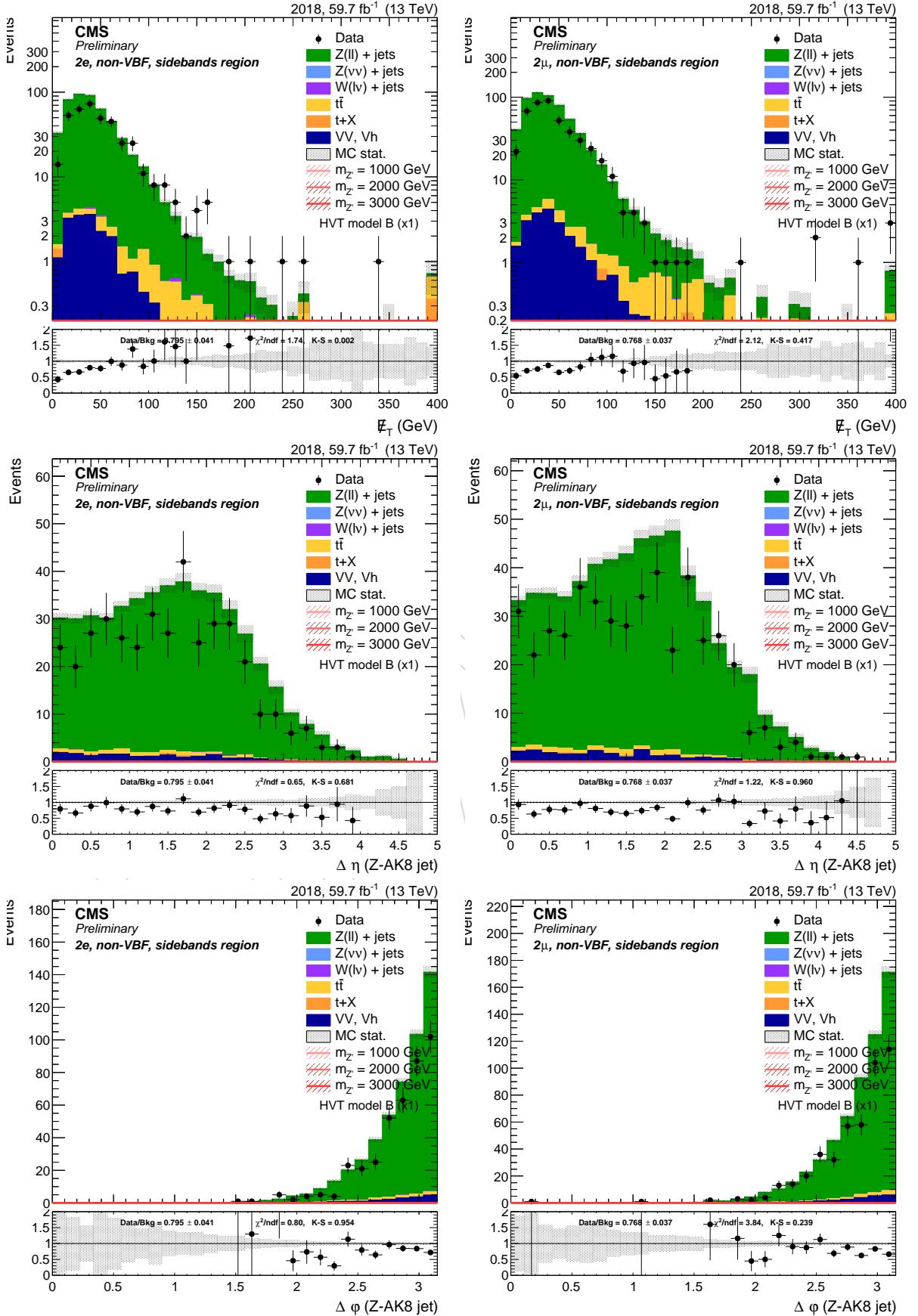


Figure 103: Top: E_T^{miss} . Center: $\Delta\eta$ between the Z and the AK8 jet. Bottom: $\Delta\phi$ between the Z and H candidates. left: di-electron channel. right: di-muon channel. Events are selected with the *inclusive* selection, and simulated backgrounds are normalized to luminosity.

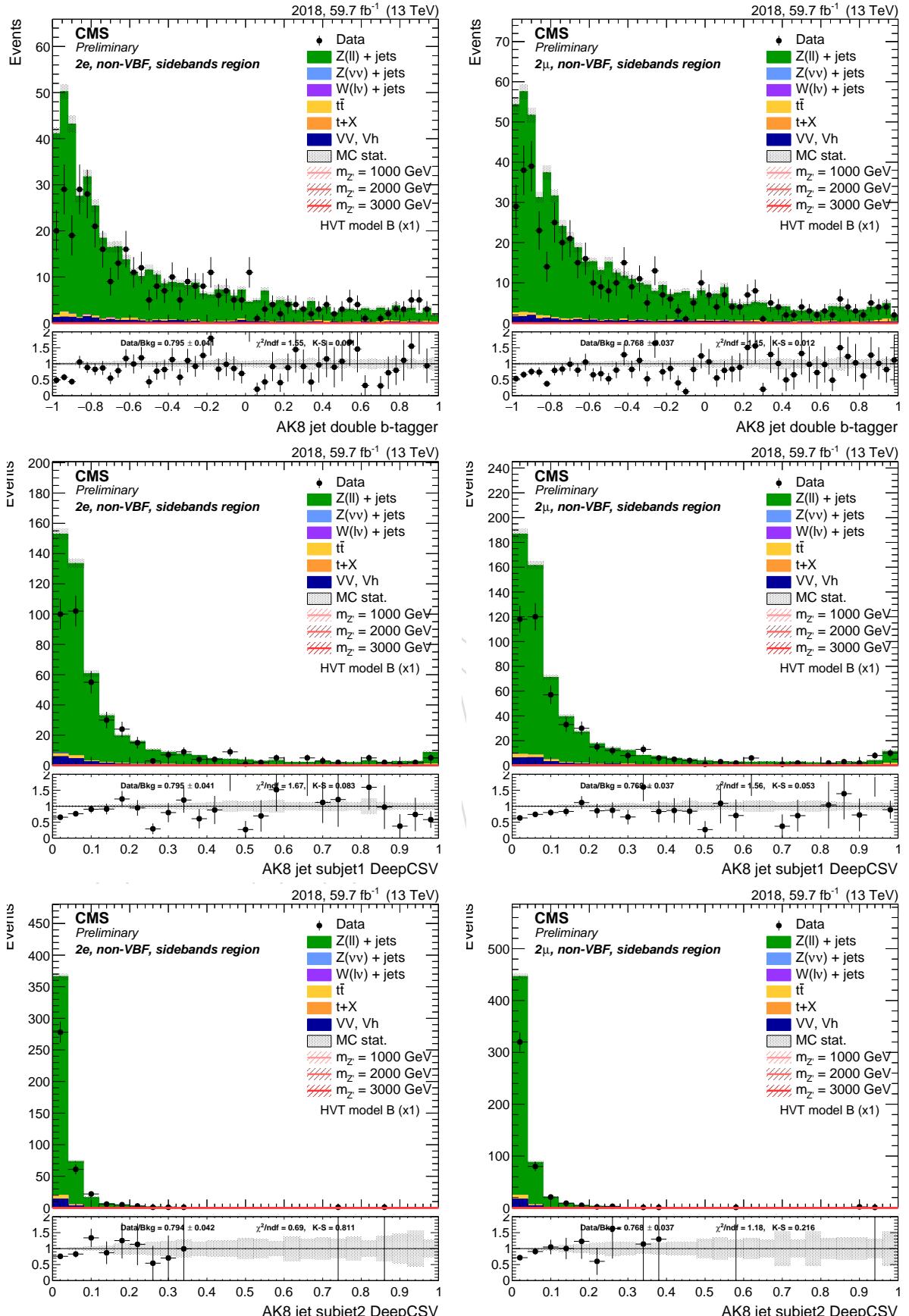


Figure 104: Top: AK8 double-b tagger discriminator . Center: DeepCSV distribution of the leading AK8 sub-jet. Bottom: DeepCSV distribution of the sub-leading AK8 sub-jet. left: di-electron channel. right: di-muon channel. Events are selected with the *inclusive* selection, and simulated backgrounds are normalized to luminosity.

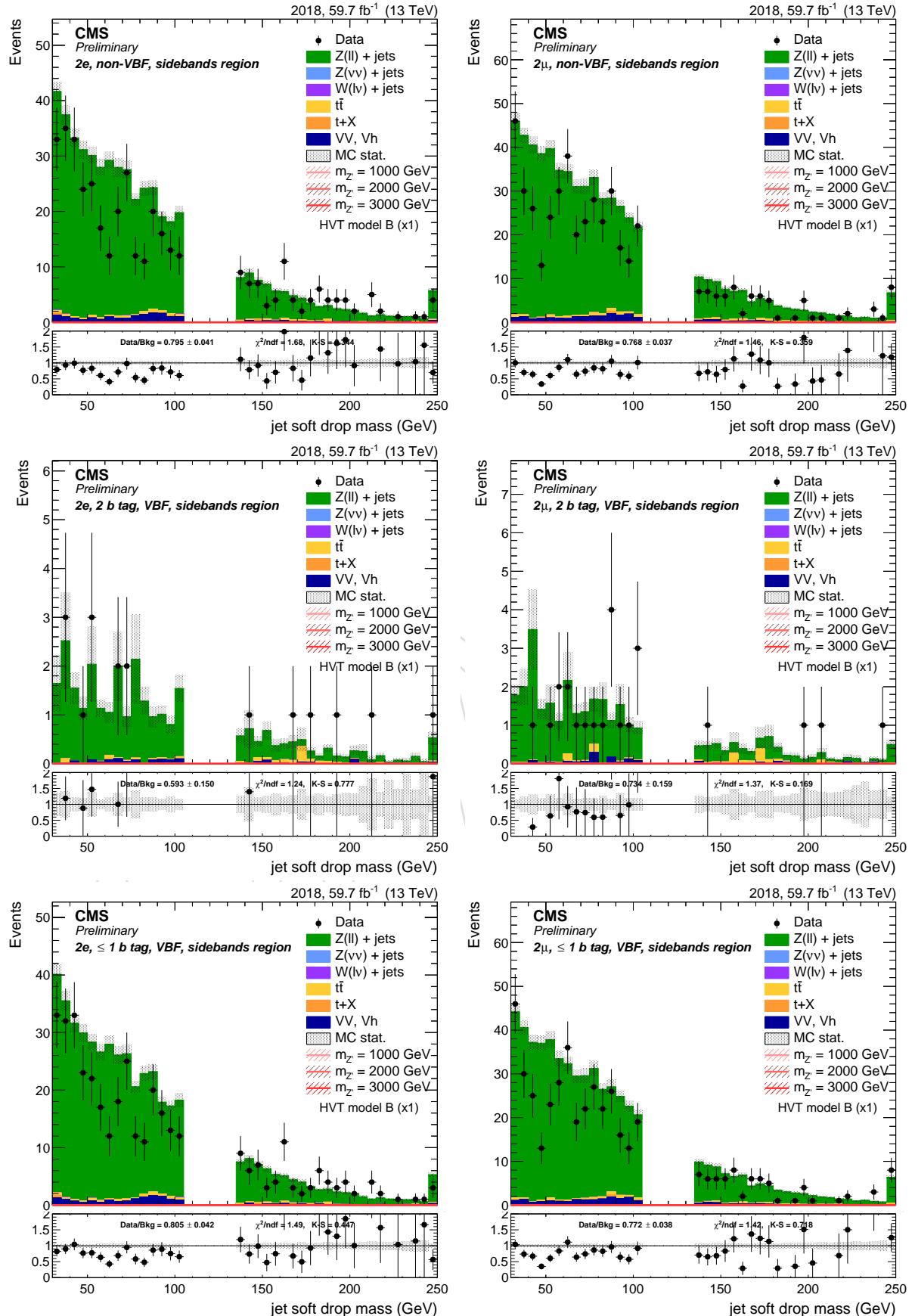


Figure 105: Leading AK8 jet soft drop PUPPI mass. Top: inclusive region. Center: mass sidebands and 2 b-tag category. Bottom: mass sidebands and no b-tag category. left: di-electron channel. right: di-muon channel.

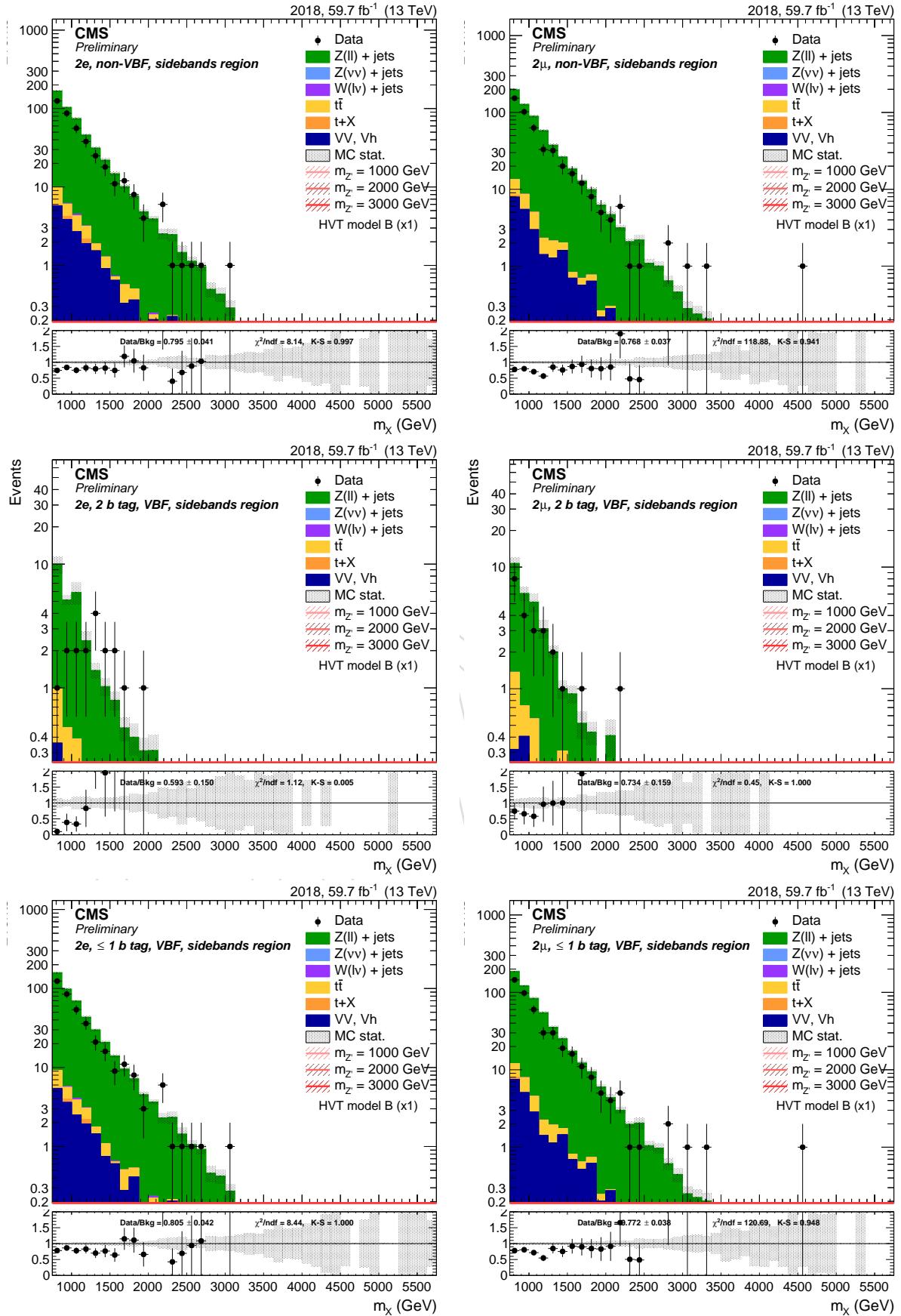


Figure 106: Resonance candidate mass. Top: inclusive region. Center: mass sidebands and 2 b-tag category. Bottom: mass sidebands and no b-tag category. left: di-electron channel. right: di-muon channel.

695 7 Top control regions

696 In the alpha method, the top contribution (composed by $t\bar{t}$ and single top processes) is taken di-
 697 rectly from simulation, for both the jet mass and the m_X distribution. Thus, the top background
 698 description has to be validated on data first.

699 Appropriate Top control regions (CR) are defined separately for the leptonic channels with 0 or
 700 2 b-tags, selecting an almost pure $t\bar{t}$ sample.

701 The 0ℓ Top control region is then selected with the same criteria as the respective sidebands
 702 regions, with one additional b-tagged AK4 jet in the event passing the DeepCSV *tight* working
 703 point.

704 The 2ℓ control region are derived by changing the lepton flavor requirement, by selecting
 705 events with opposite sign, opposite flavor leptons. The lepton requirements are the same as
 706 the ones used in the rest of the analysis, and the two leptons have to have $m_{e\mu} > 110$ GeV and
 707 $p_T^{e\mu} > 120$ GeV. Scale factors for b-tagging and lepton identification are applied consistently in
 708 these regions.

709 The figures 107-110 report the data and simulation distributions in the Top control regions.
 710 Multiplicative scale factors for $t\bar{t}$ and single top are derived for each category, and applied
 711 consistently in the alpha background prediction method. The top quark background scale fac-
 712 tors are affected by the statistical uncertainty in data, and by systematic uncertainties from the
 713 event reconstruction and modelling from simulation. The uncertainties of the 2 lepton cate-
 714 gories are derived extrapolating the $1e1\mu$ control region to the $2e$ and 2μ signal region using the
 715 lepton identification and trigger uncertainties. The VBF categories have a normalization un-
 716 certainty applied, to account for the small statistics in these control regions. The normalization
 717 uncertainty is derived as the deviation of the top SF from 1.

718 In the 0ℓ Top control regions, the significant contribution from V+jets background could in-
 719 troduce a significant bias in the estimation of the SF. For this reason, an auxiliary category of
 720 events is defined according to the b tagging score of the AK4 jet. While events entering the con-
 721 trol region is required to pass the tight working point, events comprised between the *medium*
 722 and *tight* working point are used to perform a rescaling of the V+jets background. In this way,
 723 the normalization of the top and V+jets components is derived simultaneously using both the
 724 *medium-tight* (m) and *tight* (t), in a similar way as to solve a system with 2 equations (the *medium*
 725 and *tight* regions) and 2 unknown parameters (SF_{top} and SF_{Vjets} , the latter is not used elsewhere
 726 in the analysis). The formulas used in this case are:

$$\begin{cases} N_t^{data} = N_t^{top} \cdot SF_{top} + N_t^{Vjets} \cdot SF_{Vjets} \text{ in the tight region} \\ N_m^{data} = N_m^{top} \cdot SF_{top} + N_m^{Vjets} \cdot SF_{Vjets} \text{ in the medium-tight region} \end{cases}$$

727 Expliciting SF_{Vjets} from the second equation: $SF_{Vjets} = \frac{N_m^{data} - N_m^{top} \cdot SF_{top}}{N_m^{Vjets}}$

728 and replacing it in the first equation:

$$N_t^{data} = N_t^{top} \cdot SF_{top} + \frac{N_t^{Vjets}}{N_m^{Vjets}} \cdot \left(N_m^{data} - N_m^{top} \cdot SF_{top} \right)$$

729 after some algebra, expliciting SF_{top} :

$$SF_{top} = \frac{N_t^{data} - N_m^{data} \frac{N_t^{Vjets}}{N_m^{Vjets}}}{N_t^{top} - N_m^{top} \frac{N_t^{Vjets}}{N_m^{Vjets}}}$$

where N^{data} , N^{Vjets} , and N^{top} are the number of events in data, V+jets, top quark backgrounds, respectively. The uncertainties are propagated accordingly, accounting for the fact that the total uncertainty is largely dominated by the statistics in data.

In the 2ℓ control regions, being the top quark background purity much higher than the 0ℓ regions, the top SF is evaluated directly from the CR.

Table 21: Scale factors (SF) derived for the normalization of the $t\bar{t}$ and S_T backgrounds for different event categories. Uncertainties due to the limited size of the event samples (stat) and systematic effects (syst) are reported as well.

no VBF Category		Top SF \pm stat. \pm syst.
2 b tag	0ℓ	$1.012 \pm 0.116 \pm 0.008$
	$1e, 1\mu$	$1.098 \pm 0.084 \pm 0.001$
	$2e$	$1.098 \pm 0.084 \pm 0.067$
	2μ	$1.098 \pm 0.084 \pm 0.075$
0 b tag	0ℓ	$1.028 \pm 0.048 \pm 0.009$
	$1e, 1\mu$	$1.003 \pm 0.021 \pm 0.005$
	$2e$	$1.003 \pm 0.021 \pm 0.089$
	2μ	$1.003 \pm 0.021 \pm 0.095$
VBF Category		Top SF \pm stat. \pm syst. \pm VBF norm
2 b tag	0ℓ	$0.676 \pm 0.221 \pm 0.007 \pm 0.330$
	$1e, 1\mu$	$0.676 \pm 0.154 \pm 0.004 \pm 0.330$
	$2e$	$0.676 \pm 0.154 \pm 0.096 \pm 0.330$
	2μ	$0.676 \pm 0.154 \pm 0.103 \pm 0.330$
0 b tag	0ℓ	$0.822 \pm 0.144 \pm 0.022 \pm 0.180$
	$1e, 1\mu$	$0.882 \pm 0.044 \pm 0.003 \pm 0.120$
	$2e$	$0.882 \pm 0.044 \pm 0.099 \pm 0.120$
	2μ	$0.882 \pm 0.044 \pm 0.107 \pm 0.120$

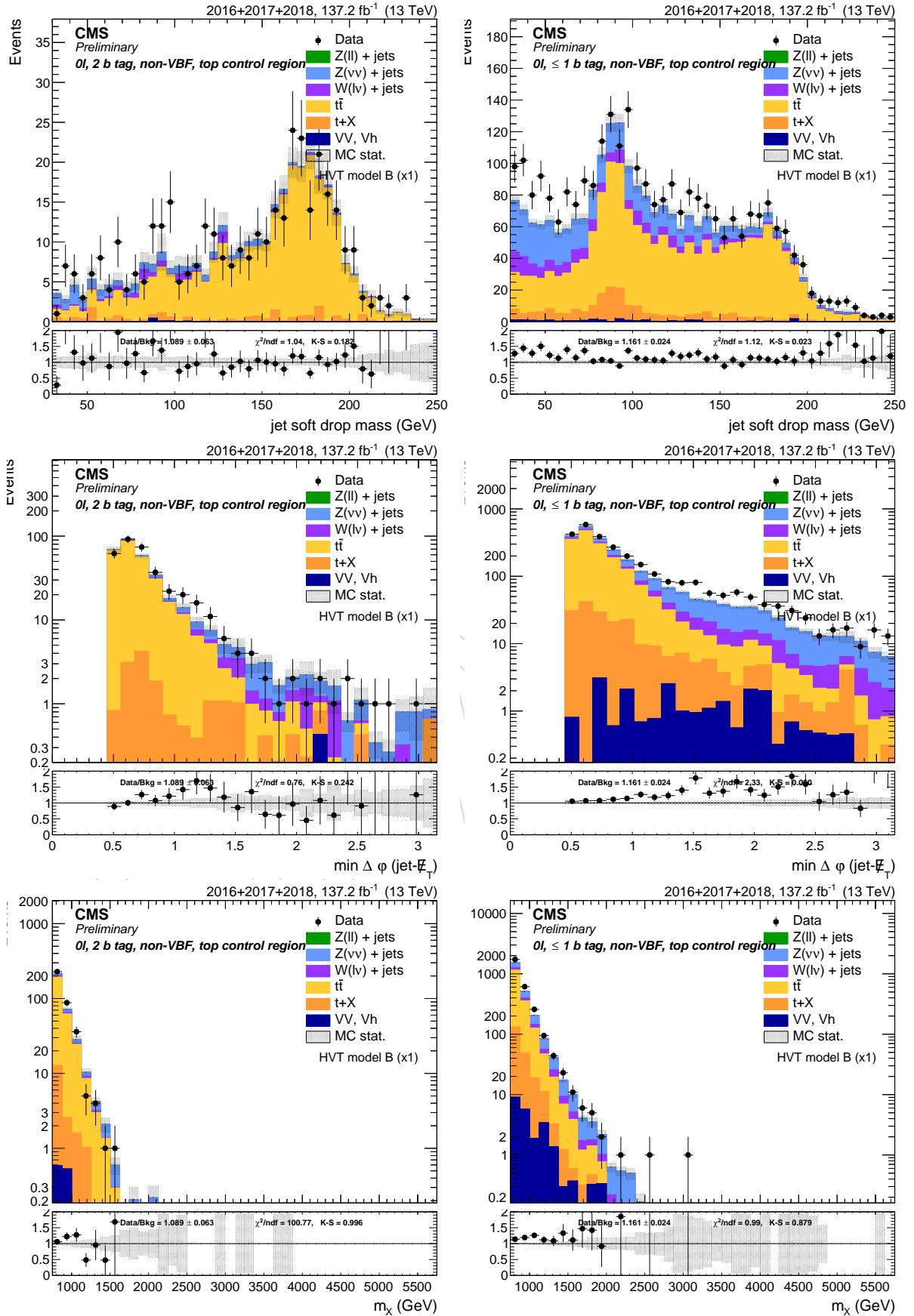


Figure 107: Jet mass (top), minimum $\Delta\phi$ between the AK4 jets and the E_T^{miss} (center) and m_X distributions (bottom) in the 0-lepton 2 b-tag (left) and no b-tag (right) Top control regions.

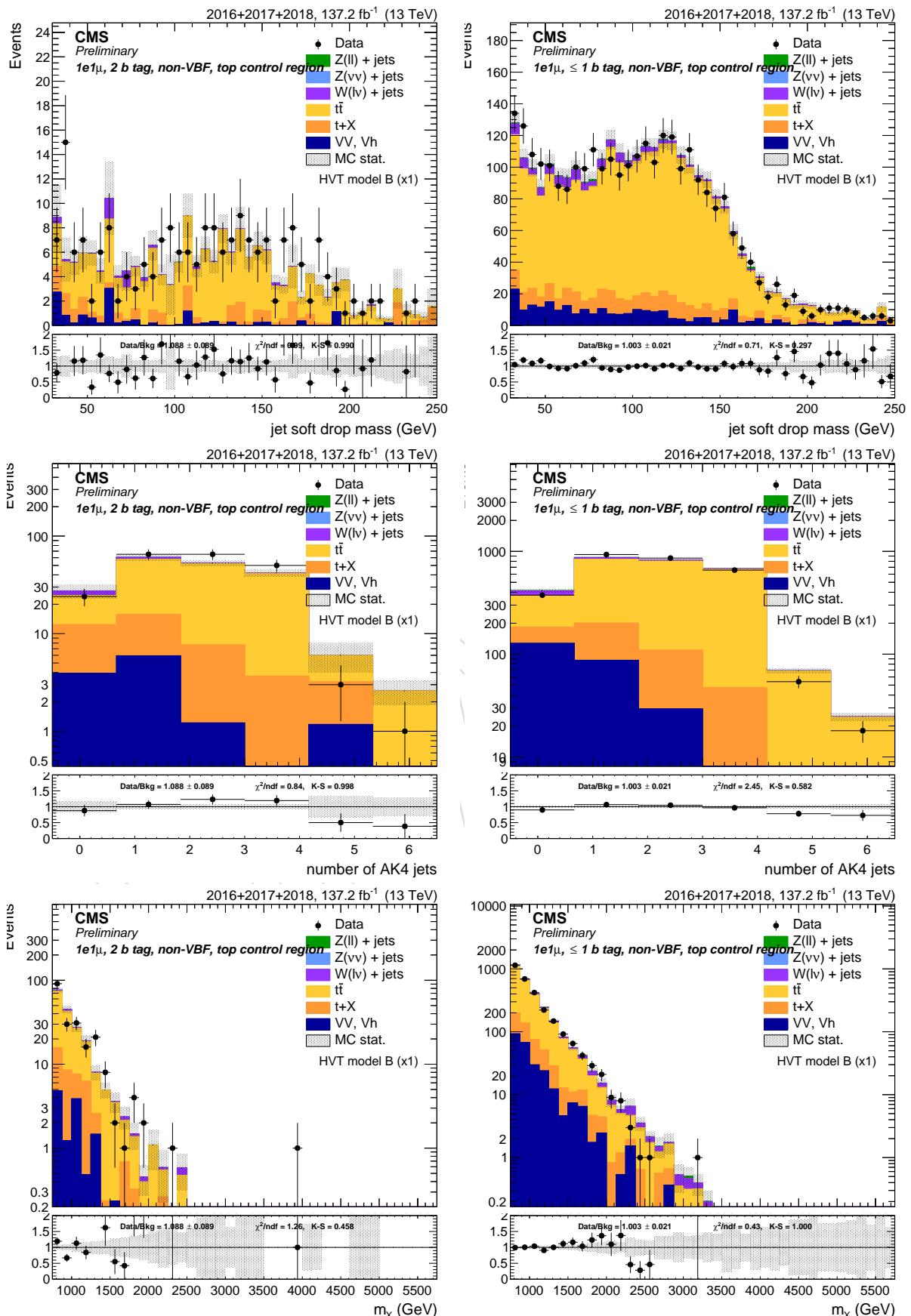


Figure 108: Jet mass (top), number of jets (center), and m_X distributions (bottom) in the 2-lepton 2 b-tag (left) and no b-tag (right) Top control regions.

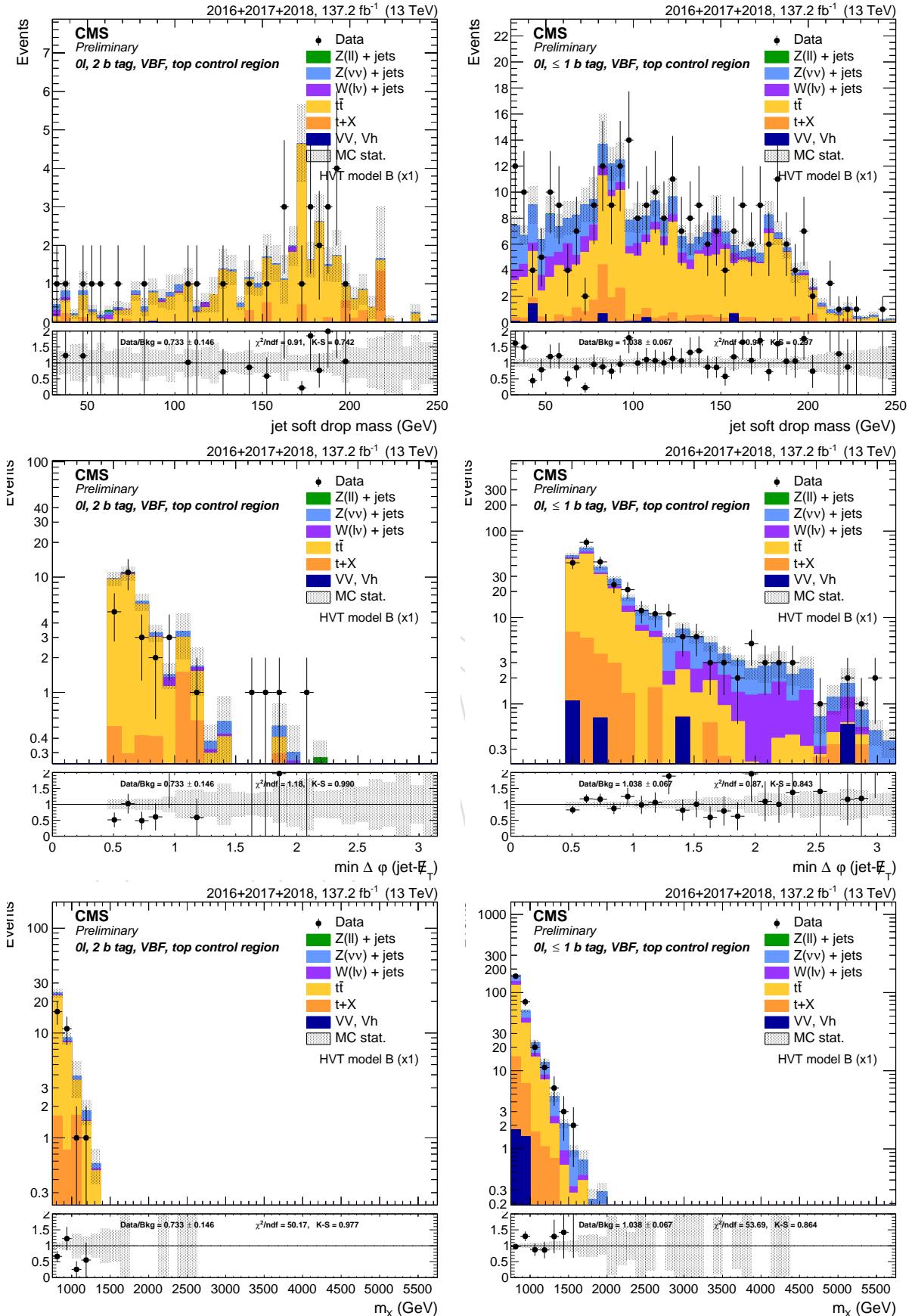


Figure 109: Jet mass (top), minimum $\Delta\phi$ between the AK4 jets and the E_T^{miss} (center) and m_X distributions (bottom) in the 0-lepton VBF 2 b-tag (left) and no b-tag (right) Top control regions.

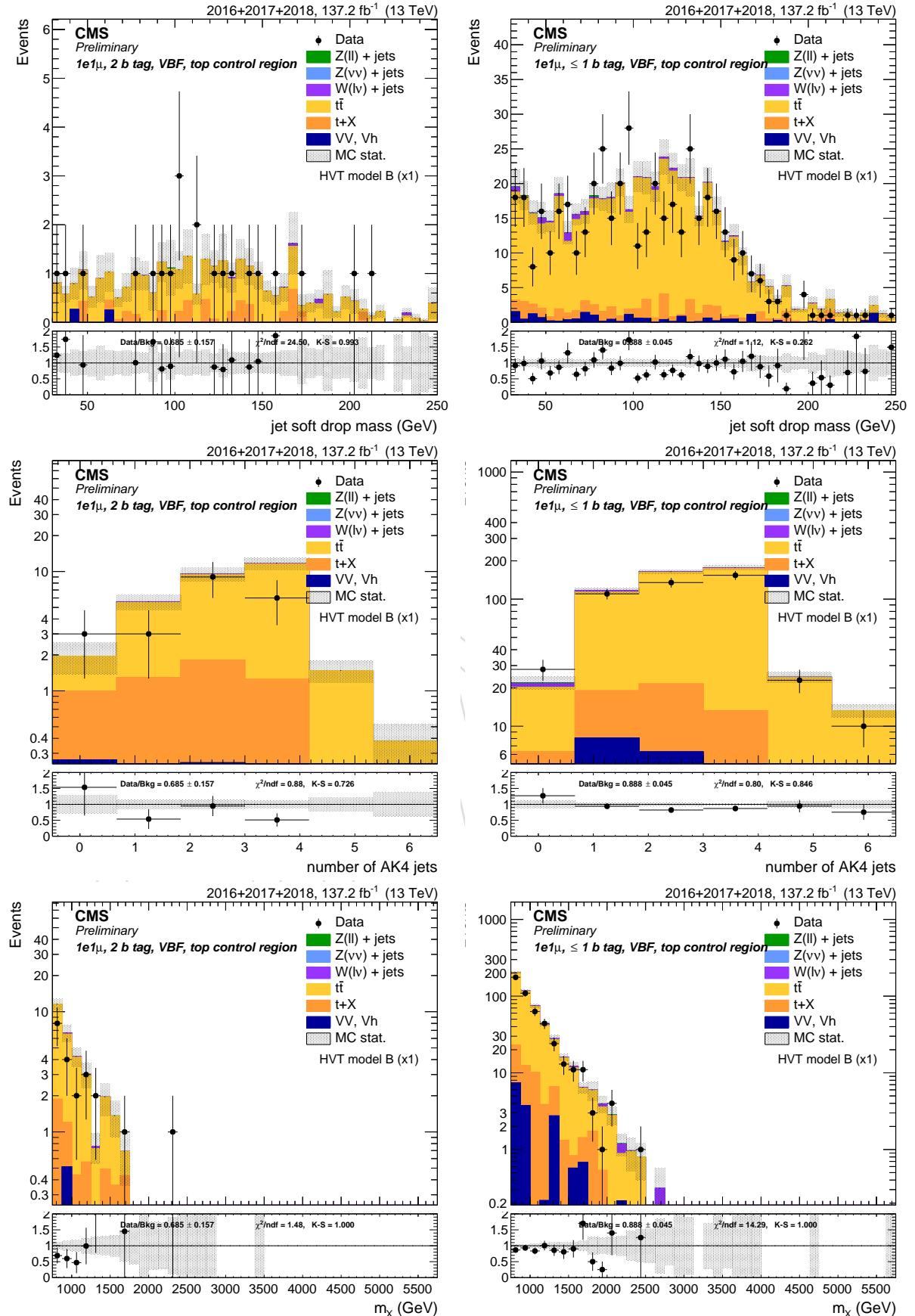


Figure 110: Jet mass (top), number of jets (center), and m_X distributions (bottom) in the 2-lepton VBF 2 b-tag (left) and no b-tag (right) Top control regions.

735 8 Alpha ratio background prediction

736 The *alpha method* was the background estimation method introduced to be less dependent on
 737 the MC simulation for the background m_X estimation, due to the many sources of systematic
 738 uncertainties that are relevant in the boosted regime and are hard to understand and control.
 739 Two exclusive regions, named *signal region* (SR) and *sidebands region* (SB), are defined in order
 740 to select a signal enriched or signal depleted phase space, respectively. First, the background
 741 normalization is extracted from data in the SB. Then, the alpha method extracts a predicted
 742 shape from the data in the SB to the SR using a transfer function (the α function) derived from
 743 simulation using a dataset combining the 2016, 2017 and 2018 Monte Carlo events. The method
 744 relies on the assumption that the correlation between m_X and the soft drop PUPPI jet mass is
 745 reasonably well reproduced by the MC. The α ratio is deemed to be more trustworthy than a
 746 pure MC-based background prediction because many systematic uncertainties would approx-
 747 imately cancel in the ratio.

The α function is defined as the ratio of the two functions describing the simulated m_X shape
 in the SR and SB:

$$\alpha(m_X) = \frac{N_{SR}^{MC,bkg}(m_X)}{N_{SB}^{MC,bkg}(m_X)}$$

and the background distribution in the SR is thus estimated as the product of $\alpha(m_X)$ with the
 shape in the data SB:

$$N_{bkg}(m_X) = N_{SB}(m_X) \times \alpha(m_X)$$

748 Notice that the above description does not include the definition of the SB and SR. Ideally,
 749 the best choice would be a variable such that the distribution of m_X in the Signal and Sideband
 750 regions are similar. In this analysis, the soft drop PUPPI corrected jet mass m_j (see Section 3.6.1)
 751 is chosen as the control variable, and the cut values are those reported in Section 5. All the
 752 selections used in the α method background prediction are the same reported in Section 5. In
 753 order to respect the blinding policy of the diboson VV searches, the Z mass window is not used
 754 neither for the background estimation (it can be potentially contaminated by a signal) nor as
 755 signal region.

756 In a real case scenario, the background is not purely composed of one single process neither in
 757 the SR nor in the SB. The background composition is assumed to be dominated by one single
 758 process (V+jets) whose modelling in simulation is considered not to be trustworthy. Other sub-
 759 dominant backgrounds ($t\bar{t}$ including single top and V V) generally have smaller contributions,
 760 and are considered quite well understood and modelled by MC generators. However, due to
 761 the b-tagging and lepton selections, in some channels the $t\bar{t}$ can be of the same order of mag-
 762 nitude or even larger than the main background. The treatment of sub-dominant backgrounds
 763 thus require a dedicated treatment.

764 The m_X distribution has a lower threshold at 1.2 TeV for the 0-btag no VBF categories in order
 765 to ensure the smoothness of the background model.

766 Top control regions are defined separately for the different lepton flavors and multiplicities,
 767 and for the number of b-tagged subjets, selecting almost pure $t\bar{t}$ samples (Section 7). The nor-
 768 malization of the $t\bar{t}$ process is then fixed in the CR, and a multiplicative scale factor is applied
 769 to the normalization in the subsequent steps of the analysis. The shape and normalization of
 770 the diboson production, instead, is taken from the simulation.

771 A different background prediction is derived for each category separately, thus dividing elec-
 772 tron and muon channels, and zero and double b-tag categories, in order to reduce systematic

773 uncertainty due to leptonic triggers, identification, isolation, and b-tagging efficiencies.

774 8.1 Background normalization

The first step in the background prediction consists in a proper estimation of the background normalization. The three main backgrounds ($V + \text{jets}$, $t\bar{t}$ and single top, and VV including VH) are considered separately due to the different shape in the jet mass distribution. The three contributions are described with functional forms determined by fits on the simulated backgrounds. The number of expected events in the SR is extracted through the same equation:

$$N_{SR}^{data} = \left[N_{SB}^{data} - N_{SB}^{Top} - N_{SB}^{VV} \right] \times \left[\frac{N_{SR}^{Vjet}}{N_{SB}^{Vjet}} \right] + N_{SR}^{Top} + N_{SR}^{VV}$$

775 where in this case N are the number of events, and not functions.

776 The empirical functional forms for each background reflect the physics properties of the sam-
 777 ples. The $V + \text{jets}$ background has a smoothly falling background with no peaks. On top of the
 778 jet mass spectrum, the VV has two peaks corresponding to the W and Z boson hadronic decays,
 779 and possibly a third one due to the presence of the Higgs. In certain channels, some of them
 780 may be not clearly visible due to the small cross section, and the lack of adequate statistics in
 781 the simulated samples. The $t\bar{t}$ and single top backgrounds are considered together, because
 782 they both have two peaks corresponding to the $W \rightarrow jj$ decays and all-hadronic top quark
 783 decays $t \rightarrow Wb \rightarrow jjb$. In some channels, and particularly those with 2 b-tags, the AK8 jets
 784 clusters both the b-quarks from the top decay, so the $W \rightarrow jj$ is not clearly visible. In case the
 785 Monte Carlo does not provide enough statistics to constrain the shape of the resonances, their
 786 parameters are fixed to the expected value (the masses of the W , Z , H and top quarks), with
 787 the resolution fixed to the measured value (10%). The normalization is always left free to float.
 788 The functional forms chosen to build the jet mass templates are:

Exp: an exponential function:

$$F_{\text{Exp}}(x) = e^{ax}$$

ExpGaus: an exponential plus one gaussian:

$$F_{\text{Exp}}(x) = f_0 \cdot e^{ax} + (1 - f_0) \cdot e^{2(x-a)^2/b}$$

ExpErf: an “error function”, that consists of an exponential multiplied by an Erf:

$$F_{\text{ErfExp}}(x) = e^{ax} \cdot \frac{1 + \text{Erf}((x - b)/w)}{2}$$

Powerlaw: a one-parameter power law:

$$F_{\text{Pow}}(x) = x^a$$

Pol: a polynomial with a variable number of parameters:

$$F_{\text{Pol}}(x) = a_0 \cdot x + a_2 \cdot x^2 + a_3 \cdot x^3$$

Gaus: one gaussian:

$$F_{\text{Gaus}}(x) = \cdot e^{2(x-a)^2/b}$$

Gaus2: two gaussians:

$$F_{\text{Gaus2}}(x) = f_0 \cdot e^{2(x-a)^2/b} + (1-f_0) \cdot e^{2(x-c)^2/d}$$

Gaus3: three gaussians:

$$F_{\text{Gaus3}}(x) = f_0 \cdot e^{2(x-a)^2/b} + f_1 \cdot e^{2(x-c)^2/d} + (1-f_0-f_1) \cdot e^{2(x-e)^2/g}$$

ExpGaus: an exponential plus one gaussian:

$$F_{\text{ExpGaus}}(x) = f_0 \cdot e^{ax} + (1-f_0) \cdot e^{2(x-b)^2/c}$$

ExpGaus2: an exponential plus two gaussians:

$$F_{\text{ExpGaus2}}(x) = f_0 \cdot e^{ax} + f_1 \cdot e^{2(x-b)^2/c} + (1-f_0-f_1) \cdot e^{2(x-d)^2/e}$$

ExpGaus3: an exponential plus three gaussians:

$$F_{\text{ExpGaus3}}(x) = f_0 \cdot e^{ax} + f_1 \cdot e^{2(x-b)^2/c} + f_2 \cdot e^{2(x-d)^2/e} + (1-f_0-f_1-f_2) \cdot e^{2(x-f)^2/g}$$

ErfExpGaus: an error function plus one gaussian:

$$F_{\text{ErfExpGaus}}(x) = f_0 \cdot F_{\text{ErfExp}}(x, a, b, c) + (1-f_0) \cdot e^{2(x-d)^2/e}$$

ErfExpGaus2: an error function plus two gaussians:

$$F_{\text{ErfExpGaus2}}(x) = f_0 \cdot F_{\text{ErfExp}}(x, a, b, c) + f_1 \cdot e^{2(x-d)^2/e} + (1-f_0-f_1) \cdot e^{2(x-f)^2/g}$$

789 The choice of the functions is channel-dependent, and it depends on the background shape and
790 the available statistics, and is summarized in Table 22.

category		V +jets	alt. V +jets	t <bar>t</bar>	VV
2 b-tag	0 ℓ	Pol5	ExpGaus	Gaus2	ErfExpGaus2
	2e	Pol5	ExpGaus	Gaus2	ErfExpGaus2
	2 μ	Pol5	ExpGaus	Gaus2	ExpGaus2
0 b-tag	0 ℓ	Pol5	ExpGaus	Gaus3	ErfExpGaus
	2e	Pol5	ExpGaus	Gaus	ExpGaus
	2 μ	Pol5	ExpGaus	Gaus	ErfExpGaus
2 b-tag VBF	0 ℓ	Pol5	ExpGaus	Gaus2	ErfExpGaus
	2e	Pol5	ExpGaus	Gaus	ExpGaus
	2 μ	Pol5	ExpGaus	Gaus2	ExpGaus
0 b-tag VBF	0 ℓ	Pol5	ExpGaus	Gaus3	ErfExpGaus
	2e	Pol5	ExpGaus	ErfExpGaus	ExpGaus
	2 μ	Pol5	ExpGaus	Gaus	ExpGaus

Table 22: Chosen functions to fit the jet mass distribution for each channel.

791 The number of parameters of the polynomial used to fit the data are derived with a Fisher test.
792 The following plots (Figure 111-119) show the mass fits to the jet mass in the different channels.
793 Table 27 summarizes the expected background yield in the signal region.

function	χ^2	RSS	ndof	F-test		result
				nnbb		
2 par	32.30	5.68	26	2 par vs 3 par CL=0.56	2 par are sufficient	
3 par	31.48	5.61	25	3 par vs 4 par CL=0.00	4 par are needed	
4 par	15.17	3.89	24	4 par vs 5 par CL=0.06	5 par are needed	
5 par	11.35	3.37	23			
Order is 4 , N par is 5						
function	χ^2	RSS	ndof	eebb		result
				eebb		
2 par	14.50	3.81	26	2 par vs 3 par CL=1.00	2 par are sufficient	
3 par	14.53	3.81	25	3 par vs 4 par CL=0.61	3 par are sufficient	
4 par	14.24	3.77	24	4 par vs 5 par CL=1.00	4 par are sufficient	
5 par	14.41	3.80	23			
Order is 1 , N par is 2						
function	χ^2	RSS	ndof	mmbb		result
				mmbb		
2 par	20.99	4.58	26	2 par vs 3 par CL=1.00	2 par are sufficient	
3 par	21.18	4.60	25	3 par vs 4 par CL=0.43	3 par are sufficient	
4 par	20.16	4.49	24	4 par vs 5 par CL=0.38	4 par are sufficient	
5 par	18.94	4.35	23			
Order is 1 , N par is 2						

Table 23: Fisher F-test for the 2 b-tag no VBF categories.

function	χ^2	RSS	ndof	F-test		result
				nn0b		
2 par	51.73	7.19	26	2 par vs 3 par CL=0.11	2 par are sufficient	
3 par	42.85	6.55	25	3 par vs 4 par CL=0.01	4 par are needed	
4 par	25.32	5.03	24	4 par vs 5 par CL=0.85	4 par are sufficient	
5 par	25.25	5.03	23			
Order is 3 , N par is 4						
function	χ^2	RSS	ndof	ee0b		result
				ee0b		
2 par	29.75	5.45	26	2 par vs 3 par CL=0.06	3 par are needed	
3 par	22.87	4.78	25	3 par vs 4 par CL=0.70	3 par are sufficient	
4 par	22.61	4.75	24	4 par vs 5 par CL=0.77	4 par are sufficient	
5 par	22.45	4.74	23			
Order is 2 , N par is 3						
function	χ^2	RSS	ndof	mm0b		result
				mm0b		
2 par	27.72	5.27	26	2 par vs 3 par CL=0.40	2 par are sufficient	
3 par	26.27	5.13	25	3 par vs 4 par CL=0.11	3 par are sufficient	
4 par	21.59	4.65	24	4 par vs 5 par CL=0.69	4 par are sufficient	
5 par	21.31	4.62	23			
Order is 1 , N par is 2						

Table 24: Fisher F-test for the 0 b-tag no VBF categories.

function	χ^2	RSS	ndof	F-test	result
nnbbVBF					
2 par	14.68	3.83	23	2 par vs 3 par CL=0.26	2 par are sufficient
3 par	13.17	3.63	22	3 par vs 4 par CL=1.00	3 par are sufficient
4 par	14.77	3.84	21	4 par vs 5 par CL=1.00	4 par are sufficient
5 par	15.32	3.91	20		
Order is 1 , N par is 2					
eebbVBF					
2 par	14.02	3.74	22	2 par vs 3 par CL=1.00	2 par are sufficient
3 par	15.53	3.94	21	3 par vs 4 par CL=1.00	3 par are sufficient
4 par	16.72	4.09	20	4 par vs 5 par CL=1.00	4 par are sufficient
5 par	16.75	4.09	19		
Order is 1 , N par is 2					
mmbbVBF					
2 par	12.87	3.59	26	2 par vs 3 par CL=1.00	2 par are sufficient
3 par	13.05	3.61	25	3 par vs 4 par CL=0.49	3 par are sufficient
4 par	12.58	3.55	24	4 par vs 5 par CL=0.58	4 par are sufficient
5 par	12.27	3.50	23		
Order is 1 , N par is 2					

Table 25: Fisher F-test for the 2 b-tag VBF categories.

function	χ^2	RSS	ndof	F-test	result
nn0bVBF					
2 par	35.71	5.98	26	2 par vs 3 par CL=0.82	2 par are sufficient
3 par	35.56	5.96	25		
Order is 1 , N par is 2					
ee0bVBF					
2 par	14.96	3.87	26	2 par vs 3 par CL=0.33	2 par are sufficient
3 par	13.91	3.73	25		
Order is 1 , N par is 2					
mm0bVBF					
2 par	28.65	5.35	26	2 par vs 3 par CL=0.83	2 par are sufficient
3 par	28.55	5.34	25	3 par vs 4 par CL=1.00	3 par are sufficient
4 par	29.20	5.40	24	4 par vs 5 par CL=0.19	4 par are sufficient
5 par	25.38	5.04	23		
Order is 1 , N par is 2					

Table 26: Fisher F-test for the 0 b-tag VBF categories.

Category		V+jets (\pm fit) (\pm alt)	$t\bar{t}, S_T$	VV	Bkg. sum	Observed
2 b tag	0ℓ	$374 \pm 34 \pm 20$	68 ± 8	31 ± 10	474 ± 42	549
	2e	$54 \pm 5 \pm 8$	3 ± 0	8 ± 2	65 ± 10	57
	2μ	$60 \pm 5 \pm 1$	3 ± 1	9 ± 2	72 ± 5	91
0 b tag	0ℓ	$637 \pm 35 \pm 51$	7 ± 1	15 ± 4	659 ± 61	697
	2e	$113 \pm 14 \pm 27$	2 ± 0	7 ± 2	122 ± 31	130
	2μ	$167 \pm 8 \pm 10$	2 ± 0	8 ± 2	177 ± 13	154
2 b tag VBF	0ℓ	$28 \pm 3 \pm 3$	4 ± 2	1 ± 1	33 ± 5	26
	2e	$7 \pm 2 \pm 2$	0 ± 0	0 ± 0	8 ± 3	10
	2μ	$6 \pm 2 \pm 0$	0 ± 0	1 ± 0	7 ± 2	8
0 b tag VBF	0ℓ	$486 \pm 13 \pm 72$	25 ± 6	6 ± 1	517 ± 73	572
	2e	$137 \pm 7 \pm 7$	5 ± 1	6 ± 1	148 ± 10	168
	2μ	$171 \pm 8 \pm 6$	5 ± 1	8 ± 2	183 ± 10	222

Table 27: Expected and observed numbers of events in the signal region, for all event categories. Three separate sources of uncertainty in the expected numbers are reported: the V+jets background uncertainty from the variation of the parameters within the fit uncertainties, and accounting for the correlation between them (fit); the difference between the nominal and alternative function choice for the fit to m_j (alt); the $t\bar{t}, S_T$ uncertainties from the m_j modeling, the statistical component of the top quark scale factor uncertainties, and the extrapolation uncertainty from the control regions to the SR; the VV normalization uncertainties relative to the m_j modeling and the uncertainties affecting the normalization.

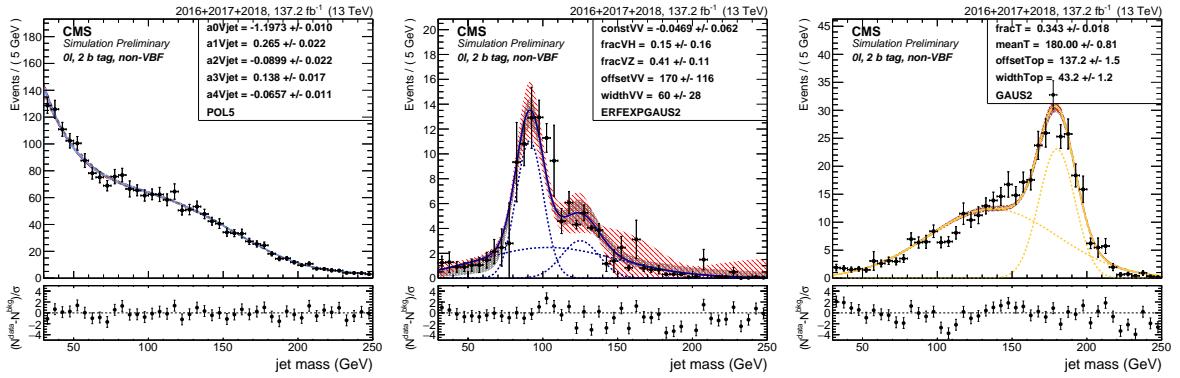


Figure 111: Fit to the simulated m_j in the 0 lepton, 2 b-tag category for the three backgrounds: V+jets (left), VV (center), Top (right).

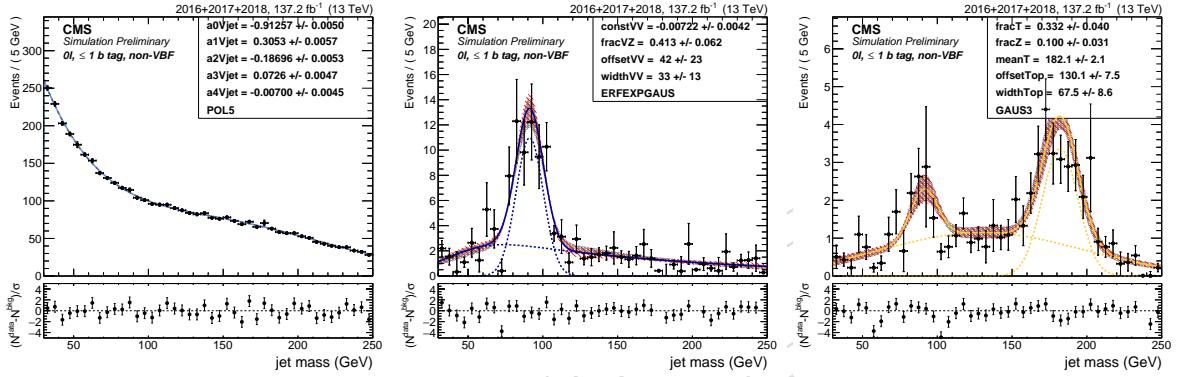


Figure 112: Fit to the simulated m_j in the 0 lepton, 0 b-tag category for the three backgrounds: V+jets (left), VV (center), Top (right).

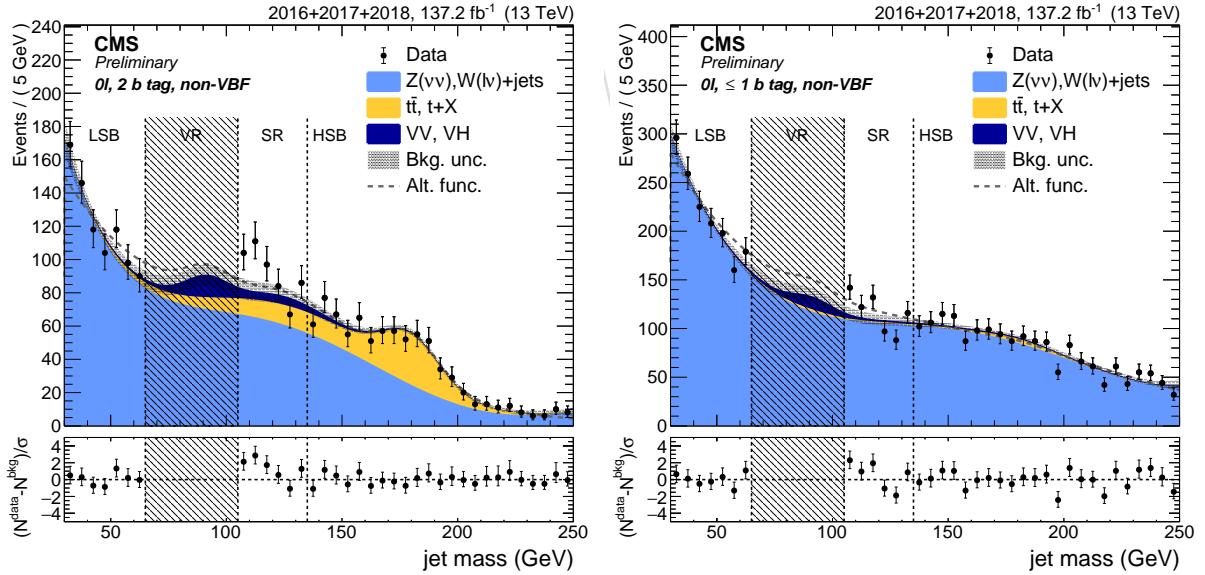


Figure 113: Fit to data m_j in the 0 lepton 2 b-tag (left) and 0 b-tag (right) category.

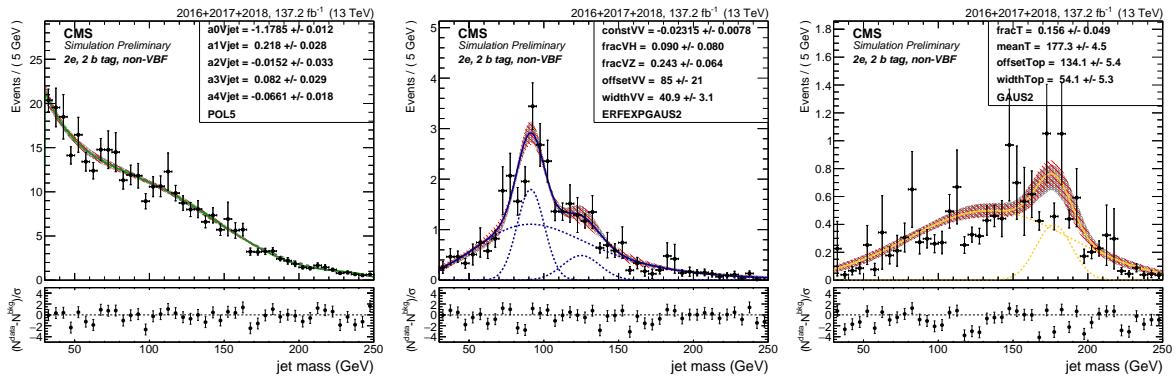


Figure 114: Fit to the simulated m_j in the 2 electrons, 2 b-tag category for the three backgrounds: $V + \text{jets}$ (left), VV (center), Top (right).

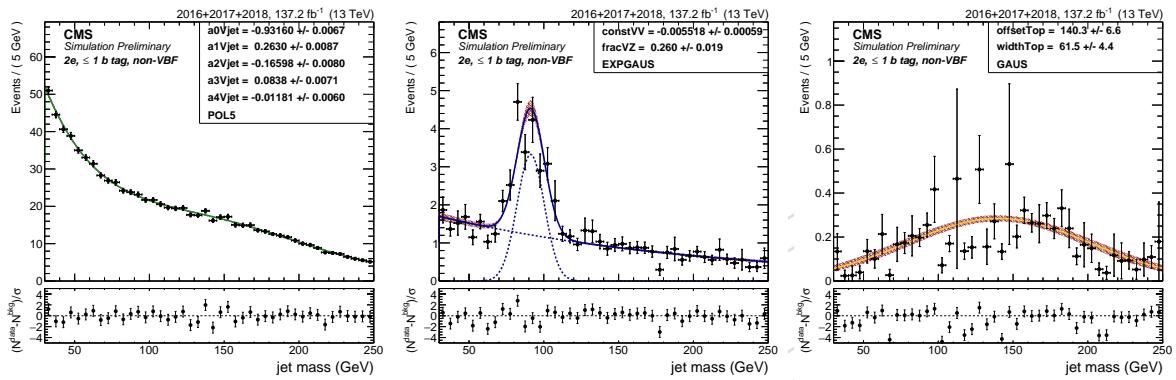


Figure 115: Fit to the simulated m_j in the 2 electrons, 0 b-tag category for the three backgrounds: $V + \text{jets}$ (left), VV (center), Top (right).

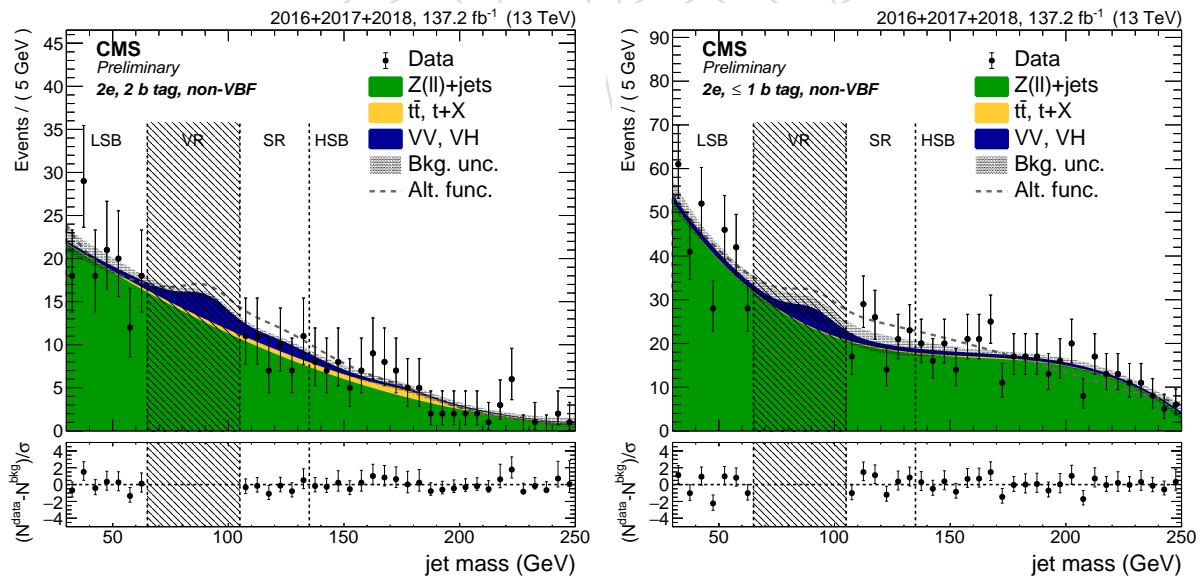


Figure 116: Fit to data m_j in the 2 electrons 2 b-tag (left) and 0 b-tag (right) category.

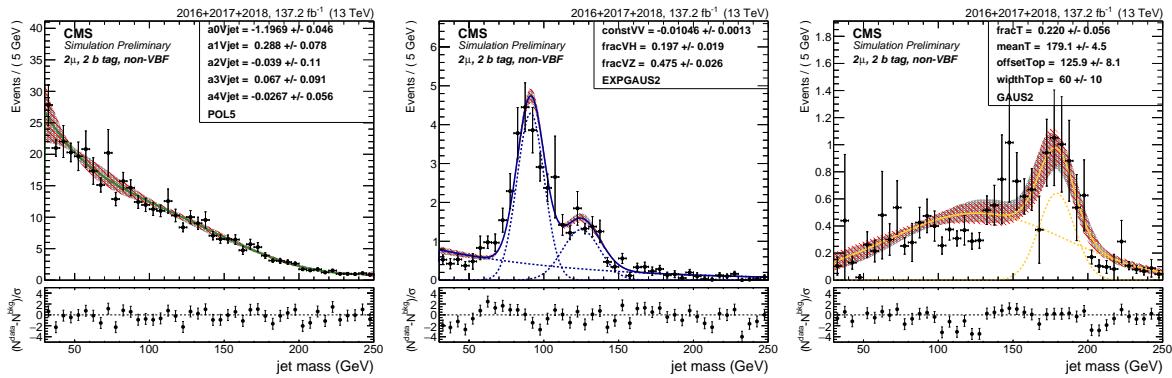


Figure 117: Fit to the simulated m_j in the 2 muons, 2 b-tag category for the three backgrounds: V+jets (left), VV (center), Top (right).

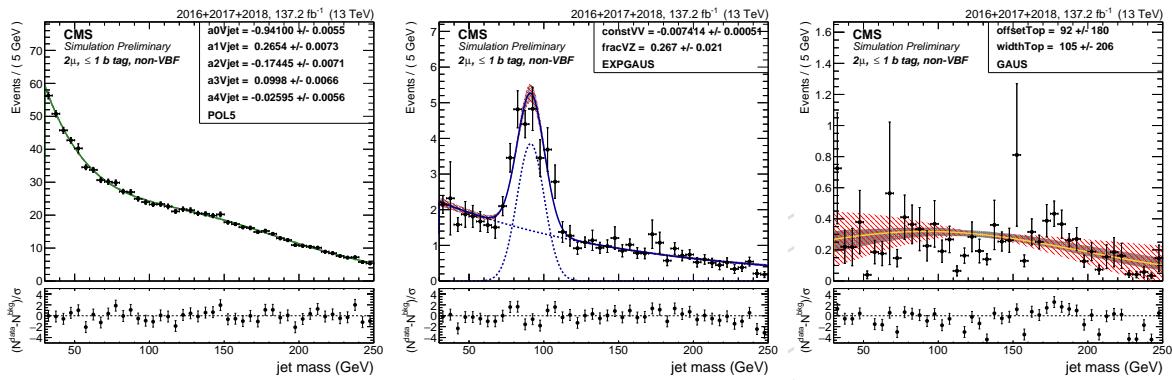


Figure 118: Fit to the simulated m_j in the 2 muons, 0 b-tag category for the three backgrounds: V+jets (left), VV (center), Top (right).

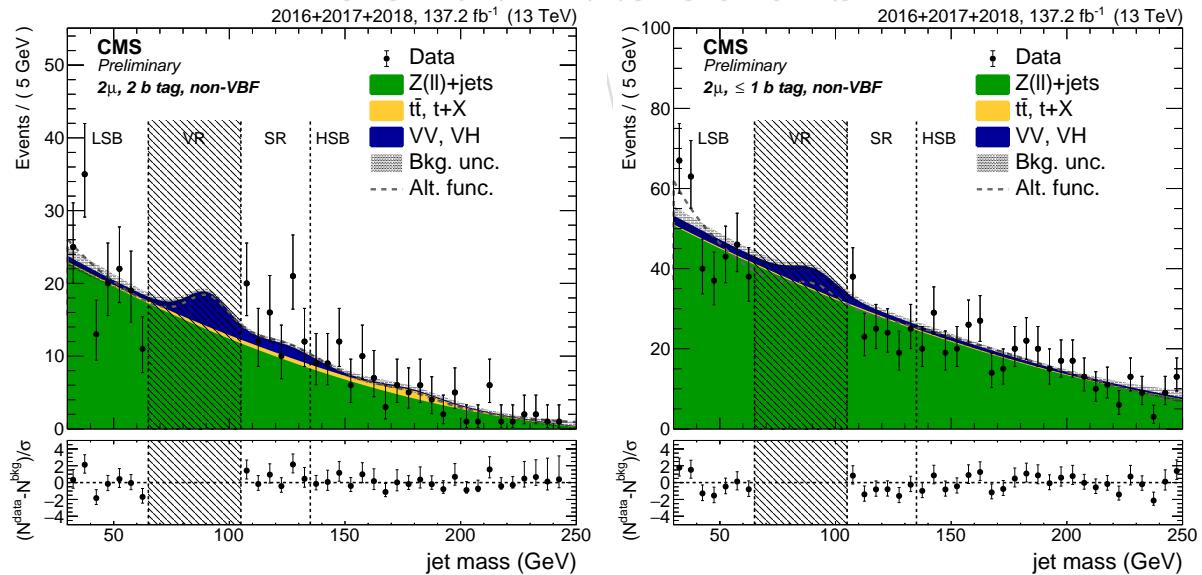


Figure 119: Fit to data m_j in the 2 muons 2 b-tag (left) and 0 b-tag (right) category.

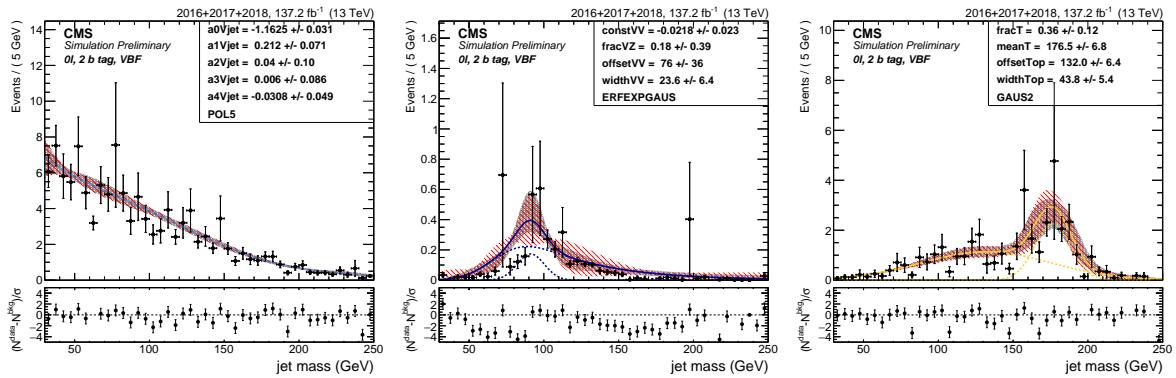


Figure 120: Fit to the simulated m_j in the 0 lepton, 2 b-tag, VBF category for the three backgrounds: V +jets (left), VV (center), Top (right).

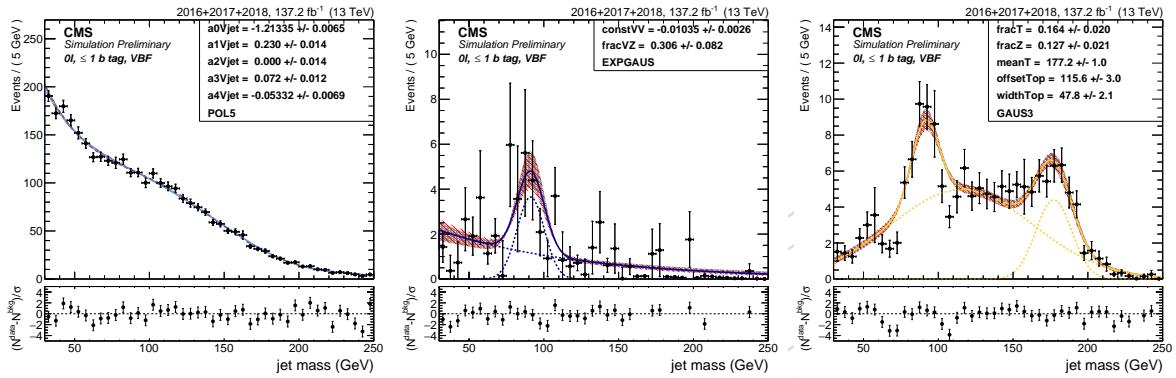


Figure 121: Fit to the simulated m_j in the 0 lepton, 0 b-tag, VBF category for the three backgrounds: V +jets (left), VV (center), Top (right).

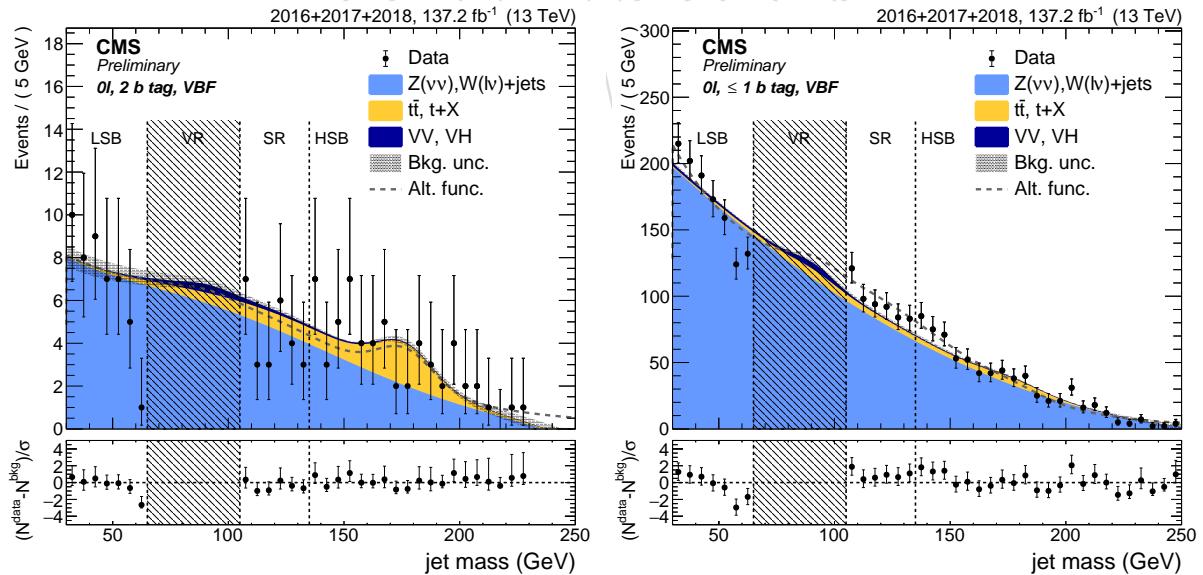


Figure 122: Fit to data m_j in the 0 lepton VBF 2 b-tag (left) and 0 b-tag (right) category.

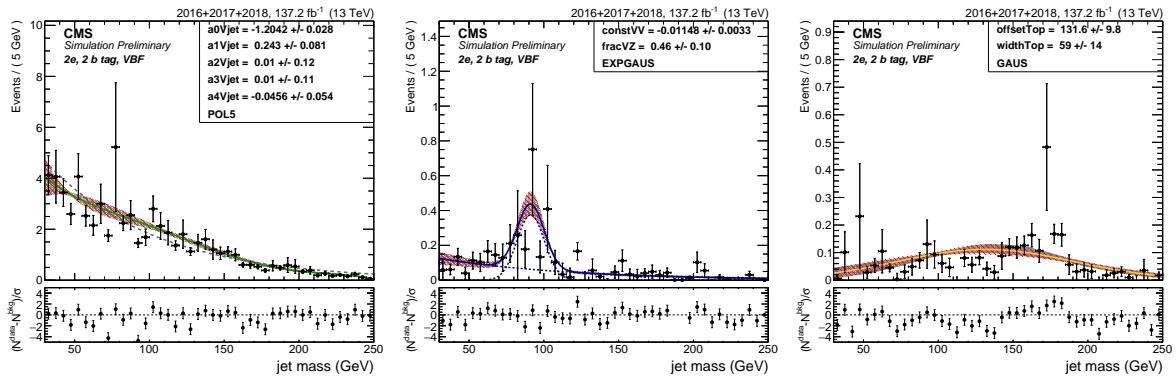


Figure 123: Fit to the simulated m_j in the 2 electrons, 2 b-tag, VBF category for the three backgrounds: V +jets (left), VV (center), Top (right).

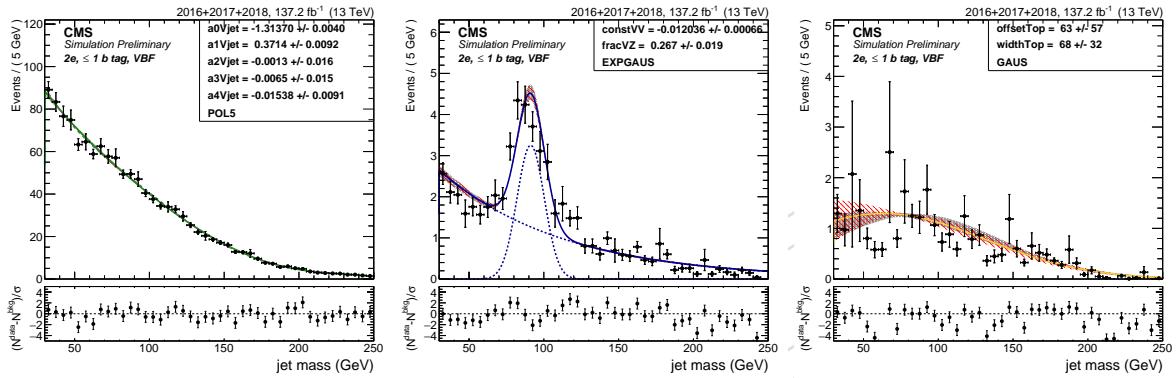


Figure 124: Fit to the simulated m_j in the 2 electrons, 0 b-tag, VBF category for the three backgrounds: V +jets (left), VV (center), Top (right).

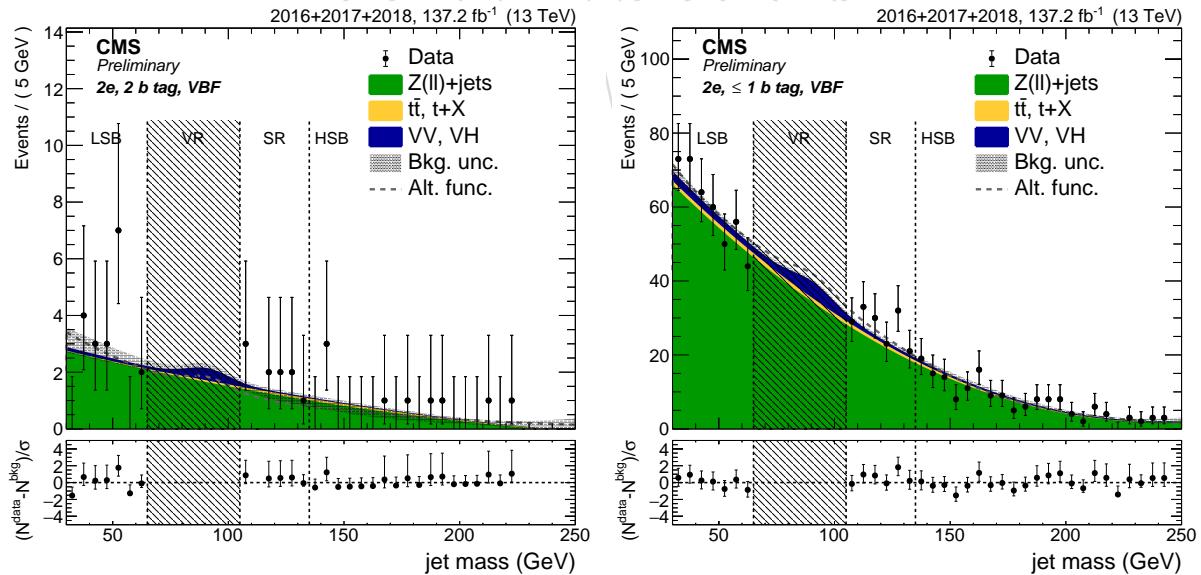


Figure 125: Fit to data m_j in the 2 electrons VBF 2 b-tag (left) and 0 b-tag (right) category.

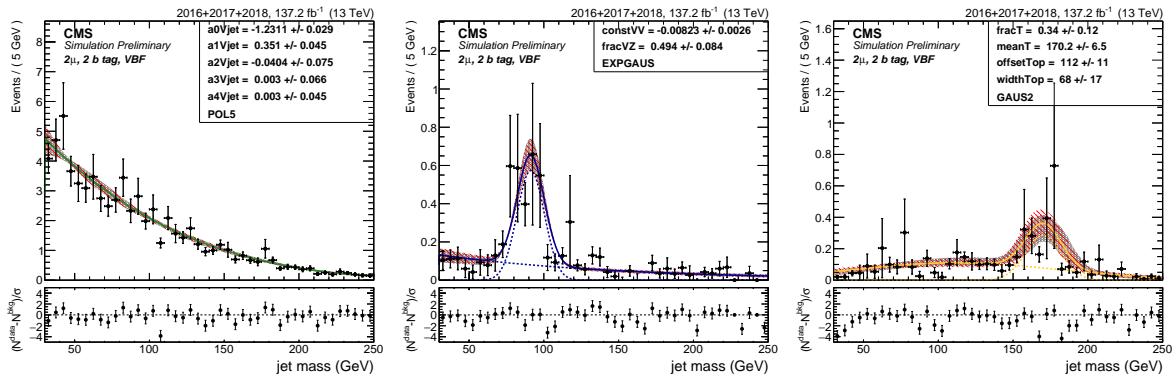


Figure 126: Fit to the simulated m_j in the 2 muons, 2 b-tag, VBF category for the three backgrounds: V+jets (left), VV (center), Top (right).

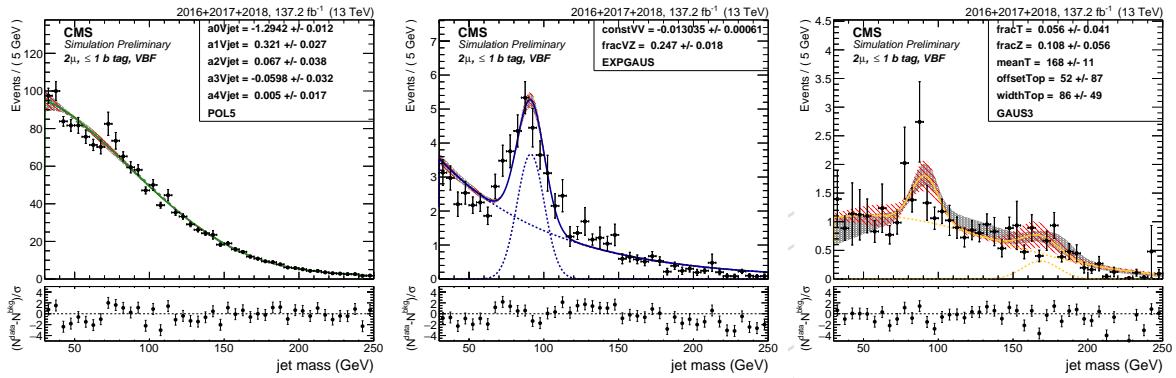


Figure 127: Fit to the simulated m_j in the 2 muons, 0 b-tag, VBF category for the three backgrounds: V+jets (left), VV (center), Top (right).

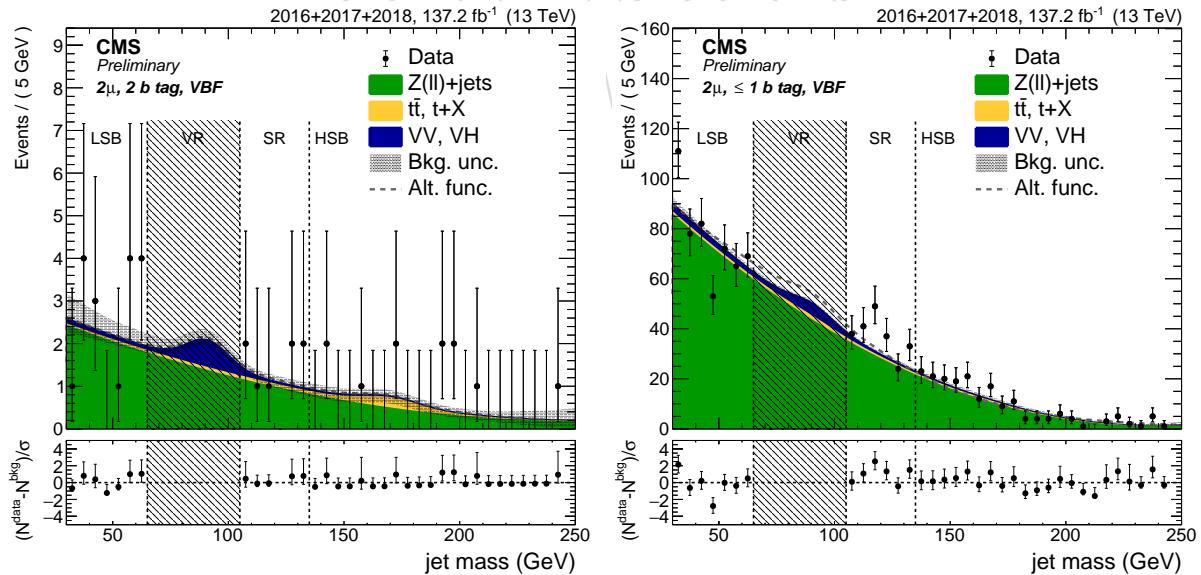


Figure 128: Fit to data m_j in the 2 muons VBF 2 b-tag (left) and 0 b-tag (right) category.

794 **8.2 Background shape**

The mass of the resonance candidate (m_X) is parametrized separately for the V+jets ($N_{SR}^{Vjet}(m_X)$, $N_{SB}^{Vjet}(m_X)$), t \bar{t} ($N_{SR}^{Top}(m_X)$, $N_{SB}^{Top}(m_X)$), and dibosons ($N_{SR}^{VV}(m_X)$, $N_{SB}^{VV}(m_X)$). These functions are extracted fitting the simulated m_X (or m_T^X in the zero-lepton channel) spectrum in SR and SB, respectively. The V+jets and t \bar{t} are weighted to match the normalization from the m_j fit, and the diboson is normalized to luminosity. The V+jets functions are used to extract the α -function:

$$\alpha(m_X) = \frac{N_{SR}^{Vjet}(m_X)}{N_{SB}^{Vjet}(m_X)}$$

795 The main background is extracted through a fit to data in the SB, after subtracting the corre-
 796 sponding Top and VV contribution from data. The resulting shape is then multiplied by the
 797 α -function in order to get the main background expectation in the SR. Finally, the Top and
 798 diboson contribution in the SR is added to the main background estimation.

799 In formulas, the procedure used to extract the total background prediction is the following:

$$N_{SR}^{main}(m_X) = N_{SB}^{main}(m_X) \times \alpha(m_X)$$

$$N_{SR,SB}^{bkg}(m_X) = N_{SR,SB}^{main}(m_X) + N_{SR,SB}^{Top}(m_X) + N_{SR,SB}^{VV}(m_X)$$

$$N_{SR}^{data}(m_X) = \left[N_{SB}^{data}(m_X) - N_{SB}^{Top}(m_X) - N_{SB}^{VV}(m_X) \right] \times \left[\frac{N_{SR}^{Vjet}(m_X)}{N_{SB}^{Vjet}(m_X)} \right] + N_{SR}^{Top}(m_X) + N_{SR}^{VV}(m_X)$$

800 The functions used to parametrize the m_X distributions are:

Exp: a simple exponential function. Its simplicity is balanced by the limited possibility to model the m_X tails in some channels:

$$F_{\text{Exp}}(x) = e^{ax}$$

Exp2: a double exponential function. It has better description of the tails, but introduces two new parameters:

$$F_{\text{Exp2}}(x) = (1 - f_0) \cdot e^{ax} + f_0 \cdot e^{bx}$$

ExpN: a product of two exponentials:

$$F_{\text{ExpN}}(x) = e^{ax+b/x}$$

ExpTail: a modified exponential function with an additional parameter to model the exponential tails:

$$F_{\text{ExpTail}}(x) = e^{-x/(a+bx)}$$

Pow: a power-law function:

$$F_{\text{Pow}}(x) = 1/(x/\sqrt{s})^a$$

801 The functions chosen to parametrize the main background and extract the α -function are re-
 802 ported in Table 28 for each category.

803 As a cross-check for the main α -function used in the background estimation, an additional α -
 804 function is extracted with alternative function choices. Table 28 reports both the main function
 and the alternative function.

category		Main bkg function	Main bkg alternative	$t\bar{t}$, t+X	VV
2 b-tag	0ℓ	ExpN	ExpTail	ExpN	ExpN
	2e	ExpN	ExpTail	ExpN	ExpN
	2μ	ExpN	ExpTail	ExpN	ExpN
0 b-tag	0ℓ	ExpN	ExpTail	ExpN	ExpN
	2e	ExpN	ExpTail	ExpN	ExpN
	2μ	ExpN	ExpTail	ExpN	ExpN
2 b-tag VBF	0ℓ	ExpN	ExpTail	ExpN	ExpN
	2e	ExpN	ExpTail	ExpN	ExpN
	2μ	ExpN	ExpTail	ExpN	ExpN
0 b-tag VBF	0ℓ	ExpN	ExpTail	ExpN	ExpN
	2e	ExpN	ExpTail	ExpN	ExpN
	2μ	ExpN	ExpTail	ExpN	ExpN

Table 28: Main and alternative functions chosen to parametrize the main background contribu-
 tion in the m_X distribution for each channel.

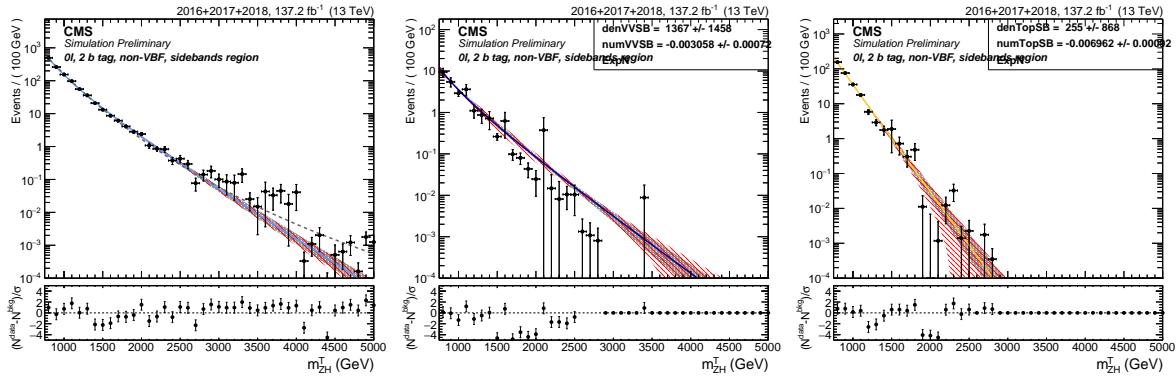


Figure 129: 0 leptons, 2 b-tag channel. Fits to the simulated background components $V + \text{jets}$ (left), VV (center), Top (right) in the sidebands (SB).

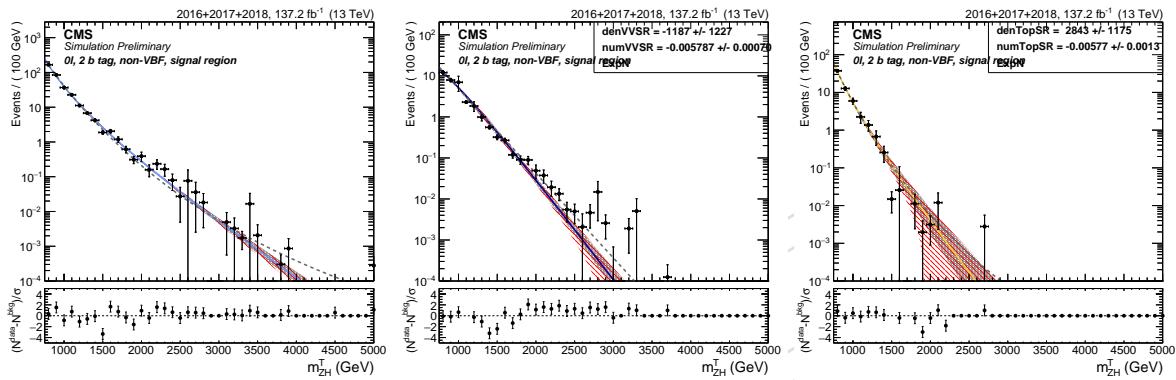


Figure 130: 0 leptons, 2 b-tag channel. Fits to the simulated background components $V + \text{jets}$ (left), VV (center), Top (right) in the signal region (SR).

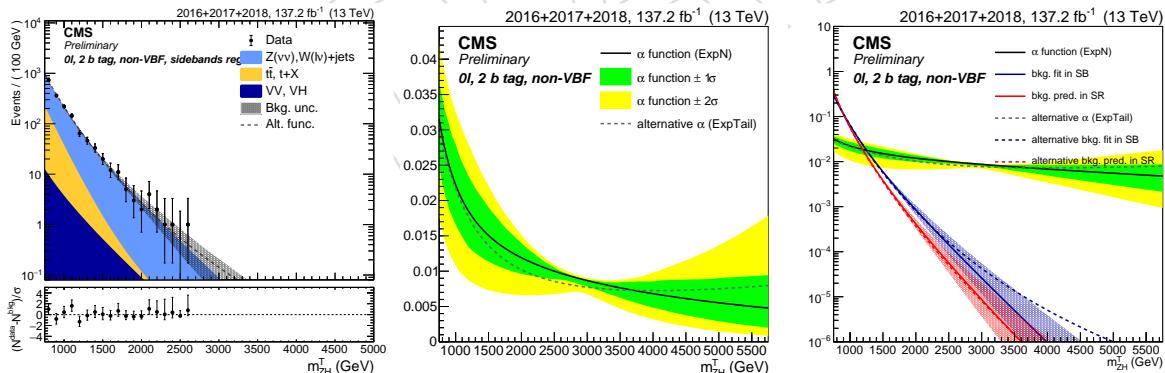


Figure 131: 0 leptons, 2 b-tag channel. Fit to data in the SB (left), alpha function (center), and alpha function compared to the background shape in both SB and SR (right). The black line, with the corresponding 1σ (green) and 2σ (yellow) uncertainty bands, represents the α -function. The gray line is the alternative α -function. The blue and red lines represent the estimated background in the SB and SR, respectively, with both the main (solid line) and alternative (dotted line) parametrization.

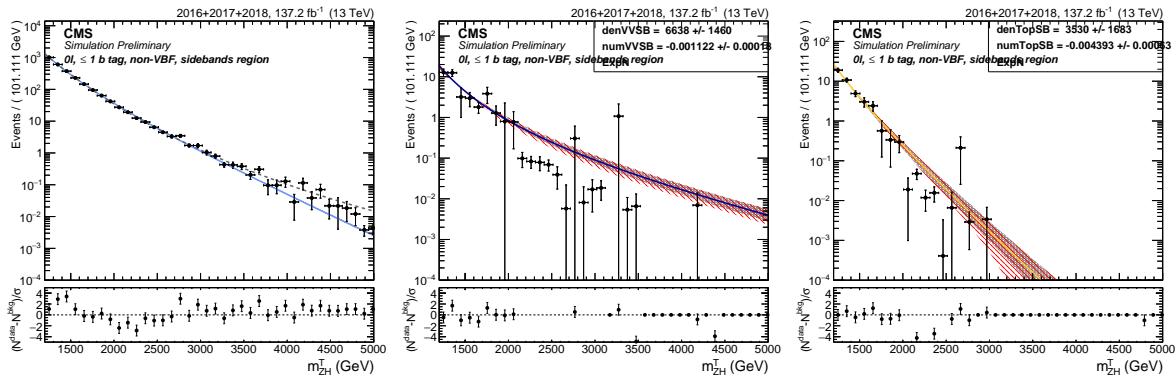


Figure 132: 0 leptons, 0 b-tag channel. Fits to the simulated background components V +jets (left), VV (center), Top (right) in the sidebands (SB).

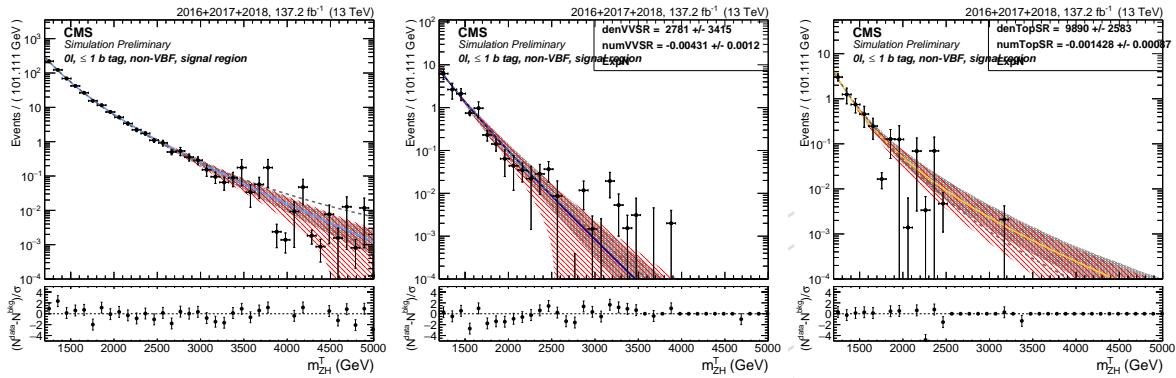


Figure 133: 0 leptons, 0 b-tag channel. Fits to the simulated background components V +jets (left), VV (center), Top (right) in the signal region (SR).

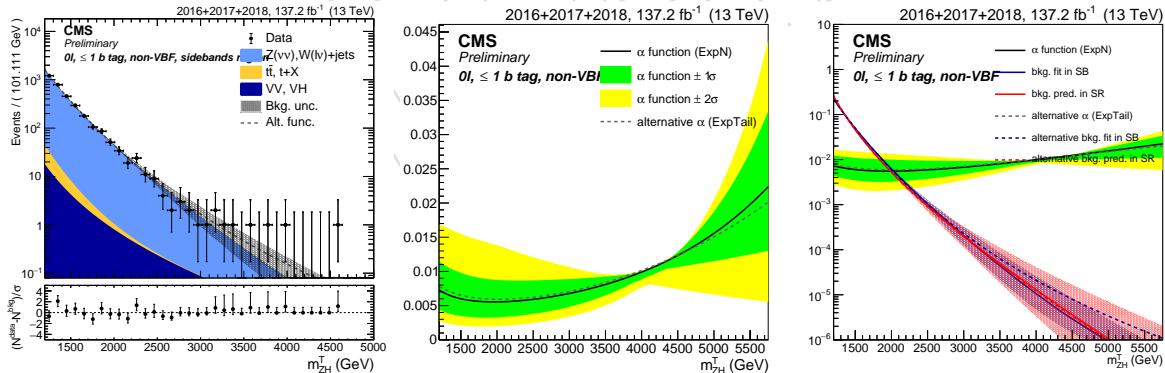


Figure 134: 0 leptons, 0 b-tag channel. Fit to data in the SB (left), alpha function (center), and alpha function compared to the background shape in both SB and SR (right). The black line, with the corresponding 1 σ (green) and 2 σ (yellow) uncertainty bands, represents the α -function. The gray line is the alternative α -function. The blue and red lines represent the estimated background in the SB and SR, respectively, with both the main (solid line) and alternative (dotted line) parametrization.

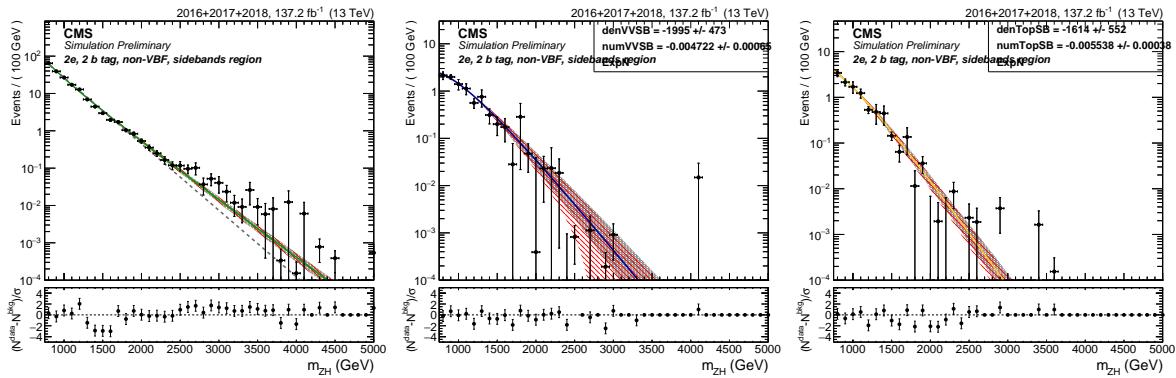


Figure 135: 2 electrons, 2 b-tag channel. Fits to the simulated background components $V + \text{jets}$ (left), VV (center), Top (right) in the sidebands (SB).

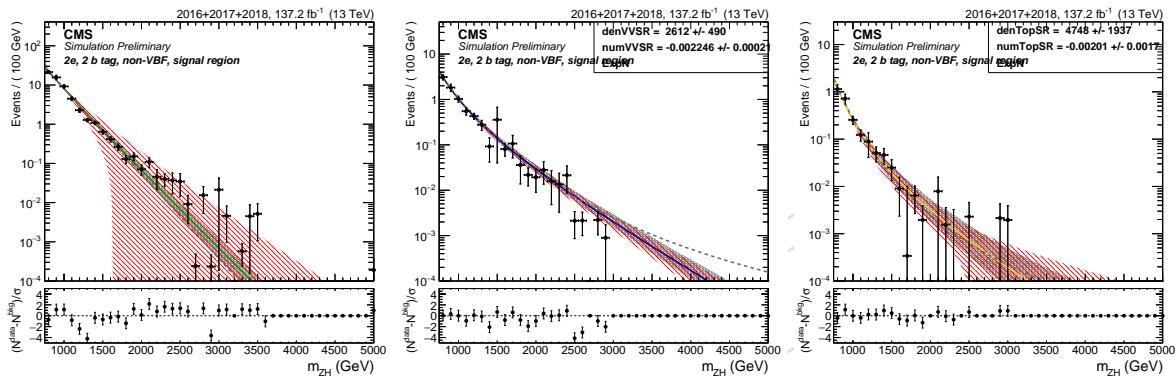


Figure 136: 2 electrons, 2 b-tag channel. Fits to the simulated background components $V + \text{jets}$ (left), VV (center), Top (right) in the signal region (SR).

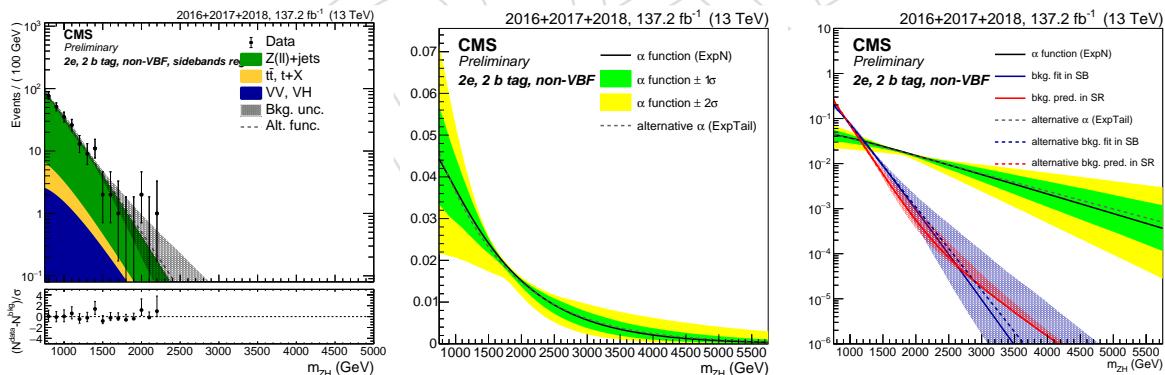


Figure 137: 2 electrons, 2 b-tag channel. Fit to data in the SB (left), alpha function (center), and alpha function compared to the background shape in both SB and SR (right). The black line, with the corresponding 1σ (green) and 2σ (yellow) uncertainty bands, represents the α -function. The gray line is the alternative α -function. The blue and red lines represent the estimated background in the SB and SR, respectively, with both the main (solid line) and alternative (dotted line) parametrization.

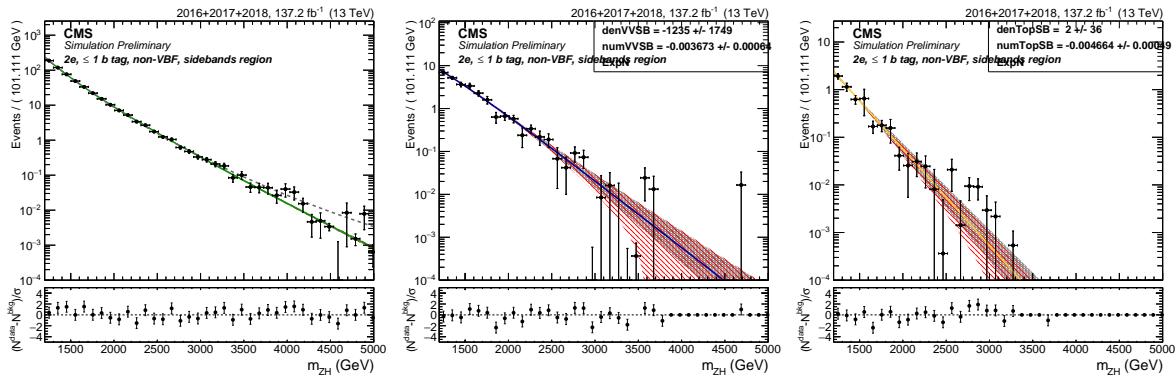


Figure 138: 2 electrons, 0 b-tag channel. Fits to the simulated background components V +jets (left), VV (center), Top (right) in the sidebands (SB).

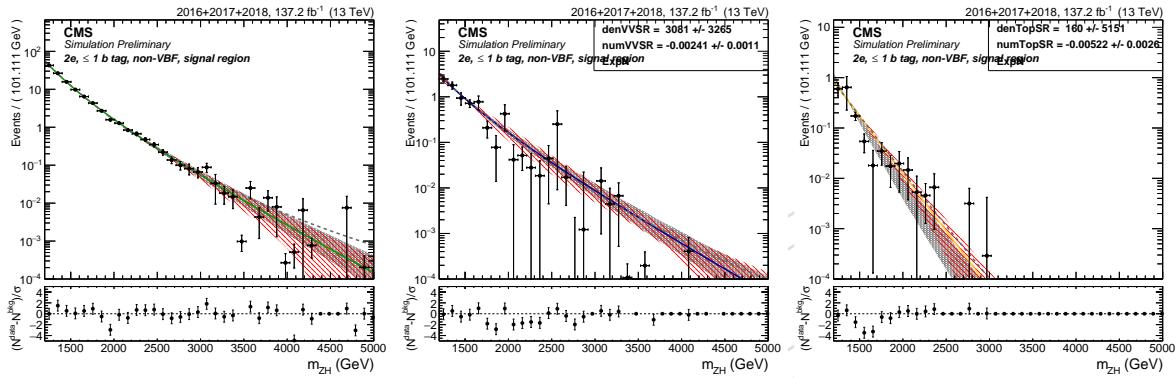


Figure 139: 2 electrons, 0 b-tag channel. Fits to the simulated background components V +jets (left), VV (center), Top (right) in the signal region (SR).

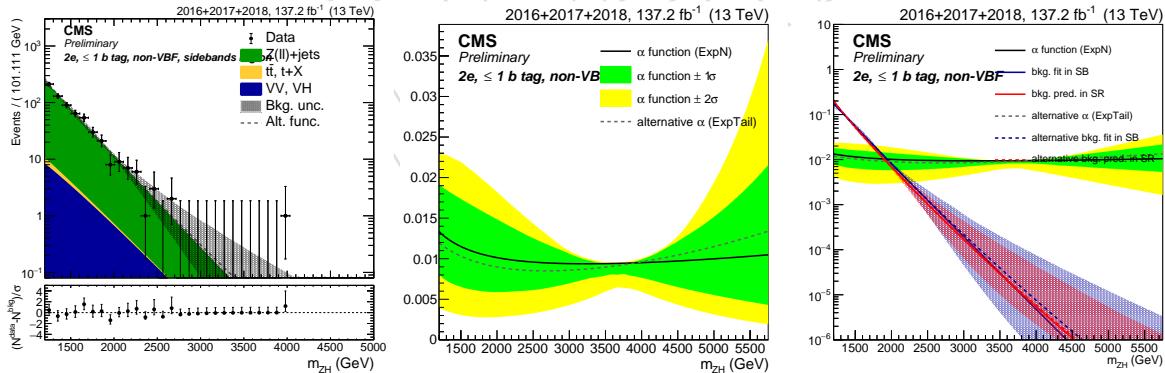


Figure 140: 2 electrons, 0 b-tag channel. Fit to data in the SB (left), alpha function (center), and alpha function compared to the background shape in both SB and SR (right). The black line, with the corresponding 1σ (green) and 2σ (yellow) uncertainty bands, represents the α -function. The gray line is the alternative α -function. The blue and red lines represent the estimated background in the SB and SR, respectively, with both the main (solid line) and alternative (dotted line) parametrization.

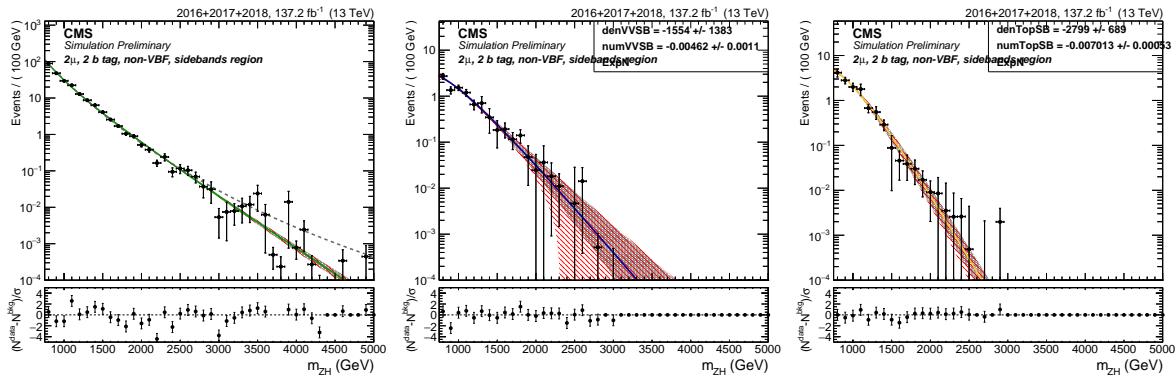


Figure 141: 2 muons, 2 b-tag channel. Fits to the simulated background components $V + \text{jets}$ (left), VV (center), Top (right) in the sidebands (SB).

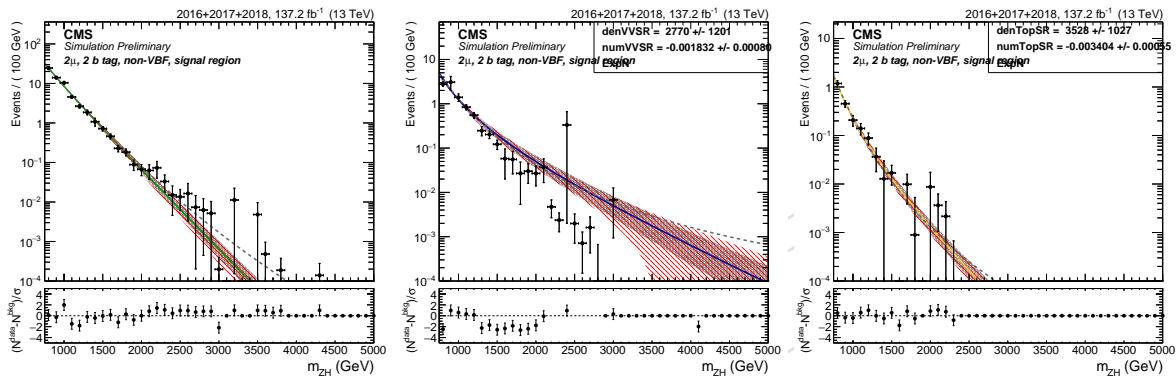


Figure 142: 2 muons, 2 b-tag channel. Fits to the simulated background components $V + \text{jets}$ (left), VV (center), Top (right) in the signal region (SR).

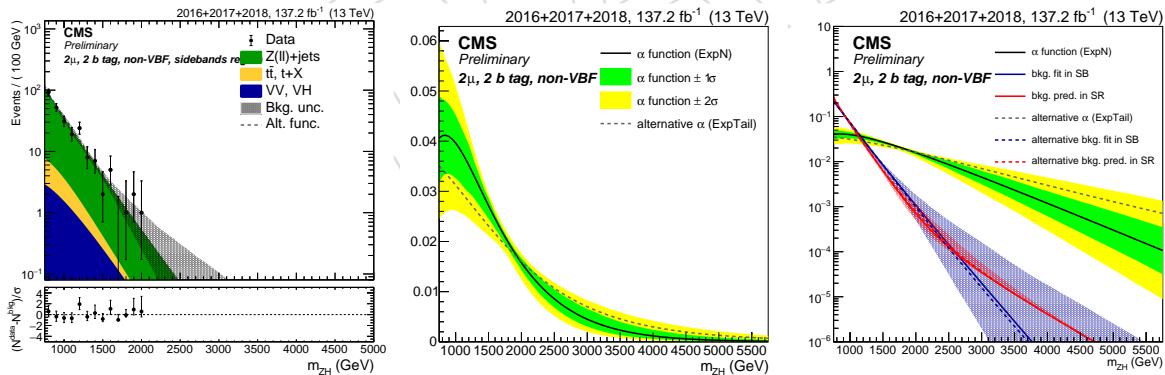


Figure 143: 2 muons, 2 b-tag channel. Fit to data in the SB (left), alpha function (center), and alpha function compared to the background shape in both SB and SR (right). The black line, with the corresponding 1σ (green) and 2σ (yellow) uncertainty bands, represents the α -function. The gray line is the alternative α -function. The blue and red lines represent the estimated background in the SB and SR, respectively, with both the main (solid line) and alternative (dotted line) parametrization.

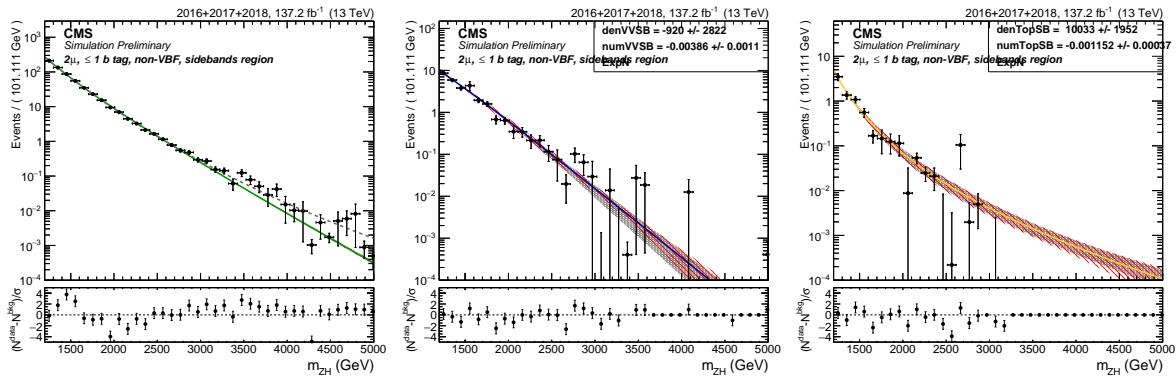


Figure 144: 2 muons, 0 b-tag channel. Fits to the simulated background components V +jets (left), VV (center), Top (right) in the sidebands (SB).

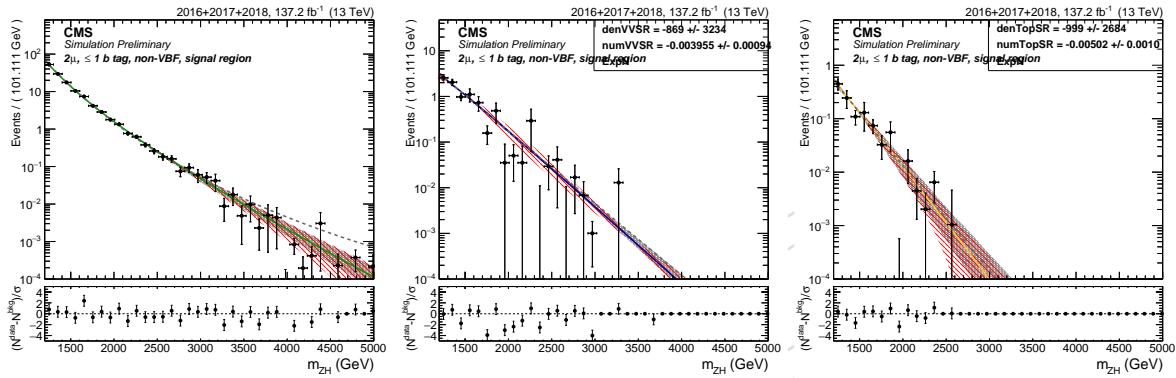


Figure 145: 2 muons, 0 b-tag channel. Fits to the simulated background components V +jets (left), VV (center), Top (right) in the signal region (SR).

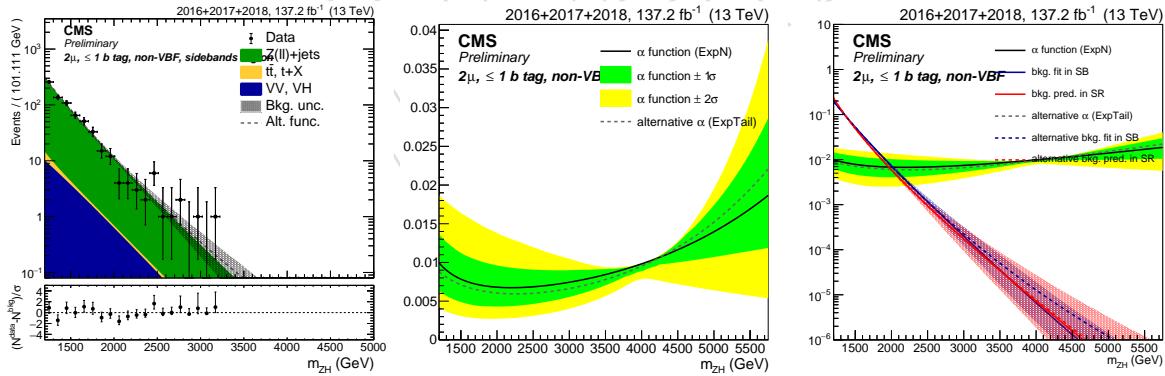


Figure 146: 2 muons, 0 b-tag channel. Fit to data in the SB (left), alpha function (center), and alpha function compared to the background shape in both SB and SR (right). The black line, with the corresponding 1 σ (green) and 2 σ (yellow) uncertainty bands, represents the α -function. The gray line is the alternative α -function. The blue and red lines represent the estimated background in the SB and SR, respectively, with both the main (solid line) and alternative (dotted line) parametrization.

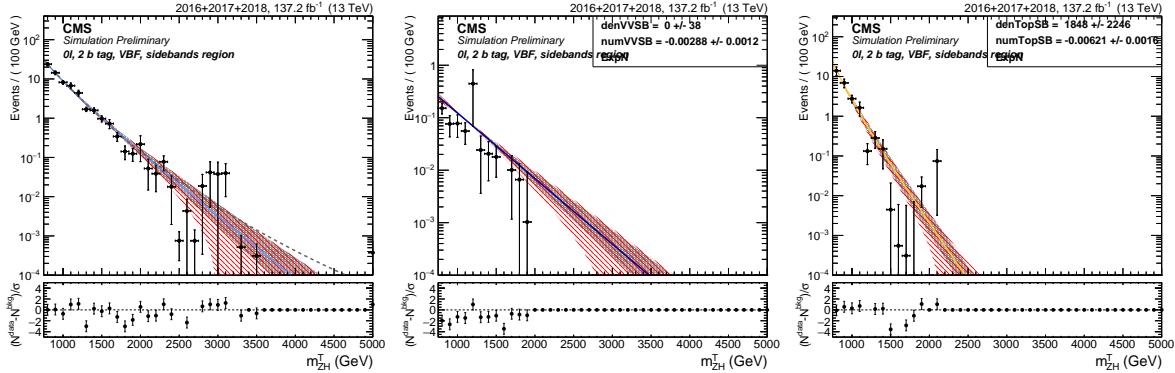


Figure 147: 0 leptons, 2 b-tag VBF channel. Fits to the simulated background components V +jets (left), VV (center), Top (right) in the sidebands (SB).

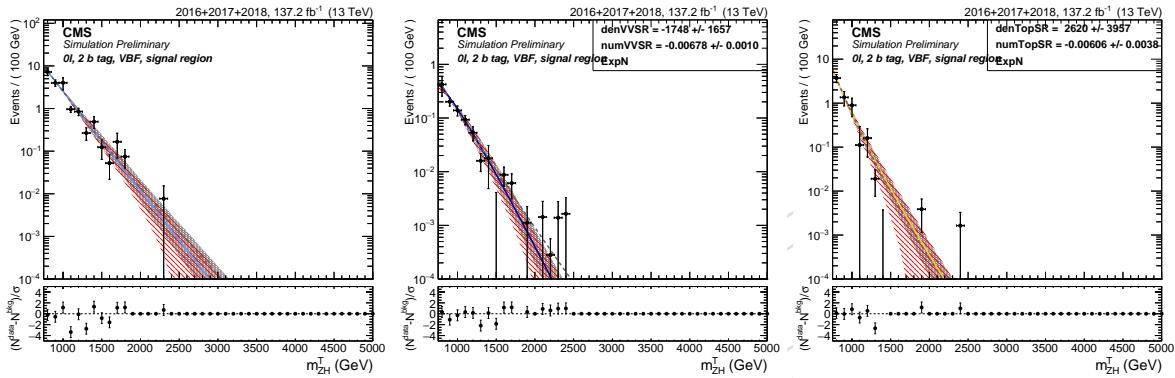


Figure 148: 0 leptons, 2 b-tag VBF channel. Fits to the simulated background components V +jets (left), VV (center), Top (right) in the signal region (SR).

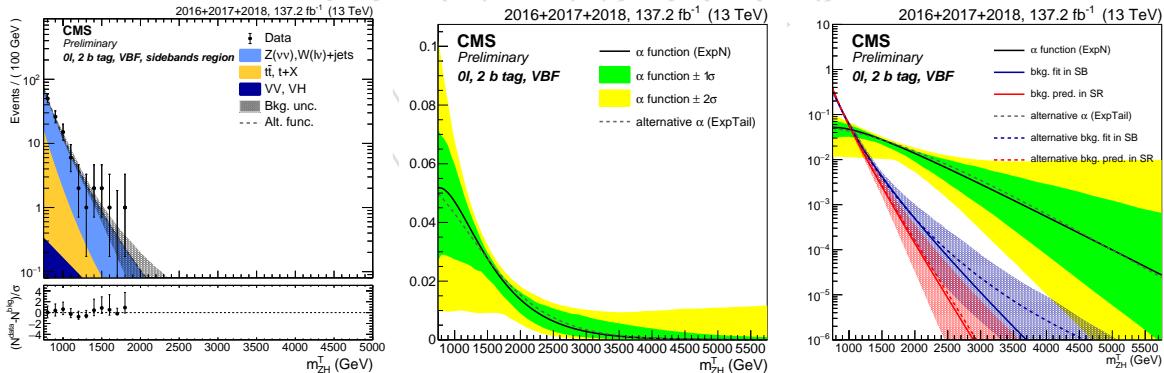


Figure 149: 0 leptons, 2 b-tag VBF channel. Fit to data in the SB (left), alpha function (center), and alpha function compared to the background shape in both SB and SR (right). The black line, with the corresponding 1σ (green) and 2σ (yellow) uncertainty bands, represents the α -function. The gray line is the alternative α -function. The blue and red lines represent the estimated background in the SB and SR, respectively, with both the main (solid line) and alternative (dotted line) parametrization.

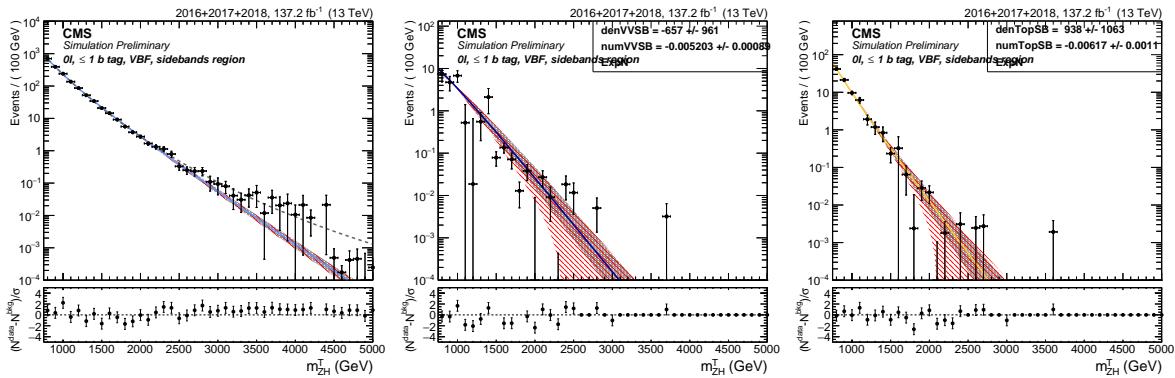


Figure 150: 0 leptons, 0 b-tag VBF channel. Fits to the simulated background components V+jets (left), VV (center), Top (right) in the sidebands (SB).

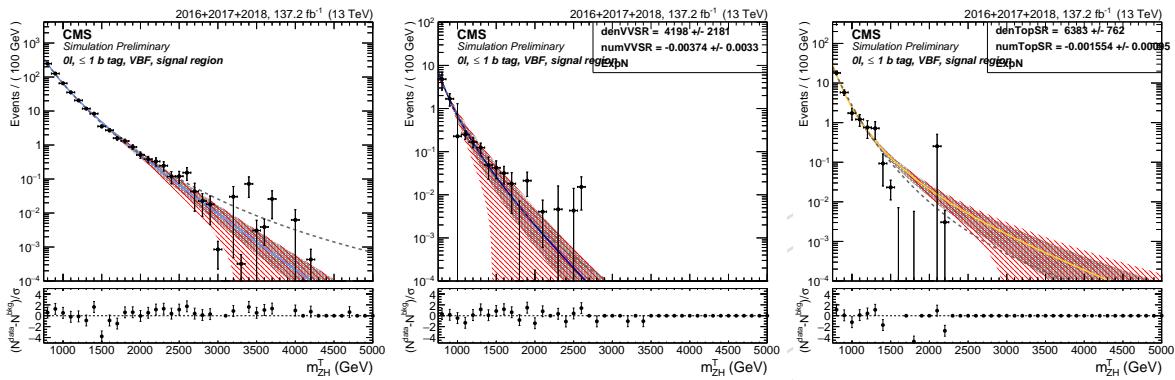


Figure 151: 0 leptons, 0 b-tag VBF channel. Fits to the simulated background components V+jets (left), VV (center), Top (right) in the signal region (SR).

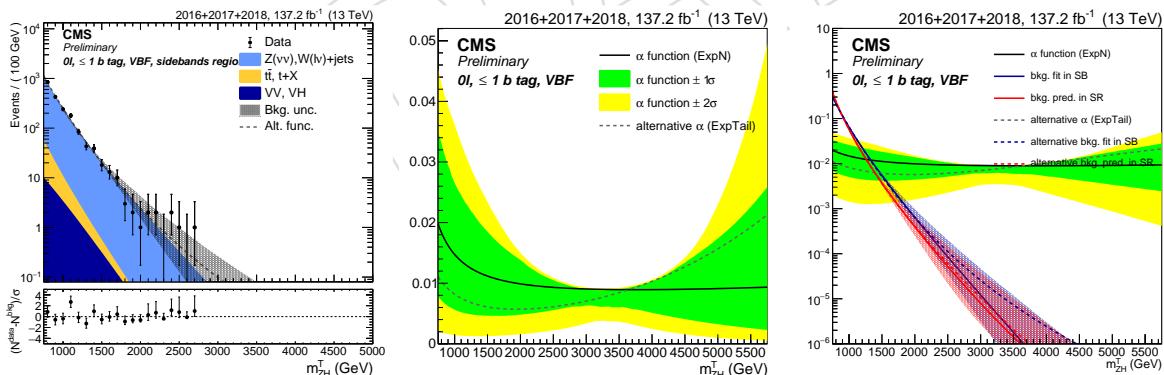


Figure 152: 0 leptons, 0 b-tag VBF channel. Fit to data in the SB (left), alpha function (center), and alpha function compared to the background shape in both SB and SR (right). The black line, with the corresponding 1σ (green) and 2σ (yellow) uncertainty bands, represents the α -function. The gray line is the alternative α -function. The blue and red lines represent the estimated background in the SB and SR, respectively, with both the main (solid line) and alternative (dotted line) parametrization.

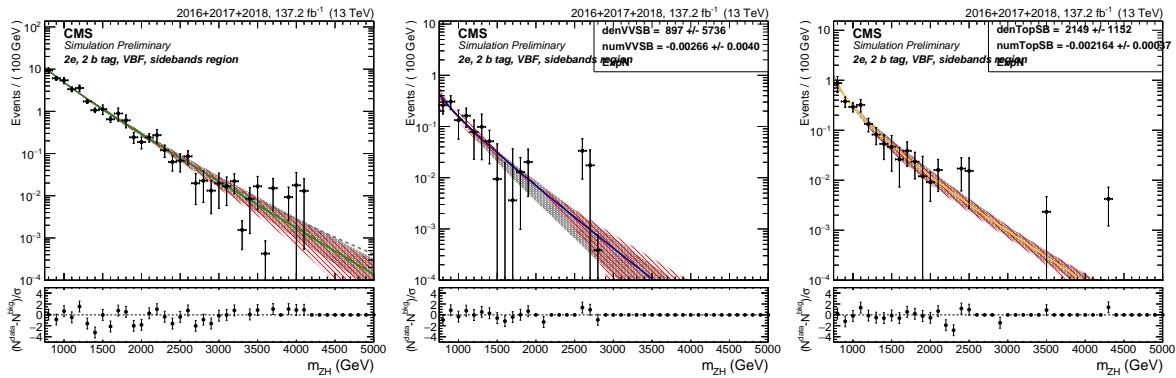


Figure 153: 2 electrons, 2 b-tag VBF channel. Fits to the simulated background components V+jets (left), VV (center), Top (right) in the sidebands (SB).

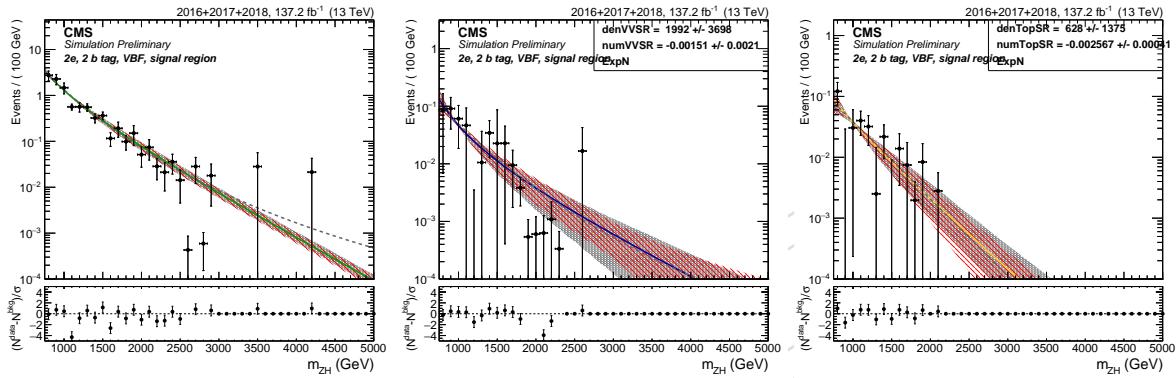


Figure 154: 2 electrons, 2 b-tag VBF channel. Fits to the simulated background components V+jets (left), VV (center), Top (right) in the signal region (SR).

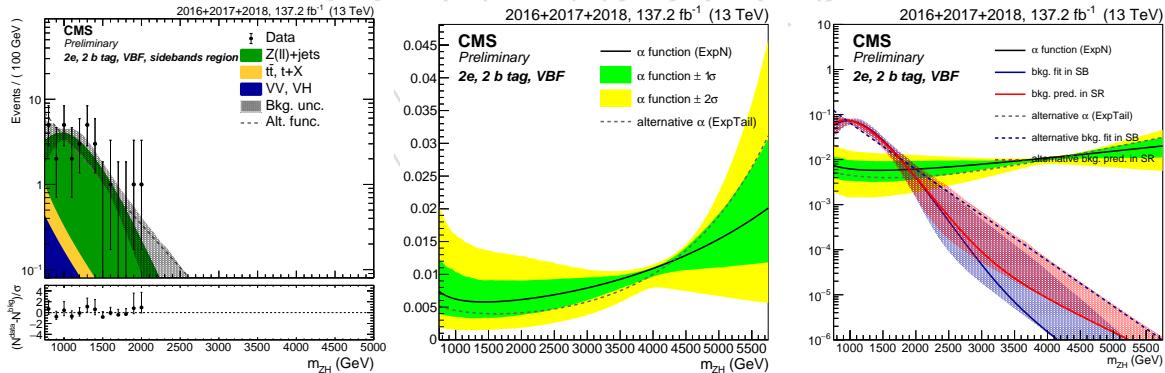


Figure 155: 2 electrons, 2 b-tag VBF channel. Fit to data in the SB (left), alpha function (center), and alpha function compared to the background shape in both SB and SR (right). The black line, with the corresponding 1σ (green) and 2σ (yellow) uncertainty bands, represents the α -function. The gray line is the alternative α -function. The blue and red lines represent the estimated background in the SB and SR, respectively, with both the main (solid line) and alternative (dotted line) parametrization.

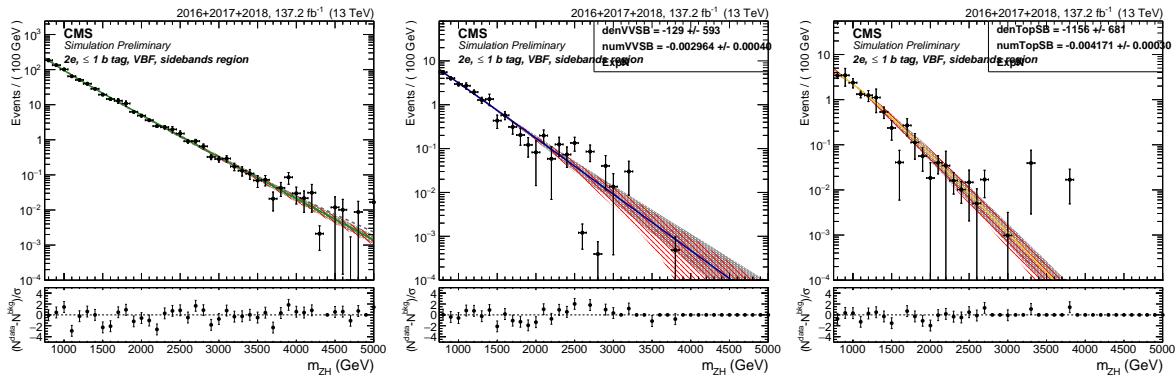


Figure 156: 2 electrons, 0 b-tag VBF channel. Fits to the simulated background components V+jets (left), VV (center), Top (right) in the sidebands (SB).

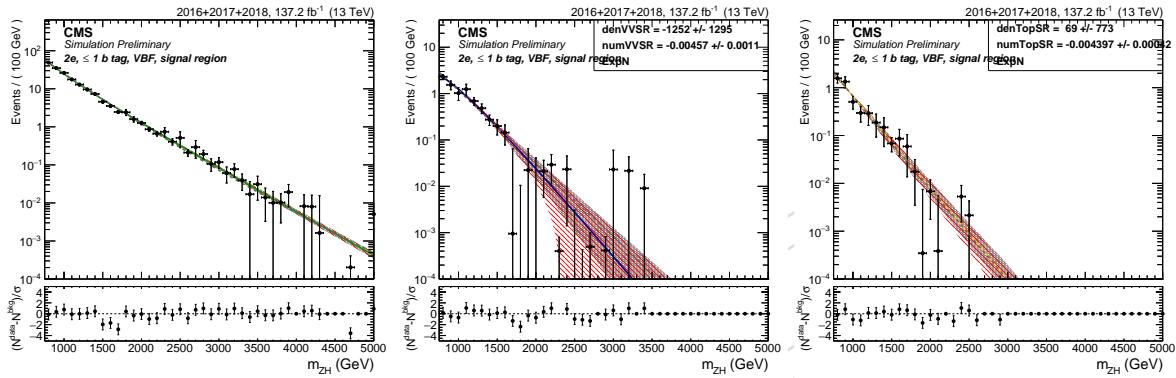


Figure 157: 2 electrons, 0 b-tag VBF channel. Fits to the simulated background components V+jets (left), VV (center), Top (right) in the signal region (SR).

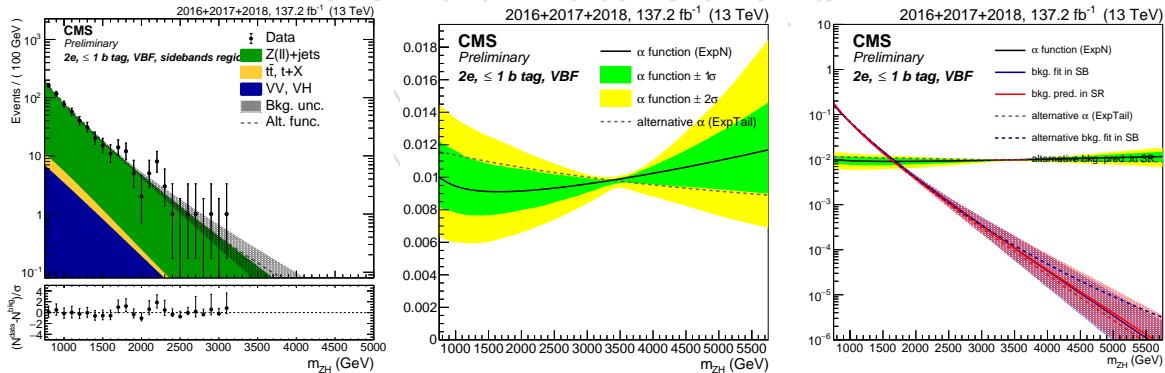


Figure 158: 2 electrons, 0 b-tag VBF channel. Fit to data in the SB (left), alpha function (center), and alpha function compared to the background shape in both SB and SR (right). The black line, with the corresponding 1σ (green) and 2σ (yellow) uncertainty bands, represents the α -function. The gray line is the alternative α -function. The blue and red lines represent the estimated background in the SB and SR, respectively, with both the main (solid line) and alternative (dotted line) parametrization.

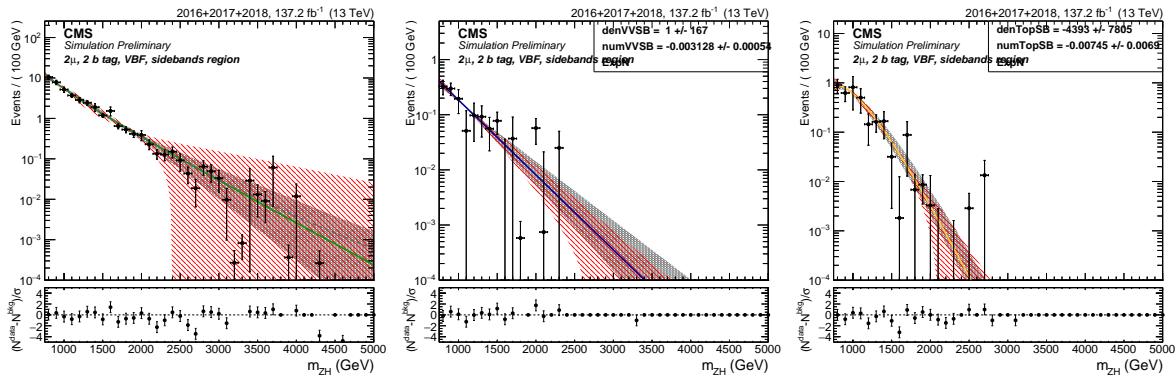


Figure 159: 2 muons, 2 b-tag VBF channel. Fits to the simulated background components V+jets (left), VV (center), Top (right) in the sidebands (SB).

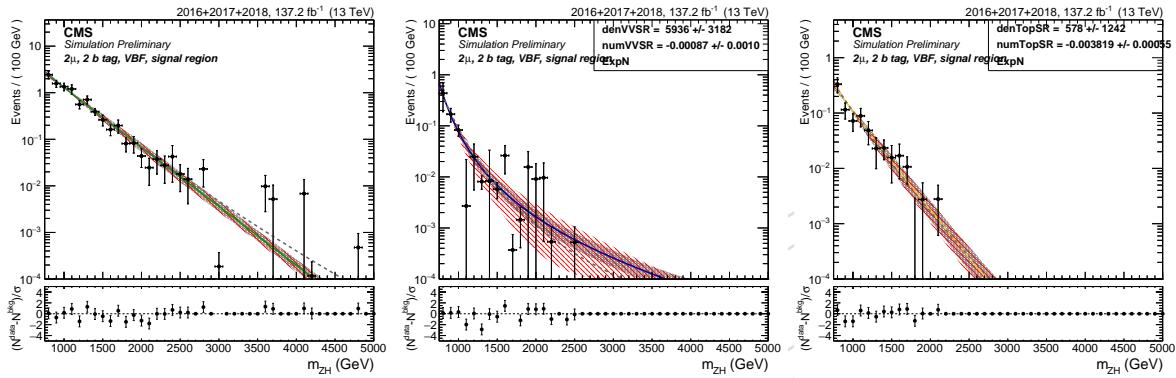


Figure 160: 2 muons, 2 b-tag VBF channel. Fits to the simulated background components V+jets (left), VV (center), Top (right) in the signal region (SR).

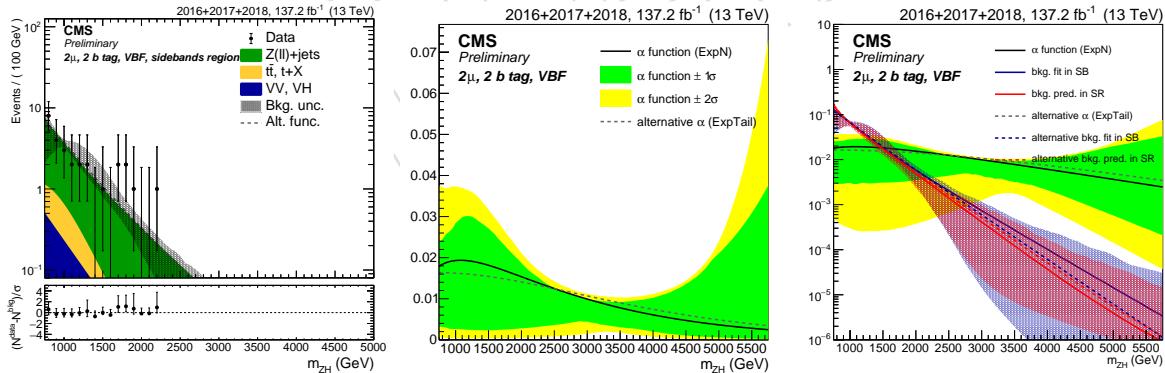


Figure 161: 2 muons, 2 b-tag VBF channel. Fit to data in the SB (left), alpha function (center), and alpha function compared to the background shape in both SB and SR (right). The black line, with the corresponding 1σ (green) and 2σ (yellow) uncertainty bands, represents the α -function. The gray line is the alternative α -function. The blue and red lines represent the estimated background in the SB and SR, respectively, with both the main (solid line) and alternative (dotted line) parametrization.

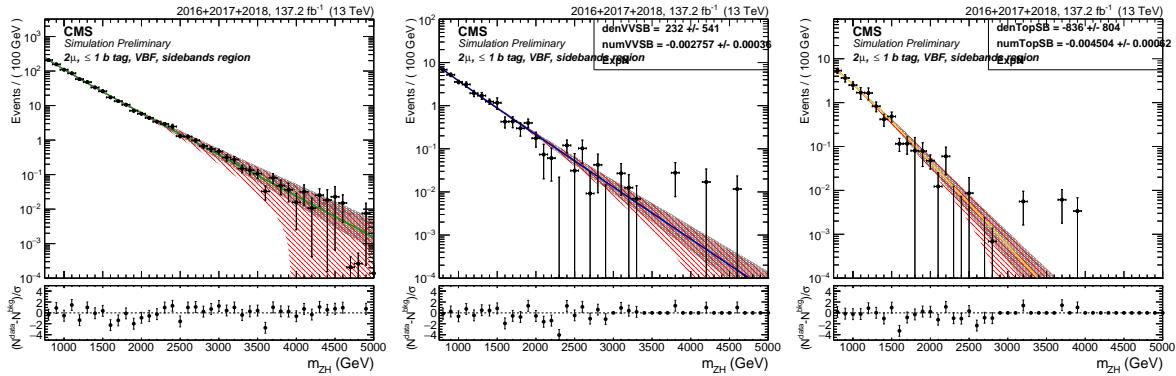


Figure 162: 2 muons, 0 b-tag VBF channel. Fits to the simulated background components V+jets (left), VV (center), Top (right) in the sidebands (SB).

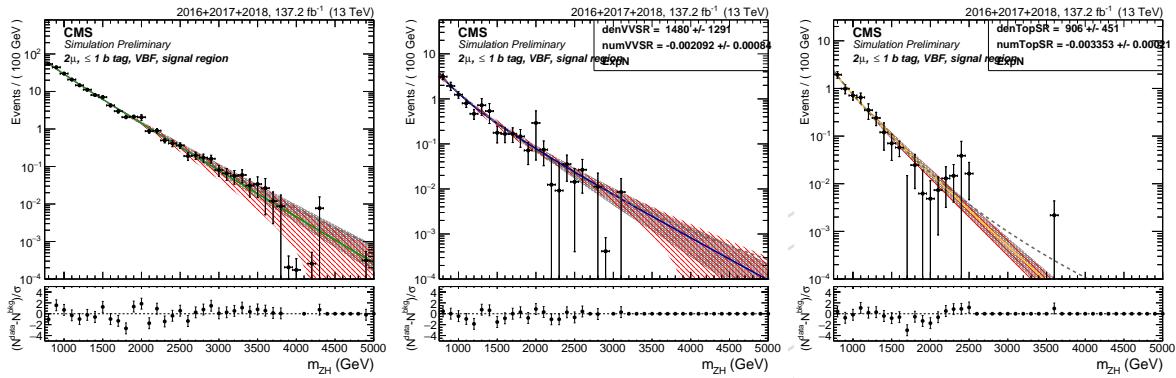


Figure 163: 2 muons, 0 b-tag VBF channel. Fits to the simulated background components V+jets (left), VV (center), Top (right) in the signal region (SR).

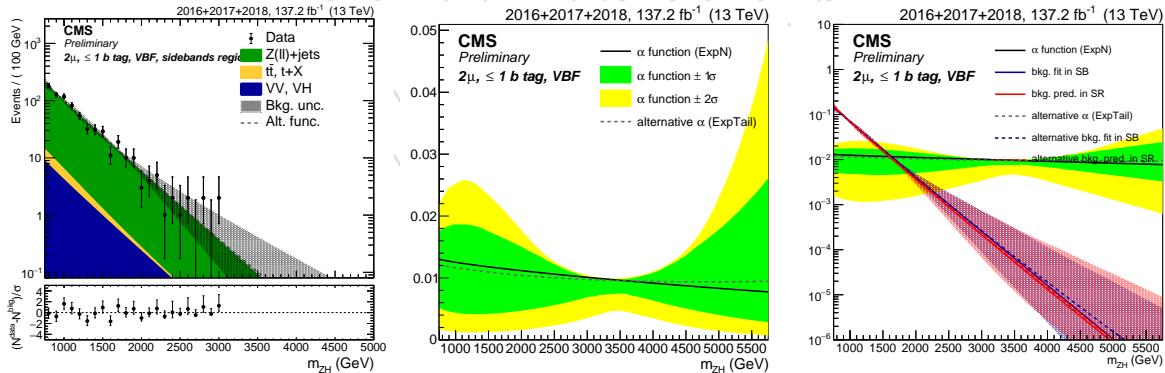


Figure 164: 2 muons, 0 b-tag VBF channel. Fit to data in the SB (left), alpha function (center), and alpha function compared to the background shape in both SB and SR (right). The black line, with the corresponding 1σ (green) and 2σ (yellow) uncertainty bands, represents the α -function. The gray line is the alternative α -function. The blue and red lines represent the estimated background in the SB and SR, respectively, with both the main (solid line) and alternative (dotted line) parametrization.

806 **8.3 Background prediction**

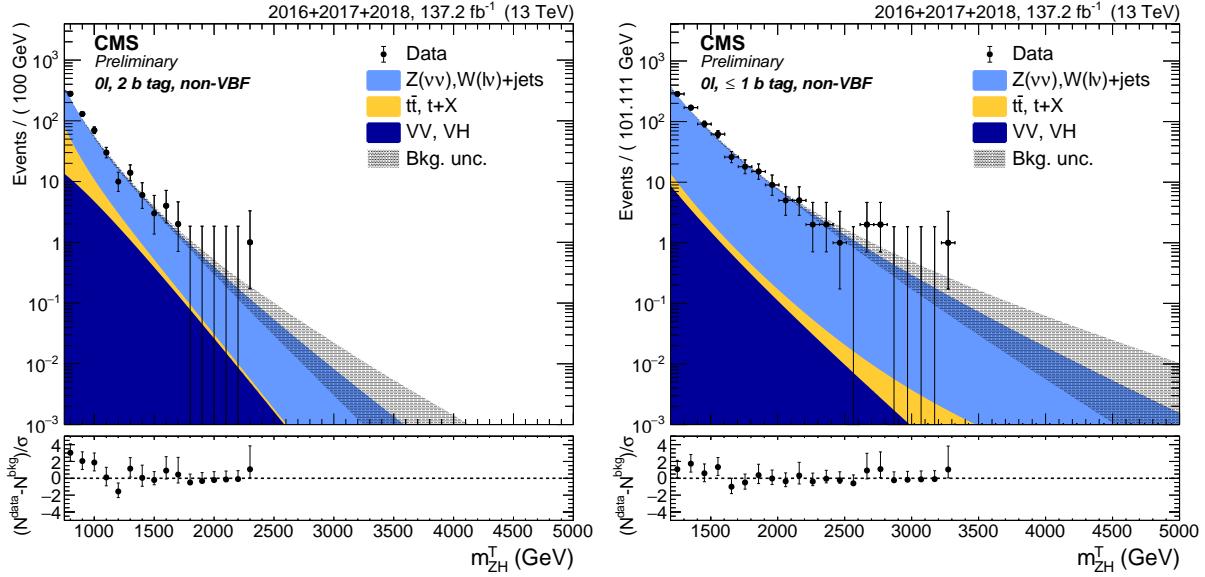


Figure 165: Expected background with the α method in the 0 lepton, 2 b-tag (left) and 0 b-tag (right) category.

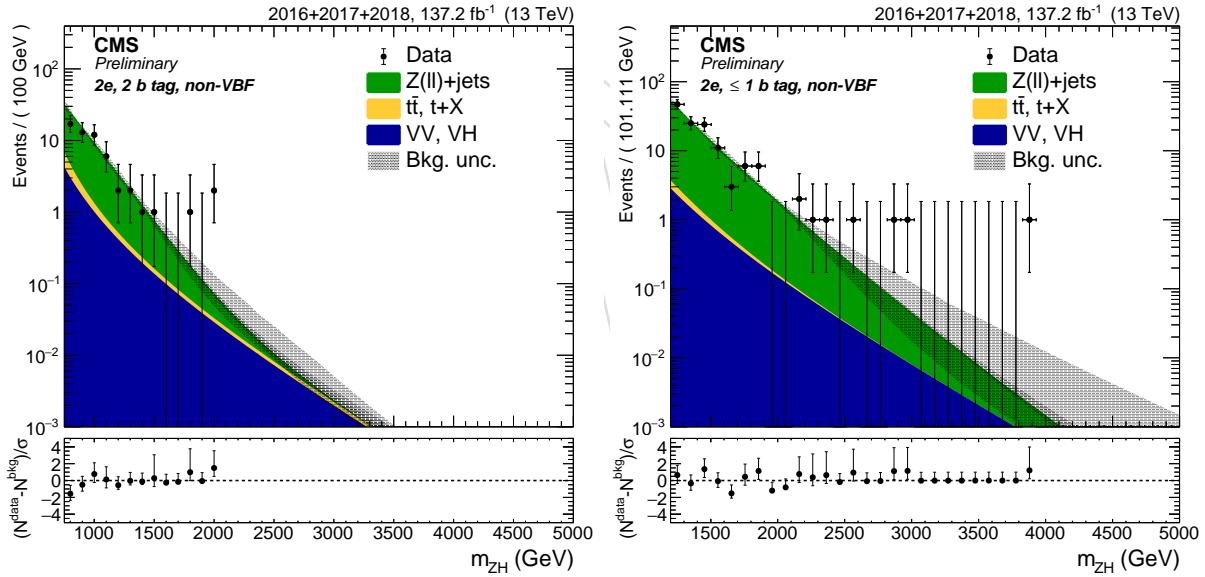


Figure 166: Expected background with the α method in the 2 electrons, 2 b-tag (left) and 0 b-tag (right) category.

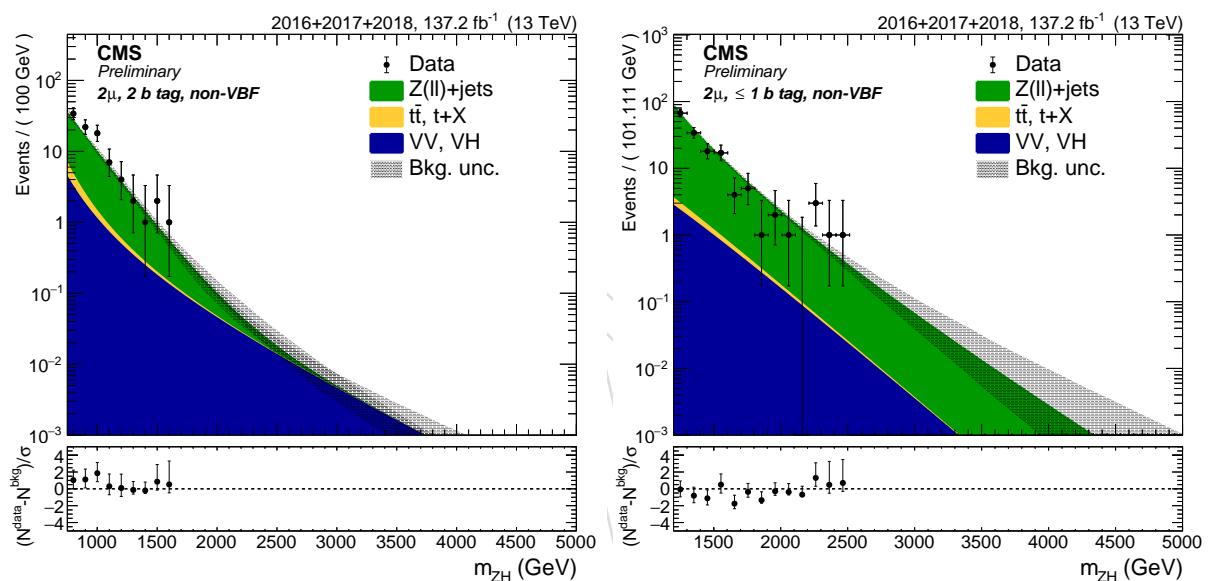


Figure 167: Expected background with the α method in the 2 muons, 2 b-tag (left) and 0 b-tag (right) category.

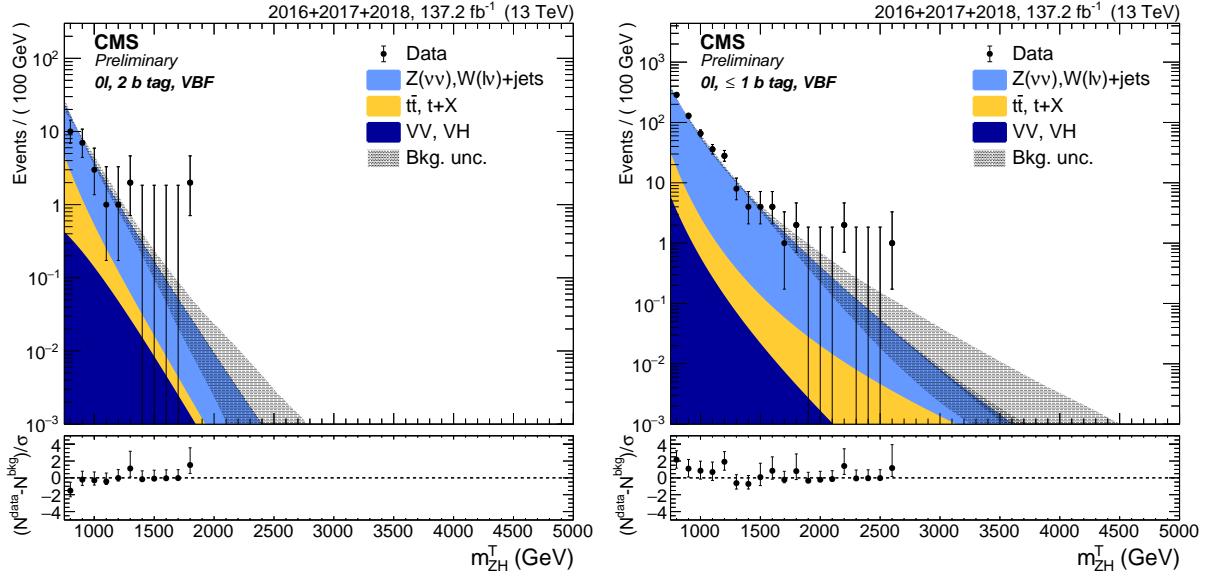


Figure 168: Expected background with the α method in the 0 lepton, VBF, 2 b-tag (left) and 0 b-tag (right) category.

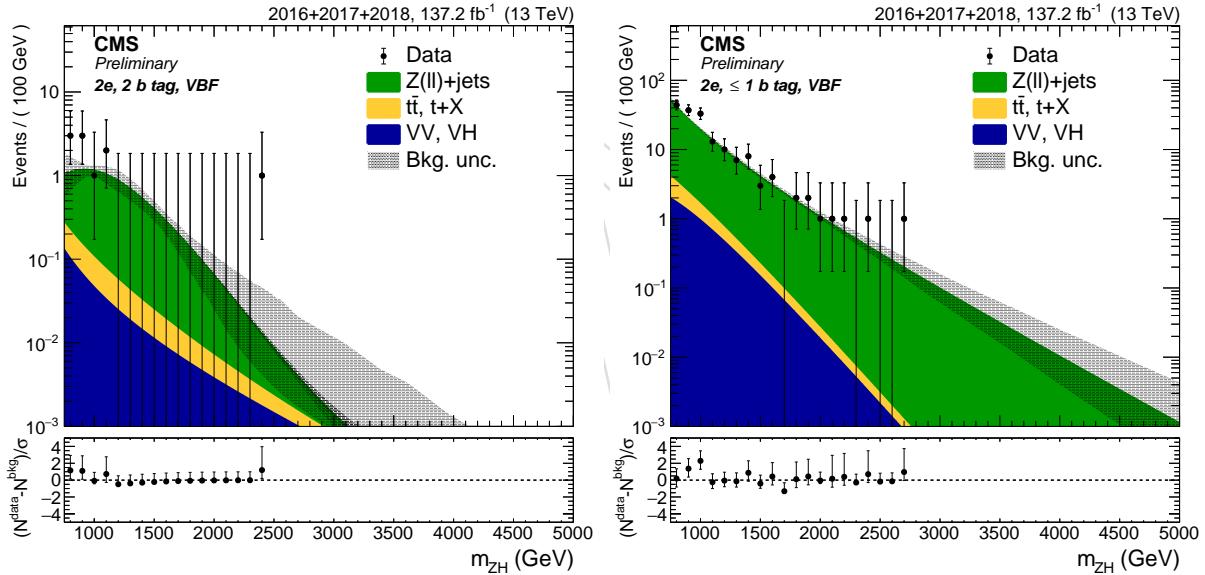


Figure 169: Expected background with the α method in the 2 electrons, VBF, 2 b-tag (left) and 0 b-tag (right) category.

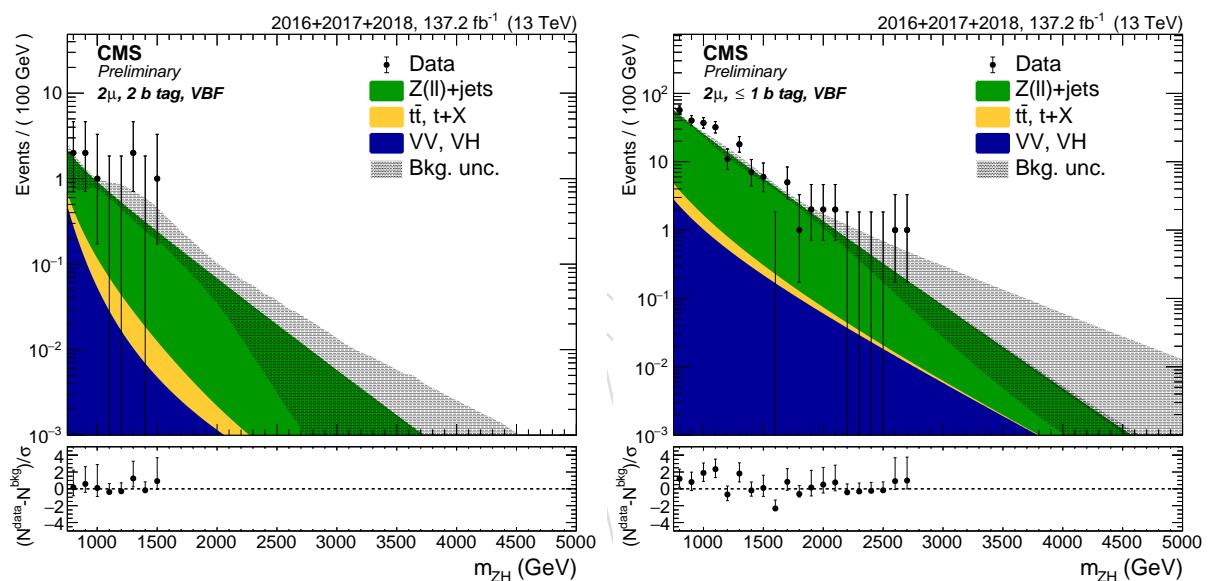


Figure 170: Expected background with the α method in the 2 muons, VBF, 2 b-tag (left) and 0 b-tag (right) category.

807 **8.4 Alpha method validation**

808 As a validation of the α -ratio method described in this Section, a closure test is performed on
 809 data. Instead of predicting the background in the real Higgs SR from both the lower and the
 810 upper jet mass sidebands, an alternative region is selected as a proxy for the SR. The lower
 811 sideband is split in two sub-regions: 30 – 50 GeV (LSB) and 50 – 65 GeV (EXT). The first is
 812 considered as the low sideband for the purpose of this test, while the latter is exploited as a
 813 pseudo-signal region (and thus it can be used even in case the VV region has to be kept blind).
 814 The high sideband is instead effectively used in the fit without any modifications with respect
 815 to the standard α -ratio method.

816 In Figure 171-172 and Table 29, the predicted shape and normalizations obtained by running
 817 the α -method are compared to the observed ones in data. This cross check confirms that the
 818 α -method to extract the V+jets background is reliable and can be used to search for the sig-
 819 nal extraction. An overall acceptable agreement both in the normalization and the shape is
 820 obtained in the different categories.

category	V +jets (\pm stat) (\pm syst)	$t\bar{t}, t+X$	VV	Bkg. sum	Observed
2 b-tag	0ℓ $304 \pm 13 \pm 5$	7 ± 1	5 ± 1	315 ± 14	306 ± 17
	$2e$ $50 \pm 5 \pm 3$	1 ± 0	2 ± 1	52 ± 6	49 ± 7
	2μ $54 \pm 5 \pm 1$	1 ± 0	2 ± 0	57 ± 5	52 ± 7
0 b-tag	0ℓ $561 \pm 19 \pm 16$	2 ± 0	7 ± 2	569 ± 25	536 ± 23
	$2e$ $98 \pm 7 \pm 10$	0 ± 0	4 ± 1	103 ± 12	115 ± 11
	2μ $111 \pm 7 \pm 10$	1 ± 0	5 ± 1	117 ± 13	126 ± 11
2 b-tag VBF	0ℓ $25 \pm 3 \pm 0$	1 ± 0	0 ± 0	25 ± 3	13 ± 4
	$2e$ $6 \pm 2 \pm 0$	0 ± 0	0 ± 0	6 ± 2	9 ± 3
	2μ $4 \pm 2 \pm 0$	0 ± 0	0 ± 0	5 ± 2	9 ± 3
0 b-tag VBF	0ℓ $466 \pm 15 \pm 3$	6 ± 2	5 ± 1	477 ± 15	412 ± 20
	$2e$ $157 \pm 9 \pm 1$	3 ± 1	6 ± 1	166 ± 10	149 ± 12
	2μ $210 \pm 11 \pm 4$	3 ± 1	7 ± 2	220 ± 12	206 ± 14

Table 29: Expected and observed background yield in the SR proxy jet mass region ($50 < m_j < 65$ GeV) categories).

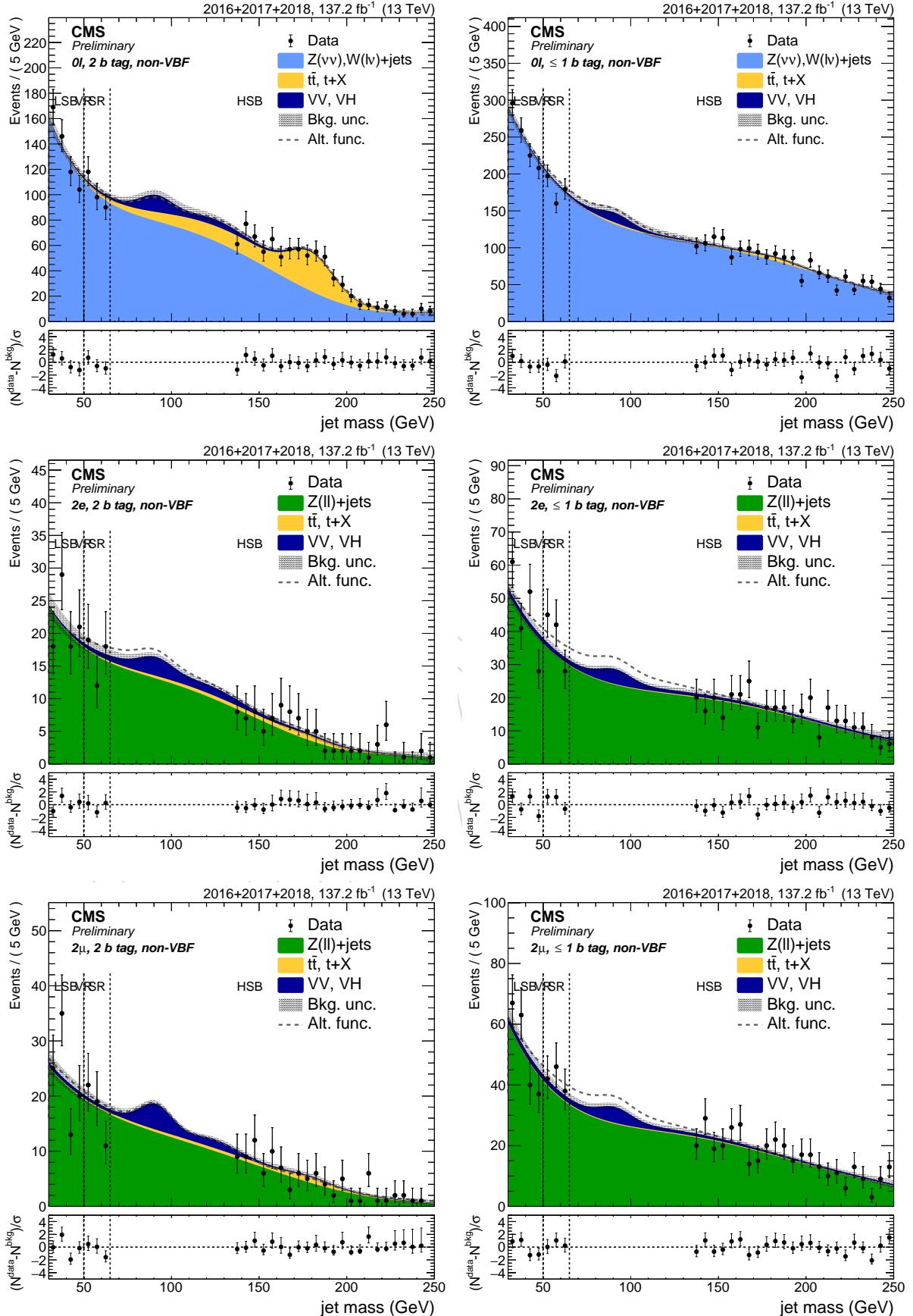


Figure 171: Fit to the m_j spectrum in data in the sidebands. The SR is replaced by splitting the lower m_j sideband ($50 < m_j < 65$ GeV) for validation purposes. Top: 0ℓ channel. Center: $2e$ channel. Bottom: 2μ channel. left: 2 b-tag category. right: 0 b-tag category

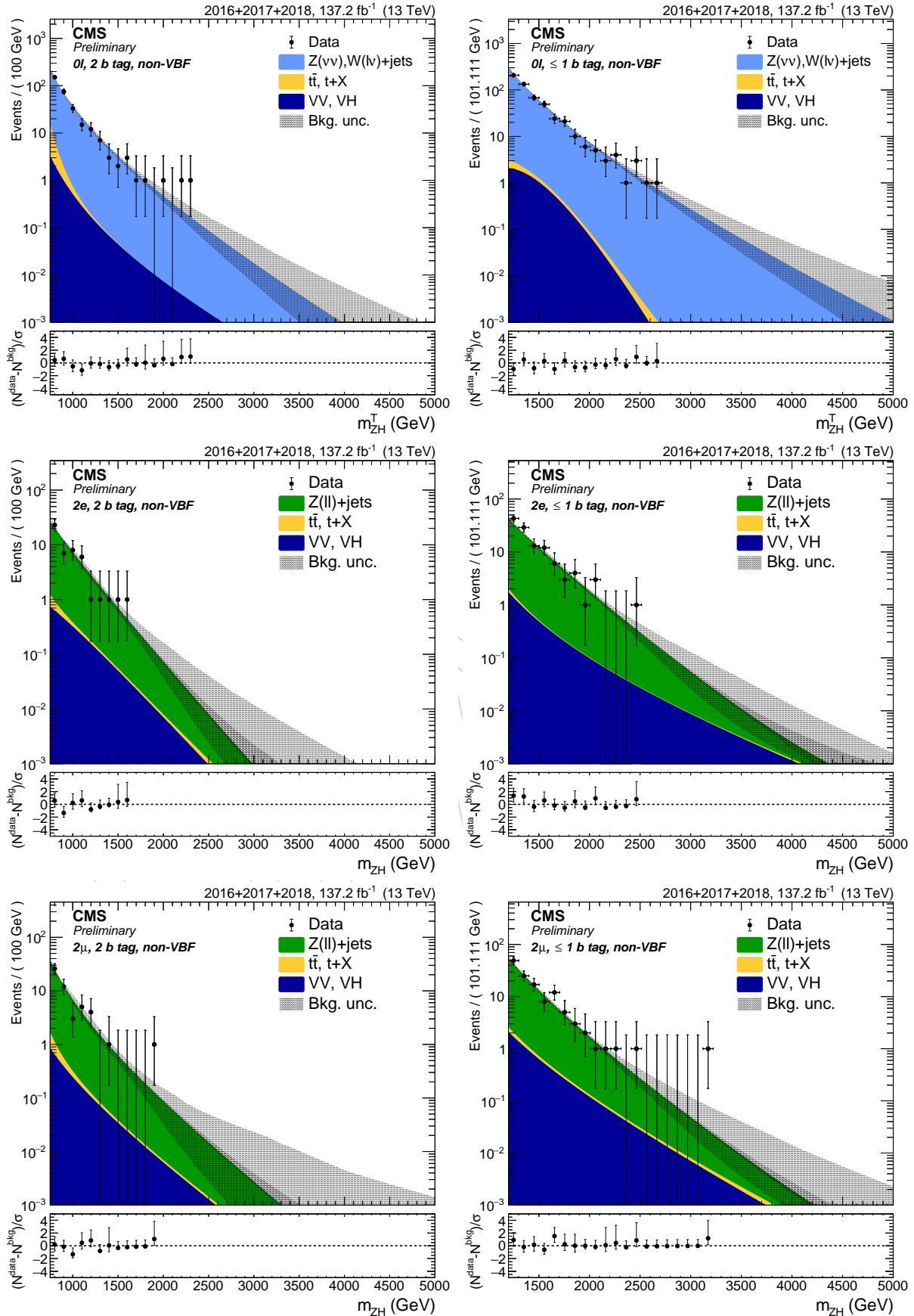


Figure 172: Fit to the m_X spectrum in data in the sidebands. The SR is replaced by splitting the lower m_j sideband ($50 < m_j < 65 \text{ GeV}$) for validation purposes. Top: 0ℓ channel. Center: $2e$ channel. Bottom: 2μ channel. left: $2 b$ -tag category. right: $0 b$ -tag category

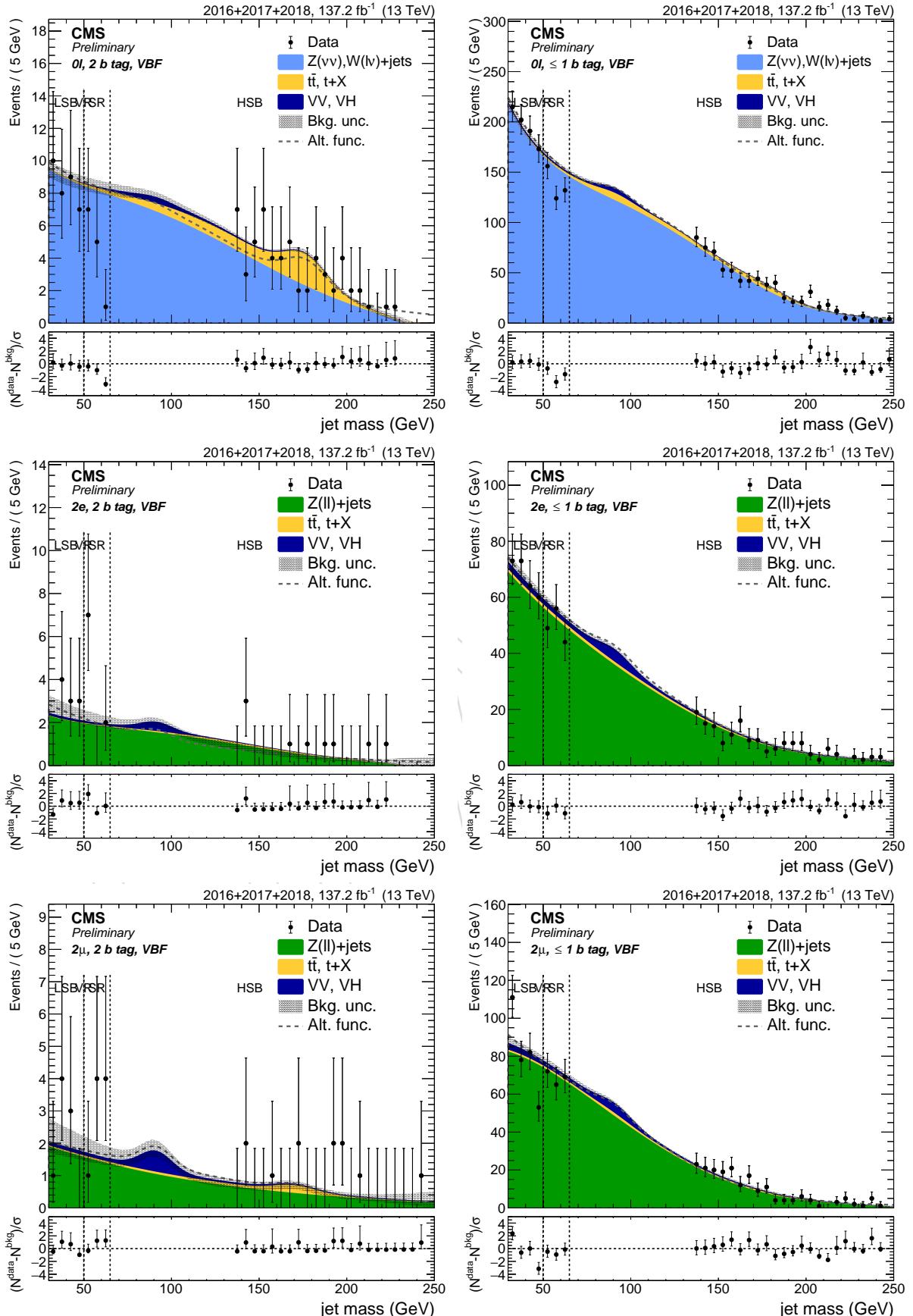


Figure 173: Fit to the m_j spectrum in data in the sidebands. The SR is replaced by splitting the lower m_j sideband ($50 < m_j < 65$ GeV) for validation purposes. Top: 0ℓ channel. Center: $2e$ channel. Bottom: 2μ channel. Left: 2b tag, VBF category. Right: 0b tag, VBF category

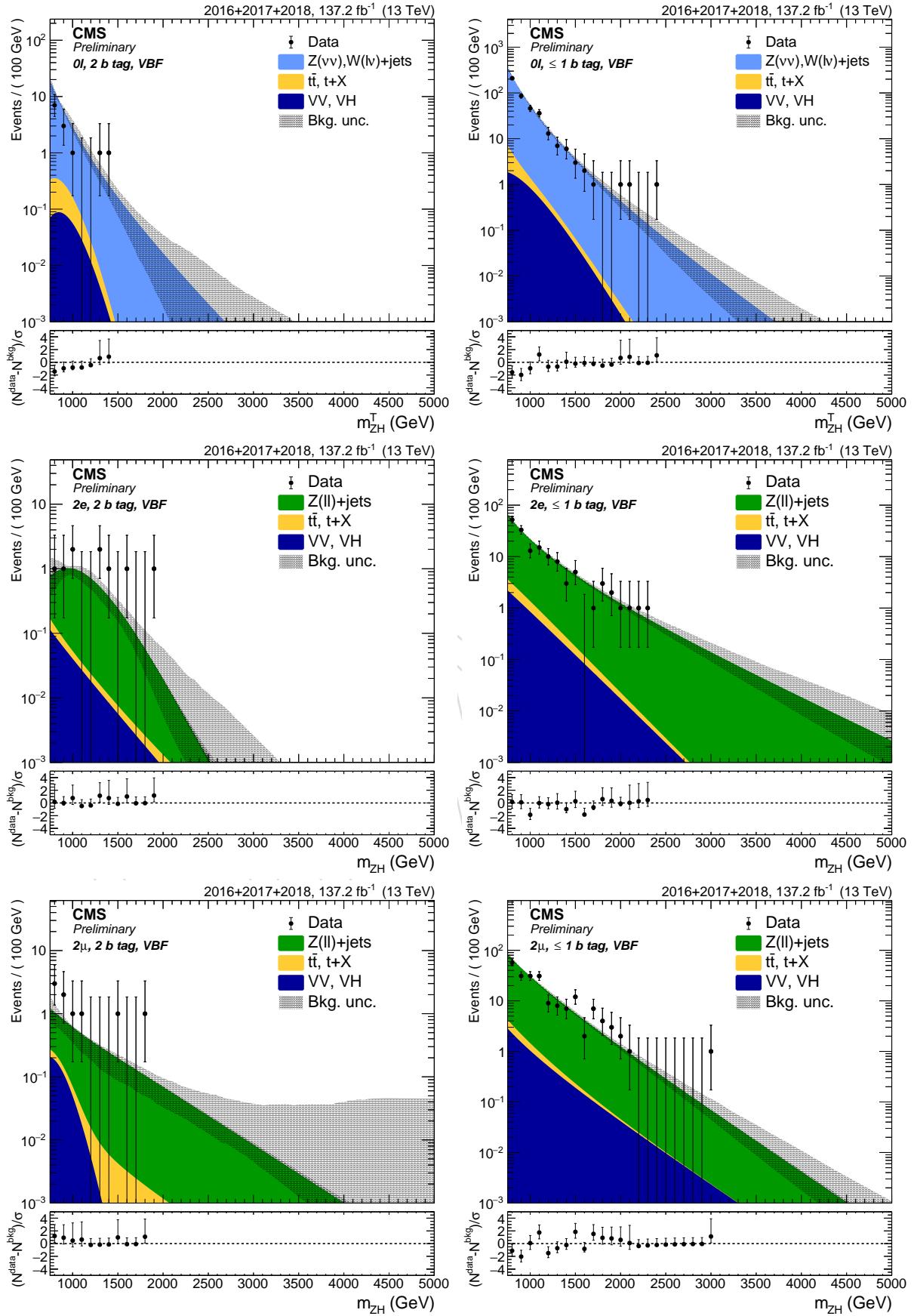


Figure 174: Fit to the m_X spectrum in data in the sidebands. The SR is replaced by splitting the lower m_j sideband ($50 < m_j < 65$ GeV) for validation purposes. Top: 0ℓ channel. Center: $2e$ channel. Bottom: 2μ channel. left: $2 b$ -tag VBF category. right: $0 b$ -tag VBF category

8.5 Signal modeling

The simulated signal mass points are fitted in the SR with an empiric function in order to be able to perform an unbinned likelihood fit for the signal extraction. The signal model is made of a gaussian-like peak plus a tail towards lower values. The function chosen to model the signal is the *Crystal Ball*, which consists in a gaussian core and a power function that describes the low-end tail, below a certain threshold.

The parametrization for intermediate mass points is determined by linearly interpolating the shape parameters derived by fitting the generated mass points. The normalization can be determined in three ways:

1. The linear interpolation is the more robust way, but it does not model particularly well some features such as the efficiency turn-on.
2. The SPline is the method adopted by default. The normalization for intermediate mass points is determined by interpolating the signal normalization with this method.
3. Another possibility is to parametrize the normalization with a polynomial, even if there is no physics behind it.

The method chosen in the SPline, and the polynomial is used to check the result. The difference between the two is usually around 1% in the turn-on region, and at the permil level at larger m_X .

For the 0-btag no VBF categories the signals are modelled for 1.4 TeV and above due to their threshold at 1.2 TeV in the $m_{Z'}$ distribution.

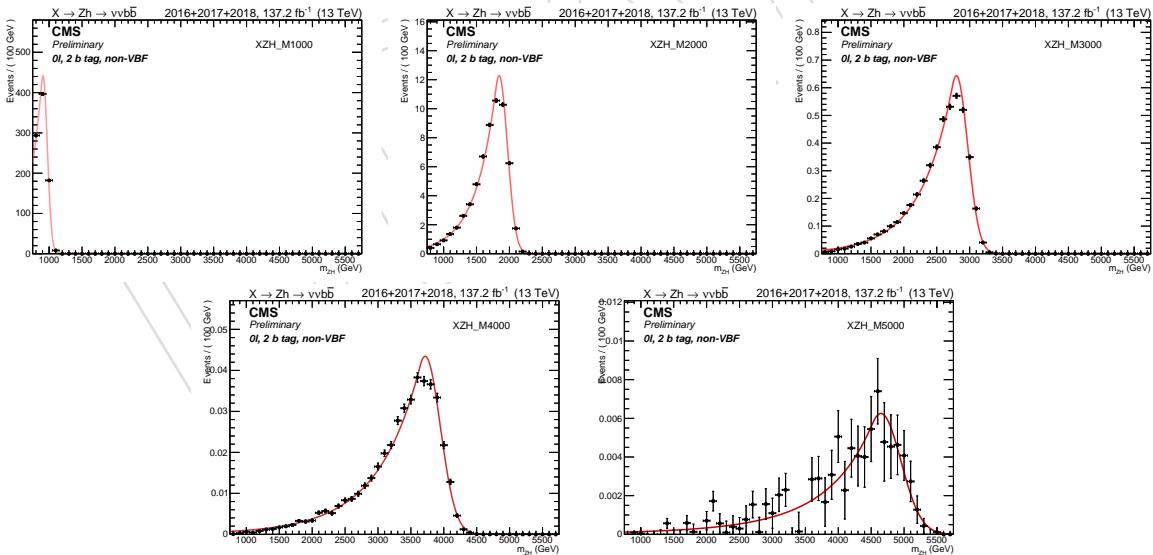
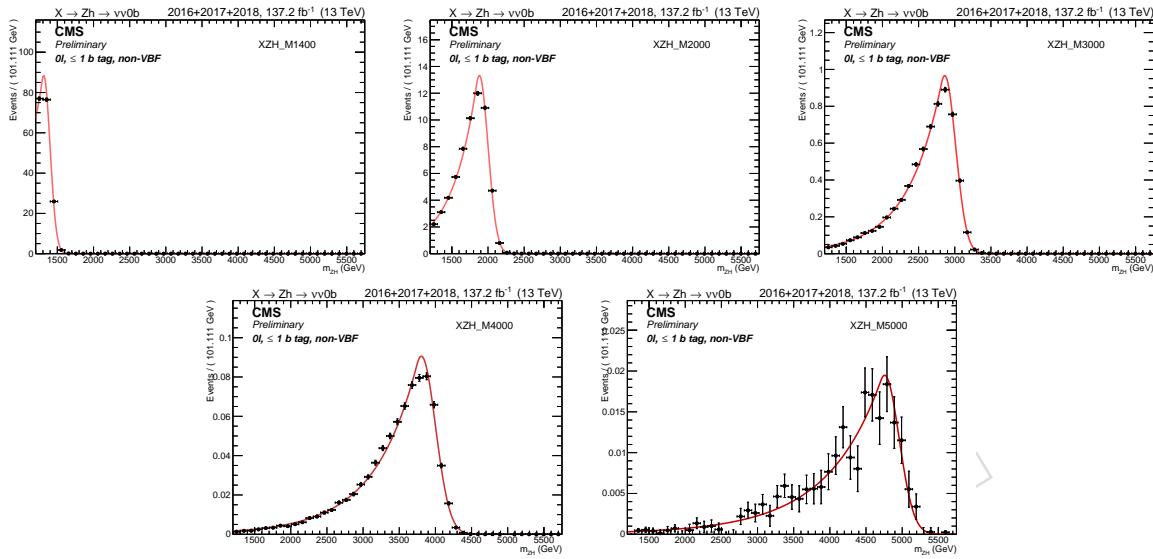
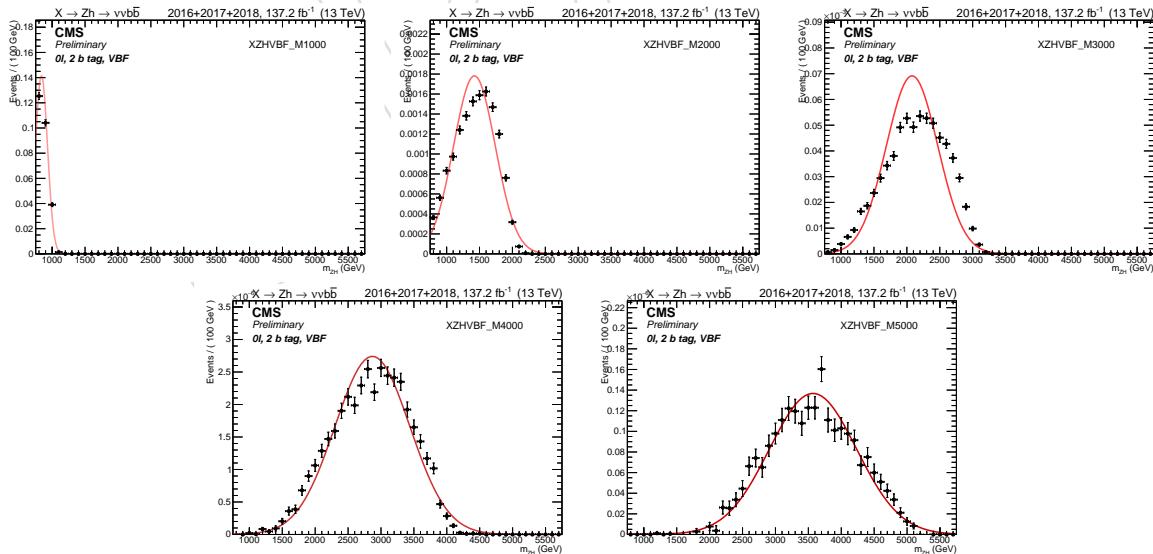


Figure 175: Signal fits for a Z' with mass 1 to 5 TeV in the $0\ell, 2$ b-tag category.

Figure 176: Signal fits for a Z' with mass 1.4 to 5 TeV in the 0ℓ , 0 b-tag category.Figure 177: Signal fits for a Z' with mass 1 to 5 TeV in the 0ℓ , VBF, 2 b-tag category.

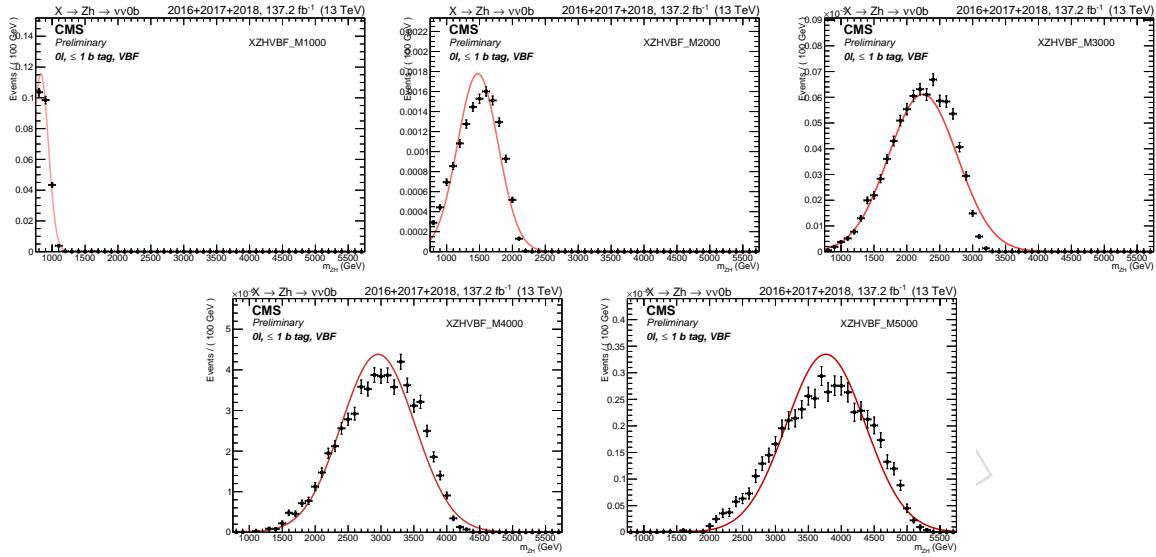


Figure 178: Signal fits for a Z' with mass 1 to 5 TeV in the 0ℓ , VBF, 0 b-tag category.

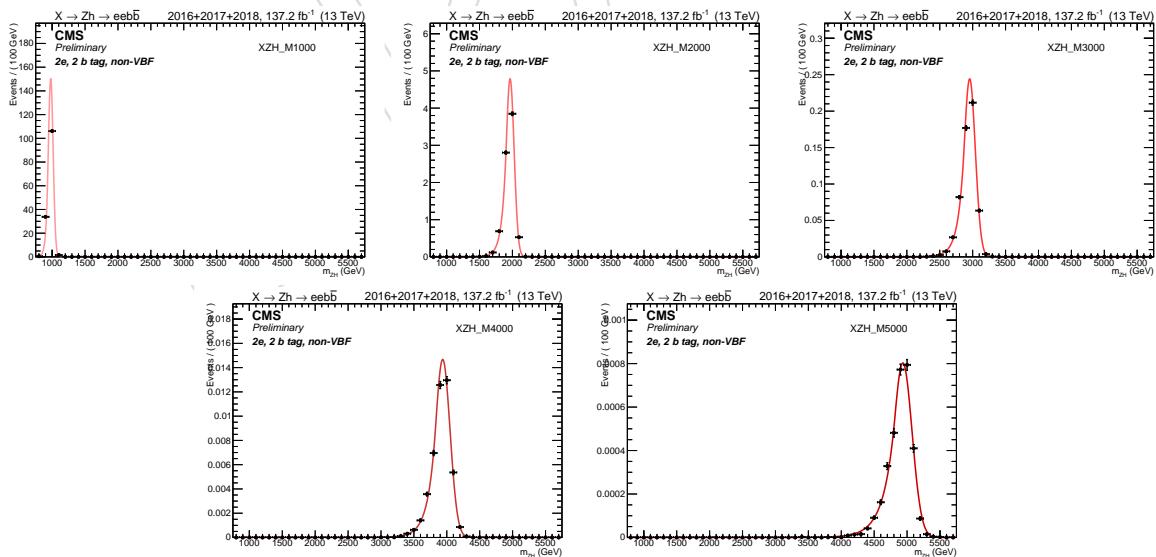
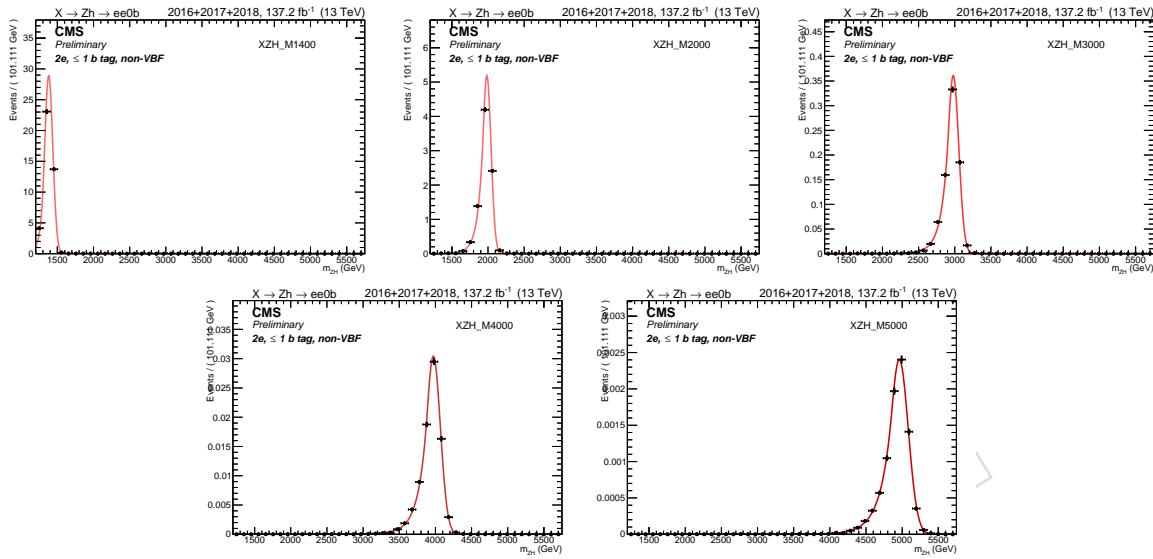
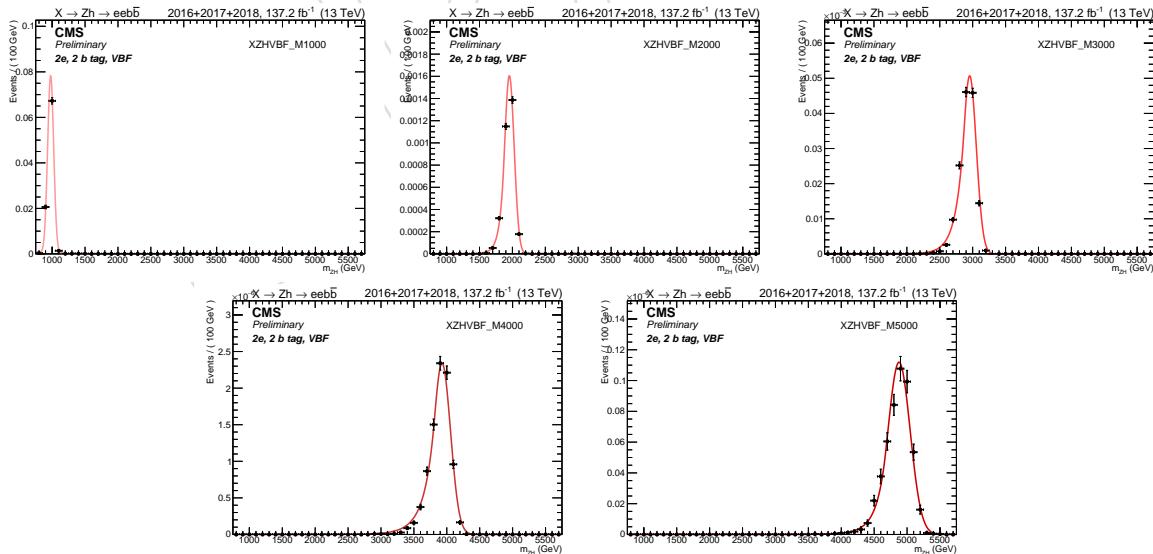


Figure 179: Signal fits for Z' with mass 1 to 5 TeV in the 2e, 2 b-tag category.

Figure 180: Signal fits for Z' with mass 1.4 to 5 TeV in the 2e, 0 b-tag category.Figure 181: Signal fits for Z' with mass 1 to 5 TeV in the 2e, VBF, 2 b-tag category.

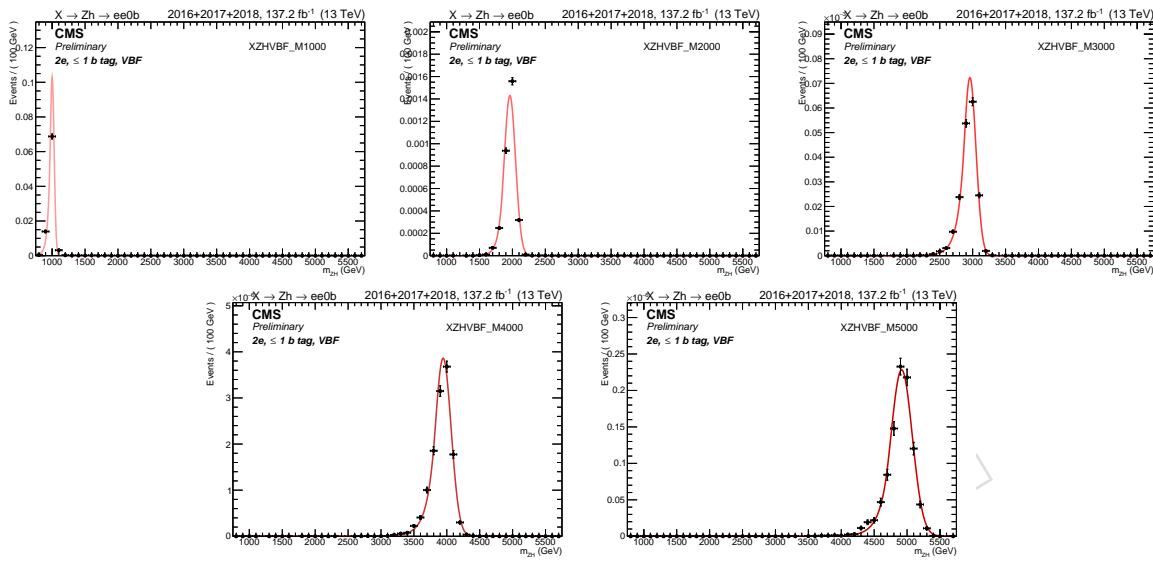


Figure 182: Signal fits for Z' with mass 1 to 5 TeV in the 2e, VBF, 0 b-tag category.

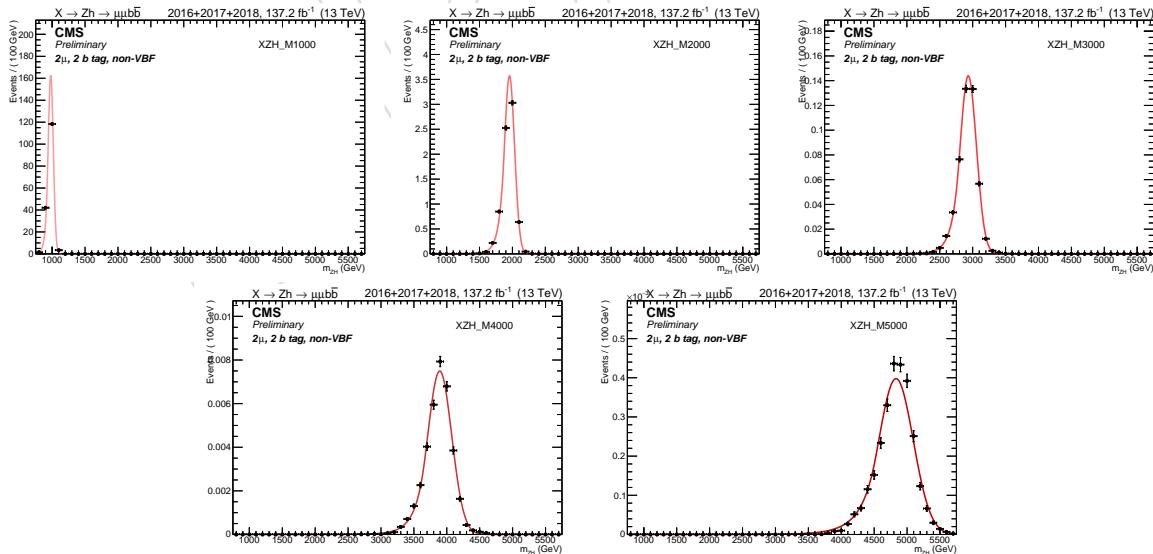
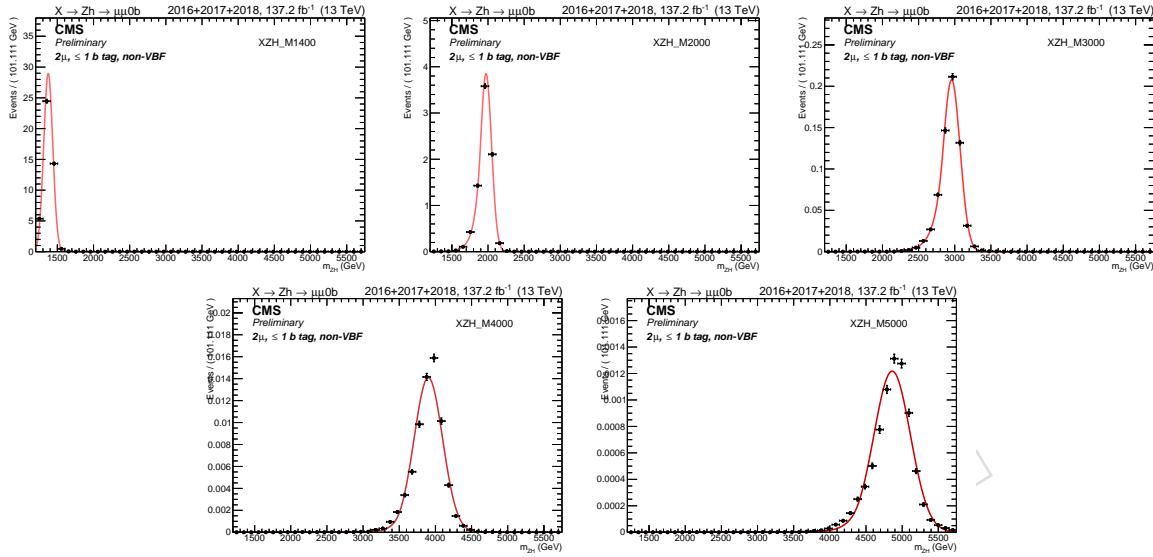
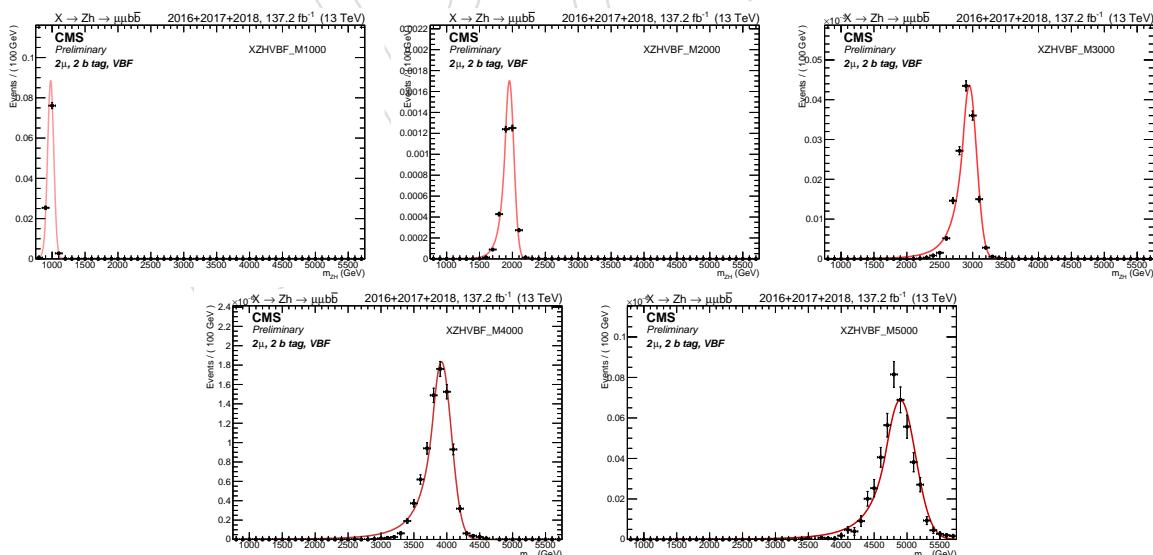


Figure 183: Signal fits for Z' with mass 1 to 5 TeV in the 2 μ , 2 b-tag category.

Figure 184: Signal fits for Z' with mass 1.4 to 5 TeV in the 2μ , 0 b-tag category.Figure 185: Signal fits for Z' with mass 1 to 5 TeV in the 2μ , VBF, 2 b-tag category.

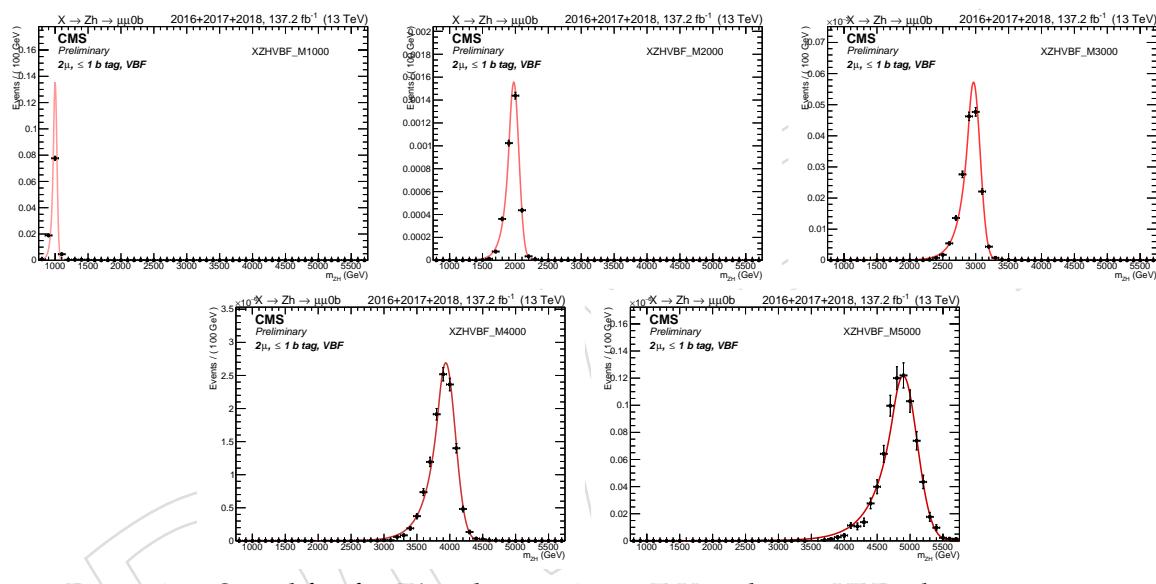


Figure 186: Signal fits for Z' with mass 1 to 5 TeV in the 2μ , VBF, 0 b-tag category.

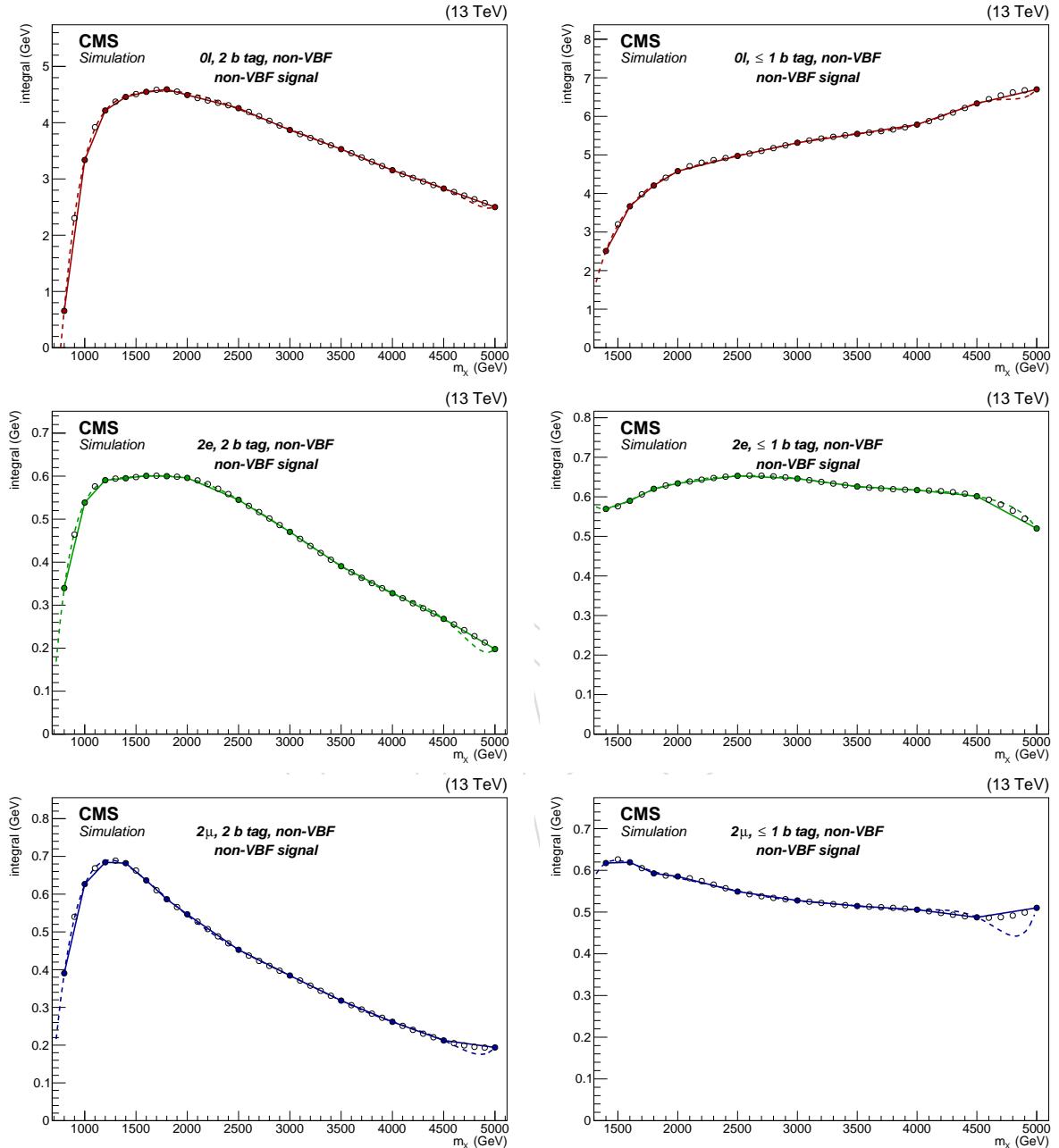


Figure 187: Interpolation of the signal normalization as a function of the generated mass m_X , separately for each channel. The filled markers represent the generated mass points. The empty circles the interpolated mass points with a spline, and the dashed line the fitting polynomial. From top to bottom: zero leptons, double electron, double muon channel. Left: double b-tag. Right: no b-tag.

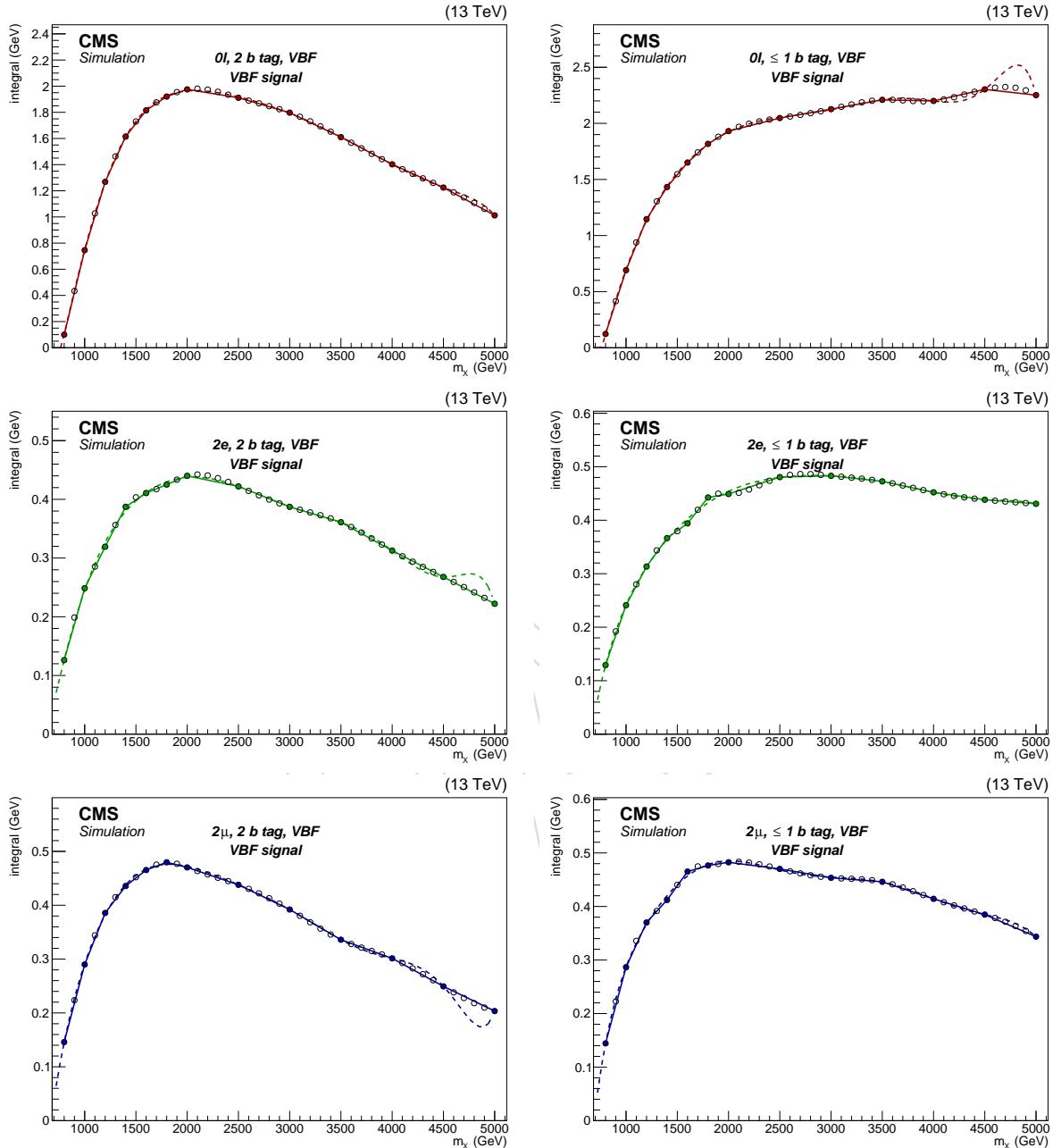


Figure 188: Interpolation of the signal normalization as a function of the generated mass m_X , separately for each channel. The filled markers represent the generated mass points. The empty circles the interpolated mass points with a spline, and the dashed line the fitting polynomial. From top to bottom: zero leptons, double electron, double muon channel. Left: VBF double b-tag. Right: VBF no b-tag.

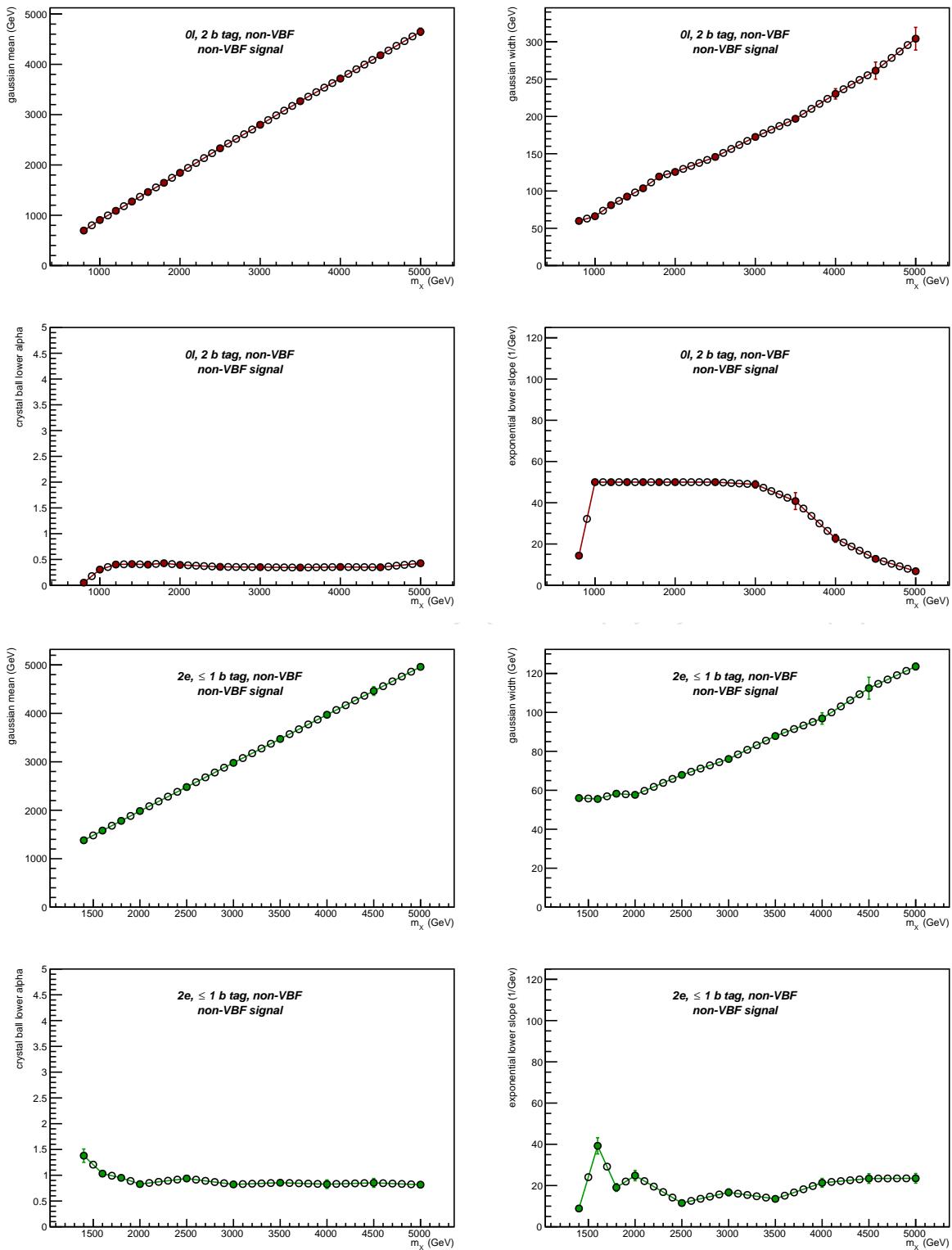


Figure 189: Interpolation of the signal parameters as a function of the generated mass m_X , for the 0ℓ , 2 b-tag channel (top) and the $2e$, 0 b-tag channel (bottom).

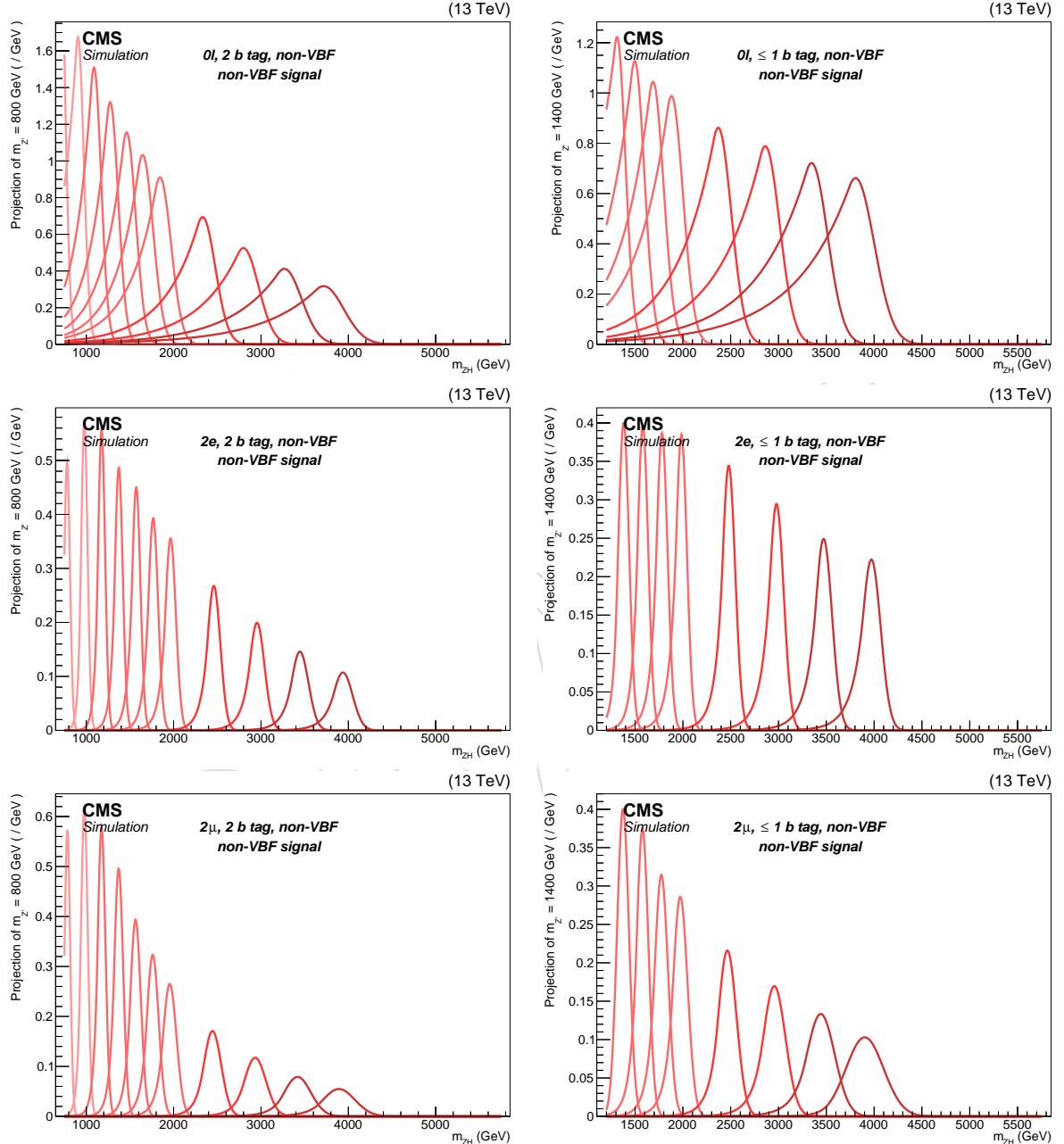


Figure 190: Signal templates as a function of the generated mass m_X , separately for 0 lepton (top), 2 electron (center) and 2 muon (bottom) in the 2 b-tag (left) and 0 b-tag (right) category.

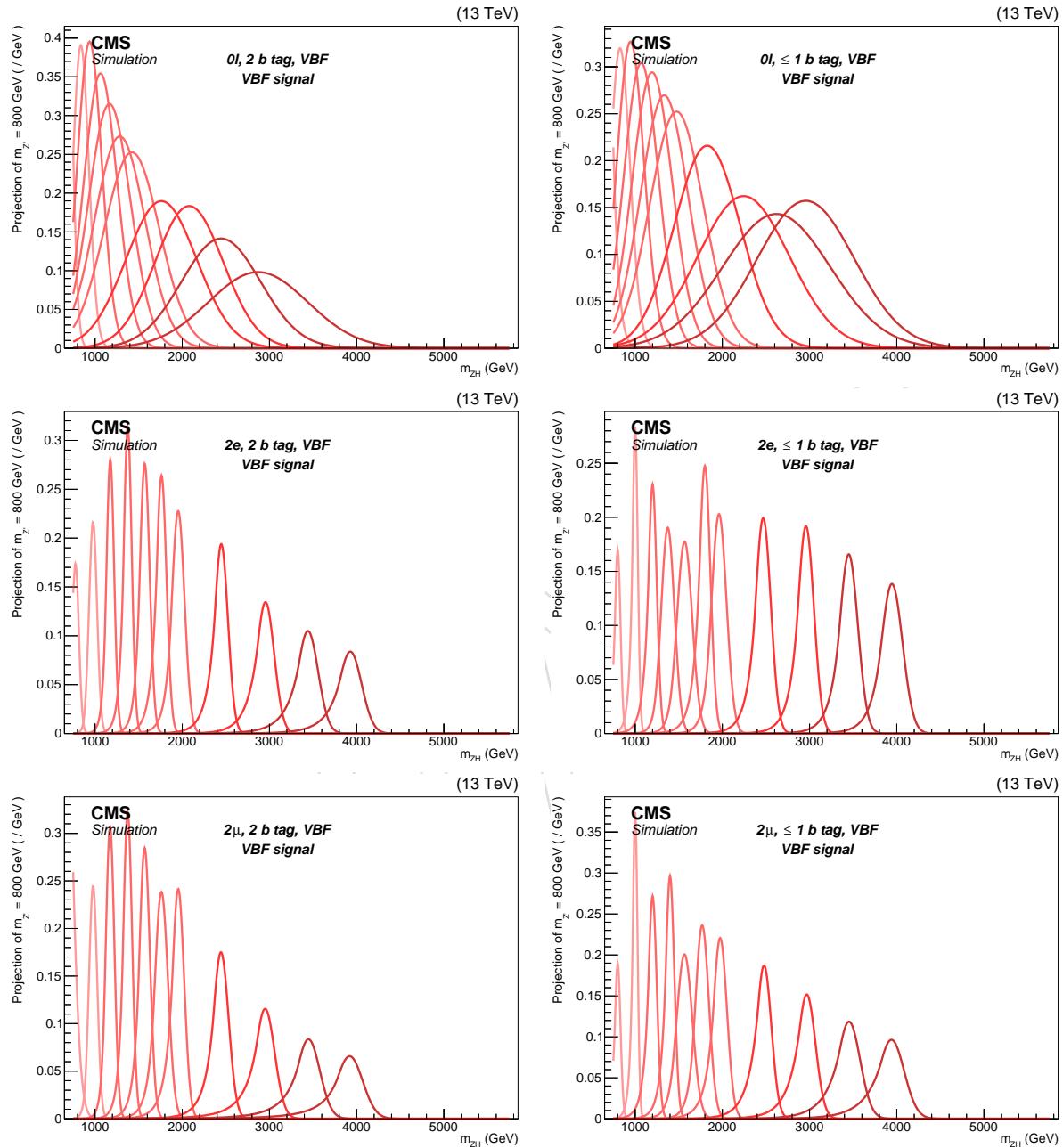


Figure 191: Signal templates as a function of the generated mass m_X , separately for 0 lepton (top), 2 electron (center) and 2 muon (bottom) in the VBF 2 b-tag (left) and VBF 0 b-tag (right) category.

841 9 Systematic uncertainties

842 The background and signal predictions are affected by systematic uncertainties that have to be
 843 estimated and taken into account in the signal fit. This section includes a list of the relevant
 844 systematic uncertainties for this analysis and how they are estimated. Most of the systematic
 845 uncertainties are dedicated to samples that are not normalized on data or the shape is taken
 846 from simulation. The systematic uncertainties are evaluated using a dataset combining the
 847 2016, 2017 and 2018 Monte Carlo events. The uncertainties are correlated between years, except
 848 luminosity, which is treated as uncorrelated.

849 9.1 Main background uncertainties

850 9.1.1 Normalization

851 The main background, V+jets, takes both the normalization and the shape from data. The
 852 normalization is extracted from fits to the jet mass sidebands with arbitrary functions tested on
 853 simulation. The tt> background is also normalized on data, but the shape is taken from simu-
 854 lation. The diboson background is taken entirely from Monte Carlo, and its normalization has
 855 its own systematic uncertainties. The uncertainty of the V+jets and tt> background normaliza-
 856 tions are obtained by propagating the uncertainties affecting all the parameters involved in the
 857 fit described in Sec. 8.1, taking into account the correlation among them.

858 An additional uncertainty on the main background derives from the choice of the shape func-
 859 tion. In order to cover potential bias effects, the jet mass fit is repeated with a separate choice
 860 of the fit function (Sec. 8.1), and the normalization of the V+jets background is estimated again.
 861 The difference in predicted number of events between the two functions is taken as a systematic
 862 uncertainty. Numerical values are reported channel by channel in Table 27.

863 The tt> and single top normalization uncertainty originates from the limited statistics in the
 864 control regions and from the variations of the leptons and b-tagging scale factors used to
 865 veto/select events in the Top CR. For the 0 lepton category the systematic uncertainty is de-
 866 rived by varying the b-tagging scale factor, in the 2 lepton categories the uncertainty on the
 867 muon and electron id and for 2 muon category also the electron and muon trigger uncertain-
 868 ties are taken into account. The values are reported in Table 21.

869 The single top normalization uncertainties due to PDF scale, PDF acceptance and QCD scales
 870 affect the Top SF as well. The impact on the single top alone is reported in the second column
 871 in Tab. 30, and the impact to the Top SF, calculated by considering the single top composition
 872 in the Top CR ($\approx 6\%$), is reported in the third column.

873 The diboson normalization uncertainty depends on the knowledge of the cross sections of these
 874 processes in the inclusive phase-space, and it is calculated to be 2.2% (PDF + α_s) and 2.5%
 875 (QCD scales). Similarly to the single top case, there are also additional uncertainties due to the
 876 extrapolation to the analysis phase-space, reported in Tab. 30.

Source	Single top	Top SF	VV
PDF scale	0.4%	0.024%	1.7%
PDF acceptance	2.2%	0.132%	2.0%
QCD scales	16.6%	0.996%	16.4%

Table 30: Summary of secondary background normalization uncertainties. Single top uncer-
 tainties affect the top scale factors, diboson uncertainties impact the normalization in the signal
 regions.

877 **9.1.2 Shape**

878 The shape uncertainties are determined with the α -method, explained in Section 8.2. The uncer-
 879 tainties on the parameters of the main background prediction in the signal regions are affected
 880 by the parameter error of the simultaneous fit to m_X in data in the jet mass sidebands, and from
 881 the α -function itself, which depends on the m_X fits to the simulated V+jets distributions in SR
 882 and SB. These uncertainties are propagated to the shape of the main background in the signal
 883 region. Before being provided to the likelihood fit, these parameters are decorrelated through
 884 a linear transformation. A similar treatment is applied to the secondary backgrounds as well.

885 In order to check that the potential bias in the choice of the function is small, we repeat the back-
 886 ground prediction with a different and orthogonal alternative set of functions. The alternative
 887 alpha function and alternative background predictions are compatible within the uncertainties
 888 with the nominal alpha and background prediction, giving an indication that the bias is small.

889 **9.2 Triggers**

890 Trigger uncertainty due to the limited statistics is evaluated by shifting by one standard de-
 891 viation the trigger scale factors, as reported in Section 2.4. Additionally, a flat 4% systematic
 892 uncertainty is assigned for the muon trigger as suggested by the Muon POG [57].

893 The trigger uncertainties are reported in Tab. 31.

894 **9.3 Leptons**

895 Identification and isolation systematics are evaluated by moving up and down the scale factors
 896 for tracking, reconstruction, identification, and isolation by their uncertainties (Section 3). For
 897 muons, additional flat uncertainties for identification and isolation, accounting for 1% and 2%
 898 respectively, are applied following the Muon POG prescription [57]. The numerical values are
 899 reported in Tab. 31. These uncertainties do not depend on the mass of the resonance, and they
 900 are considered as flat. The uncertainties affecting different flavors are considered as uncor-
 901 related, but those relative to a specific object (electrons or muons) are conservatively considered
 902 as correlated.

	Trigger	Id+Iso (2ℓ)
Electrons	0.9%	3.6%
Muons	3% (4%)	1.9% (3%)

Table 31: Summary of lepton normalization uncertainties. Number in parenthesis are systematic uncertainties.

903 Uncertainties on the energy/momentum scale of leptons impact mostly on the signal shape,
 904 changing the mean and/or the resolution of the expected Crystal Ball function. For muons,
 905 $\eta - \phi$ dependent scale factors, evaluated by the Muon POG in the framework of the $Z' \rightarrow \mu\mu$
 906 searches, are used to correct the curvature of each muon, i.e. its charge divided by its p_T . This
 907 quantity is added to the muon p_T . Once both muons are corrected, the resonance invariant mass
 908 is recalculated. Results are presented as percentage relative differences of the mean, width and
 909 integral of the two distributions, with and without the corrections.

910 For electrons, the impact of the scale/smear corrections provided by the EGamma POG, prop-
 911 agated to the resonance invariant mass, is instead considered. The impact of the lepton scales
 912 correspond to shape uncertainties propagated to the mean and resolution of the signal reso-
 913 nance.

914 In the 0 lepton channel systematic uncertainties of 1% for the muons, 1% for the electrons and
 915 3% for the taus are added to account for the different veto efficiencies.

Scale unc.	e		μ	
	1 TeV	4 TeV	1 TeV	4 TeV
m_X				
Δ events	1.0%	1.0%	2.0%	0.5%
Δ mean	<0.1%	<0.1%	<0.1%	<0.1%
Δ RMS	0.1%	0.1%	5%	3%

Table 32: Summary of lepton scale uncertainties.

916 9.4 Jet energy scale and resolution

917 Jets uncertainties are evaluated in the signal regions by moving up and down by one standard
 918 deviation the source of the uncertainty. The two sources are the uncertainty on the jet energy
 919 correction, also identified as jet energy scale (JES), and the uncertainty due to the different
 920 jet momentum resolution (JER). For the jet energy scale the p_T of the jets are shifted by the
 921 error value of the jet energy corrections. The resolution is smeared with a hybrid method:
 922 If a matching particle-level jet is found the scaling method is used, otherwise the stochastic
 923 method. The difference in the normalization of the jet energy correction is propagated to the
 924 signal region. The JEC are considered correlated among years. The resulting normalization
 925 uncertainty is $\pm 1.2\%$ for diboson background, and are rather small ($\lesssim 1\%$) across the mass
 926 range for the signal samples. The JER effect on the normalization is evaluated to be small $\sim 1\%$
 927 in signal and diboson background samples.

928 The JEC uncertainties also impact the signal shape, and specifically the mean and width of the
 929 Crystal Ball. The uncertainty is found to be stable with the resonance mass between channels
 930 and categories, and is found to be 0.1% for the mean, and 1.0% for the width.

931 9.5 Jet mass scale and resolution

932 The uncertainty of the corrections on the scale and resolution on the PUPPI soft-drop jet mass
 933 are propagated to the signals in the corresponding signal regions. A 0.6% uncertainty has been
 934 measured for the mass scale, and a 9% uncertainty is assigned to the resolution [58] for PUPPI
 935 soft drop mass. The SM diboson background jet mass scale account for 0.6% and 9% for the
 936 resolution.

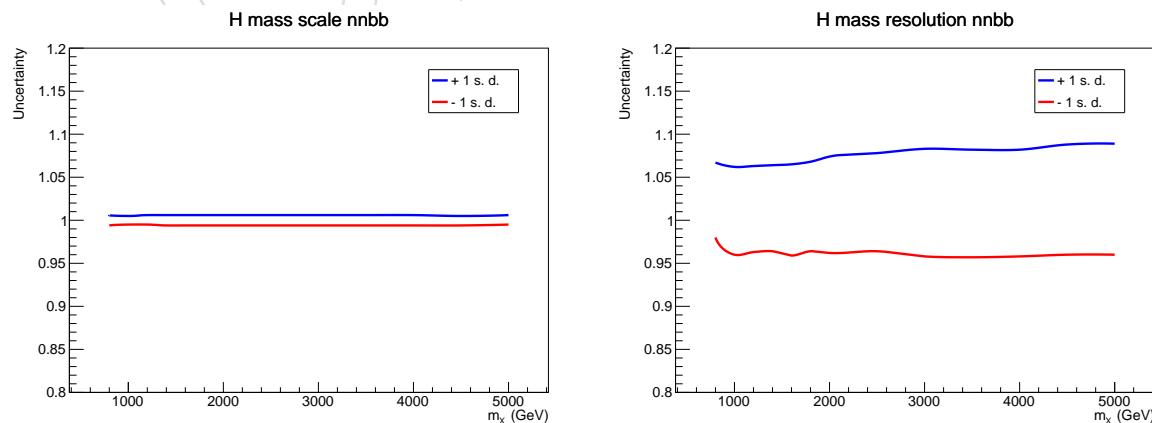


Figure 192: Signal normalization variations obtained varying the Higgs mass scale (left) and resolution (right).

9.6 Higgs mass extrapolation uncertainty

This study has been performed in the all-hadronic analysis, but it's still valid in the leptonic final states. In order to estimate the uncertainty for Higgs mass tagging a double ratio estimate between Bulk Graviton decaying to WW and HH is performed, choosing a mass window for the W and H, in order to calculate the ratio of efficiency between them for PYTHIA and HERWIG showering algorithms. Subsequently, the double ratio $R_{\text{HERWIG}}/R_{\text{PYTHIA}}$ is calculated. The double ratio provides an estimate of how different showering algorithms handle the difference between hadronically decaying W and H. Results are shown in Fig. 193 for different substructure selections. The difference of the double ratio from 1 is taken as systematic uncertainty, and estimated to be 6%.

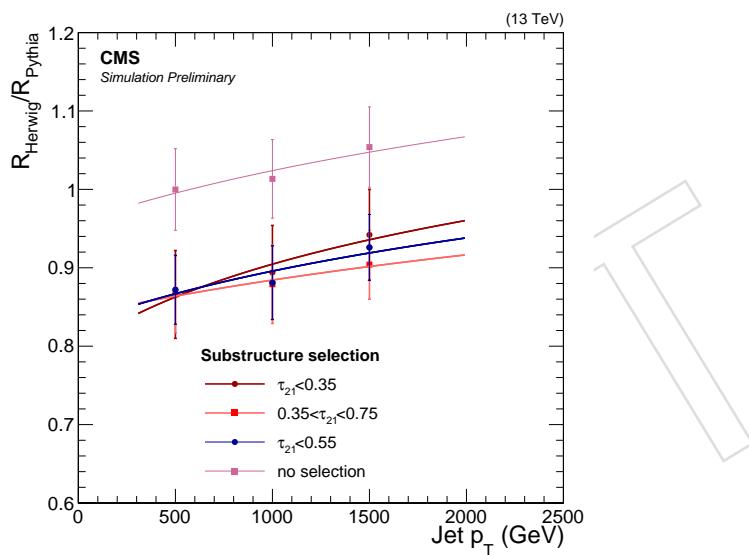


Figure 193: $R_{\text{HERWIG}}/R_{\text{PYTHIA}}$ as function of the jet p_T for different substructure selections, and parametrized as a function of the jet p_T . The function chosen to fit the points is $a \cdot \log(p_T + b)$. Without a τ_{21} selection, the uncertainty is assumed to be the maximum between the central value and the end of the uncertainty band, which results in a flat 6% uncertainty over the full p_T range.

9.7 b-tagging

The impact of b-tagging uncertainty is evaluated by moving the DeepCSV scale factors provided by the BTV POG [56] as a function of p_T and η . The uncertainty on the overall normalization is shown in figure 194. The systematic uncertainty for the 2 b-tag category ranges between 5% at 1 TeV and 15% at 5 TeV and between 0.7% and 6% for the 0 b-tag category. A 6.5% and 0.6% uncertainty is assigned to diboson samples in the double and zero b-tagged categories, respectively. The b-tagging variations are considered as correlated between backgrounds, but anti-correlated between b-tagging categories. No shape uncertainty due to b-tagging is considered.

There is an effect from the b-tagging efficiency also for the $t\bar{t}$ normalization in the 0ℓ channel, due to the inversion of the b-tag veto and the subsequent variation in the Top scale factors. This uncertainty, which has been evaluated with the same method as the Higgs b-tagging uncertainty, is found to be consistent for all the 0ℓ Top scale factors, and is evaluated to be 1.4%. The uncertainty is correlated with the b-tagging uncertainty for the signal.

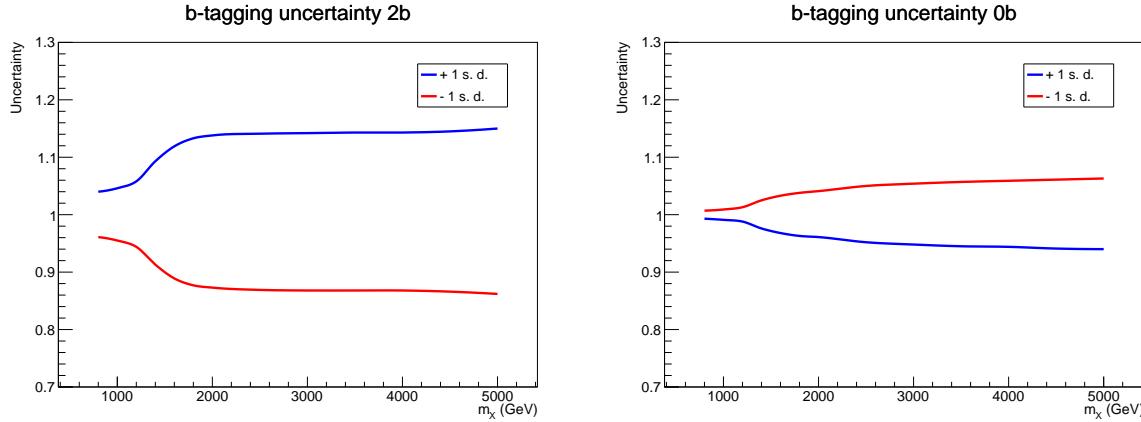


Figure 194: Signal normalization variations obtained varying the b-tagging SF by one standard deviation in the 2 (left) and 0 (right) b-tags category. The colors indicate the upward and downward variations, which are anti-correlated in the b-tagging case.

961 The diboson background has a 0.6% uncertainty due to the b-tag veto, and a 0.6% (6.5%) un-
962 certainty in the 0 b-tag (2 b-tag) categories due to b-tagging the Higgs jet. The b-tagging un-
963 certainties between the Higgs tagging and the b-tagging veto are treated as anti-correlated for 2
964 b-tag and correlated for 0 b-tag.

9.8 Missing Energy

966 The E_T^{miss} is a composed object, built upon all the reconstructed particles in the detector. There-
967 fore, it is affected by the energy scale and resolution of all the reconstructed objects, i.e. charged
968 and neutral hadrons (clustered in jets and non-clustered), muons, electrons, photons and hadronic
969 taus. Dedicated uncertainties have been derived in the analysis B2G-17-004 [59] by propagat-
970 ing the original object scales and resolutions to the E_T^{miss} itself. This resulted in a systematic
971 uncertainty of 1%. Therefore the systematic uncertainty is omitted in this analysis.

9.9 Prefire

973 The darkening of ECAL crystals leads to a gradual timing shift. In 2016 and 2017 this timing
974 shift was not properly propagated to L1 trigger primitives resulting in a significant number of
975 high η trigger primitives mistakenly associated to the previous bunch crossing. Prefire weights
976 to account for this effect were derived, but the effect is minimal. Prefire doesn't effect the
977 background samples as they are normalized with data. To account for the effect on the signal
978 normalization an systematic uncertainty of 1% is added to the signal normalization. The Prefire
979 weights for the 1000 GeV signal in two categories are shown in figure 195.

9.10 Pile-up

981 An additional source of systematic error is the limited knowledge of the total inelastic cross-
982 section at 13 TeV, used to get the expected primary vertices distribution used for pile-up reweight-
983 ing. A 5% uncertainty is assumed for the default value of 69.2 mb [42], and the expected pri-
984 mary vertices distributions are varied accordingly. Changing the pile-up weight varies also the
985 MC normalization in the signal regions, and the relative difference is estimated to be 0.1%. No
986 shape uncertainties are considered for PU.

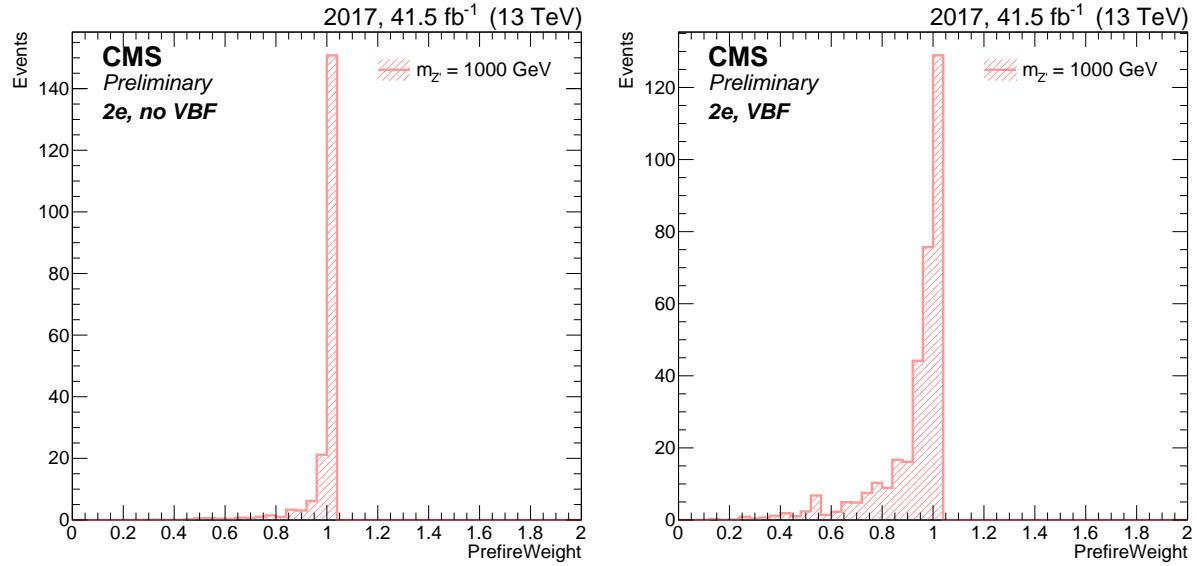


Figure 195: PrefireWeight for inclusive $Z \rightarrow ee$ category (left) and inclusive VBF $Z \rightarrow ee$ category (right).

9.11 QCD renormalization and factorization scale

Per-event weights are provided for a variation of the QCD renormalization and factorization scales by a factor 2. The two scales can be varied separately and independently, or together assuming 100% correlation. The largest exclusion in each event is then taken as the uncertainty. The weight is propagated up to the final distributions, accounting for both shape and normalization uncertainties. The envelope of all the considered variations is then considered as the template for the scale uncertainty.

The normalization uncertainty due to the QCD scales ranges between 3% at 1 TeV and 15% at 4 TeV for signal samples. It is also observed that the uncertainty in signal are very consistent between all the different channels. The QCD scales also have negligible effect on the mean and sigma of the Crystal Ball (< 0.1%), and no shape uncertainties are considered for the signal.

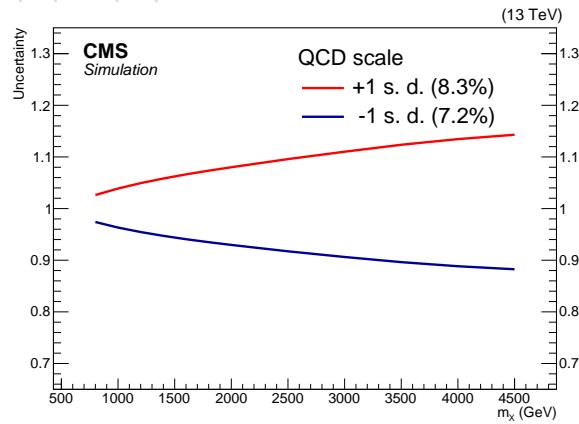


Figure 196: Normalization variations due to the QCD scales.

998 **9.11.1 PDF**

999 Systematic uncertainties coming from PDF uncertainties have been considered for this analysis,
1000 according to the PDF4LHC prescriptions, and using the NNPDF3.0 set. The 100 weights have
1001 been considered together, by calculating the envelope of the weight distribution around the
1002 central value for each distribution, and propagated as a normalization and shape uncertainty
1003 to the final distributions. The effect of the PDF uncertainty on the acceptance is found to be
1004 consistent between all the $X \rightarrow ZH$ and $Z \rightarrow WH$ signal samples, and it is around 0.5%.

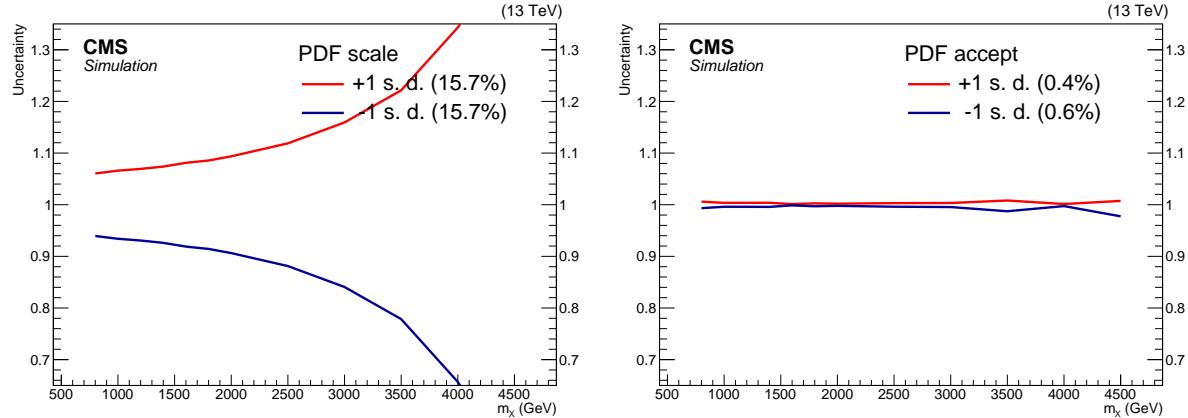


Figure 197: Shape variations due to PDF scale (left) and acceptance (right).

1005 **9.12 Uncertainties on the alpha**

1006 The systematic uncertainties on the background, except the limited MC statistics, are not prop-
1007 agated to the α ratio and therefore not associated to dedicated nuisance parameters in the sig-
1008 nal + background fit. The reason is that most of the effect of the uncertainties is correlated
1009 among SB and SR, and cancels out in the α ratio. The remaining effects, mostly dominated by
1010 bin-by-bin migrations of single large-weight events, are smaller than the MC statistical un-
1011 certainty. The latter is instead considered, as it represents the largest uncertainty that affects the
1012 background estimation (besides the limited statistics in data in the SB, which is also taken into
1013 account), and is propagated to the uncertainties on the parameters of the functions $N_{SR}^{Vjet}(m_X)$,
1014 $N_{SB}^{Vjet}(m_X)$, $N_{SB}^{main}(m_X)$ (in total, 6 parameters for each category). Because the `combine` tool
1015 used for fitting does not account for partial correlations between nuisance parameters (the only
1016 options are 0% correlation or $\pm 100\%$ correlation), these parameters are decorrelated through
1017 a linear transformation before the corresponding nuisance parameters are provided to the fit.
1018 The same applies to the uncertainties on the functions of the secondary backgrounds.

1019 The figures 198-199 show the variations of the α function (binned in these plots for simplicity)
1020 compared to the 1 and 2 sigma uncertainty bands that come from the limited MC statistics, the
1021 latter being largely dominating over all other uncertainties.

1022 **9.13 Summary**

1023 A summary of all systematics is listed in Tab. 33. In addition to those described in the previous
1024 sections, a 2.5% uncertainty for luminosity [60][61][62] is added.

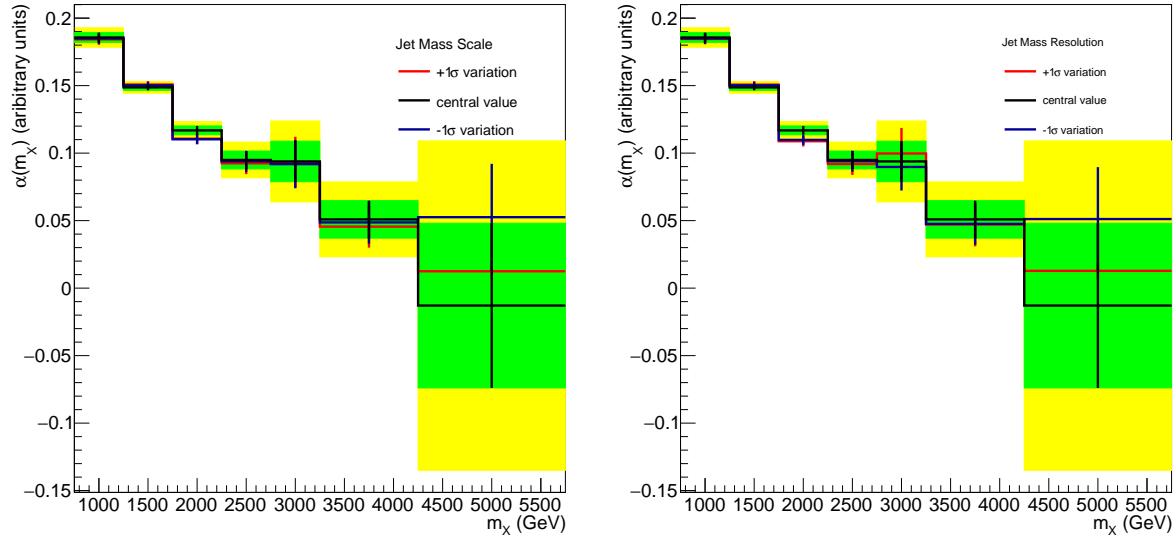


Figure 198: Variations of the (binned) α function after varying the jet mass scale (left) and resolution (right).

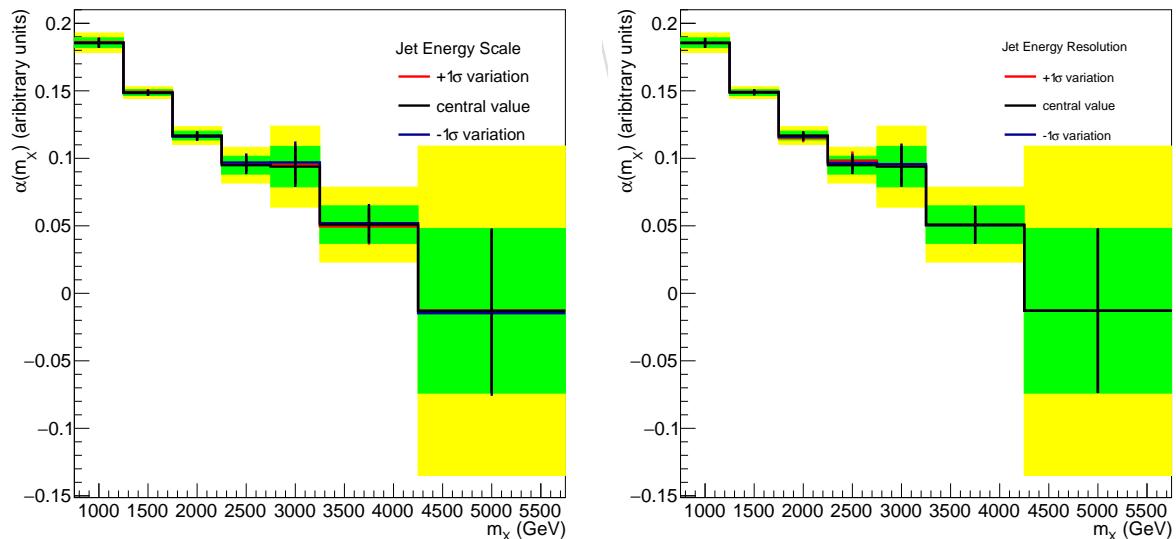


Figure 199: Variations of the (binned) α function after varying the jet energy scale (left) and resolution (right).

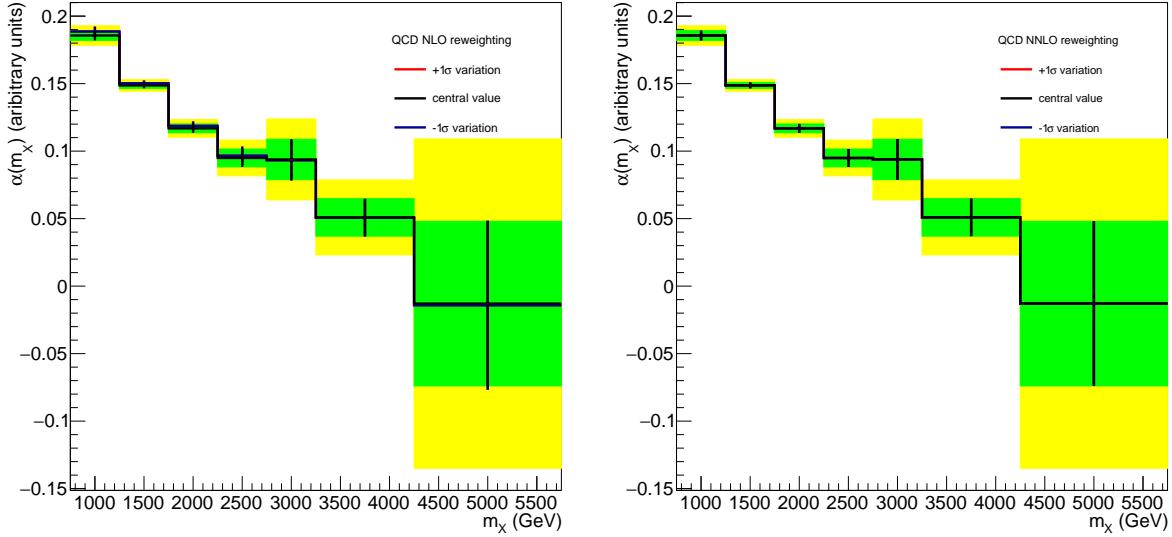


Figure 200: Variations of the (binned) α function after removing the QCD NLO (left) and QCD NNLO (right) corrections on the Z and W p_T spectra.

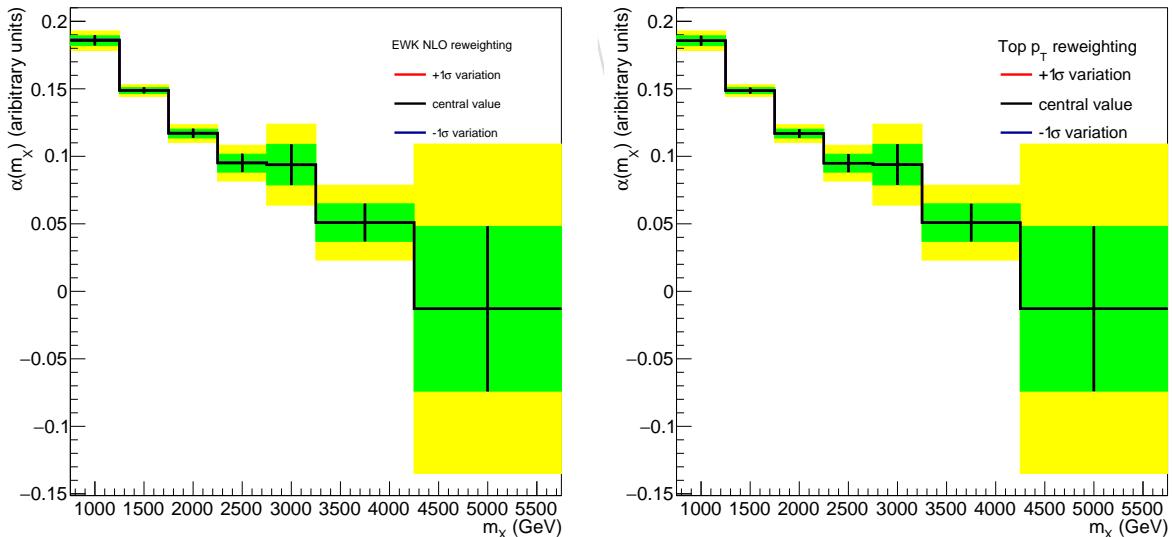


Figure 201: Variations of the (binned) α function after removing the EWK NLO correction on the Z and W p_T spectra (left) and the $t\bar{t}$ p_T reweighting (right).

Table 33: Summary of systematic uncertainties for the backgrounds and signal samples. The entries labelled with † are also propagated to the shapes of the distributions. Uncertainties marked with ‡ impact to the signal cross section. Uncertainties in the same line are treated as correlated. The uncertainties except luminosity are correlated between years.

	V+jets	$t\bar{t}$, t+X	VV	Signal
fit parameters†	✓	✓	✓	-
bkg. normalization	1–25%	-	-	-
top scale factors	-	0.4–9.5%	-	-
jet energy scale †	-	-	3.0%	1.0%
jet energy resolution †	-	-	0.1%	0.1%
jet mass scale	-	-	0.6%	0.6%
jet mass resolution	-	-	9.0%	9.0%
electron Id, Iso	-	-	-	3.6%
muon Id, Iso	-	-	-	4.9%
lepton scale and res. †	-	-	-	1–3%
E_T^{miss} scale and res.	-	-	1%	1%
electron trigger	-	-	-	0.9%
muon trigger	-	-	-	7%
b-tagging	-	1.4% (0ℓ)	0.6% (0b), 6.5% (2b)	1–6% (0b), 4–15% (2b)
Higgs tagging	-	-	-	6%
pile-up	-	-	0.1%	0.1%
prefire	-	-	-	1%
QCD scale extrapolation	-	1.0%	-	-
QCD scales	-	-	18.9%	3–15% ‡
PDF scale	-	0.1%	4.7%	8–30% ‡
PDF acceptance	-	0.1%	0.2%	0.5%
luminosity	-	-	2.5%	2.5%

10 Results

The CL_s criterion [63, 64] is used to determine the 95% confidence-level limit on the signal contribution in the data, using the `RooStats` package [65]. In order to extract the limit on the production cross section times the branching ratios, the CMS standard `combine` tool [66] has been used. The `Asymptotic` method is used to calculate preliminary 95% C.L. upper limits with 1σ and 2σ bands using the CLs frequentist calculation currently recommended by the LHC Higgs Combination Group [67]. The `ProfileLikelihood` method is used for significance and the background p-value; finally, the `MaxLikelihoodFit` method allows to get the signal Best Fit Ratio, the fit pulls and the pre/post fit distributions.

Results are obtained from a combined signal and background fit to the unbinned m_{ZH} distribution, based on a profile likelihood defined as

$$\mathcal{L} = \prod_i \frac{\mu_i^{n_i} \cdot e^{-\mu_i}}{n_i!} \quad \text{with} \quad \mu_i = \sigma N_i(S) + N_i(B)$$

where $N_i(S)$ and $N_i(B)$ are the signal and background events in the i -th bin, and σ is the signal strength modifier parameter. Systematic uncertainties are treated as nuisance parameters and are profiled in the statistical interpretation. The background-only hypothesis is tested against the $X \rightarrow ZH$ signal in all the categories, and with no evidence of significant deviations from background expectation, the asymptotic modified frequentist method is used to determine the limit at the 95% confidence level (CL) on the contribution from signal.

The observed upper limit on the resonance cross section times $\mathcal{B}(X \rightarrow ZH)$, as well as the expected limit and its relative 68% and 95% uncertainty bands, are reported as a function of the resonance mass in Figures 202–210.

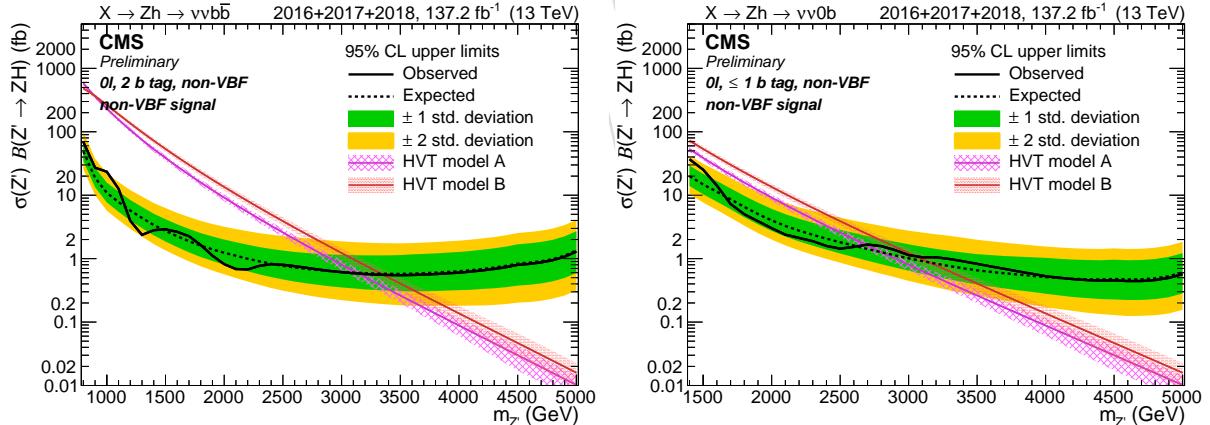


Figure 202: Observed and expected (with $\pm 1(2)\sigma$ band) 95% C.L. upper limit on $\sigma \times \mathcal{B}(X \rightarrow ZH)$ in the 0ℓ 2 b-tag (left) and 0 b-tag (right) category for the no VBF signal, including all statistical and systematics uncertainties.

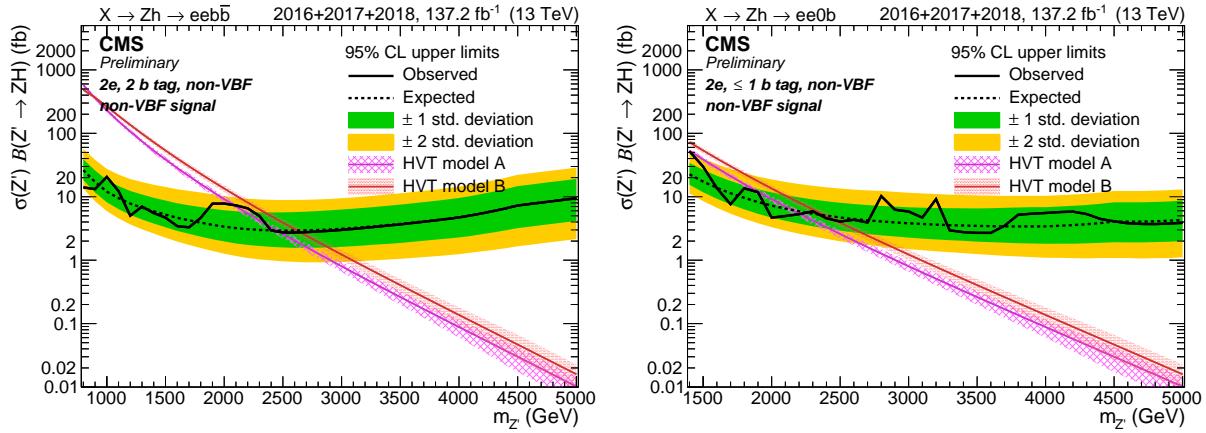


Figure 203: Observed and expected (with $\pm 1(2)\sigma$ band) 95% C.L. upper limit on $\sigma \times \mathcal{B}(X \rightarrow Zh)$ in the 2e 2 b-tag (left) and 0 b-tag (right) category for the no VBF signal, including all statistical and systematics uncertainties.

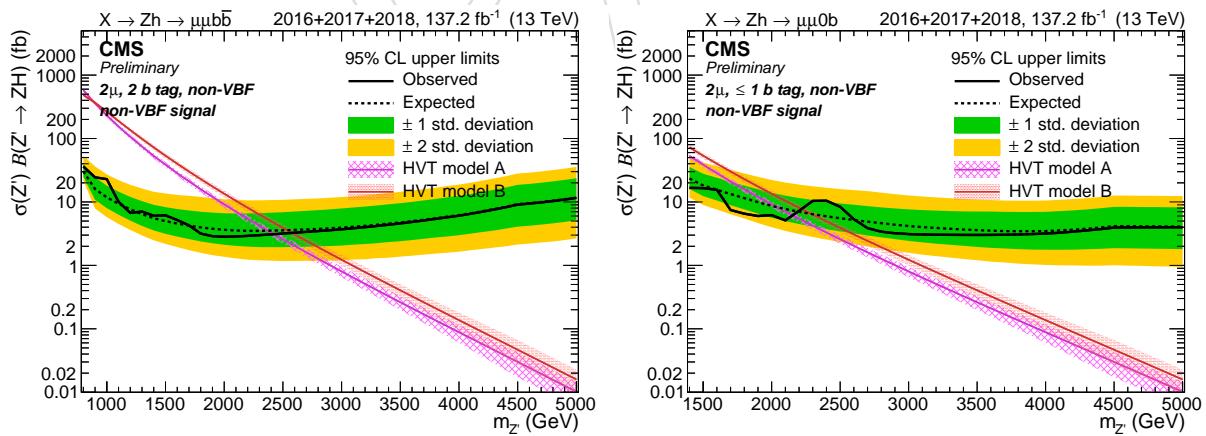


Figure 204: Observed and expected (with $\pm 1(2)\sigma$ band) 95% C.L. upper limit on $\sigma \times \mathcal{B}(X \rightarrow Zh)$ in the 2 μ 2 b-tag (left) and 0 b-tag (right) category for the no VBF signal, including all statistical and systematics uncertainties.

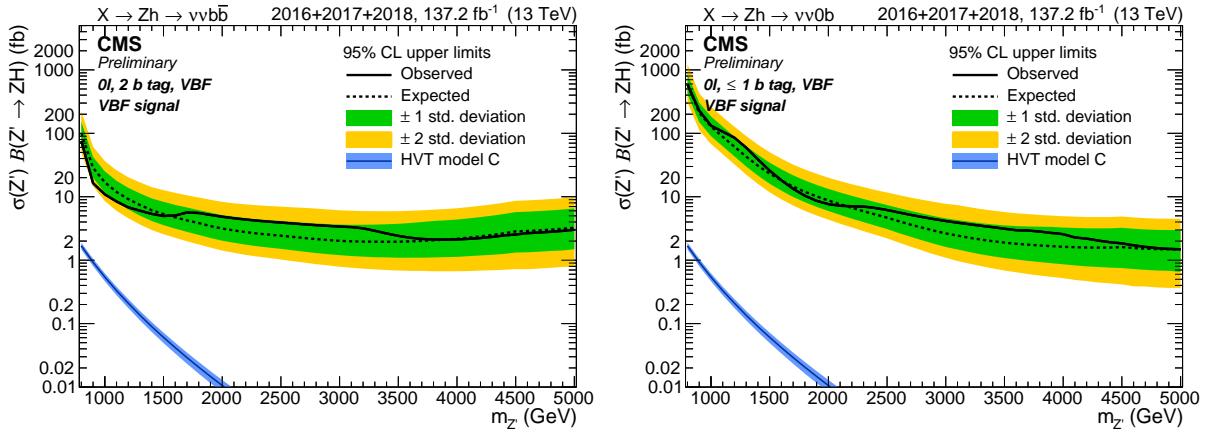


Figure 205: Observed and expected (with $\pm 1(2)\sigma$ band) 95%C.L. upper limit on $\sigma \times \mathcal{B}(X \rightarrow ZH)$ in the 0ℓ VBF 2 b-tag (left) and 0ℓ b-tag (right) category for the VBF signal, including all statistical and systematics uncertainties.

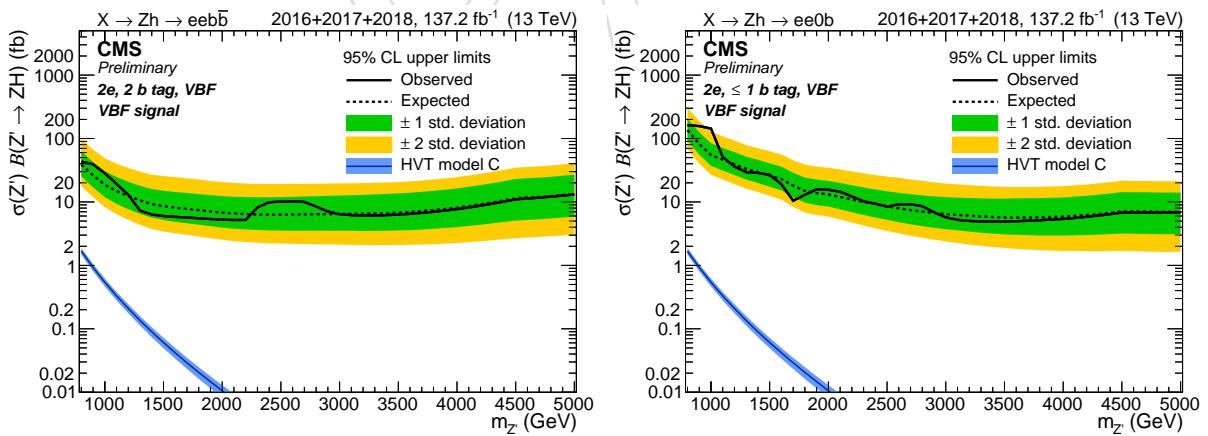


Figure 206: Observed and expected (with $\pm 1(2)\sigma$ band) 95%C.L. upper limit on $\sigma \times \mathcal{B}(X \rightarrow ZH)$ in the $2e$ VBF 2 b-tag (left) and $2e$, ≤ 1 b-tag (right) category for the VBF signal, including all statistical and systematics uncertainties.

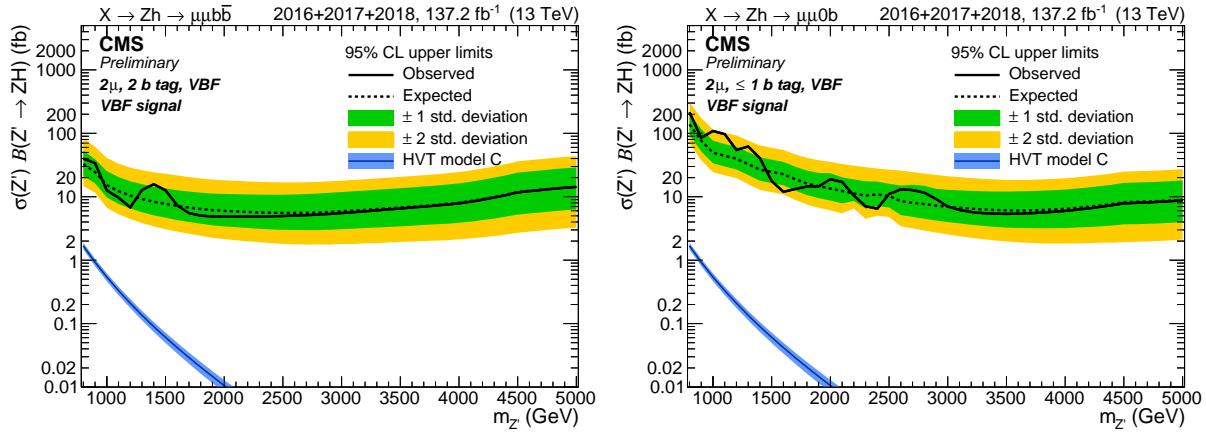


Figure 207: Observed and expected (with $\pm 1(2)\sigma$ band) 95%C.L. upper limit on $\sigma \times \mathcal{B}(X \rightarrow ZH)$ in the 2μ VBF 2 b-tag (left) and 0 b-tag (right) category for the VBF signal, including all statistical and systematics uncertainties.

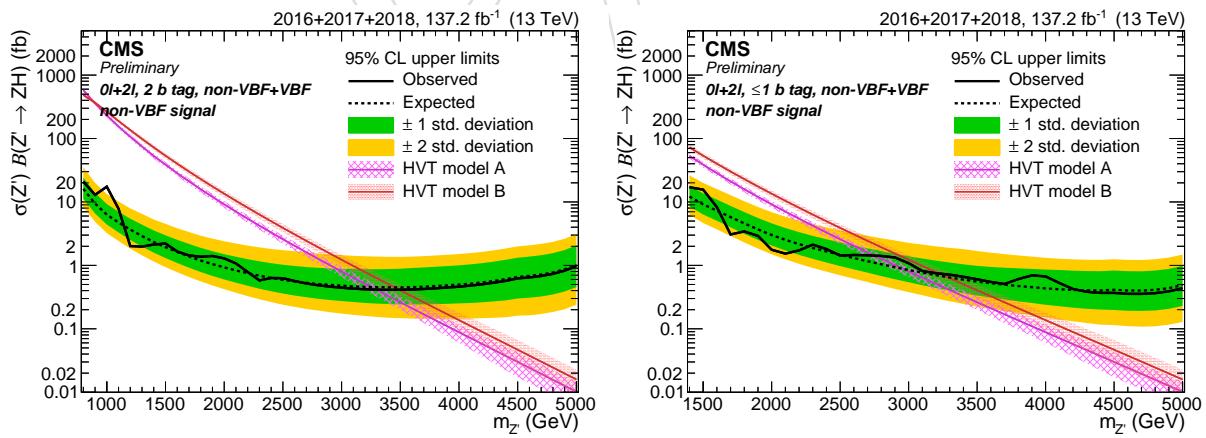


Figure 208: Observed and expected (with $\pm 1(2)\sigma$ band) 95%C.L. upper limit on $\sigma \times \mathcal{B}(X \rightarrow ZH)$ in the 2 b-tag combined (left) and 0 b-tag combined (right) category for the no VBF signal, including all statistical and systematics uncertainties.

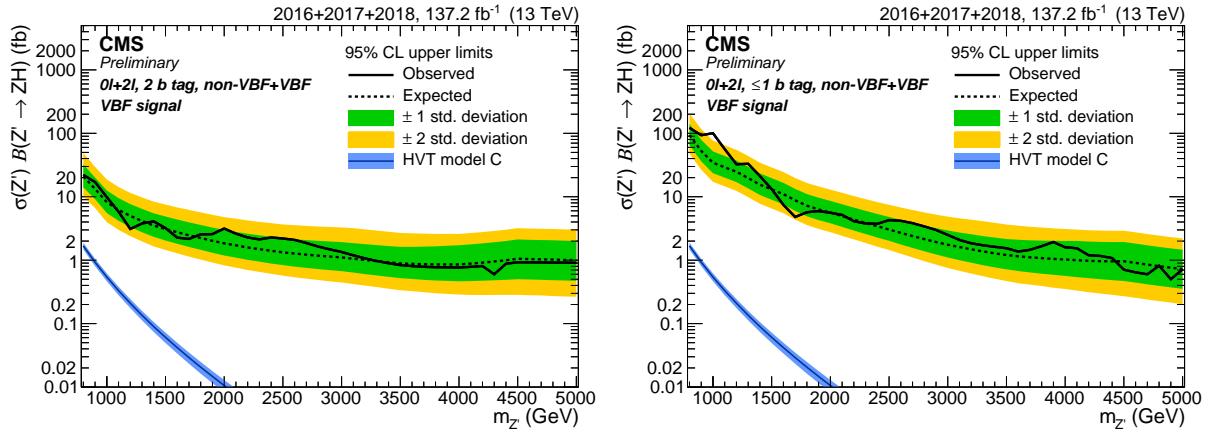


Figure 209: Observed and expected (with $\pm 1(2)\sigma$ band) 95%C.L. upper limit on $\sigma \times \mathcal{B}(X \rightarrow ZH)$ in the 2 b-tag combined (left) and 0 b-tag combined (right) category for the VBF signal, including all statistical and systematics uncertainties.

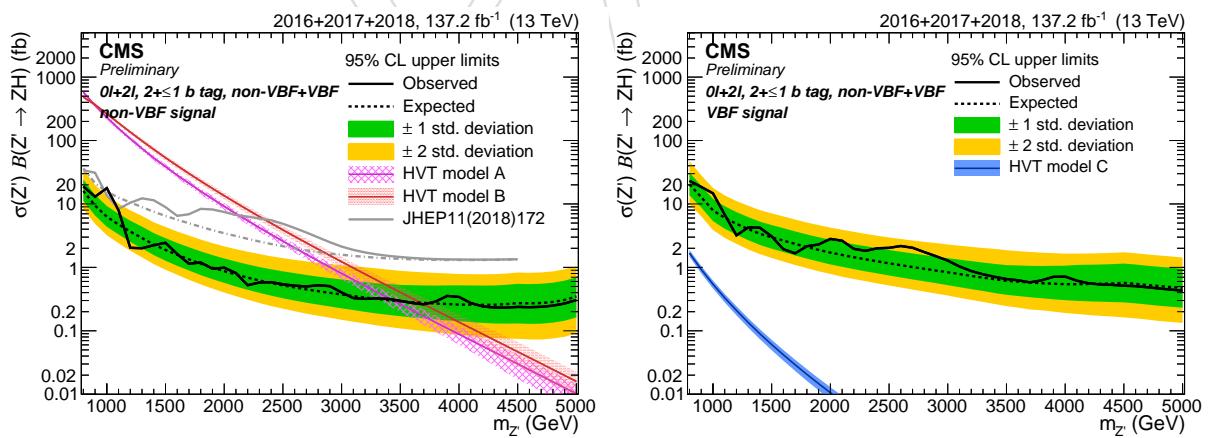


Figure 210: Observed and expected (with $\pm 1(2)\sigma$ band) 95%C.L. upper limit on $\sigma \times \mathcal{B}(X \rightarrow ZH)$ in the categories combined for the non VBF signal (left) and the VBF signal (right), including all statistical and systematics uncertainties.

1043 10.1 Fit pulls

1044 The signal extraction procedure described above allows the background to vary within the
1045 systematics uncertainties modifying the corresponding nuisance parameters. In this section
1046 these variations in the background are shown when the fit to the data is performed, both with
1047 the background-only and with background plus signal hypothesis.

1048 Prior to the data unblinding, the procedure is tested leaving the signal strength free to float,
1049 thus avoiding any information on the signal presence.

1050 The results are presented as histograms, where the bin values represent the pull values $\Delta x / \sigma_{in}$,
1051 and its error bar the fit constraining on the gaussian width of the nuisance parameter $\sigma_{out} / \sigma_{in}$,
1052 for both the background-only and the signal+background fit. The pull distributions are shown
1053 in Fig. 211 and Fig. 212.

DRAFT

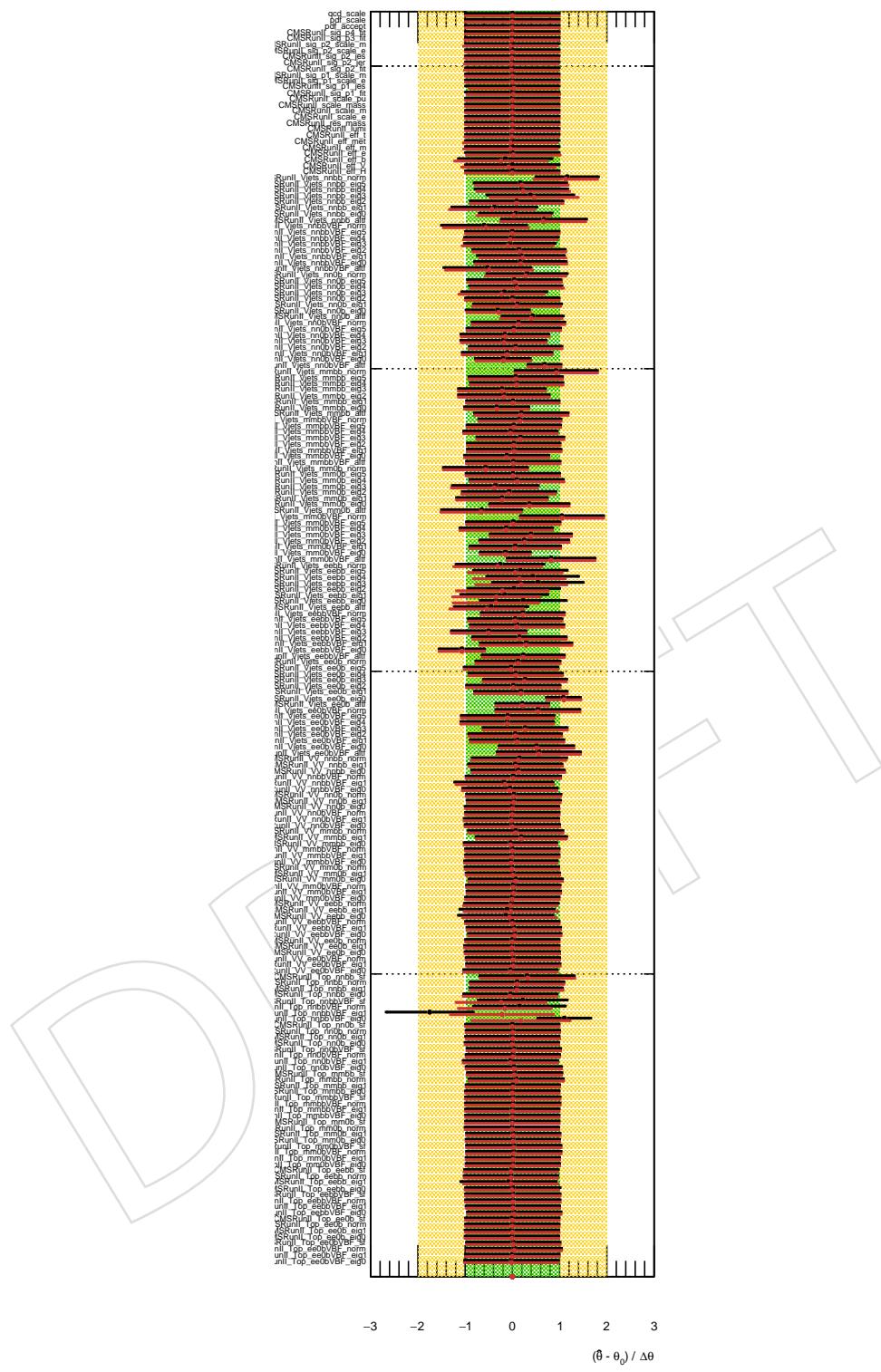


Figure 211: Pull values for the combination of all 0- and 2-lepton channels in both the background-only and signal+background hypotheses for the no VBF signal. The signal strength is left free to float. The considered signal is $m_\chi = 2000$ GeV.

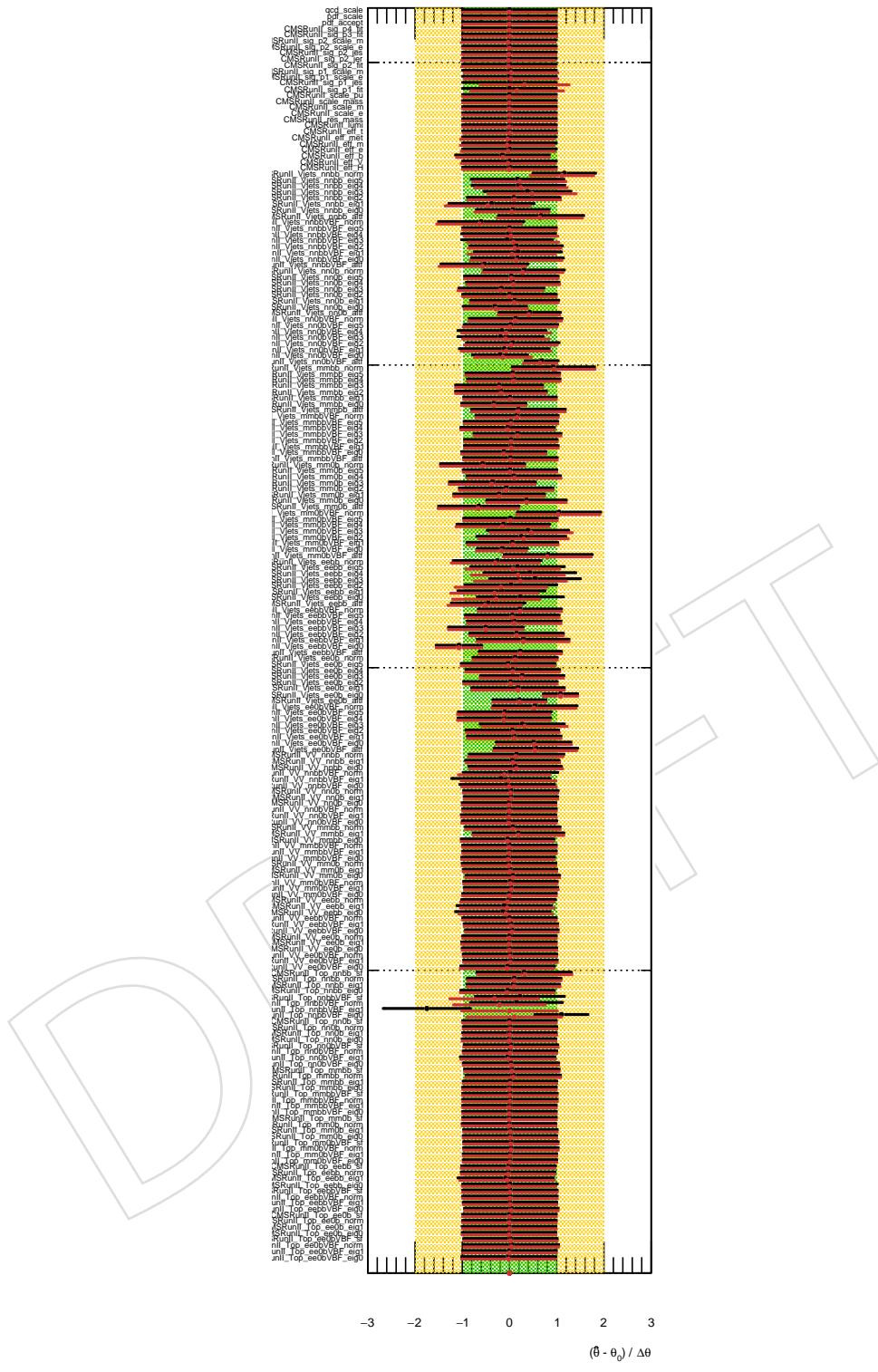


Figure 212: Pull values for the combination of all 0- and 2-lepton channels in both the background-only and signal+background hypotheses for the VBF signal. The signal strength is left free to float. The considered signal is $m_X = 2000$ GeV.

10.2 Impacts

The signal extraction procedure described above allows the background to vary within the systematics uncertainties modifying the corresponding nuisance parameters. The plots report the impacts and the pulls of the fits, performed on data in the $m_X = 1000$ GeV signal hypothesis. The signal normalization uncertainties due to PDF and QCD scales are profiled in the fits. The impacts are shown in Fig. 213 and Fig. 214.

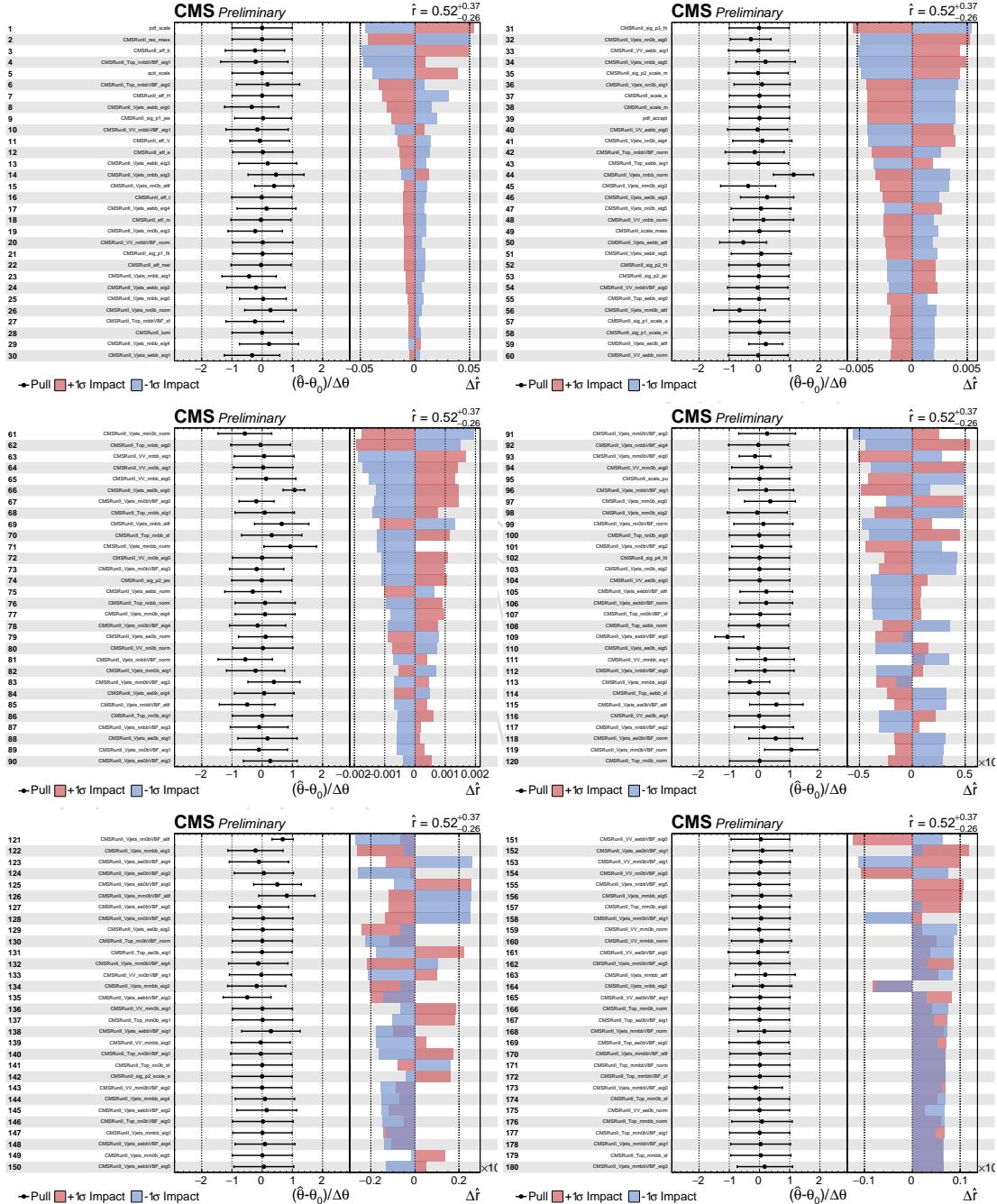


Figure 213: Impacts for the combination of all channels and the $m_X = 2000$ GeV signal hypothesis for the no VBF signal.

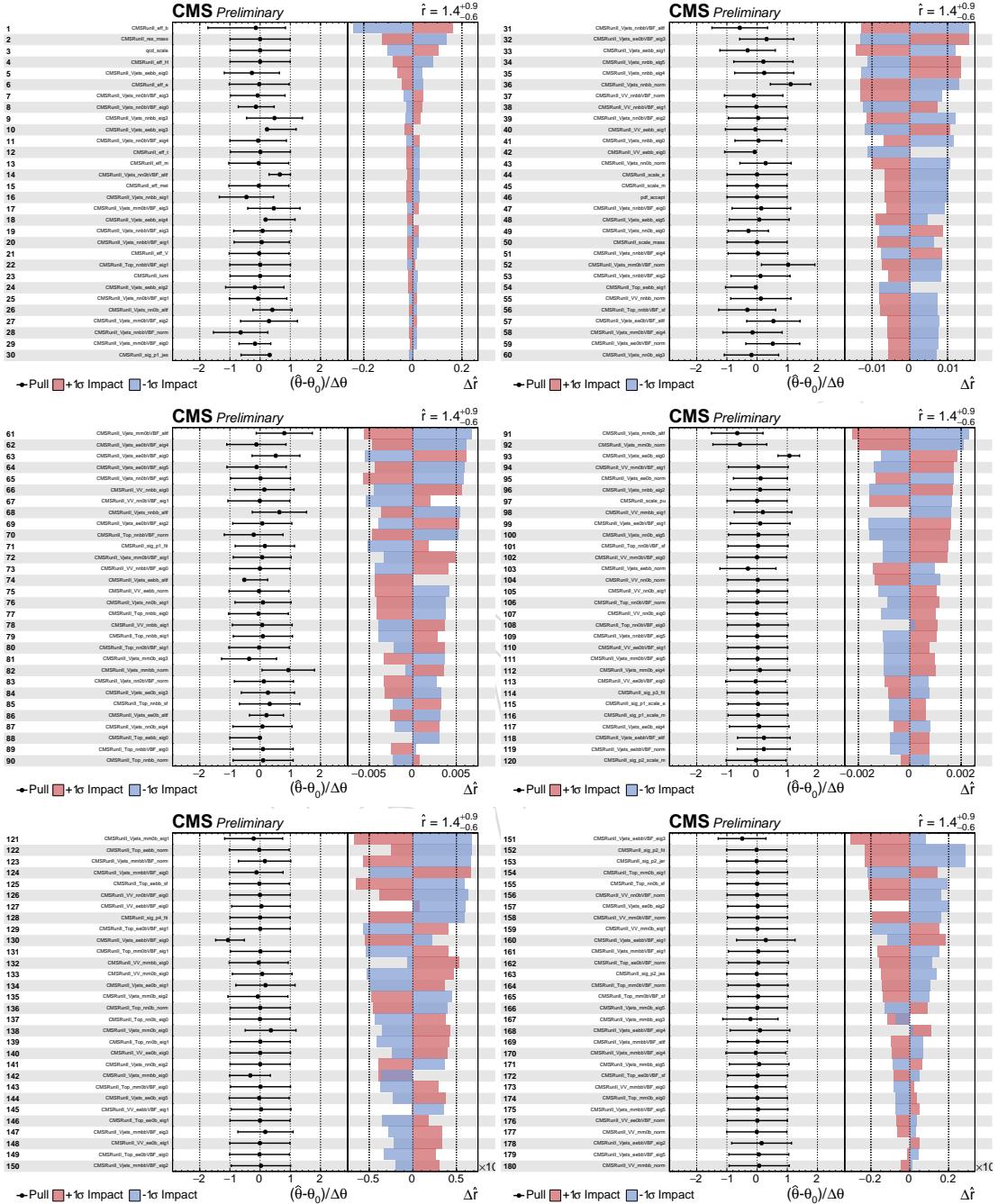


Figure 214: Impacts for the combination of all channels and the $m_X = 2000$ GeV signal hypothesis for the VBF signal.

1060 10.3 Bias tests

1061 These tests are performed to demonstrate that the alpha background estimation has a small or
 1062 negligible bias.

1063 In the first test, toys are generated from the background distributions in all the considered
 1064 categories combined. In the generation of the toy datasets, the signal strength is set to 0
 1065 (background-only toy datasets). The signal strength r is fitted to the toy datasets, and the fitted
 1066 value along with its uncertainty are used to calculate the pull, defined as r/σ_r . The pull
 1067 distributions are thus expected to have a mean at 0 and a standard deviation of 1. Figure 215
 1068 shows the pull distributions for 3 mass points. The distributions are fitted with a gaussian
 1069 function, whose mean and variance are compatible with the expected values. Additionally, the
 1070 maximum bias tolerated in exotic searches is 30% (relative to the statistical uncertainty in data).
 1071 The bias found in some mass points, although it is affected by a large statistical uncertainty,
 1072 is certainly within these bounds. Therefore, no significant correction or systematic uncertainty
 1073 appear to be necessary.

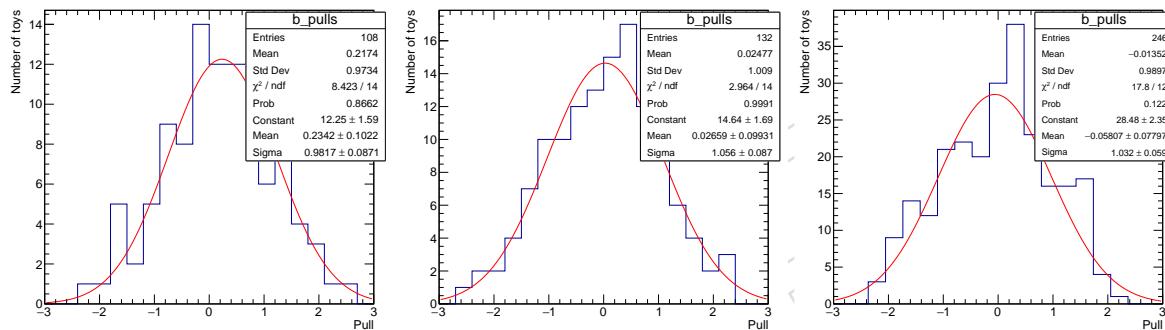


Figure 215: Pull distributions for the background-only toys in the $m_X = 1$ (left), 2 (center), and 3.5 TeV (right) mass points. A gaussian fit (red line) is superimposed to the pulls distributions.

1074 The second test consists in injecting the signal and re-fitting it. Also in this case, all categories
 1075 combined are considered, but a signal with a significance close to 3σ is injected on top of the ex-
 1076 pected background. As in the previous step, toy datasets are generated from the S+B template
 1077 and refitted with a free signal strength r . In this case, the pull definition is changed because of
 1078 the presence of the injected signal, and the pull is now defined as $(r - 1)/\sigma_r$ to make the pull
 1079 distribution peaking at 0. Figure 216 and 217 shows the distributions of the pulls for 5 mass
 1080 points for a Drell-Yan and VBF signal, respectively. Even if the number of toys is larger than
 1081 in the previous tests, the absence of large biases is confirmed. The bias (the mean of the fitted
 1082 gaussian) is always comprised between 6 and 18%, which is well below the tolerated amount.

1083 10.4 Goodness of fit

1084 The goodness of fit is tested using the Anderson-Darling method implemented in `combine`.
 1085 A total of 1000 toys are generated for all the considered categories, while setting the signal
 1086 strength to 0 in order to generate and fit background-only datasets that do not depend on the
 1087 signal hypothesis. Finally, the fit procedure only is performed on the real data, and its value is
 1088 represented by the red arrow in Fig 218. As the figure shows, the data shows an excellent sta-
 1089 tistical compatibility with the expected background, as it falls in the middle of the distributions
 1090 of the toy experiments.

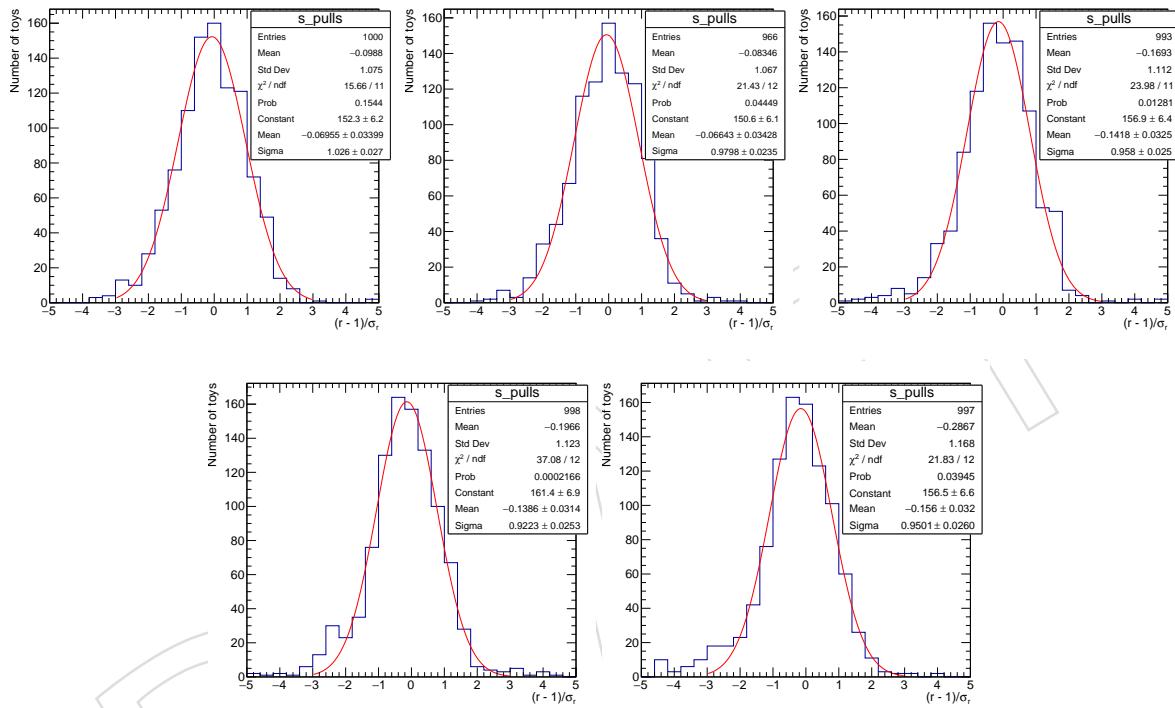


Figure 216: Pull distributions for the signal+background toys (signal injection test) in the $m_X = 1$ (top left), 2 (top center), 3 TeV (top right), 3.5 (bottom left), and 4 TeV (bottom right) mass points. A gaussian fit (red line) is superimposed to the pulls distributions. The signal considered is produced through Drell-Yan processes only.

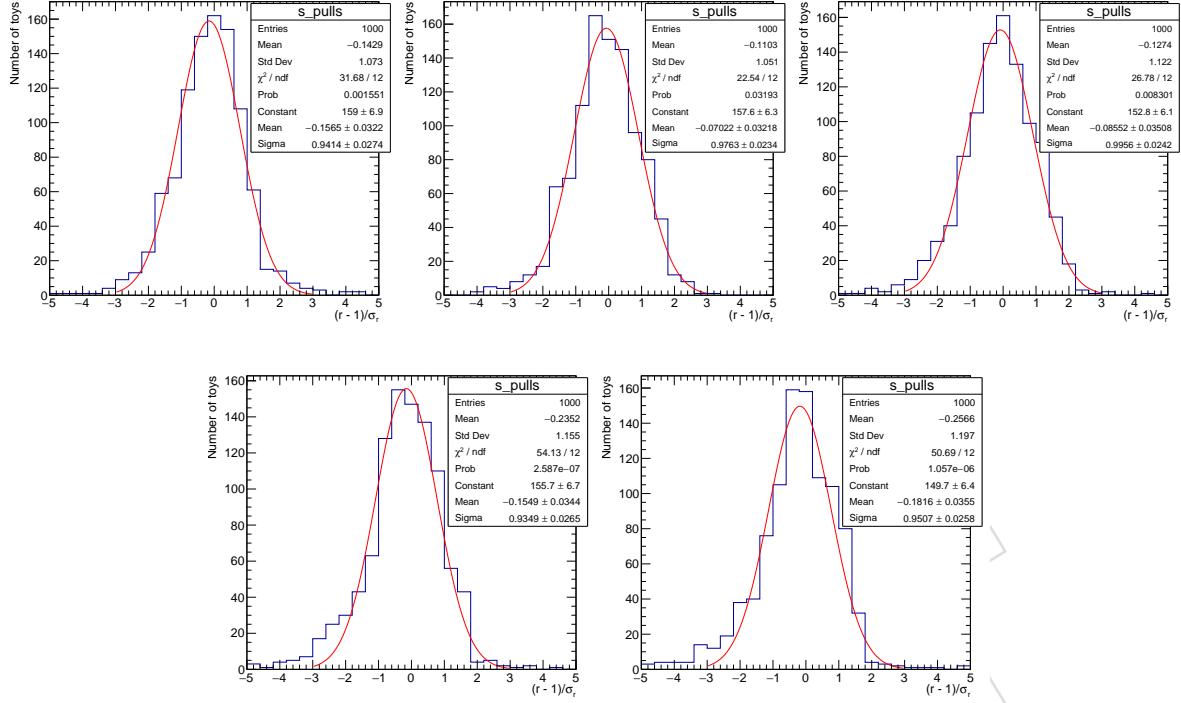


Figure 217: Pull distributions for the signal+background toys (signal injection test) in the $m_X = 1$ (top left), 2 (top center), 3 TeV (top right), 3.5 (bottom left), and 4 TeV (bottom right) mass points. A gaussian fit (red line) is superimposed to the pulls distributions. The signal considered is produced through VBF processes only.

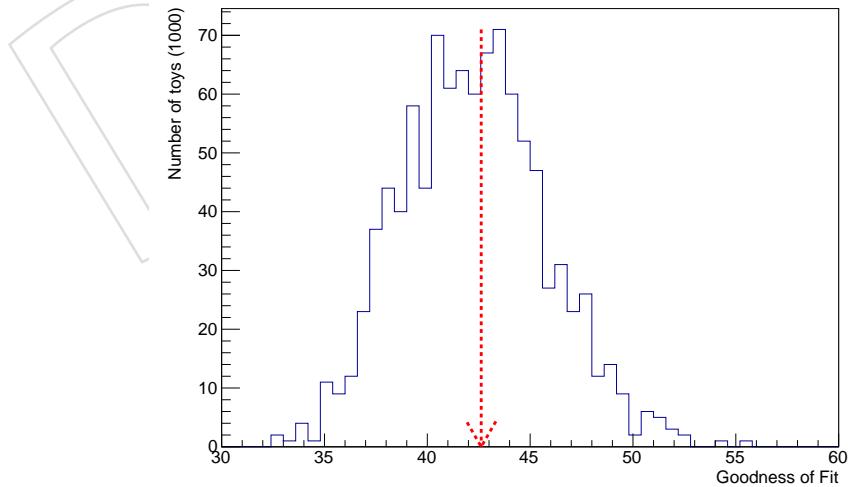


Figure 218: Distributions of the toy experiments (blue lines) and the data (red arrow) using the Anderson-Darling goodness-of-fit test. These distributions account for all the categories considered.

1091 11 Summary

1092 A search for a heavy resonance with mass between 800 and 5000 GeV, decaying into a Z boson
1093 and a Higgs boson, has been described. The data sample was collected by the CMS experiment
1094 at $\sqrt{s} = 13$ TeV during 2016 to 2018 and corresponds to integrated luminosity of 137.2 fb^{-1} .
1095 The final states explored include the leptonic decay modes of the Z boson, in events with zero
1096 and two charged electrons or muons. Higgs bosons are reconstructed from their decays to $b\bar{b}$
1097 pairs or the inclusive decay channel.

DRAFT

1098 **References**

- 1099 [1] ATLAS Collaboration, "Observation of a new particle in the search for the Standard
 1100 Model Higgs boson with the ATLAS detector at the LHC", *Phys. Lett. B* **716** (2012) 1,
 1101 doi:[10.1016/j.physletb.2012.08.020](https://doi.org/10.1016/j.physletb.2012.08.020), arXiv:[1207.7214](https://arxiv.org/abs/1207.7214).
- 1102 [2] CMS Collaboration, "Observation of a new boson at a mass of 125 GeV with the CMS
 1103 experiment at the LHC", *Phys. Lett. B* **716** (2012) 30,
 1104 doi:[10.1016/j.physletb.2012.08.021](https://doi.org/10.1016/j.physletb.2012.08.021), arXiv:[1207.7235](https://arxiv.org/abs/1207.7235).
- 1105 [3] CMS Collaboration, "Observation of a new boson with mass near 125 GeV in pp
 1106 collisions at $\sqrt{s} = 7$ and 8 TeV", *JHEP* **06** (2013) 081,
 1107 doi:[10.1007/JHEP06\(2013\)081](https://doi.org/10.1007/JHEP06(2013)081), arXiv:[1303.4571](https://arxiv.org/abs/1303.4571).
- 1108 [4] CMS Collaboration, "Precise determination of the mass of the Higgs boson and tests of
 1109 compatibility of its couplings with the standard model predictions using proton
 1110 collisions at 7 and 8 TeV", *Eur. Phys. J. C* **75** (2015) 212,
 1111 doi:[10.1140/epjc/s10052-015-3351-7](https://doi.org/10.1140/epjc/s10052-015-3351-7), arXiv:[1412.8662](https://arxiv.org/abs/1412.8662).
- 1112 [5] ATLAS Collaboration, "Measurement of the Higgs boson mass from the $H \rightarrow \gamma\gamma$ and
 1113 $H \rightarrow ZZ^* \rightarrow 4\ell$ channels in pp collisions at center-of-mass energies of 7 and 8 TeV with
 1114 the ATLAS detector", *Phys. Rev. D* **90** (2014) 052004,
 1115 doi:[10.1103/PhysRevD.90.052004](https://doi.org/10.1103/PhysRevD.90.052004), arXiv:[1406.3827](https://arxiv.org/abs/1406.3827).
- 1116 [6] ATLAS Collaboration, "Evidence for the spin-0 nature of the Higgs boson using ATLAS
 1117 data", *Phys. Lett. B* **726** (2013) 120, doi:[10.1016/j.physletb.2013.08.026](https://doi.org/10.1016/j.physletb.2013.08.026),
 1118 arXiv:[1307.1432](https://arxiv.org/abs/1307.1432).
- 1119 [7] CMS and ATLAS Collaborations, "Combined Measurement of the Higgs Boson Mass in
 1120 pp Collisions at $\sqrt{s} = 7$ and 8 TeV with the ATLAS and CMS Experiments",
 1121 doi:[10.1103/PhysRevLett.114.191803](https://doi.org/10.1103/PhysRevLett.114.191803), arXiv:[1503.07589](https://arxiv.org/abs/1503.07589). *Phys. Rev. Lett.*
- 1122 [8] A. Belyaev et al., "Technicolor Walks at the LHC", *Phys. Rev. D* **79** (2009) 035006,
 1123 doi:[10.1103/PhysRevD.79.035006](https://doi.org/10.1103/PhysRevD.79.035006), arXiv:[0809.0793](https://arxiv.org/abs/0809.0793).
- 1124 [9] F. Sannino and K. Tuominen, "Orientifold theory dynamics and symmetry breaking",
 1125 *Phys. Rev. D* **71** (2005) 051901, doi:[10.1103/PhysRevD.71.051901](https://doi.org/10.1103/PhysRevD.71.051901),
 1126 arXiv:[hep-ph/0405209](https://arxiv.org/abs/hep-ph/0405209).
- 1127 [10] R. Foadi, M. T. Frandsen, T. A. Ryttov, and F. Sannino, "Minimal Walking Technicolor: Set
 1128 Up for Collider Physics", *Phys. Rev. D* **76** (2007) 055005,
 1129 doi:[10.1103/PhysRevD.76.055005](https://doi.org/10.1103/PhysRevD.76.055005), arXiv:[0706.1696](https://arxiv.org/abs/0706.1696).
- 1130 [11] T. Han, H. E. Logan, B. McElrath, and L.-T. Wang, "Phenomenology of the little Higgs
 1131 model", *Phys. Rev. D* **67** (2003) 095004, doi:[10.1103/PhysRevD.67.095004](https://doi.org/10.1103/PhysRevD.67.095004),
 1132 arXiv:[hep-ph/0301040](https://arxiv.org/abs/hep-ph/0301040).
- 1133 [12] M. Schmaltz and D. Tucker-Smith, "Little higgs theories", *Annual Review of Nuclear and
 1134 Particle Science* **55** (2005), no. 1, 229–270,
 1135 doi:[10.1146/annurev.nucl.55.090704.151502](https://doi.org/10.1146/annurev.nucl.55.090704.151502),
 1136 arXiv:<http://dx.doi.org/10.1146/annurev.nucl.55.090704.151502>.
- 1137 [13] M. Perelstein, "Little higgs models and their phenomenology", *Progress in Particle and
 1138 Nuclear Physics* **58** (2007), no. 1, 247 – 291,
 1139 doi:[http://dx.doi.org/10.1016/j.ppnp.2006.04.001](https://doi.org/10.1016/j.ppnp.2006.04.001).

- [14] R. Contino, D. Pappadopulo, D. Marzocca, and R. Rattazzi, "On the effect of resonances in composite higgs phenomenology", *Journal of High Energy Physics* **2011** (2011), no. 10, 1–50, doi:10.1007/JHEP10(2011)081.
- [15] D. Marzocca, M. Serone, and J. Shu, "General composite higgs models", *Journal of High Energy Physics* **2012** (2012), no. 8, 1–52, doi:10.1007/JHEP08(2012)013.
- [16] B. Bellazzini, C. Csaki, and J. Serra, "Composite Higgses", *Eur. Phys. J.* **C74** (2014), no. 5, 2766, doi:10.1140/epjc/s10052-014-2766-x, arXiv:1401.2457.
- [17] D. Pappadopulo, A. Thamm, R. Torre, and A. Wulzer, "Heavy vector triplets: bridging theory and data", *Journal of High Energy Physics* **2014** (2014), no. 9, 1–50, doi:10.1007/JHEP09(2014)060.
- [18] V. D. Barger, W.-Y. Keung, and E. Ma, "A Gauge Model With Light W and Z Bosons", *Phys. Rev.* **D22** (1980) 727, doi:10.1103/PhysRevD.22.727.
- [19] T. Sjöstrand, S. Mrenna, and P. Skands, "A brief introduction to PYTHIA 8.1", *Comput. Phys. Commun.* **178** (2008) 852, doi:10.1016/j.cpc.2008.01.036, arXiv:0710.3820.
- [20] T. Sjöstrand, S. Mrenna, and P. Skands, "PYTHIA 6.4 physics and manual", *JHEP* **05** (2006) 026, doi:10.1088/1126-6708/2006/05/026, arXiv:hep-ph/0603175.
- [21] P. Skands, S. Carrazza, and J. Rojo, "Tuning PYTHIA 8.1: the Monash 2013 Tune", *Eur. Phys. J. C* **74** (2014) 3024, doi:10.1140/epjc/s10052-014-3024-y, arXiv:1404.5630.
- [22] CMS Collaboration, "Event generator tunes obtained from underlying event and multiparton scattering measurements", *Eur. Phys. J. C* **76** (2016) 155, doi:10.1140/epjc/s10052-016-3988-x, arXiv:1512.00815.
- [23] CMS Collaboration, "Extraction and validation of a new set of CMS PYTHIA8 tunes from underlying-event measurements", *Submitted to: Eur. Phys. J. C* (2019) arXiv:1903.12179.
- [24] S. Agostinelli et al., "Geant4—a simulation toolkit", *Nuclear Instruments and Methods in Physics Research Section A: Accelerators, Spectrometers, Detectors and Associated Equipment* **506** (2003), no. 3, 250 – 303, doi:10.1016/S0168-9002(03)01368-8.
- [25] CMS Collaboration, "Investigations of the impact of the parton shower tuning in Pythia 8 in the modelling of $t\bar{t}$ at $\sqrt{s} = 8$ and 13 TeV", CMS Physics Analysis Summary CMS-PAS-TOP-16-021, CERN, Geneva, 2016.
- [26] J. Alwall et al., "MadGraph 5 : Going Beyond", *JHEP* **1106** (2011) 128, arXiv:1106.0522.
- [27] Particle Data Group, J. Beringer et al., "Review of Particle Physics", *Phys. Rev. D* **86** (2012) 010001, doi:10.1103/PhysRevD.86.010001.
- [28] CMS Collaboration, "SummaryTable1G25ns - <https://twiki.cern.ch/twiki/bin/viewauth/CMS/SummaryTable1G25ns>",.
- [29] LHC Higgs Cross Section Working Group et al., "Handbook of LHC Higgs Cross Sections: 1. Inclusive Observables", CERN-2011-002 (CERN, Geneva, 2011) doi:10.5170/CERN-2011-002, arXiv:1101.0593.

- [1181] [30] Y. Li and F. Petriello, “Combining QCD and electroweak corrections to dilepton
 1182 production in FEWZ”, *Phys. Rev. D* **86** (2012) 094034,
 1183 doi:[10.1103/PhysRevD.86.094034](https://doi.org/10.1103/PhysRevD.86.094034), arXiv:[1208.5967](https://arxiv.org/abs/1208.5967).
- [1184] [31] J. M. Lindert et al., “Precise predictions for v+jets dark matter backgrounds”, *Eur. Phys. J.*
 1185 C **77** (2017) 829, doi:[10.1140/epjc/s10052-017-5389-1](https://doi.org/10.1140/epjc/s10052-017-5389-1), arXiv:[1705.04664](https://arxiv.org/abs/1705.04664).
- [1186] [32] P. Nason, “A new method for combining NLO QCD with shower Monte Carlo
 1187 algorithms”, *JHEP* **11** (2004) 040, doi:[10.1088/1126-6708/2004/11/040](https://doi.org/10.1088/1126-6708/2004/11/040),
 1188 arXiv:[hep-ph/0409146](https://arxiv.org/abs/hep-ph/0409146).
- [1189] [33] S. Frixione, P. Nason, and C. Oleari, “Matching NLO QCD computations with Parton
 1190 Shower simulations: the POWHEG method”, *JHEP* **11** (2007) 070,
 1191 doi:[10.1088/1126-6708/2007/11/070](https://doi.org/10.1088/1126-6708/2007/11/070), arXiv:[0709.2092](https://arxiv.org/abs/0709.2092).
- [1192] [34] S. Alioli, P. Nason, C. Oleari, and E. Re, “A general framework for implementing NLO
 1193 calculations in shower Monte Carlo programs: the POWHEG BOX”, *JHEP* **06** (2010) 043,
 1194 doi:[10.1007/JHEP06\(2010\)043](https://doi.org/10.1007/JHEP06(2010)043), arXiv:[1002.2581](https://arxiv.org/abs/1002.2581).
- [1195] [35] M. Czakon and A. Mitov, “Top++: A program for the calculation of the top-pair
 1196 cross-section at hadron colliders”, *Comput. Phys. Commun.* **185** (2014) 2930,
 1197 doi:[10.1016/j.cpc.2014.06.021](https://doi.org/10.1016/j.cpc.2014.06.021), arXiv:[1112.5675](https://arxiv.org/abs/1112.5675).
- [1198] [36] CMS Collaboration, “MET POG - Recommended MET Filters for Run II -
 1199 <https://twiki.cern.ch/twiki/bin/view/CMS/MissingETOptionalFiltersRun2>”,.
- [1200] [37] CMS Collaboration, “Approved and ongoing electron and photon trigger scale factor
 1201 measurements for Run2 data -
 1202 <https://twiki.cern.ch/twiki/bin/viewauth/CMS/EgHLTScaleFactorMeasurements>”,.
- [1203] [38] CMS Collaboration, “Reference muon id, isolation and trigger efficiencies for Run-II -
 1204 <https://twiki.cern.ch/twiki/bin/view/CMS/MuonReferenceEffsRun2>”,.
- [1205] [39] CMS Collaboration, “Performances of E_T^{miss} trigger for heavy diboson searches in 2017
 1206 data”, CMS Note 2017/045, 2017.
- [1207] [40] CMS Collaboration, “Performances of E_T^{miss} trigger for heavy diboson searches in 2018
 1208 data”, CMS Note 2018/048, 2018.
- [1209] [41] A. Rizzi, S. Donato, P. Azzurri, “Primary vertex sorting”,
 1210 <https://indico.cern.ch/event/369417/contributions/1788757/attachments/734933/1008272/pv->
 1211 sorting-xpog.pdf, CERN,
 1212 2015.
- [1213] [42] CMS Collaboration, “Pileup Reweighting Procedure -
 1214 <https://twiki.cern.ch/twiki/bin/viewauth/CMS/PileupReweighting>”,.
- [1215] [43] CMS Collaboration, “Utilities for Accessing Pileup Information for Data -
 1216 <https://twiki.cern.ch/twiki/bin/view/CMS/PileupJSONFileforData>”,.
- [1217] [44] CMS Collaboration, “EGamma POG - Cut based electron ID for Run2 -
 1218 <https://twiki.cern.ch/twiki/bin/view/CMS/CutBasedElectronIdentificationRun2>”,.
- [1219] [45] CMS Collaboration, “Performance of CMS muon reconstruction in pp collision events at
 1220 $\sqrt{s} = 7 \text{ TeV}$ ”, *JINST* **7** (2012) P10002, doi:[10.1088/1748-0221/7/10/P10002](https://doi.org/10.1088/1748-0221/7/10/P10002),
 1221 arXiv:[1206.4071](https://arxiv.org/abs/1206.4071).

- [46] CMS Collaboration, "Muon POG - Muon ID and Isolation for Run2 - <https://twiki.cern.ch/twiki/bin/view/CMS/SWGuideMuonIdRun2>",
- [47] CMS Collaboration, "Particle-flow event reconstruction in CMS and performance for jets, taus, and E_T^{miss} ",
- [48] CMS Collaboration, "Commissioning of the particle-flow event reconstruction with the first LHC collisions recorded in the CMS detector",
- [49] CMS Collaboration, "Pileup Removal Algorithms", Technical Report CMS-PAS-JME-14-001, CERN, Geneva, 2014.
- [50] D. Bertolini, P. Harris, M. Low, and N. Tran, "Pileup per particle identification", *Journal of High Energy Physics* **2014** (2014), no. 10, 59, doi:10.1007/JHEP10(2014)059.
- [51] R. Salam, "Fastjet package", technical report, CNRS, 2011.
- [52] M. Cacciari, G. P. Salam, and G. Soyez, "The anti- k_t jet clustering algorithm", *JHEP* **04** (2008) 063, doi:10.1088/1126-6708/2008/04/063, arXiv:0802.1189.
- [53] A. J. Larkoski, S. Marzani, G. Soyez, and J. Thaler, "Soft Drop", *JHEP* **05** (2014) 146, doi:10.1007/JHEP05(2014)146, arXiv:1402.2657.
- [54] CMS Collaboration, "Measurement of $B\bar{B}$ angular correlations based on secondary vertex reconstruction at $\sqrt{s} = 7 \text{ TeV}$ ", *JHEP* **03** (2011) 136, doi:10.1007/JHEP03(2011)136.
- [55] CMS Collaboration, "Identification of b-quark jets with the CMS experiment", *JINST* **8** (2013) P04013, doi:10.1088/1748-0221/8/04/P04013, arXiv:1211.4462.
- [56] "Recommendation for using b-tag objects in physics analyses", 2019. <https://twiki.cern.ch/twiki/bin/viewauth/CMS/BtagRecommendation>.
- [57] CMS Collaboration, "Reference measurements and calibrations for Run-II - <https://twiki.cern.ch/twiki/bin/view/CMS/MuonReferenceSelectionAndCalibrationsRun2>",
- [58] "W/z-tagging of jets", 2016. <https://twiki.cern.ch/twiki/bin/viewauth/CMS/JetWtagging>.
- [59] CMS Collaboration, "Search for heavy resonances decaying into a vector boson and a Higgs boson in final states with charged leptons, neutrinos, and b quarks at $\sqrt{s} = 13 \text{ TeV}$ ", *JHEP* **11** (2018) doi:10.1007/JHEP11(2018)172, arXiv:1807.02826.
- [60] CMS Collaboration Collaboration, "CMS Luminosity Measurement for the 2016 Data Taking Period", Technical Report CMS-PAS-LUM-17-001, CERN, Geneva, 2016.
- [61] CMS Collaboration Collaboration, "CMS luminosity measurement for the 2017 data-taking period at $\sqrt{s} = 13 \text{ TeV}$ ", Technical Report CMS-PAS-LUM-17-004, CERN, Geneva, 2017.
- [62] CMS Collaboration Collaboration, "CMS luminosity measurement for the 2018 data-taking period at $\sqrt{s} = 13 \text{ TeV}$ ", Technical Report CMS-PAS-LUM-18-002, CERN, Geneva, 2018.
- [63] A. L. Read, "Presentation of search results: the cls technique", *J. Phys.* **G28** (2002) 2693, doi:10.1088/0954-3899/28/10/313.

- [64] T. Junk, "Confidence level computation for combining searches with small statistics", *Nucl. Instrum. Meth.* **A434** (1999) 435, arXiv:9902006.
- [65] L. Moneta et al., "The RooStats Project", in *13th International Workshop on Advanced Computing and Analysis Techniques in Physics Research (ACAT2010)*. SISSA, 2010. arXiv:1009.1003. PoS(ACAT2010)057.
- [66] "Cms higgs combine tool", 2013. <https://twiki.cern.ch/twiki/bin/view/CMS/SWGuideHiggsAnalysisCombinedLimit>.
- [67] CMS Collaboration, "Search for standard model higgs boson in pp collisions at $\sqrt{s} = 7$ tev", Physics Analysis Summary CMS-PAS-HIG-11-011, CERN, 2011.

DRAFT